# Autonomous Frequency Domain Identification: Theory and Experiment

Y. Yam
D.S. Bayard
F.Y. Hadaegh
E. Mettler
M.H. Milman
R.E. Scheid

April 15, 1989

NASA

19980309 307

U5682

Autonomous Frequency Domain Identification: Theory and Experiment

Y. Yam
D.S. Bayard
F.Y. Hadaegh
E. Mettler
M.H. Milman
R.E. Scheid

April 15, 1989

FOREWORD

The research documented herein was carried out over a two year period beginning in FY'87; and represents the first phase of a multi-year plan to develop a system of methods, algorithms and software for the on-orbit identification of structural dynamic parameters and system transfer function characterization for control of large space platforms and flexible spacecraft. An interim objective is to demonstrate technology readiness for application of on-orbit identification in ground-based and flight experiments. Specific research areas include development of non-parametric frequency domain and parametric time domain techniques and algorithms, on-line methods for initialization of recursive and data block algorithms, globally convergent identification methods, and integrated identification and robust control.

Control performance of spacecraft with extended structures and on-orbit assembly/ deployment operations such as manned and unmanned space platforms, large antennas, and large optical reflectors or interferometers will be very sensitive to inevitable uncertainties in predicted dynamics. Past experience indicates that in-flight instabilities may occur because of deficiencies in the pre-flight dynamical model embedded in the on-board control system design. The activity under this research plan is unique in that, in addition to conducting innovative research in on-orbit identification methods, it also develops the technology to a level of readiness to support advanced spacecraft control subsystem designs and automated in-flight tuning of plant models and controller performance.

The problem of on-orbit identification differs significantly from the problem of identification performed on the ground. In particular, the actuators and sensors are severely restricted in number, type, and placement, the time allocated for experimentation is relatively short, and data which is required must often be processed quickly for use in controller tuning, etc. These requirements are quite challenging and require a significant advance over techniques presently used for ground testing.

ACKNOWLEDGEMENTS

TECHNICAL ABSTRACT

The analysis, design, and on-orbit tuning of robust controllers require more information about the plant than simply a nominal estimate of the plant transfer function. Information is also required concerning the uncertainty in the nominal estimate, or more generally, the identification of a model set within which the true plant is known to lie. The identification methodology that was developed and experimentally demonstrated makes use of a simple but useful characterization of the model uncertainty based on the output error. This is a characterization of the "additive uncertainty" in the plant model, which has found considerable use in many robust control analysis and synthesis techniques. The identification process is initiated by a stochastic input u which is applied to the plant p giving rise to the output y. Spectral estimation ($h = P_{uy}/P_{uu}$) is used as an estimate of p and the model order is estimated using the product moment matrix (PMM) method. A parametric model $\widehat{p}$ is then determined by curve fitting the spectral estimate to a rational transfer function. The additive uncertainty $\delta_m = p - \widehat{p}$ is then estimated by the cross-spectral estimate $\Delta = P_{ue}/P_{uu}$ where $e = y - \widehat{y}$ is the output error, and $\widehat{y} = \widehat{p}u$ is the computed output of the parametric model subjected to the actual input u. The experimental results demonstrate the curve fitting algorithm produces the reduced-order plant model which minimizes the additive uncertainty. The nominal transfer function estimate $\widehat{p}$ and the estimate Δ of the additive uncertainty δ_m are subsequently available to be used for optimization of robust controller performance and stability.

EXECUTIVE SUMMARY

On-orbit system identification of large flexible space systems enables on-line design of robust, high performance control systems. This capability has the potential to improve the performance robustness and control accuracy under operational constraints and environmental uncertainties far beyond that attainable by using nominal system descriptions obtained from ground testing and analysis alone.

This research successfully demonstrates that on-orbit identification is a realistic objective. A novel automated frequency domain identification methodology was developed and experimentally verified on the JPL/AFAL experiment facility which is designed for emulation of on-orbit testing and control scenarios. The testbed structure is shown in Figure E-1. The basic approach of this research is to nonparametrically identify the transfer function of the system using different forms of excitations and then obtain a parametric model of the system by curve fitting the spectral estimates to a rational transfer function. The model order is estimated using the product moment matrix. Uncertainty bounds needed for on-line robust control designs and fine tuning are estimated using the cross-spectral analysis of the output error. Thus, the approach avoids recreating in an on-orbit environment the extensive instrumentation required for ground testing and makes efficient use of the actuators and sensors already available on the space system for control applications.

Some practical issues associated with the approach taken by this research for on-orbit identification and other results obtained from both the theoretical and practical developments in the course of this work on the facility testbed are discussed as follows:

1) The system identification is being designed to operate with a high degree of autonomy and restrict the "human in the loop" requirements.

2) It is well known that frequency domain curve fitting techniques based on equation error representations have implicit high frequency emphasis. This problem is overcome in the present study by using an iterative reweighting scheme. A novel smoothing technique is also introduced to alleviate the problem of resonances estimated early in the sequence reinforcing themselves in the reweighting scheme and becoming fixed points of the iteration.

3) The additive uncertainty is estimated by the output error cross-correlation. This approach is shown to provide a superior estimation of additive uncertainty than the traditional approach of utilization of the curve fitted error.

4) Input signals considered here are wideband, narrowband, and sine-dwell processes. On-line capability of conducting digital filter design is available to support other input designs. The issue of "optimal" input design subject to on-orbit constraints is a topic for continuing investigation.

5) Special techniques for Sine-Dwell gain and phase estimation were required to avoid errors associated with using sampled data sinusoidal inputs. Standard correlation techniques produced very poor results, particularly with respect to the low frequency structural modes. A recursive least squares algorithm with exponential forgetting was developed to ensure robust and accurate estimation for this class of problems.

6) The length of the experiment time is driven by the frequency of the lowest mode. This has strong relevance to the on-orbit time allocated to performing on-orbit identification. It is shown that a reasonable experiment time provided a good assessment of the low frequency component of the structure, i.e., approximately 27 minutes for the 0.09 Hz mode of the structure.

7) The present investigation considers identification of single-input single-output transfer functions. Multiple-input multiple-output system identification would also be accommodated with the present scheme by processing each input/output pair separately. More efficient processors are desired for the multiple-input multiple-output case.

8) A two step approach is taken for the determination of model order. First, an initial estimate of the model order is obtained using a product moment matrix (PMM) test. Second, the optimal order in the vicinity of this estimate is searched for by a sequence of curve fits with varying orders. The optimal order is judged by comparing the quality of the output error profiles for each curve fit. Although this approach appears to work well in practice, the efficiency of the search depends on the initial estimate from the PMM test.

9) Two approaches have been developed for implementing the product moment matrix test. The deterministic algorithm PMMD (i.e., exact assuming no measurement noise), gave consistently better performance than the stochastic algorithm PMMS (which approximates sums by correlations). However, even PMMD had a tendency to underestimate the model order when compared to the best estimate obtained based on minimizing output error. Methods to improve the PMM estimate in the future include proper choice of threshold value (i.e., on the determinant or determinant ratios), and proper treatment of noise disturbance effects.

10) The experiment results demonstrate that the identification algorithm developed produces the reduced-order plant model which minimizes a uniform bound on the additive uncertainty.

PHOTOGRAPH

SCHEMATIC
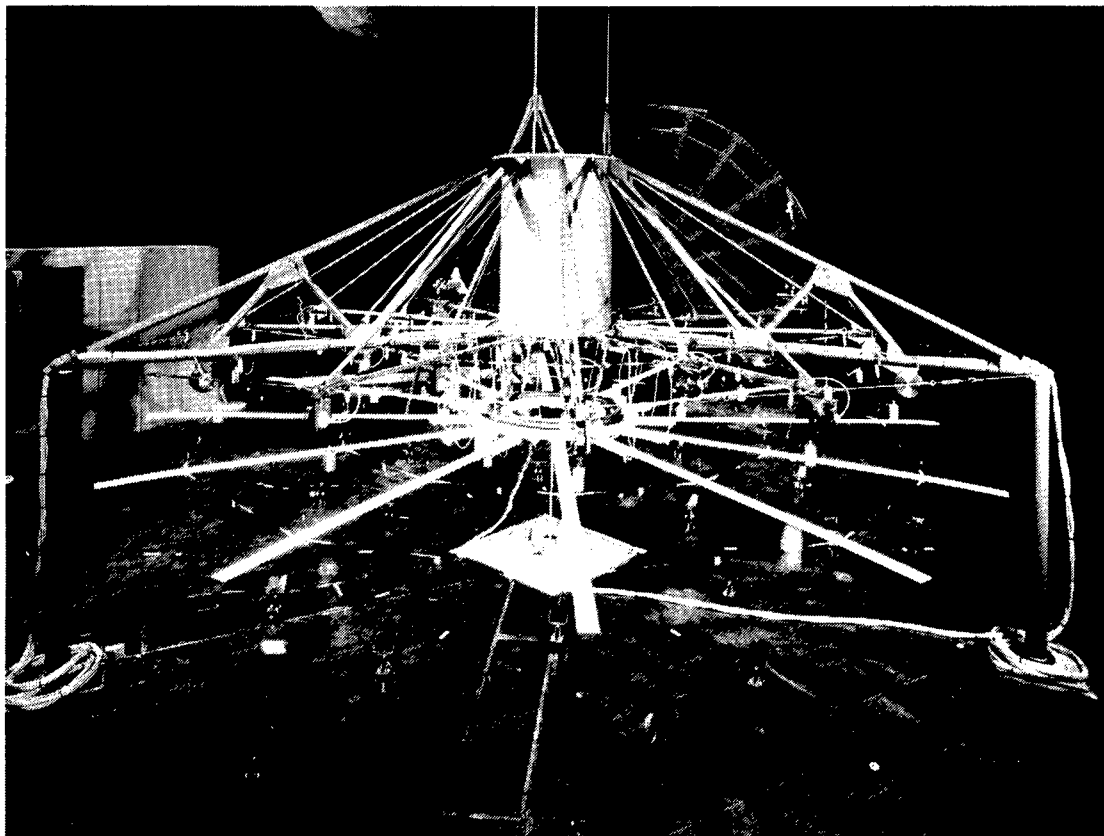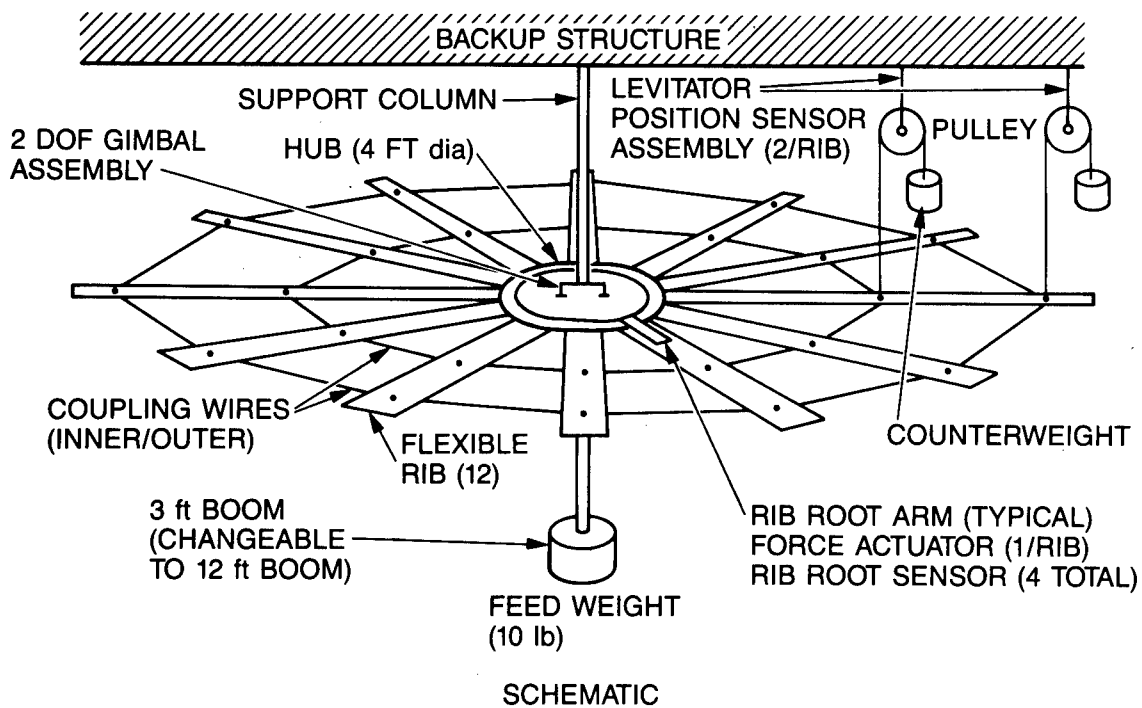
Fig. E-1. JPL/AFAL Flexible Structure Testbed

TABLE OF CONTENTS

Chapter 3. EXPERIMENT RESULTS

Chapter 4. CONCLUSION

Chapter 1. IDENTIFICATION SYSTEM DESCRIPTION

1.1 Introduction and Objectives

This report summarizes the development and experimental verification of a frequency domain identification methodology for large space structures. This methodology is focused to support the following objectives

1) Estimation of system quantities useful for robust control analysis and design

2) To perform system identification in an on-orbit environment

3) Automated operations

The overall functional architecture of the identification system is depicted in Fig. 1.1-1, and will be discussed in detail in Sect. 1.2. Briefly, the basic approach is to non-parametrically identify the sampled-data plant $p(e^{j\omega T})$ in the frequency domain using either stochastic or sine-dwell input excitation experiments, and then to obtain a parametric model $\hat{p}(e^{j\omega T})$ of the transfer function by curve-fitting techniques. Finally, a cross-spectral analysis of the output error is used to determine the additive uncertainty $\delta_m = p - \hat{p}$ in the estimated transfer function. The nominal transfer function estimate $\hat{p}$ and the estimate Δ of the associated additive uncertainty δ_m are then ready to be used for robust control analysis and design.

Some special features of the scheme are outlined below,

- On-line digital filter design to support on-orbit optimal input design and data composition (Sect. 2.3)

- Data composition of experimental data in overlapping frequency bands to overcome finite actuator power constraints (Sect. 2.5)

- Recursive least squares sine-dwell estimation to accurately handle digitized sinusoids and low frequency modes (Sect.2.6)

- Automated estimation of model order using a product moment matrix method (Sect. 2.7).

- Sample-data transfer function parametrization to support digital control design

- Curve fitting algorithm with iterative reweighting technique to assure minimum variance estimation (Sect. 2.9)

- Robust root solvers which accurately factorize high order polynomials to determine frequency and damping estimates from plant denominator coefficients (Sect. 2.9.5)

- Output error characterization of model additive uncertainty to support robustness analysis (Sect. 2.10)

The test bed for this effort is the large ground test structure developed by JPL/AFAL for emulation of on-orbit testing and control scenarios. The experiment is housed in the JPL celestarium, and has been described in detail [1]. A brief overview of the physical structure is provided in Sect. 1.3 as background for the identification experiments.

The overall algorithm and software development required to implement the identification system has been quite extensive. A brief historical account may be helpful. Algorithms were first developed on IBM PC-AT's by individual analysts responsible for each task. Software developed at this stage was mostly in the form of scientific subroutines and diagnostic programs. Original software was written as required to support algorithm development, and a multitude of Fortran scientific subroutines were utilized from various sources (e.g., Numerical Recipes [2], IEEE Programs for Digital Signal Processing [3], Lawson and Hanson [4]). Modularization of the project in this fashion allowed extensive development and optimization of individual algorithms before integration was required. Needless to say, many difficult analytical and numerical problems were overcome at this stage. The wisdom gained is summarized in Chapter 2, along with Fortran code for various special purpose subroutines (software developed at this stage will compile and run with Lahey Fortran on a PC-AT computer).

Debugged software subroutines were then "handed off" for integration into the identification system software. System software was developed on the GC-VAX (in anticipation of rehosting on the experiment facility micro-VAX) and was designed to meet the experiment interface requirements given in [5]. The system software was then rehosted on the facility micro-Vax and final integration was completed. The final menu layout is outlined in Sect. 1.2, and the final software specification document is given in [14].

The results of the identification experiments are summarized in Chapter 3, where they are organized according to a typical on-orbit testing scenario. All of Chapter 3 is comprised of real experimental data, in contrast to much of the development work in Chapter 2 which was performed on simulated data. Very little difference was found between algorithm performance on real and simulated data. In retrospect, this appears to be due essentially to the robustness of the numerical design of the individual algorithms, rather than the ideality of the plant or cleanliness of the data.

Several documents will be referenced in the course of this report which provide additional information on various aspects of the JPL/AFAL structure and system identification efforts. This includes details on the construction and modeling of the physical structure [1][6], the overall system identification experiment plan [7], a detailed description of the final experimental software [8], and an overview of the ID software subsystem using simulated data [9]. Furthermore, the underlying theory behind the nonparametric frequency domain identification approach and curve fitting can be found in [10], and the basic philosophy of the on-orbit identification in support of on-line control redesign is discussed in [11][12][13].
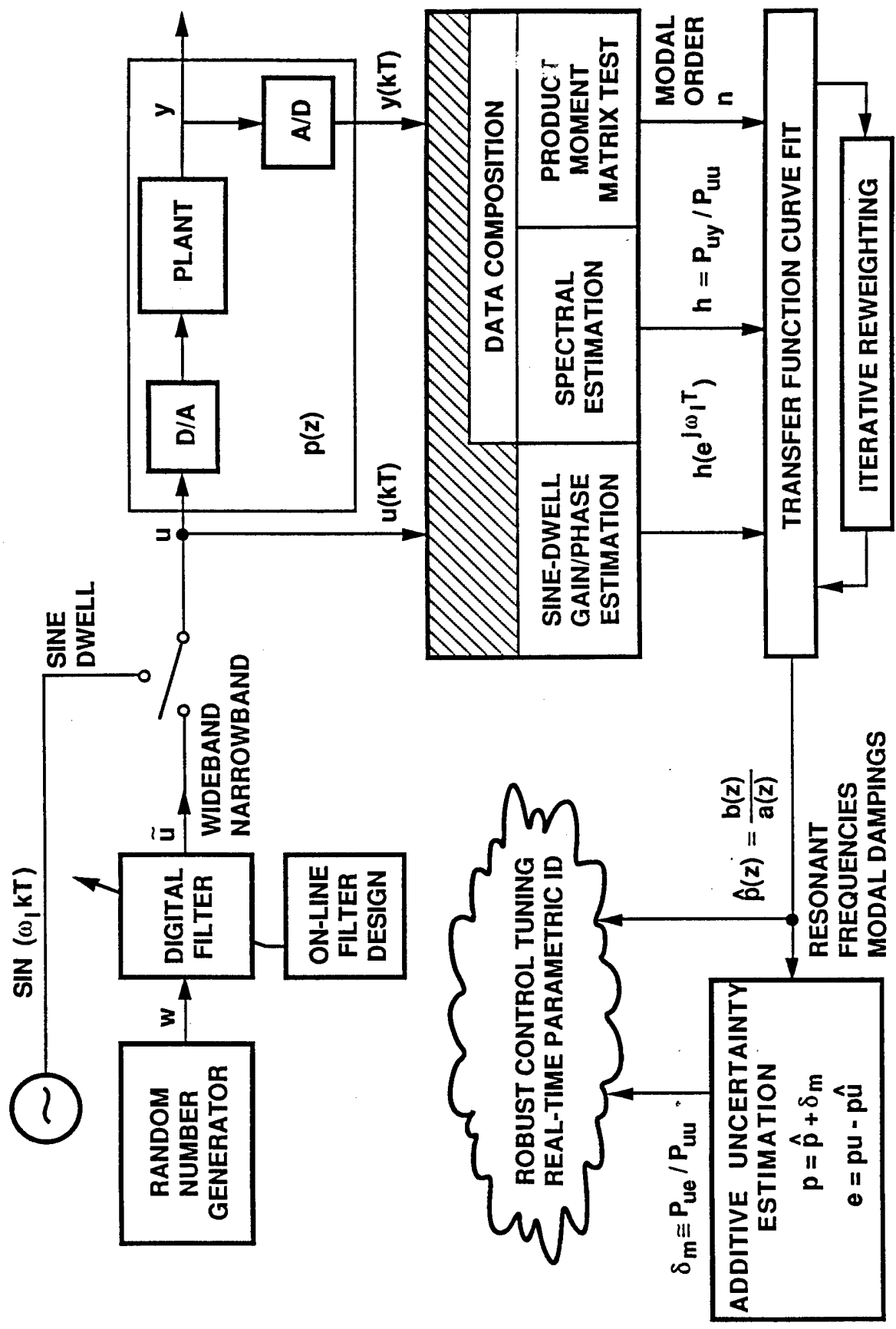
Fig. 1.1-1 Functional Architecture of System ID Experiment Software.

1.2 Functional Architecture and Software Description

The functional architecture is outlined schematically in Fig. 1.1-1. The flow of the various processes is menu driven and controlled from a single human operator. The overall menu layout is given in Fig. 1.2-1. Although a user's manual for the identification system is beyond the scope of this report, we will try to present an overview of the system software, and typical use of the system functions. If more information is desired, specific use of individual menus and the internal workings of the software subroutines can be obtained by consulting various sections of Chapter 2, and typical sequences of menu commands are exemplified in the experimental demonstrations of Chapter 3. The complete software description as well as the FORTRAN listing of the integrated identification system software is given in [14].

The functional flow of the identification system is described below. Bold type paragraphs provide a summary of the system functions. Additional detail on any particular function is found in the intervening ordinary type paragraphs.

1) **The plant $p(e^{j\omega T})$ is excited by one of a variety of possible input excitations $u(kT)$ of both stochastic (i.e., wideband or narrowband) or deterministic (i.e., sine-dwell) types giving rise to plant output $y(kT)$.**

The wideband input is simply a random number generator which produces independent uniformly distributed variates (Sect. 2.2, MENU(4,4,2)). The narrowband input is produced by digitally filtering the wideband input according to desired spectral characteristics (Sect. 2.4, MENU(4,4,2)). The capability for on-line digital filter design is provided as part of the system software (Sect. 2.3, MENU(4,4,9)). The sine-dwell inputs are piecewise constant approximations to true sinusoids, consistent with the sample-and-hold discretization (Sect. 2.6, MENU(4,4,3)).

Wideband experiments can also be constructed artificially using a technique which we call data composition (Sect. 2.5, MENU(4,4,8)). This is done by designing a bank of bandpass filters to cover a wideband portion of the frequency axis, and then running a separate experiment for each bandpass process. The input and output sequences from all bandpass experiments are then composed (i.e., added together respectively) to give data for what is effectively a single wideband experiment. To realize such a wideband excitation in a single experiment would otherwise be impossible due to actuator power constraints.

2) **The plant transfer function is identified nonparametrically by spectral estimation (in the case of stochastic inputs) and by gain and phase estimation in the case of sine-dwell inputs.**

For experiments using stochastic input excitation, spectral estimation (Sect. 2.8, MENU (4,4,4)) is invoked to compute the correlations R_{uu}, R_{yy}, R_{uy} and spectral estimates P_{uu}, P_{yy}, P_{uy} from the input and output data, as well as the plant transfer function estimate from the cross-spectral estimate $h = P_{uy}/P_{uu}$.

For experiments using sine-dwell input excitation, the gain, phase, real and imaginary parts of $p(e^{j\omega T})$ at sine-dwell frequencies are determined in real-time using a recursive least squares estimator with exponential forgetting factor (Sect. 2.6, MENU(4,4,3)). This approach is particularly well suited to provide accurate estimation using sampled-data

4

MENU (4)
NONPARAMETRIC ID EXPERIMENT

MENU (4,3)
MODE OF OPERATION

MENU (4,8)
PLOTTING

MENU (4,4)
PARAMETER MODIFICATION

MENU (4,4,1)
EXPERIMENTAL
CONSTANTS

MENU (4,4,2)
WIDEBAND/NARROWBAND
EXCITATION

MENU (4,4,3)
SINE-DWELL

MENU (4,4,4)
SPECTRAL ESTIMATION

MENU (4,4,5)
PRODUCT MOMENT TEST

MENU (4,4,6)
TRANSFER FUNCTION
CURVE FIT

MENU (4,4,7)
RESONANT
TUNING

MENU (4,4,8)
DATA COMPOSITION

MENU (4,4,9)
FILTER DESIGN

Fig. 1.2-1   Menu Layout For System Identification Experiment Software.

5

sinusoidal responses and to operate in the presence of low frequency resonances. The time constant for the forgetting factor is typically chosen to be several cycles of the sine-dwell response. The sine-dwell estimates of plant gain, phase and real and imaginary parts of $p(e^{j\omega T})$ over several frequencies can be stored for later use by the transfer function curve fitting routine.

3) **Anticipating parametric curve fitting to follow, the model order is estimated using a product moment matrix (PMM) test.**

Some efforts have been made to automate the determination of model order and hence overcome much of the guessing and "human in the loop" efforts typically associated with this task. The approach is to get an initial estimate of the model order by using a PMM test, and then search for the optimal order in the vicinity of this estimate by a sequence of curve fits with varying orders. The quality of each fit is judged by the output error profile.

Several product moment matrix algorithms have been designed, tested and can be invoked (Sect. 2.7, MENU(4,4,5)). One form (PMMD, Sect. 2.7.3) operates on raw data, and generates the PMM directly from the plant input and output. Another form (PMMS, Sect. 2.7.4) assumes statistical stationarity for the underlying process and generates the PMM from the smoothed estimates of the auto and cross covariances produced from the spectral estimation software. It was found that the algorithms which operated on raw data were much superior. This is apparantly due to the fact that the method is exact on finite data lengths (assuming no noise disturbances) and hence avoids stationarity and statistical convergence assumptions otherwise required when using covariance data.

4) **The plant is identified parametrically by fitting transfer function coefficients to the nonparametric data. Model order is determined by a sequential search starting at the PMM estimate.**

A parametric transfer function estimate $\hat{p}$ is determined by curve fitting the coefficients of a rational transfer function (Sect. 2.9, MENU(4,4,6)), to the nonparametric frequency domain data. The data in this case is specified to be the spectral estimate $h = P_{uy}/P_{uu}$ and/or sine-dwell estimates. The model order is determined by successively increasing the number of modes in the curve fit, starting at the PMM estimate, until an adequate output error profile is observed (see output error discussion next). The curve fit involves the use of a least squares algorithm (Sect. 2.9.3), with a special iterative reweighting technique (Sect. 2.9.4), to remove high frequency emphasis (typically associated with equation error methods), and to assure minimum variance estimation of the transfer function coefficients. Resonant frequencies and damping estimates are automatically found by robustly factorizing the plant denominator polynomial with a special purpose routine (Sect. 2.9.5).

5) **The output error is determined to characterize the quality of the parametric transfer function estimate, and for later use in robust control analysis and design.**

The output error $e = pu - \hat{p}u$ is computed by subtracting the predicted output $\hat{y} = \hat{p}u$ from the measured data $y = pu$ (Sect. 2.10) and then the additive uncertainty $\delta_m = p - \hat{p}$ is estimated by the cross-spectral estimate $\Delta = P_{ue}/P_{uu}$. The nominal plant transfer function estimate $\hat{p}$ and the estimate Δ of the additive uncertainty δ_m can then be used

6

directly for robust control analysis and design. The motivation and usefulness of using the output error characterization of additive uncertainty, and its role in robust control design is discussed in Sect. 2.10.

1.3 Testbed Description

Experimental demonstration and verification of the integrated ID software performance were conducted on the JPL/AFAL Flexible Structure Testbed. Extensive consideration was put into the design of this facility to support a three-year, four-phase experiment plan in the technology areas of static shape determination and control, unified modelling and control, robust and adaptive control, and system identification. The final design of an 3-D antenna-like structure was adopted as it exhibits many characteristics of a typical large space structure. These include many low frequency modes, densely packed modes, low structural damping, and three-dimensional structural interaction among components. In this section, a brief description of the testbed facility is given. Detail description can be found in [1].

1.3.1 Configuration

The main component of the testbed facility is shown in figure 1.3-1. It consists of a central rigid hub to which are attached 12 ribs. The ribs are coupled together by two rings of pretensioned wires. Functionally, the wires are intended to simulate the coupling effects of a reflective mesh installed over the rib frame in an actual antenna. The ribs are 2.25 m in length. The hub is of radius 0.6 m, making the dish structure 5.7 m in diameter. The tensioning wires are installed in two rings at approximate diameters of 3 m and 4.8 m. As intended to achieve low modal frequencies, the ribs are very flexible. Stand alone, they are unable to support their own weight without excessive droop. To prevent structural collapse due to gravity, each rib is supported at two locations along its free length by levitators. Each levitator is constituted by a counterweight attached to the rib with a wire which passes over a low-friction pulley. The support locations were calculated to minimize the rms shape deviation along the rib from the root to tip. The calculations led to supporting the rib at the 40% and 80% points which are 0.9 m and 1.8 m from the rib root, the same locations for coupling wire attachments. A flexible boom is attached to the central axis of the hub and has a mass at its lower end to simulate the feed horn of an antenna of the secondary mirror assembly or an optical system. The original boom length was 3.6 m long, but for the convenience of conducting the experiment at ground level, a second, 1 m long boom is being used for most of the Phase I experiments. The feed mass is 4.5 kg. The hub is mounted to a backup structure via a two-axis gimbal which allows rotational freedom about two perpendicular axes in the horizontal plane. The gimbal bearings support roughly one quarter the weight of the ribs, the entire weight of the hub, boom, and feed, and their respective sensing and actuation devices.

1.3.2 Actuators

Each of the ribs can be excited dynamically by a single rib-root actuator with a lever arm of about 0.3 m from the hub attachment point. Each rib-root actuator consists of

PHOTOGRAPH

SCHEMATIC

BACKUP STRUCTURE

SUPPORT COLUMN

LEVITATOR
POSITION SENSOR
ASSEMBLY (2/RIB)

PULLEY

2 DOF GIMBAL
ASSEMBLY

HUB (4 FT dia)

COUPLING WIRES
(INNER/OUTER)

FLEXIBLE
RIB (12)

COUNTERWEIGHT

3 ft BOOM
(CHANGEABLE
TO 12 ft BOOM)

RIB ROOT ARM (TYPICAL)
FORCE ACTUATOR (1/RIB)
RIB ROOT SENSOR (4 TOTAL)

FEED WEIGHT
(10 lb)
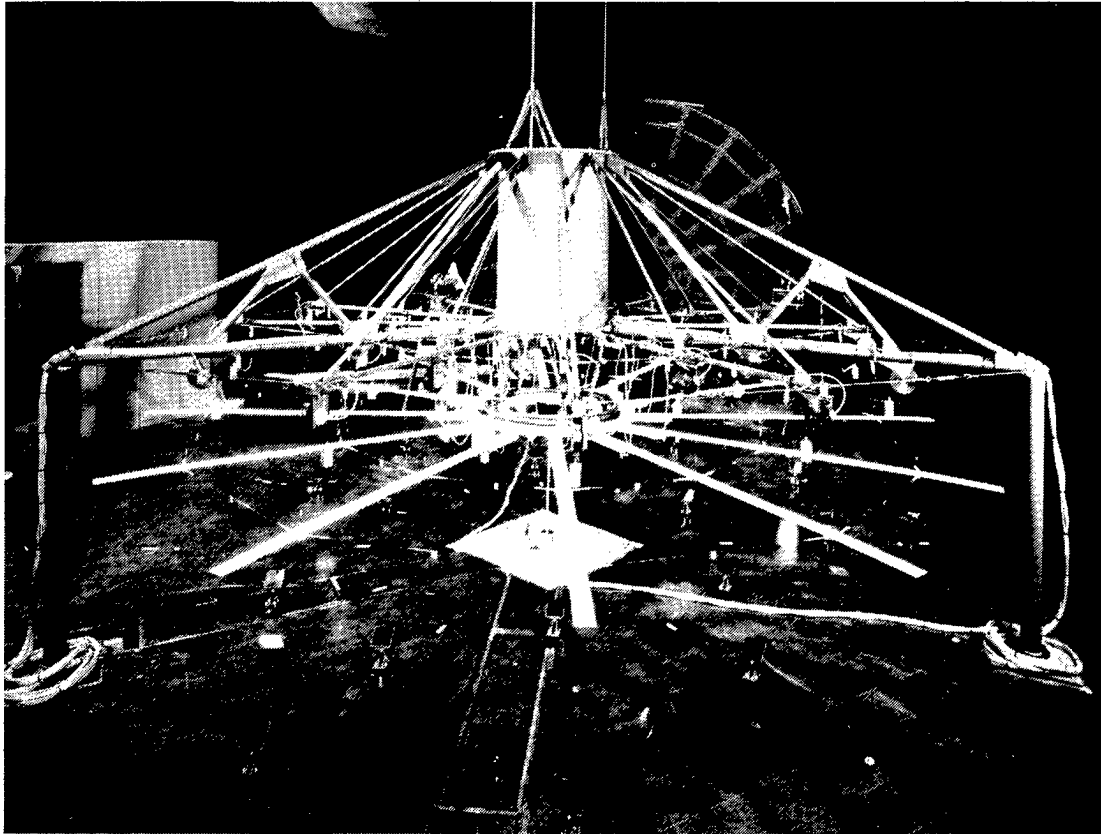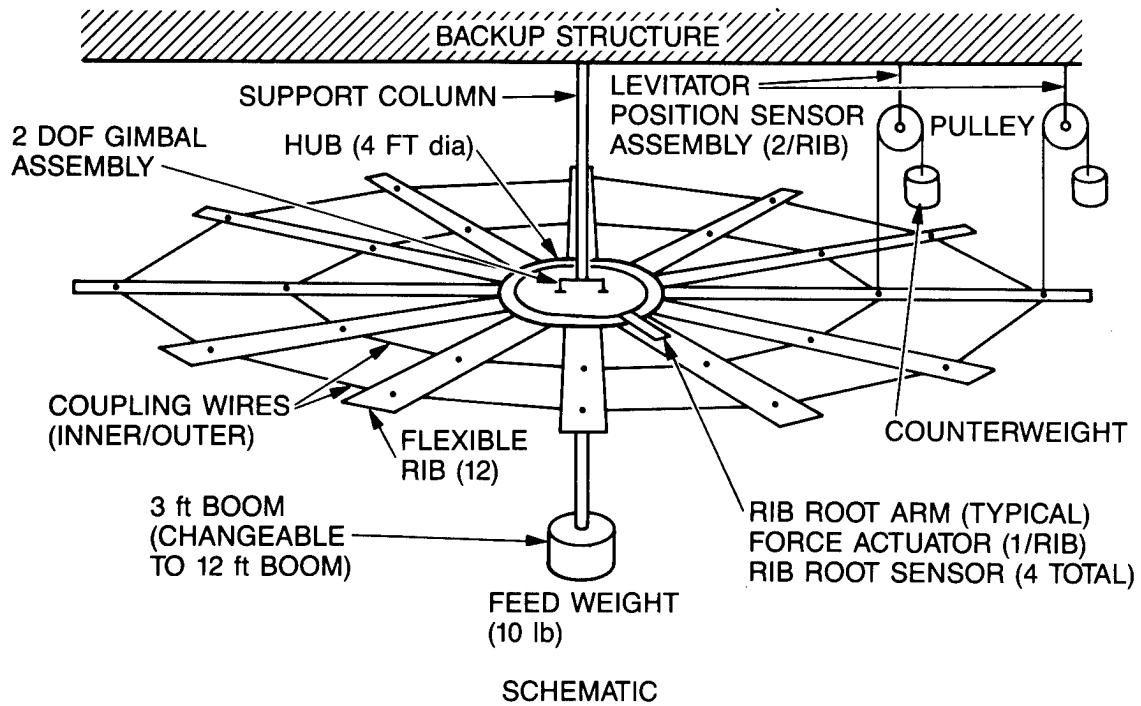
Fig. 1.3-1. JPL/AFAL Flexible Structure Testbed

8

a speaker-coil type device which reacts against a mount rigidly attached to the hub. In addition, two speaker coil type actuators are mounted on the hub to provide controlled torquing about the two gimbal axes. These hub torquers apply linear forces to the hub at its outer circumference to yield the required torques about the axis of rotation. Together, these 14 actuators are capable of controlling all flexible modes of the structure. The location of these actuators is shown in figure 1.3-2, together with the assignments of the rib numbers. As is, the axes of rotation are construed to be along rib#1 and rib#7, and rib#4 and rib#10, with respective rotations excited by hub actuators HA10 and HA1. For convenience, the axes are labelled as the 1-7 axis and 4-10 axis in all later references.

1.3.3 Sensors

Each of the 24 levitators is equipped with an incremental optical encoder which measures the relative angular rotation of the levitator pulley. These angular measurements are then translated into the vertical motion of the ribs at the levitator/rib attachment points, relative to the backup structure. Additional linear variable differential transformers (LVDT) sensors are provided to determine the rib displacment measurements at four evenly spaced rib root actuator locations. Hub angular rotations about the two axes are measured by two rotary variable differential transformers (RVDT) mounted directly at the gimbal bearings. The locations of these 30 sensors are also shown in figure 1.3-2. As assigned, angular displacement about the 1-7 axis are measured by sensor HS1, and that about the 4-10 axis by sensor HS10.

1.3.4 Computer System

The primary function of the computer is to implement the various algorithms for different control and identification technology experiments. Through the Data Acquisition System, the computer samples the various sensors, uses the data to update some sort of state estimation filter, computes appropriate actuator outputs, and then sends the commands to the actuators. For the identification experiments here, the computer merely performs sampling of the sensor samplings and actuator command implementations. The computer system selected for the experiment facility is the DEC VAX Workstation II comprised of 5 MB of main memory, dual 819.2 KB floppy disk drives, 71 MB hard disk, and a 95 MB tape cartridge recorder, equipped with a graphic display terminal and a dot matrix printer as well. The system software is written in Ada, while the experiment softwares are written in a compatible version of FORTRAN.

1.3.5 Data Acquisition System

The Data Acquisition System (DAS) is to sample the sensors and to send commands to the actuators under MicroVAX II control via a high speed parallel interface. It absorbs the time delays associated with sensing and actuations, and frees the computer to handle other computations associated with control experiments. The DAS is housed in a separate enclosure containing the power supplies, amplifiers, A/D and D/A converters, and other circuits needed to interface the sensors and actuators with the computer. The DAS is built around an 8088 microprocessor to direct its operation. Anticipating future upgrade of the

experiment facility, the existing DAS hardware and software are capable of accommodating additional I/O channels.

1.3.6 Dynamic Model

The finite element method was used to generate a system model for the testbed structure. Simply, the method approximates the original distributed parameter system with its unlimited number of degrees of freedom by a discrete system with finite dimensionality. The ribs and boom are each divided into a finite number of elements. Displacements and slopes at the element boundaries are utilized as the finite element degrees of freedom. Displacements of the ribs and boom between within the elements are then approximated by a cubic spline function. "Mass" and "stiffness" matrices are generated from the matrix quadratic expressions which approximate, respectively, the kinetic and potential energies of the continuous parameter system in terms of the finite element degrees of freedom. Normal modes of the system can then be obtained by solving a generalized matrix eigenvalue problem.

Figure 1.3-3 shows the finite element degrees of freedom assigned to a typical rib. The rib is divided into a 10 beam-type element and hence has 20 finite element degrees of freedom. Similar degrees of freedom can be assigned to the boom, except for the fact that the boom can displace in the two orthogonal directions in the horizontal plane. The boom therefore has a total of 40 finite element degrees of freedom. For the hub, it is modelled as a stiff circular ring constrained to rotate about the two perpendicular gimbal axes. As such, the generalized eigenvalue problem

$$Kx = \omega^2 Mx \qquad (1.3.1)$$

resulted can have a dimension as high as 308, depending on how the rib to hub interface is handled. In eqn. (1.3.1), K is the stiffness matrix, M is the mass matrix, x is the eigenvector, and ω is the frequency. To reflect the actual physical system to its fullness, the mass and stiffness matrices were formulated taking into account the inertia of the levitator pulleys and the mass of the counterweights, the tension in the boom caused by gravity, and compression in the ribs caused by the coupling wires.

While the eigenvalue problem of eqn. (1.3.1) is a standard problem and presents no special difficulties for the several solution algorithms available, it is large and its solution can be expensive computationally. Fortunately, it is possible to reduce the dimension of the problem through the use of cyclic reduction. The symmetry of the dish structure makes it possible to separate variables and express a given mode shape as the product of a shape function which is independent of the rib number and a scalar function which depends on the rib number. This scalar function, which reflects the circular dependence of the given mode shape, can be written by inspection in the following form:

$$Sin\left[\frac{2\pi ik}{n} + \phi_k\right] \qquad (1.3.2)$$

10
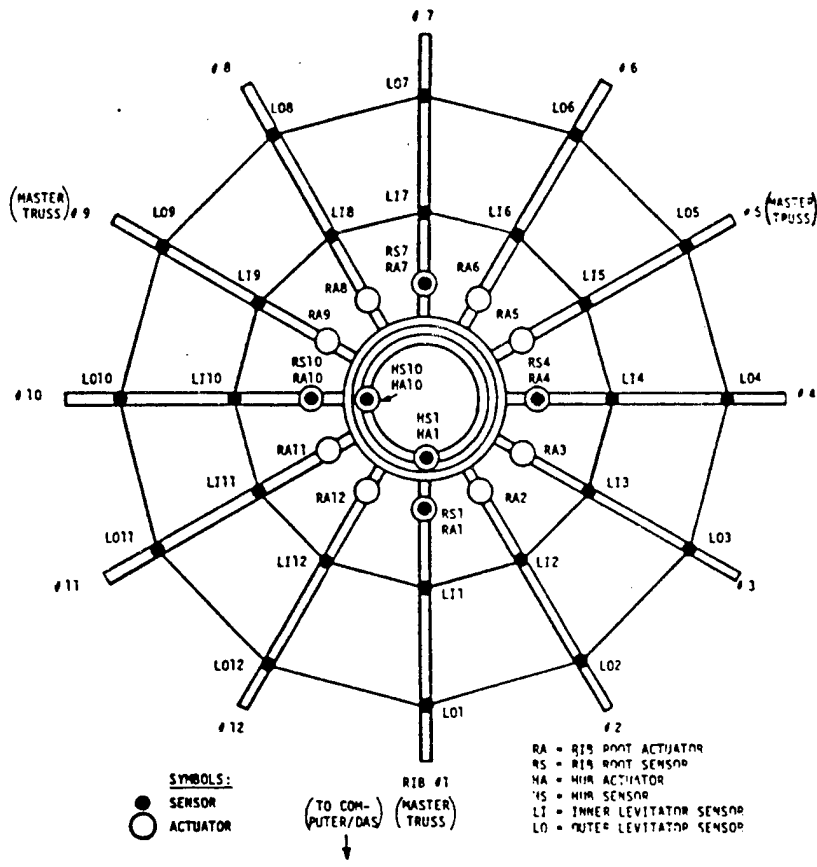
Fig. 1.3-2 Assignment of Rib Numbers and Locations of Sensors and Actuators.

SYMBOLS:
● SENSOR
○ ACTUATOR

RA = RIB ROOT ACTUATOR
RS = RIB ROOT SENSOR
HA = HUB ACTUATOR
HS = HUB SENSOR
LI = INNER LEVITATOR SENSOR
LO = OUTER LEVITATOR SENSOR

RIBS

COUPLING WIRES

HUB

↷ ROTATION
↑ TRANSLATION
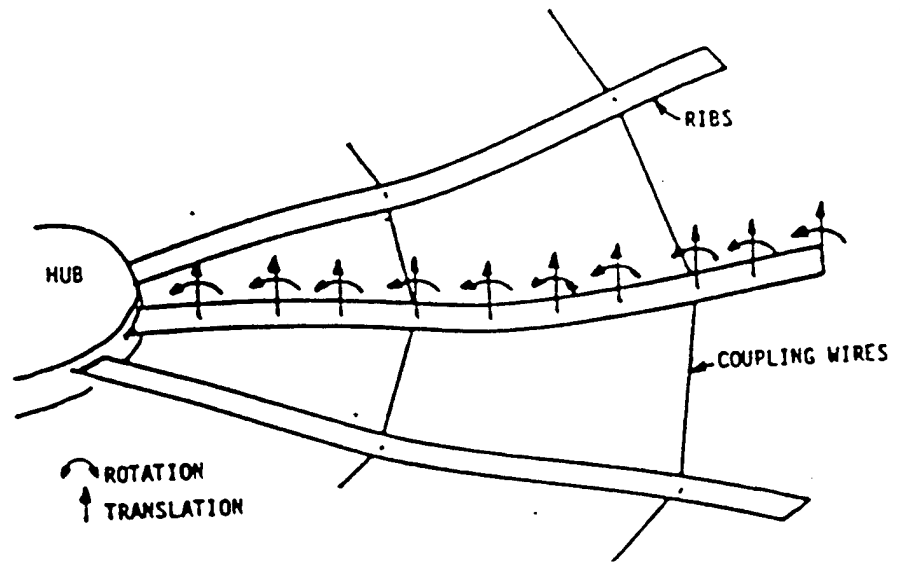
Fig. 1.3-3 Finite Element Model Degrees of Freedom.

11

where i is the number of the rib, n is the number of ribs in the dish structure (12 in this case), and k is the circular wave number for a given mode ranging from $k = 0$ to $k = 6$, and ϕ_k is phase angle depending on the coordinate system transfromation. The shape function is obtained by solving a generalized eigenvalue problem of now a much reduced dimension of 44. A mode is thus completely specified by its frequency, circular wave number, phase angle, and the boom and rib shape functions.

1.3.7 Mode Shapes and Frequencies

Mode shapes of the structure can be grouped according to their circular wave number k. For $k = 0, 2, 3, 4, 5, 6$, all reaction forces on the hub caused by rib motion cancel out, and thus neither hub nor boom motion is involved in these modes. These modes behave as if the hub was clamped in its resting position and hence are termed dish modes. As such, degrees of freedom of the hub and boom can be taken out, reducing further the dimension of the eigenvalue problem associated with the dish modes to 20. In addition, the dish modes corresponding to $k = 2, 3, 4, 5$ are each two-fold degenerate, while degeneracy does not exist for $k = 0$ and $k = 6$. This is due to the fact that for $k = 0$ and $k = 6$, modal excitations about the two orthogonal gimbal axes generate identical motion for the ribs and thus constitute one mode. The mode shapes and frequencies of the first 20 dish modes are shown in figure 1.3-4 and Table 1.3-1, respectively. Only one mode shape is shown for the degenerate dish modes with the same circular wave number k; the other mode shape can be obtained by adding to it a different phase angle.

For $k = 1$, the reaction forces on the hub do not cancel, and the modes appear as a rocking of the entire structure. These modes are called boom-dish modes as they involve motion of the boom, hub, and dish structure together. For a perfectly symmetric structure, the "boom-dish modes" are degenerate. However, for the present structure of which the hub is not quite symmetric, they are not. Table 1.3-2 show the modal frequencies of the first 12 boom-dish modes, 6 for each of the gimbal axes. The small differences in the frequency values reflect the slight hub non-symmetry. Figure 1.3-5 shows the boom-dish mode shapes. Only one set of modes shapes is shown because mode shapes corresponding to two pivot axes are nearly identical.

It is to be noted that the dish modes, with their symmetric mode shapes about the hub, are not controllable and observable from the hub. Thus, hub actuation would manage only to excite and control the boom-dish modes. Since these modes constitute a small subset of all system modes, and they have larger frequency separation, they provide a good first test of the performance of the integrated ID algorithms. As a result, the identification experiments described in this report investigate only the boom-dish modes via actuation at the hub. As experience and confidence in experimentation and algorithm performance grow, the dish modes will be tackled in phase II identification experiments.

Table 1.3-1 Modal Frequencies of Dish Modes

Mode Number	Frequency (Hz)	Wave Number k
1	0.210	0
2	0.253*	2
3	0.290*	3
4	0.322*	4
5	0.344*	5
6	0.351	6
7	1.517	0
8	1.533*	2
9	1.550*	3
10	1.566*	4
11	1.578*	5
12	1.583	6

* two-fold degenerate modes
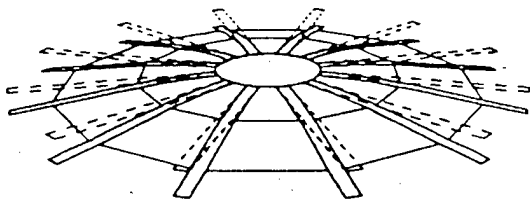
(1) 0.210 Hz, k=0
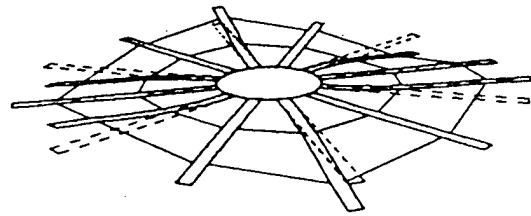
(3) 0.290 Hz, k=3
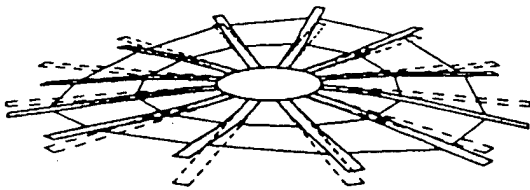
(2) 0.253 Hz, k=2
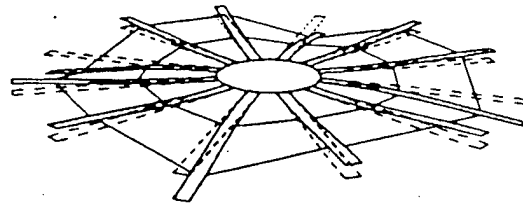
(4) 0.322 Hz, k=4

Fig. 1.3-4 Mode Shapes of Dish Modes.

13
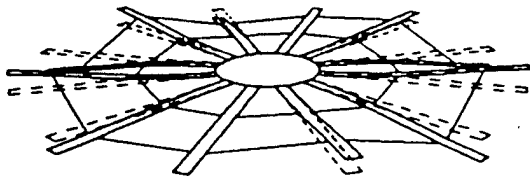
(5) 0.344 Hz, k=5
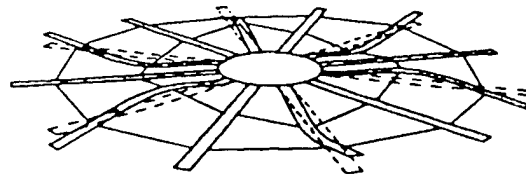
(9) 1.550 Hz, k=3
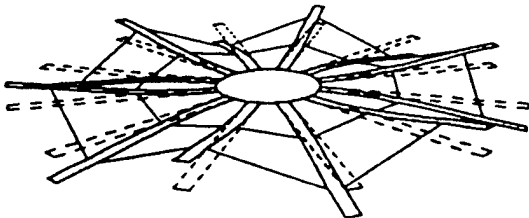
(6) 0.351 Hz, k=6
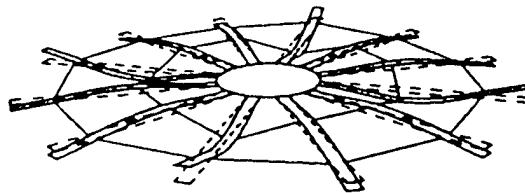
(10) 1.566 Hz, k=4
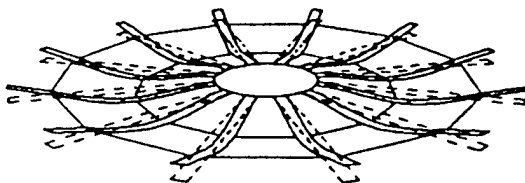
(7) 1.517 Hz, k=0
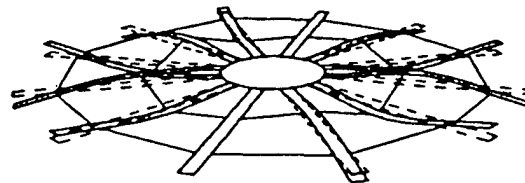
(11) 1.578 Hz, k=5
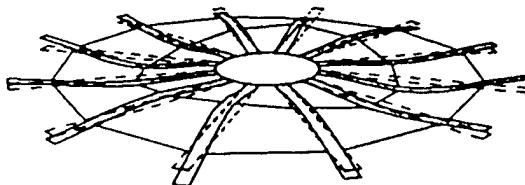
(8) 1.533 Hz, k=2
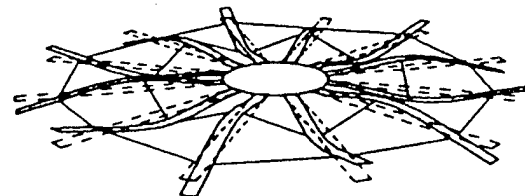
(12) 1.583 Hz, k=6

Fig. 1.3-4 Mode Shapes of Dish Modes (Continued).

14

Table 1.3-2 Modal Frequencies of Boom-Dish Modes

Mode Number	Frequency (Hz)		Wave Number k
	1-7 Axis	4-10 Axis	
1	0.091	0.091	1
2	0.628	0.616	1
3	1.687	1.685	1
4	2.682	2.577	1
5	4.897	4.858	1
6	9.892	9.822	1
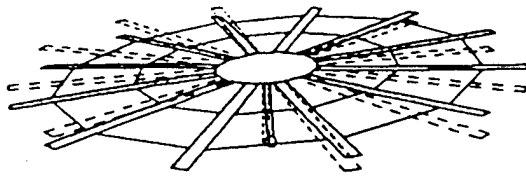
(1) 0.09 Hz
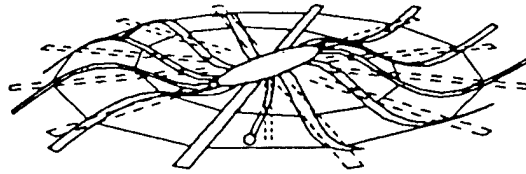
(4) 2.7 Hz
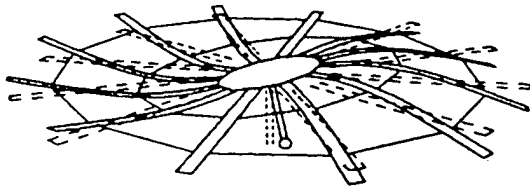
(2) 0.6 Hz
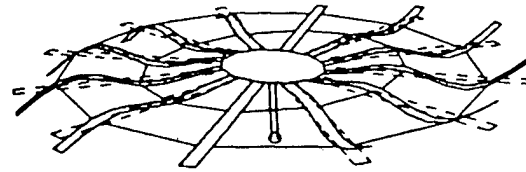
(5) 4.9 Hz
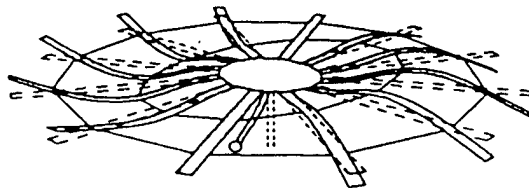
(3) 1.6 Hz
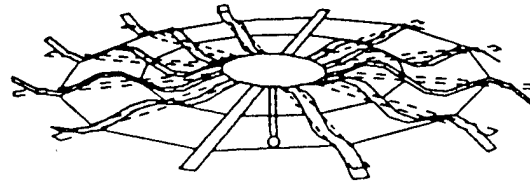
(6) 9.9 Hz

(Circular wave number k = 1)

Fig. 1.3-5 Mode Shapes of Boom-Dish Modes.

Chapter 2. THEORY, ALGORITHM, AND SOFTWARE DEVELOPMENT

2.1 Introduction

In this chapter, we present the results of the theoretical, algorithmic and software development efforts required to successfully implement the frequency domain identification system. Algorithms were developed and optimized by independent researchers on IBM PC-AT's in the form of scientific subroutines and diagnostic programs, before being integrated into the system software. This chapter summarizes the major theoretical, analytical and numerical problems which were overcome at this earlier stage of development, and includes Fortran code for various special purpose subroutines which were developed as part of this task. The software in this chapter was developed to compile and run using Lahey Fortran on a PC-AT computer.

2.2 Wideband Excitation

Wideband excitation utilizes a stochastic, white process as the input sequence. Such an input is characterized by the fact that it has uniform energy density for all frequency starting from 0 Hz going up to one half of the sampling frequency. The available actuation energy is thus being evenly distributed throughout the range. All the structural modes within this "broadband" are excited for observation and analysis. Wideband excitation can be performed in its own right or to serve as preliminary survey to guide subsequent narrowband or sine-dwell investigation for more detail analysis.

In the experiment software, the wideband excitation is set up via the following menu:

```
MENU(4,4,2)
WIDEBAND EXCITATION PARAMETERS
0  - Exit
51 - PARAM(51)    0.   ;WBMEAN= mean of excitation
52 - PARAM(52)    1.5  ;WBSTAN= amplitude of excitation

NARROWBAND EXCITATION PARAMETERS
71 - PARAM(71)   100.0  ;PER= (narrow/wideband)*100 excit. power
72 - PARAM(72)     2.0  ;NBFIL= narrowband fltr storage location
```

Only parameters WBMEAN and WBSTAN need to be set to determine the wideband excitation input. As there is a saturation limit for the actuators, a uniformly distributed white random sequence is chosen for the present experimentation. Actuator saturation can be avoided by selecting appropriate parameters WBMEAN and WBSTAN which are respectively the mean and maximum excursion about the mean of the uniformly distributed sequence. For this work, WBMEAN is set at WBMEAN=0. Since only hub actuation is being utilized, WBSTAN is chosen to be less than 2 nt-m which is the maximum output from the hub torquers. The nominal value for WBSTAN is 1.5 nt-m. At the beginning of every sampling period, the wideband excitation algorithm generates the input command via the following FORTRAN command, in double precison:

$$ACT1=WBSTAN*(2.0*DBLE(RAN(IRAN))-1.0D0)+WBSTAN$$

where RAN(-) is the random number generator the output of which is a floating-point number uniformly distributed between 0.0 and 1.0 exclusive. The seed IRAN=ISEED is one of the experimental constants and is set at 3333 right at the beginning of the experiment run. To play safe, the input sequence is hard-limited in the program before applying to the structure. As a final note, there is no direct access to the actual output of the torquers, so the commanded input sequence constitutes the only measured input data to the system.

2.3 Digital Filter Design

2.3.1 Introduction

In this section, the on-line design of digital filters is discussed. As depicted earlier in Figure 1.1-1, digital filters are used to generate narrowband excitation processes which focus the input energy into specific ranges of plant frequencies. In general, these narrowband input processes will be either of the lowpass or bandpass type, and are generated by filtering white noise sequences by appropriately designed digital filters.

2.3.2 Background

The main developmental effort for this task involved hosting and integrating the EQIIR computer subroutine from the IEEE Digital Signal Processing software collection [3]. EQIIR is a very versatile general purpose routine which provides the capability for on-line design of lowpass, highpass, bandpass, and bandstop Butterworth and Chebyshev filters. These routines have been discussed from a practical perspective in [15].

EQIIR designs a variety of infinite impulse response (IIR) filters using closed-form design formulas. This is in contrast to finite impulse response (FIR) filters which generally require an iteration process to meet given specifications since closed-form design equations do not exist. Another advantage to using IIR filters is that specified amplitude response specifications may be met more efficiently (with lower order filters) than with FIR filters. This is important in our application since we are trying to effectively demarcate frequency bands of interest to allow maximum input power for the identification process. In EQIIR, once the user has specified cutoff frequencies and passband and stopband tolerances, the program obtains the desired IIR filter coefficients by straightforward substitution into a set of design equations. The filter is realized as a cascade of second-order sections.

For our purposes, only Butterworth filters will be designed using the EQIIR program. Advantages of the Butterworth filter are that the frequency characteristic is monotonic in both the passband and the stopband, the magnitude response is maximally flat in the passband, and the filter itself is easily implemented. The squared magnitude function for an analog Butterworth filter is of the form

$$|H_a(jw)|^2 = \frac{1}{\left[1 + \left(\frac{w}{w_o}\right)^{2N}\right]}$$

17

where the design parameter N specifies the filter order and ω_0 is the cutoff frequency.

2.3.3 Integration with System Software

The subroutine EQIIR has been integrated into the experiment software, and filters can be designed via the experiment menus. The filter design menu is given as follows,

```
MENU (4,4,9)
FILTER DESIGN PARAMETERS
0 — Exit                 ;
231 — PARAM(231) 3.      ;  ITYPE = type of filter
232 — PARAM(232) 1.      ;  IAPRO = type of approx. (1=Butterworth)
233 — PARAM(233) 12.     ;  NDEG = prescribed filter order
234 — PARAM(234) .2      ;  EDEG = relative extension of the degree
235 — PARAM(235) .5      ;  FR(1) = critical frequency #1 (Hz)
236 — PARAM(236) 1.      ;  FR(2) = critical frequency #2 (Hz)
237 — PARAM(237) 3.      ;  FR(3) = critical frequency #3 (Hz)
238 — PARAM(238) 3.5     ;  FR(4) = critical frequency #4 (Hz)
239 — PARAM(239) .02     ;  ADELP = tolerance in passband
240 — PARAM(240) .01     ;  ADELS = tolerance in stopband
241 — PARAM(241) 2.      ;  IFIL = filter coeff. storage location
```

Here, the variables are defined pictorially in Figure 2.3-1. It is noted that four design frequencies are required for the design of bandpass filters, while only two are required for lowpass filters.

As an example, the nominal values in the menu are set to design a Butterworth bandpass filter between 1 and 3 Hz. The setting of EDEG=.2 will automatically extend the specified filter degree of 12, as required to meet the specifications. The coefficients are stored in a file addressed by IFIL = 2 for later use.

2.4 Narrowband Excitation

Wideband excitation yields only a general knowledge of the structural dynamics. Equipped with such information, further investigations into certain modal dynamics within certain frequency ranges may be desirable for more detail analysis. One of such investigations is the narrowband excitation. By concentrating the available actuation energy within a narrow frequency range of interest, narrowband excitation can lead to an improvement in the signal to noise ratio and hence, better identification results and understanding of the modal dynamics. There are two parts to narrowband excitation. The first part which is the design of a filter with a specified frequency range as passband is described earlier in the section 2.3. The present section concerns with the passing of a zero-mean-white sequence through the filter to generate the desired narrowband excitation input.

The narrowband excitation experiment is set up via the same menu as the wideband excitation:

ADELS

ADELP

f_{s1} f_{p1} f_{p2} f_{s2}

$$ITYP = \begin{cases} 1 & \text{Lowpass Filter} \\ 3 & \text{Bandpass Filter} \end{cases}$$

NDEG = Filter Degree

IAPRO = 1; Butterworth Design

$$EDEG = \begin{cases} 0.0 & \text{Minimum Filter Degree} \\ 0.2 & \text{Degree Extension} \end{cases}$$
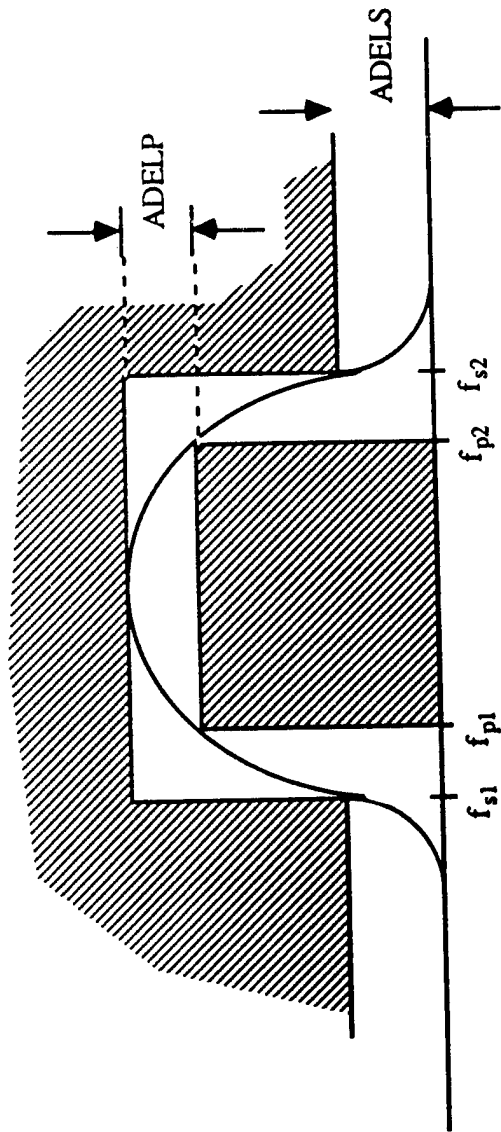
	LOWPASS	BANDPASS
FR(1)	f_{p2}	f_{p1}
FR(2)	f_{s2}	f_{s1}
FR(3)	—	f_{p2}
FR(4)	—	f_{s2}

Fig. 2.3-1 Specifications for Filter Design Subroutine EQIIR.

MENU(4,4,2)
WIDEBAND EXCITATION PARAMETERS
0 - Exit
51 - PARAM(51)   0.   ;WBMEAN= mean of excitation
52 - PARAM(52)   1.5   ;WBSTAN= amplitude of excitation

NARROWBAND EXCITATION PARAMETERS
71 - PARAM(71)   100.0   ;PER= (narrow/wideband)*100 excit. power
72 - PARAM(72)   2.0   ;NBFIL= narrowband fltr storage location

Here, NBFIL specifies the storage location of the filter coefficients of interest. The parameter WBMEAN and WBSTAN determine the wideband input sequence w to be passed into the filter to result the narrowband input u_n. PER specifies the energy ratio, in %, which is defined as the ratio of actuation energy of u_n to that of w. From [16], the power spectrum of u_n is given as

$$S_{u_n u_n}(\omega) = S_{ww}(\omega)|H(e^{j\omega T})|^2 \qquad (2.4-1)$$

where T is the sampling period, and

$$H(e^{j\omega T}) = \frac{b_0 + ... + b_N e^{-jN\omega T}}{1 + ... + a_N e^{-jN\omega T}} \qquad (2.4-2)$$

where a_1, a_2, ..., a_N, b_0, b_1, ..., b_N, are the filter coefficients. Approximating the power spectrum $S_{ww}(\omega)$ as uniform, the energy ratio of u_n and w can be estimated as

$$\int_o^{\Omega} |H(e^{j\omega T})|^2 d\omega \qquad (2.4-3)$$

where Ω equals half the sampling frequency of the experiment. Before the start of the excitation, the program first performs the following functions:

1. Read in the filter coefficients from the location specified by NBFIL.

2. Using eqn (2.4-3), compute the "would-be" power ratio of u_n and w without any scaling of u_n. The integration of eqn (2.4-3) is performed numerically.

3. Compute the constant *sca* that needs to be multiplied to u_n so as the make the energy ratio=PER.

20

With *sca* computed, the program goes into the real-time mode. At every sampling period, the wideband excitation sequence w is generated first as for the wideband case via the random generator. The narrowband excitation command is then calculated via the recursion equation

$$u_n(m) + a_1 u_n(m-1) + ... + a_N u_n(m-N) = sca * [b_0 w(m) + ... + b_N w(m-N)] \quad (2.4-4)$$

where $u_n(m)$ and $w(m)$ are zero for m¡0. As such, the narrowband excitation sequence is generated real time and will have the correct energy ratio of PER. Real-time generation of u_n is desirable here to prepare for possible accommodation of ID schemes capable of adjusting the input excitation based on identified parameters. A hard-limit is again imposed on the input sequence so as not to saturate the torquers. It is well to point out that though w is uniformly distributed, computing u_n through egn (2.4-4) results in a near Gaussian distribution for u_n (This is sometimes called the "filter hypothesis"). If PER is set at 100%, the standard deviations σ^2 for u_n and w will be the same and equal to (assume WBMEAN=0)

$$\sigma^2 = \frac{WBSTAN^2}{3} \quad (2.4-5)$$

For the nominal value of WBSTAN=1.5 nt-m, σ is equal to 0.866 nt-m. Assuming u_n is a Gaussian distributed sequence with this σ value, most of the numbers in the sequence would lie in a range from -3σ to $+3\sigma$, i.e., from -2.6 nt-m to +2.6 nt-m. This means that the torquers will be saturated quite frequently. To alleviate the problem, the nominal value for PER is 66.7%, which results in most of the narrowband input commands inside the range -2 nt-m to +2 nt-m. As a result, hard-limiting the narrowband input sequence will not greatly distort its distribution and power spectrum. Again, as for the wideband case, the input sequence constitutes the only measured input data to the system. There is no direct access to the actual output of the actuators.

2.5 Data Composition

Data composition is a technique to allow the inputs and outputs of several experiments to be added together and form composite input UDC and output YDC for processing and analysis. Such a process is useful in the following cases:

a. Narrowband excitation concentrates the actuation energy into a narrow frequency range for more effective modal excitation. Data composition combining inputs and outputs of several narrowband experiments, each covering different parts of the spectrum, yields the data of an experiment effectively covering a wide frequency range and of large actuation power at all frequencies.

b. Several runs of the same wideband/narrowband experiment can be performed and composed together to result in an improved signal to noise ratio for UDC and YDC.

c. A combination of (a.) and (b.).

In short, data composition is a means to overcome the limited level of actuation power in the system. The menu governing data composition is given as follows:

```
MENU(4,4,8)
DATA COMPOSITION PARAMETERS
0 - Exit
211 - PARAM(211)    1.              ;IDC=processing type
                                    0-initialize UDC & YDC to zero
                                    1-add U and Y to UDC and YDC
                                    2-swap U & UDC
                                    3-swap Y & YDC
                                    4-swap Y & YEST
                                    5-swap Y & YERR
```

Here, U and Y denote the input u and output y of the experiment. UDC and YDC denote the data arrays where the composed data are stored. The procedures for conducting data composition are as given below:

1. Set PARAM(211)=IDC=0, run the DATA COMPOSITION mode of operation. This will clear the storage arrays of UDC and YDC to zeros.

2. Conduct the first of the wideband/narrowband experiment planned.

3. Set IDC=1, run the DATA COMPOSITION mode of operation. The input u and output y are added to the contents of the arrays UDC and YDC, respectively.

4. Repeat Step 2 and Step 3 for each of the planned experiments.

5. Set IDC=2, run the DATA COMPOSITION mode of operation. The array UDC will change position with the array u.

6. Set IDC=3, run the DATA COMPOSITION mode of operation. The array YDC will change position with the array y.

7. The arrays u and y, now containing the composed data are ready to be analyzed, processed, and plotted.

The options of IDC=4 and IDC=5 are concerned with the OUTPUT ERROR ANAL-YSIS. They will be discussed in Sect. 2.10.

2.6 Sine-Dwell

2.6.1 Introduction

The sine-dwell method is a standard technique for frequency domain identification of a transfer function. The idea is to input sinusoids at a variety of frequencies, and to measure the phase and amplitude of the steady-state response to each input. This characterizes the phase and amplitude of the transfer function at the sine-dwell frequencies, hence providing nonparametric identification (e.g., a Bode plot) of the plant. The phase/amplitude response can then be curve fit to determine parametric representations of the plant.

Motivated by the on-orbit LSS application, we will assume that
1) the sine-dwell inputs are computer generated in discrete time using a zero-order-hold (i.e., piecewise constant over equal sampling instants)
2) The plant contains low frequency modes (under .1 Hz)
3) The noise is additive and uncorrelated with the sine-dwell input and its quadrature component.

These assumptions will drive the discretization and estimator design.

2.6.2 Background

There are many different methods for discretizing a continuous time plant. We will take a moment to be clear about the discretization technique being used here.

Suppose the continuous time plant is represented by the following convolution integral.

$$y(t) = \int_0^\infty g(\tau)u(t - \tau)d\tau \qquad (2.6-1)$$

The continuous time transfer function $G(s)$ is defined as the Laplace transform of the impulse response $g(t)$ i.e.,

$$G(s) = \int_0^\infty g(t)\, e^{-st}dt \qquad (2.6-2)$$

Assume that the input is kept constant between sampling instants i.e.,

$$u(t) = u_k, \quad kT \le t < (k+1)T \qquad (2.6-3)$$

Then it can be shown that the following discrete-time convolution relation holds exactly,

$$y_k = \sum_{\ell=0}^k g_\ell\, u_{k-\ell} \qquad (2.6-4)$$

where,

$$y_k = y(kT) \qquad (2.6-5)$$

23

$$g_\ell = \int_{(k-1)T}^{kT} g(\tau)d\tau \qquad (2.6-6)$$

A discrete time transfer function $h(z)$ is defined as the Z transform of the sequence $\{g_\ell\}$,

$$p(z) = \sum_{k+0}^{\infty} g_k \, z^{-k} \qquad (2.6-7)$$

The $h(z)$ and $G(s)$ can be shown to be related by

$$p(z) = (1 - z^{-1}) \, Z\big[G(s)/s\big] \qquad (2.6-8)$$

where the $Z[\cdot]$ operator provides an impulse invariant discretization of its argument (i.e., the Z transform of the sampled inverse Laplace Transform).

Computer generated sine-dwell input signals are in the form of the following digitized sinusoid,

$$u_k = Y \sin(\omega kT) \qquad (2.6-9)$$

The system response at steady state is given by the relation

$$y_k = Y|p(e^{j\omega T}| \, \sin\big(\omega kT + \arg p(e^{j\omega T})\big) \qquad (2.6-10)$$

As noted from (2.6-10), the usefulness of the sine-dwell method follows from the fact that the amplitude and phase of the discretized transfer function $p(e^{j\omega T})$ at the sine-dwell frequency ω can be determined by the amplitude and phase, respectively, of the sine-dwell response.

2.6.3 Sine-Dwell Estimator Design

It is desired to estimate the gain and phase of the sinusoidal steady-state response. In order to avoid a nonlinear estimation problem, this is transformed into a linear problem by noticing that,

$$\begin{aligned} y_k &= Y|p(e^{j\omega T}| \sin\big(\omega kT + \arg p(e^{j\omega T})\big) \\ &= a\cos(\omega kT) + b\sin(\omega kT) \end{aligned} \qquad (2.6-11)$$

where

$$Y|p(e^{j\omega T})| = \sqrt{a^2 + b^2} \qquad (2.6-12)$$

$$\arg p(e^{j\omega T}) = \tan^{-1}(b/a) \qquad (2.6-13)$$

The quantities a and b are estimated in place of the amplitude and phase of the plant. Here, a and b are related to the real and imaginary parts of the transfer function by,

$$a/Y = \operatorname{Re} p(e^{j\omega T}) = \text{GREAL} \qquad (2.6-14a)$$

$$b/Y = \operatorname{Im} p(e^{j\omega T}) = \text{GIMAG} \qquad (2.6-14b)$$

24

The notations GREAL and GIMAG are used as Fortran names for the indicated quantities, and will become useful in later discussion. Equation (2.6-11) can be rewritten as,

$$y_k = \theta^T \phi_k \qquad (2.6-15)$$

$$\theta = [a, b]^T \qquad (2.6-16)$$

$$\phi_k = [\sin(\omega kT), \cos(\omega kT)]^T \qquad (2.6-17)$$

The estimation of a and b from y and ϕ is "linear in the parameters" and is performed using a least squares algorithm with exponentially fading memory,

$$\hat{\theta}_N = \arg\min_\theta \sum_{k=0}^{N} \lambda^{N-k} |y_k - \theta^T \phi_k|^2 \qquad (2.6-18)$$

where $0 < \lambda < 1$. The least squares algorithm is implemented recursively according to the well known formulas [26],

$$P_k = \frac{1}{\lambda}[P_k - P_k\phi_k\phi_k^T P_k/(\lambda + \phi_k^T P_k \phi_k)] \qquad (2.6-19)$$

$$\hat{\theta}_k = \hat{\theta}_k + P_k\phi_k(y_k - \hat{\theta}_k^T\phi_k)/(\lambda + \phi_k^T P_k \phi_k) \qquad (2.6-20)$$

$$\hat{\theta}_0 = [0, 0]^T \qquad (2.6-21)$$

$$P_0 = I\varepsilon \qquad (2.6-22)$$

The exponential fading memory window is used (instead of a growing rectangular memory window) since a and b will be time varying quantities until the system reaches steady state. The estimation is performed recursively to monitor the behavior of the estimate and to watch them "settle out" into their steady-state values.

The subroutine GRIME in Fig. 2.6-1 estimates a and b using recursive least squares routine with exponential forgetting. A UDU factorized form of the estimation equations is used to assure robustness of the estimator, and follows closely the routine outlined in Thorton and Bierman [17]. The time constant of the exponential window is specified by a quantity TGRIM from which the value of λ is determined as follows,

$$\lambda = e^{-T/\text{TGRIM}} \qquad (2.6-23)$$

It is noted that λ in the above equations corresponds to RL in the Fortran code. In general, the size of TGRIM should be chosen as a few cycles at the sine-dwell frequency and larger if possible to assure good noise rejection. The latter choice will be explained in more detail below.

25

```
C       FILE: GRIME.FOR
C

        SUBROUTINE GRIME(Y,YP,FREQ,TIME,THETA,P,RL,RES,GREAL,GIMAG)
C
C       FITS A AND B TO MODEL YP=A*COS(W*TIME)+B*SIN(W*TIME)
C       WHERE A=THETA(1), B=THETA(2), W=2*PI*FREQ
C       IF INPUT TO PLANT G(S) IS Y*SIN(W*TIME) THEN
C                       B/Y=GREAL (I.E.,REAL PART OF G(jW)
C                       A/Y=GIMAG (I.E.,IMAG PART OF G(JW))
C       FITTING OF A&B IS DONE WITH A GENERAL ROUTINE FOR
C       RECURSIVE LEAST SQUARES ALGORITHM WITH UDU FACTORIZATION
C
C       THIS ROUTINE IMPLEMENTS:
C
C           P=1/RL{P-P*PHI*PHI*P/(RL+PHI*P*PHI)}
C           RES=YP-PHI*THETA
C           THETA=THETA+{P*PHI/(RL+PHI*P*PHI)}*RES
C
C       THIS ROUTINE CLOSELY FOLLOWS THORTON & BIERMAN
C       CONTROL & DYNAMIC SYSTEMS,VOL 16,1980,PG.241
C
C       Y -     (I) AMPLITUDE OF PLANT INPUT SINE I.E, Y*SIN(W*TIME)
C       YP -    (I) PLANT OUTPUT (SINE-DWELL RESPONSE)
C       NN -    TOTAL # OF PARAMETERS
C       THETA - (I/O) 2VECTOR OF PARAMETERS
C       P -     (I/O) 2X2 COVARIANCE MATRIX, (D ON DIAG & NONTRIV ON OFFDIAG)
C       PHI - 2VECTOR REGRESSOR
C       YP - PLANT OUTPUT
C       FREQ -  (I) SINE DWELL FREQUENCY
C       TIME -  (I) EXPERIMENT TIME ELAPSED I.E. YP(TIME)
C       GREAL - (O) REAL PART OF G(JW)
C       GIMAG - (O) IMAG PART OF G(JW)
C       RL-WEIGHTING FACTOR FOR EXP WINDOW RL=EXP(-T/TGRIM)
C       RES-RESIDUAL YP-PHI*THETA
C       C-UPPER CLAMP ON ENTRIES OF D IN UDU
C
        REAL*4 THETA(2),P(2,2),PHI(2),F(2),G(2),
     1 Y,RES,ALPHA,DD,GAMMA,BETA,AL,S,C,RL
        PARAMETER (NN=2,C=1.E36,TWOPI=6.28318530717959)
        LOGICAL*1 FLAG
C
        CALL OVEFL(FLAG)
        W=TWOPI*FREQ
        PHASE=W*TIME
        PHI(1)=COS(PHASE)
        PHI(2)=SIN(PHASE)
        RES=YP
        DO 10 J=1,NN
 10     RES=RES-PHI(J)*THETA(J)
        DO 30 I=2,NN
        J=NN+2-I
        ALPHA=PHI(J)
        J1=J-1
        DO 20 KK=1,J1
```

Fig. 2.6-1 GRIME Subroutine for Sine-Dwell Estimation.

```
   20 ALPHA=ALPHA+P(KK,J)*PHI(KK)
      F(J)=ALPHA
   30 G(J)=P(J,J)*ALPHA
      G(1)=P(1,1)*PHI(1)
      F(1)=PHI(1)
C
      ALPHA=RL+F(1)*G(1)
      GAMMA=0.
      IF(ALPHA.GT.0.) GAMMA=1./ALPHA
      IF(G(1).NE.0.) P(1,1)=GAMMA*P(1,1)
      DO 50 J=2,NN
      BETA=ALPHA
      DD=G(J)
      ALPHA=ALPHA+DD*F(J)
      IF(ALPHA.EQ.0.0) GO TO 50
      AL=-F(J)*GAMMA
C
      J1=J-1
      DO 40 I=1,J1
      S=P(I,J)
      P(I,J)=S+AL*G(I)
   40 G(I)=G(I)+DD*S
      GAMMA=1.0/ALPHA
      P(J,J)=BETA*GAMMA*P(J,J)/RL
C     P(J,J)=DMIN1(P(J,J),C)
   50 CONTINUE
C     AT THIS POINT ALPHA=RL+PHI*P*PHI ; THE INNOVATIONS COV
      DO 60 I=1,NN
   60 THETA(I)=THETA(I)+G(I)*RES/ALPHA
      GREAL=THETA(2)/Y
      GIMAG=THETA(1)/Y
      RETURN
      END
```

Fig. 2.6-1 GRIME Subroutine for Sine-Dwell Estimation (continued).

2.6.4 Noise Rejection Properties of Estimator

The noise rejection properties of the estimator are briefly analyzed. Assume that there is noise in equation (2.6-15) giving rise to the modified form,

$$y_k = \theta^T \phi_k + v_k \qquad (2.6-24)$$

where v_k represents an additive noise disturbance. In practice this can correspond to input noise, environment disturbances, and/or measurement error. The estimate at time N can be written as [27],

$$\theta_N = \theta + \left[\frac{1}{N} \sum_{k=1}^{N} \lambda^{N-k} \phi_k \, \phi_k^T \right]^{-1} \frac{1}{N} \sum_{k=1}^{N} \lambda^{N-k} \phi_k v_k \qquad (2.6-25)$$

From this expression we can deduce the following properties of the estimator,

1) If the noise v_k is uncorrelated with the regressor ϕ_k (i.e., the input and its quadrature component), the estimate of θ is unbiased, and the noise rejection properties of the estimator can be improved by "opening up" the filter window i.e., by increasing λ, or increasing TGRIM.

2) If the noise v_k is correlated with the regressor ϕ_k, the bias is proportional to the degree of correlation.

3) The estimation problem is well posed since the quantity in the brackets of (2.6-25) is always invertible for λ sufficiently large (e.g., let TGRIM equal to several cycles of the sine-dwell frequency).

2.6.5 Sine-Dwell Example

The performance of the estimator encoded in the GRIME subroutine is tested by simulation. For this purpose, the top level program SDWELL.FOR in Fig. 2.6-2 was written to perform the following operations

1) generate a sinusoidal input (call subroutine SINWT)
2) apply input to plant dynamics (call subroutine MODEL)
3) calculate GREAL and GIMAG recursively (call subroutine GRIME)

The top level program SDWELL.FOR calls the subroutines SINWT, MODEL, and GRIME which are depicted in Figures 2.6-3, 2.6-4 and 2.6-1, respectively.

Simulation was performed using the following parameters,

Sampling Period T=.03
Sine-Dwell Amplitude $Y = 1$.
Sine-Dwell Frequency FREQ = 0.06027 Hz
Forgetting time constant TGRIM = 20 Sec

The plant model for the simulation study had a single mode with 5% damping with natural resonance exactly at the sine-dwell frequency 0.06027 Hz.

28

```
C       FILE: SDWELL.FOR
C
C       THIS IS TOP LEVEL PROGRAM FOR SINE-DWELL STRUCTURAL TESTING.
C       THIS PROGRAM APPLIES A SINUSOID TO A PLANT MODEL, GENERATES THE
C       RESPONSE, AND THEN CALCULATES THE REAL PART (GREAL) AND
C       IMAGINARY PART (GIMAG) OF THE TRANSFER FUNCTION AT THE SINE-DWELL
C       FREQUENCY. GREAL AND GIMAG ARE ESTIMATED IN TIME, AND SHOULD SETTLE
C       OUT TO CONSTANT VALUES WITH A LONG ENOUGH EXPERIMENT RUN.
C
C
        REAL*4 X1(4),X2(4),GTHETA(2),GP(2,2)
C
C
C       INITIALIZE  EXPERIMENT RUN
        PARAMETER (T=.03, TMAX=600.)
C           T-SAMPLING PERIOD
C           TMAX-TOTAL EXPERIMENT RUN TIME
C
C       INITIALIZE INPUT DESIGN
        PARAMETER (Y=1., FREQ=.06027)
C           Y-SINEDWELL AMPLITUDE
C           FREQ-SINEDWELL FREQUENCY (HERTZ)
C
C       INITIALIZE PLANT MODEL
        PARAMETER (NM=1)
        DATA X1/0.,0.,0.,0./, X2/0.,0.,0.,0./
C           NM-NUMBER OF MODES IN PLANT MODEL
C           X1,X2-INITIAL PLANT STATE
C
C       INITIALIZE GRIME ROUTINE
        DATA GTHETA/0.,0./,TGRIM/20./
        DATA GP(1,1)/1.E10/,GP(1,2)/0./,GP(2,1)/0./,GP(2,2)/1.E10/
C           GTHETA-GRIME ESTIMATOR STATE
C           GP-GRIME ESTIMATOR COVARIANCE
C           TGRIM-GRIME ESTIMATOR TIME CONSTANT
C
        OPEN(7,FILE='SDWELL.M',STATUS='OLD')
C
        NMAX=INT(TMAX/T)
        RL=EXP(-T/TGRIM)
        DO 10 NRUN=1,NMAX
        TRUN=NRUN*T
        CALL SINWT(Y,T,NRUN,FREQ,YSIN,YCOS)
        CALL MODEL(T,NM,X1,X2,YSIN,YP)
        CALL GRIME(Y,YP,FREQ,TRUN,GTHETA,GP,RL,RES,GREAL,GIMAG)
C
C       OUTPUT TO FILE EVERY 10 SECONDS
        IF (MOD(NRUN,100).NE.0) GO TO 30
        WRITE(7,20) TRUN, YSIN, YP, GREAL, GIMAG
   30   CONTINUE
   10   CONTINUE
   20   FORMAT(1X,5(E10.4,2X))
        STOP
        END
```

Fig. 2.6-2 Top Level Program for Sine-Dwell Testing Simulation.

```
C      FILE: SINWT.FOR
C
       SUBROUTINE SINWT(Y,T,N,FREQ,YSIN,YCOS)
C
C      THIS SUBROUTINE IMPLEMENTS A SINUSOID
C
C      Y - (I) AMPLITUDE OF SINUSOID
C      T - (I) SAMPLING PERIOD
C      N - (I) PRESENT TIME SAMPLE NUMBER (TIME=N*T)
C      FREQ - (I) FREQUENCY OF SINUSOID
C      YSIN - (O)· Y*SIN(2*PI*FREQ*N*T)
C      YCOS - (O)  Y*COS(2*PI*FREQ*N*T)
C
C
       TWOPI=6.28318530717959
       TIME=TWOPI*FREQ*N*T
       YSIN=Y*SIN(TIME)
       YCOS=Y*COS(TIME)
       RETURN
       END
```

Fig. 2.6-3 Subroutine for Generating Sinusoidal Input.

```fortran
C       FILE: ODEL.FOR
C
        SUBROUTINE MODEL(T,N,X1,X2,U,Y)
C
C
        REAL*4 B(16),C(16),FREQ(16),X1(*),X2(*)
        LOGICAL*4 IFLAG
C
C       DEFINITIONS:
C           N=NUMBER OF MODES
C           X1=NVECTOR OF MODAL AMPLITUDES
C           X2=NVECTOR OF MODAL VELOCITIES
C           U=SCALAR INPUT
C           Y=SCALAR OUTPUT
C           B=NVECTOR,INPUT INFLUENCE COEFF.
C           C=NVECTOR,OUTPUT INFLUENCE COEFF.
C           ZETA=SCALAR % MODAL DAMPING
C
C       SISO HUB TO FEED TRANSFER FUNCTION
C       ASSUMES NO BOOM MASS
C       SAMPLE&HOLD INPUT
C       IDEAL SAMPLED OUTPUT
C
        DATA B/.0982,.1064,.252,.455,1.,1.,1.,1.,1.,1.,1.,
     1 1.,1.,1.,1.,1./
        DATA C/-.824,-10.189,4.665,3.420,1.,1.,1.,1.,1.,1.,
     1 1.,1.,1.,1.,1.,1./
        DATA FREQ/.06027,.550,.7308,2.657,2.8,3.,3.2,3.5,3.7,
     1 3.9,4.,4.2,4.4,4.6,4.8,5./
        DATA ZETA/.05/,TWOPI/6.283185530717959/,IFLAG/.TRUE./
C
C
        CALL UNDERO (IFLAG)
        Y=0.
        DO 10 I=1,N
        WI=TWOPI*FREQ(I)
        R=EXP(-ZETA*WI*T)
        S=SQRT(1.-ZETA**2.)
        THETA= ACOS(S)
        WN= WI*S
        CS= COS(WN*T)
        SN=SIN(WN*T)
        Z1= (R/S)*(COS(WN*T-THETA)*X1(I)+SN*X2(I)/WI)
        Z2=(R/S)*(COS(WN*T+THETA)*X2(I)-WI*SN*X1(I))
        D=ZETA/S
        E=B(I)/WI**2.
        Z1=Z1+E*(1.-R*(CS+D*SN))*U
        X2(I)=Z2+E*R*WI*SN*U/S
        X1(I)=Z1
        Y=C(I)*Z1+Y
10      CONTINUE
        RETURN
        END
```

Fig. 2.6-4 Subroutine to Simulate Model Dynamics.

The results of a 600 second simulation experiment are shown in Fig. 2.6-5. The plant input and output are plotted in Fig. 2.6-5a and GREAL and GIMAG are plotted as a function of time in Fig. 2.6-5b. It is seen that the steady state is achieved approximately after 150 secs, while the estimates of GREAL and GIMAG take somewhat longer to settle out. The convergence properties of the algorithm are further seen in Fig. 2.6-5c which shows a "zig-zag" trajectory in the GREAL-GIMAG plane. The final phase is given by,

$$\tan^{-1}(GIMAG/GREAL) = 90.56°$$

2.6.6 Resonance Tuning

A useful feature of sine-dwell testing is the ability to refine modal frequency estimates by tuning the sine-dwell frequency to achieve some specified resonance condition. Assuming a single lightly damped mode, the condition for resonance is precisely +/- 90 phase shift and/or a peak amplitude in the response. This condition must be modified for multiple modes and nonzero damping effects. The amplitude condition will generally be more robust to these effects than the phase condition.

The testing of the amplitude criteria for resonance requires a unimodal search. Search strategies such as golden search, Fibonacci search etc. are well known and can be found for example in [2]. The testing of the phase condition for resonance requires a zero-crossing search. The binary search routine is one of the most popular for this purpose. The phase condition will be used in the present implementation.

The Fortran subroutine BS in Fig. 2.6-6 was devised to implement a binary search for resonance frequencies based on the phase condition. The phase condition was modified slightly to become,

GREAL/GIMAG = 0

since this condition is easily tested and is met for either the +90 or -90 degree resonance conditions.

In order to test the BS routine, the top level program BSTST.FOR in Fig. 2.6-7 was designed, and the previous top level program SDWELL.FOR was turned into a subroutine SDWELLS in Fig. 2.6-8. The test program BSTST.FOR performs the following operation,

1) Initialize search by determining GIMAG/GREAL at frequencies FMIN, FMAX, FMID (call SDWELLS three separate times to find RATMIN, RATMAX, RATMID, respectively).
2) Update FMID by performing bisection (call BS).
3) Calculate GIMAG/GREAL at frequency FMID (call SDWELLS to find RATMID).
4) Go to (2) until satisfied with result.

2.6.7 Resonance Tuning Example

A simulation experiment is run using a plant having 4 modes at the following frequencies, 0.06027, .550, .7308, 2.657 Hz. Modal damping is assumed at 5%.

32
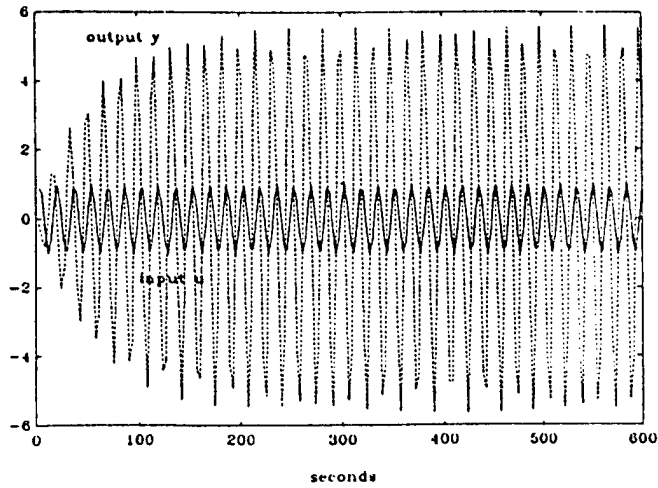
(a) Plant Input and Output.
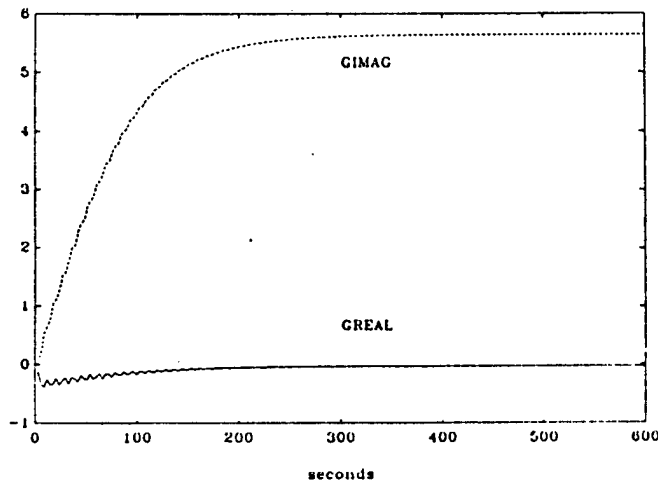
(b) Outputs of GRIME Estimator.
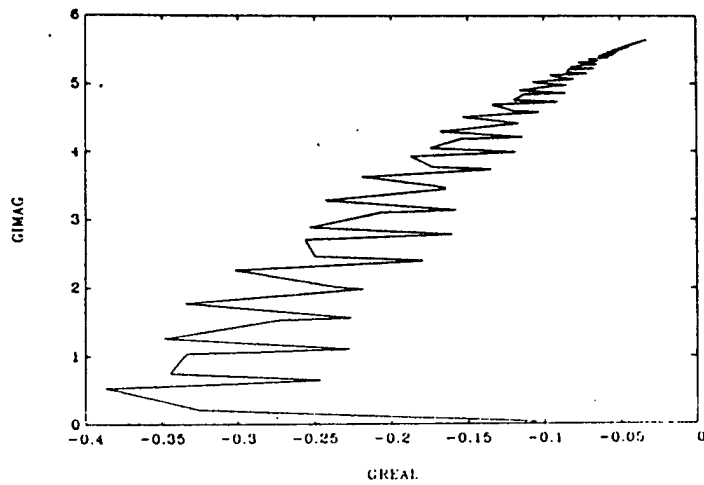
(c) Convergence of GRIME Estimator in Complex Plane.

Fig. 2.6-5 Sine-Dwell Simulation: (a) Plant Input and Output, (b) Outputs of GRIME Estimator, and (c) Convergence of GRIME Estimator in Complex Plane.

33

```
C     FILE: BS.FOR
C
C
      SUBROUTINE BS(FMIN,RATMIN,FMAX,RATMAX,FMID,RATMID,FNEW)
C
C     THIS SUBROUTINE PERFORMS ONE ITERATION OF A BINARY
C     SEARCH TO FIND THE ZERO CROSSING OF REAL/IMAG OF G(j*2PI*F).
C     AT EACH ITERATION THE ROUTINE ASSUMES THAT THE ZERO
C     CROSSING IS ON THE INTERVAL (FMIN,FMAX) AND THAT THE VALUE
C     OF REAL/IMAG IS SPECIFIED FOR FMIN,FMAX, AND AT SOME
C     INTERMEDIATE POINT FMID. THE ROUTINE RETURNS A NEW FREQUENCY
C     FNEW TO TRY NEXT, AND SHRINKS THE INTERVAL (FMIN,FMAX)
C     BY REDEFINING THE ENDPOINTS ACCORDINGLY. THE SET-UP FOR
C     THE NEXT CALL IS FMID=FNEW, AND MUST BE DONE EXTERNALLY BY THE
C     CALLING ROUTINE, ALONG WITH THE CALCULATION OF RATMID.
C
C
C     FMIN-(I/O) LOWER END OF FREQUENCY INTERVAL (HERTZ)
C     FMAX-(I/O) UPPER END OF FREQUENCY INTERVAL (HERTZ)
C     FMID-(I/O) INTERMEDIATE POINT OF (FMIN,FMAX)
C     FNEW-(O) NEW FREQUENCY TO TEST NEXT
C     RATMIN=(I/O) REAL/IMAG OF G(jW) AT W=2PI*FMIN
C     RATMAX=(I/O) REAL/IMAG OF G(jW) AT W=2PI*FMAX
C     RATMID=(I/O) REAL/IMAG OF G(jW) AT W=2PI*FMID
C
      ISMIN=INT(RATMIN/ABS(RATMIN))
      ISMAX=INT(RATMAX/ABS(RATMAX))
      ISMID=INT(RATMID/ABS(RATMID))
      IF(ISMID.NE.ISMAX) GO TO 10
      FMAX=FMID
      RATMAX=RATMID
      FNEW=(FMID+FMIN)/2.
   10 IF(ISMID.NE.ISMIN) GO TO 20
      FMIN=FMID
      RATMIN=RATMID
      FNEW=(FMAX+FMID)/2.
   20 CONTINUE
      RETURN
      END
```

Fig. 2.6-6 BS Subroutine for Single Iteration of Binary Search for Resonance.

```fortran
C     FILE BSTST:FOR
C     THIS FILE TESTS THE BINARY SEARCH SUBROUTINE BS
      FMIN=.04
      CALL SDWELLS(FMIN,GREAL,GIMAG)
      RATMIN=GREAL/GIMAG
      PRINT *,'FMIN=',FMIN,'RATMIN=',RATMIN
      FMAX=.08
      CALL SDWELLS(FMAX,GREAL,GIMAG)
      RATMAX=GREAL/GIMAG
      PRINT *,'FMAX=',FMAX,'RATMAX=',RATMAX
      FMID=(FMIN+FMAX)/2.
      CALL SDWELLS(FMID,GREAL,GIMAG)
      RATMID=GREAL/GIMAG
      DO 10 I=1,10
      THETA=360.*ATAN2(GIMAG,GREAL)/(2.*3.14)
      PRINT *,'FMID=',FMID,'RATMID=',RATMID,'THETA=',THETA
      CALL BS(FMIN,RATMIN,FMAX,RATMAX,FMID,RATMID,FNEW)
      FMID=FNEW
      CALL SDWELLS(FMID,GREAL,GIMAG)
      RATMID=GREAL/GIMAG
10    CONTINUE
      END
```

Fig. 2.6-7 Top Level Routine for Resonance Tuning Simulated Testing.

```fortran
C     FILE: SDWELLS.FOR
C
C     THIS IS A SUBROUTINE FOR SINE-DWELL STRUCTURAL TESTING.
C     THIS SUBROUTINE APPLIES A SINUSOID TO A PLANT MODEL, GENERATES THE
C     RESPONSE, AND THEN CALCULATES THE REAL PART (GREAL) AND
C     IMAGINARY PART (GIMAG) OF THE TRANSFER FUNCTION AT THE SINE-DWELL
C     FREQUENCY. GREAL AND GIMAG ARE ESTIMATED IN TIME, AND SHOULD SETTLE
C     OUT TO CONSTANT VALUES WITH A LONG ENOUGH EXPERIMENT RUN.
C
C
      SUBROUTINE SDWELLS(FREQ,GREAL,GIMAG)
      REAL*4 X1(4),X2(4),GTHETA(2),GP(2,2)
C
C
C     INITIALIZE. EXPERIMENT RUN
      PARAMETER (T=.03, TMAX=600.)
C         T-SAMPLING PERIOD
C         TMAX-TOTAL EXPERIMENT RUN TIME
C
C     INITIALIZE INPUT DESIGN
      PARAMETER (Y=1.)
C         Y-SINEDWELL AMPLITUDE
C         FREQ-SINEDWELL FREQUENCY (HERTZ)
C
C     INITIALIZE PLANT MODEL
      PARAMETER (NM=4)
C         NM-NUMBER OF MODES IN PLANT MODEL
C         X1,X2-INITIAL PLANT STATE
C
C     INITIALIZE GRIME ROUTINE
      DATA GTHETA/0.,0./,TGRIM/20./
      DATA GP(1,1)/1.E10/,GP(1,2)/0./,GP(2,1)/0./,GP(2,2)/1.E10/
C         GTHETA-GRIME ESTIMATOR STATE
C         GP-GRIME ESTIMATOR COVARIANCE
C         TGRIM-GRIME ESTIMATOR TIME CONSTANT
C
C
      DO 50 J=1,4
      X1(J)=0.
      X2(J)=0.
   50 CONTINUE
      NMAX=INT(TMAX/T)
      RL=EXP(-T/TGRIM)
      DO 10 NRUN=1,NMAX
      TRUN=NRUN*T
      CALL SINWT(Y,T,NRUN,FREQ,YSIN,YCOS)
      CALL MODEL(T,NM,X1,X2,YSIN,YP)
      CALL GRIME(Y,YP,FREQ,TRUN,GTHETA,GP,RL,RES,GREAL,GIMAG)
C
   10 CONTINUE
   20 FORMAT(1X,5(E10.4,2X))
      RETURN
      END
```

Fig. 2.6-8 Sine-Dwell Testing Subroutine for use with Resonance Tuning Simulation.

Assume for the moment that it is known that the low frequency resonance lies between .04 and .08 Hz and it is desired to find it more accurately via sine-dwell experiments. The resonance tuning simulation is run with the following parameters

FMIN=.4
FMAX=.8
TMAX=600
TGRIM=20

The results are given below

FMIN=	0.400000E-01 RATMIN=	-8.95374		
FMAX=	0.800000E-01 RATMAX=	5.23976		
FMID=	0.600000E-01 RATMID=	-0.100850	THETA=	95.8074
FMID=	0.700000E-01 RATMID=	2.87578	THETA=	19.1839
FMID=	0.650000E-01 RATMID=	1.47348	THETA=	34.1806
FMID=	0.625000E-01 RATMID=	0.709344	THETA=	54.6780
FMID=	0.612500E-01 RATMID=	0.310266	THETA=	72.7996
FMID=	0.606250E-01 RATMID=	0.106211	THETA=	83.9798
FMID=	0.603125E-01 RATMID=	0.306516E-02	THETA=	89.8699
FMID=	0.601562E-01 RATMID=	-0.487951E-01	THETA=	92.8406
FMID=	0.602344E-01 RATMID=	-0.228411E-01	THETA=	91.3548
FMID=	0.602734E-01 RATMID=	-0.988245E-02	THETA=	90.6121

Since spillover effects are small for this mode, the true resonance is determined accurately after 10 iterations.

Assume that the second frequency is known to lie between .44 and .6 Hz. The resonance tuning experiment is run with the following parameters,

FMIN=.44
FMAX=.6
TMAX=100
TGRIM=20

The results are summarized as,

FMIN=	0.440000	RATMIN=	-3.50633	
FMAX=	0.600000	RATMAX=	2.65671	
FMID=	0.520000	RATMID=	-0937059	THETA= 133.206
FMID=	0.560000	RATMID=	0.485611	THETA= 64.1308
FMID=	0.540000	RATMID=	-0.256629	THETA= 104.446
FMID=	0.550000	RATMID=	0.100512	THETA= 84.3031
FMID=	0.545000	RATMID=	-0.806356E-01	THETA= 94.6781
FMID=	0.547500	RATMID=	0.920637E-02	THETA= 89.5179
FMID=	0.546250	RATMID=	-0.358859E-01	THETA= 92.1019
FMID=	0.546875	RATMID=	-0.133831E-01	THETA= 90.8128
FMID=	0.547187	RATMID=	-0.180379E-02	THETA= 90.1490
FMID=	0.547344	RATMID=	0.399663E-02	THETA= 89.8164

37

Convergence to .547 Hz is obtained after 10 iterations. The value differs from its true value of .55 Hz due to the effects of spillover on the phase resonance criteria.

Assume that the third frequency is know to lie between .7 and .8 Hz. The resonance tuning experiment is run with the following parameters,

FMIN=.7
FMAX=.8
TMAX=100
TGRIM=20

The results are summarized as follows,

FMIN= 0.700000 RATMIN= -1.65786
FMAX= 0.800000 RATMAX= 0.954088
FMID= 0.750000 RATMID= 0.190979   THETA= -100.863
FMID= 0.725000 RATMID= -0.489801   THETA= -63.9367
FMID= 0.737500 RATMID= 0.117818   THETA= -83.3228
FMID= 0.743750 RATMID= 0.435983E-01 THETA= -92.5433
FMID= 0.740625 RATMID= -0.327591E-01 THETA= -88.1684
FMID= 0.742188 RATMID= 0.599738E-02 THETA= -90.3894
FMID= 0.741406 RATMID= -0.132425E-01 THETA= -89.2866
FMID= 0.741797 RATMID= -0.358763E-02 THETA= -89.8400
FMID= 0.741992 RATMID= 0.134687E-02 THETA= -90.1229
FMID= 0.741894 RATMID= -0.105319E-02 THETA= -89.9853

A resonance at .74 Hz is determined after 10 iterations. The value differs from its true value of .7308 due to the effects of spillover on the phase resonance criteria. Also note that the algorithm locks on to a -90 degree phase implying a positive influence coefficient for this mode.

2.6.8 Integration with System Software

As described earlier, subroutines GRIME and BS were developed, tested and improved off-line in a completely self-contained Fortran environment on an IBM PC-AT clone. After the subroutines were fully tested, they were transported to the experiment MicroVAX and integrated with the experimental software.

In the experiment software, the sine-dwell test is set up via the following menu,

```
MENU (4,4,3)
SINE-DWELL PARAMETERS
0 - Exit
61 - PARAM(61) 1.          ;  SAMP=sine-dwell amplitude
62 - PARAM(62) 2.          ;  SDFREQ=sine-dwell frequency (Hz)
63 - PARAM(63) 20.         ;  TGRIM= GRIME estimator time constant (sec)
68 - PARAM(68) 1.          ;  SDIO= I/O flow parameter
                              1-FMIN  2-FMAX  3=FMID  4-Res. Tuning
69 - PARAM(69)             ;  ISDFIL= storage file
```

As an example, the nominal values in MENU(4,4,3) are set to perform a sine-dwell experiment at a 2Hz frequency with input amplitude 1, using a 20 second exponential forgetting factor for the GRIME estimator.

The SDIO parameter controls the mode of operation for setting up the resonance tuning operations. In particular, the resonance tuning task is initialized by performing 3 successive sine-dwell experiments where the SDIO parameter is advanced from SDIO=1 to SDIO=2 to SDIO=3. This sets up the binary search routine with values of GIMAG/GREAL for FMIN, FMAX and FMID, respectively. The resonance tuning search can then be invoked on the very next pass by setting SDIO=4.

2.6.9 Remarks

The most direct method to determine amplitude and phase in the sine-dwell application is by correlation i.e., multiply the input and output together and lowpass filter the result. The solution presented here based on recursive least squares was arrived at after correlation methods were tried and gave poor results. The major difficulties were due to the sampled data approximation and the need for extremely high-order LP filters when determining low frequency sine-dwell estimates.

Resonance tuning is generally very time consuming. For example, determining the .06027 Hz resonance required 10 sine-dwell experiments at 10 minutes each for a total of 100 minutes. Furthermore, additional time is required to allow the structure to come to rest between experiments. This results in a process which is quite time consuming for on-orbit implementation. A better on-orbit approach would be to adjust the input frequency on-line to achieve a resonance condition. Such "plant in the loop" phase-lock techniques do not presently exist in the literature, and appear to be an important area for future research.

Generally speaking, the phase resonance condition is only valid when the modes are widely separated and the damping is small. When this is not the case, the amplitude resonance condition would provide a more robust criteria. This also remains as an area for future investigation.

2.7 Model Order Determination

In this section, a methodology is presented for the determination of order of a linear model representing the input/output transfer function. The algorithm is based on the concept of product moment matrix (PMM) and is presented both in deterministic and stochastic forms. Alternate and modified forms of the algorithm will be used depending on the quality and nature of the noise which is present in the data. The PMM test is applied to simulated data obtained from system models of different orders, as well as the actual data obtained from various identification experiments.

2.7.1 Introduction

The mathematical modeling of large flexible space systems has been a challenging task for several decades. The models for such systems should predict the behavior of the actual system under restricted experimental conditions. Furthermore, when correlated and tested against the actual data, they should explain the observed behavior of the system through post-mission data analysis. In practice, the identification problem is often separated into two parts: a) determination of the order for a linear model and b) estimation of the parameter values of the resulting model. Clearly, in a linear system the model structure is determined by the choice of the order. Hence, an incorrect structural assumption may manifest itself in biased parameter estimates or may even lead to erroneous conclusions on the results of the identification process (e.g., a large model order leads to over parameterizations and identifiability problems; whereas a small order may result in a large bias in parameter estimates). This is of particular interest when model parameters have physical significance and the accuracy of the parameter estimate is the primary objective of the system identification experiment. Different techniques for model order determination have been discussed [19]. Here, the product moment matrix approach is chosen for a variety of reasons and in each case it proves advantageous over alternate methods. For example, the PMM requires no a priori assumption on the model parameterization and form and it requires no knowledge of density or distribution functions of unknown parameters or data. This technique is applicable to both deterministic and stochastic systems. Finally, the PMM algorithm is robust with respect to uncertainties and it produces meaningful results even in the presence of significant additive measurement noise [20][23].

The PMM is used for model order determination for a linear time-invariant dynamic model of the facility. Narrow-band and wide-band input signals are applied to the system in the form of hub torquers. The system response is observed by means of hub and levitator sensors for various identification experiments. The PMM test, both in deterministic and stochastic forms, are also applied to the simulated data obtained from the state space models of the system with different orders. The simulation and the real data case studies are then compared. A brief discussion of the PMM algorithm follows.

2.7.2 The Product Moment Matrix

The idea behind the PMM approach is to analyze the correlation function of the input-output variables for a linear model of changing structure. This will subsequently lead to a pronounced dynamic behavior around the "true" order of the system. This behavior may be observed through the determinant or eigenvalues of a matrix with elements constructed as follows.

Let $\{x_k\}$ and $\{y_k\}$ be a set of observations of input and output respectively (data) which are contaminated by measurement noise. Let us also assume that the input signal is sufficiently rich such that it persistently excites all system modes of interest. A linear system of order n has a system function which is given by

$$H(z) = \frac{Y(z)}{X(z)} = \frac{\sum_{i=1}^{n} \theta_{2i-1} z^{-i}}{1 - \sum_{i=1}^{n} \theta_{2i} z^{-i}} \qquad (2.7-1)$$

letting

$$\theta^T(n) = [\theta_1, \ldots, \theta_{2n}] \qquad (2.7-2)$$

and

$$\Lambda^T(k,n) = [x_{k-1}, y_{k-1}, x_{k-2}, y_{k-2}, \ldots, x_{k-n}, y_{k-n}] \qquad (2.7-3)$$

Then in time-domain, the measured system response is given by

$$y_k = \theta^T(n) \wedge (k,n) \qquad (2.7-4)$$

For N measurements, the "generalized Hankel matrix" $H(N)$ is as follows.

$$H(N) = \begin{pmatrix} y_0 & y_1 & \cdots & y_{N-1} \\ y_1 & y_2 & \cdots & y_N \\ \vdots & \vdots & & \\ y_{N-1} & y_N & & y_{2N-2} \end{pmatrix} \overset{\Delta}{=} y_{i+j-2} \qquad i,j > 0 \qquad (2.7-5)$$

Similarly, the generalized Hankel matrix for the $N \times N$ block matrices formed out of the shifted sequence $y_{k+\ell}$ will be

$$H(N) = [y_{i+j+\ell-2}]$$

If a finite-dimensional realization for the system exists, denoting n^* as the rank of its minimal realization, then [21]

$$n^* = \text{Rank } H(N) \qquad (2.7-6)$$

Since n^* is the dimension of a **minimal** realization of the system which is unknown, it will subsequently be referred to as the "true" order of the system. Note also that the ordering of components in the vectors $\wedge(k,n)$ and $\theta(n)$ is such that for a higher-order model, additional components are simply added to the end of these vectors. The product moment matrix of the system is defined by:

$$Q[n,N] \equiv Q_n \overset{\Delta}{=} \frac{1}{N} \sum_{k=1}^{N} \wedge(k,n) \wedge^T(k,n)$$

41

$$= \frac{1}{N} \begin{pmatrix} \sum_{k=1}^{N} x_{k-1}^2 & \sum_{k=1}^{N} x_{k-1} y_{k-1} & \cdots & \sum_{k=1}^{N} x_{k-1} y_{k-n} \\ \sum_{k=1}^{N} y_{k-1} x_{k-1} & \sum_{k=1}^{N} y_{k-1}^2 & \cdots & \sum_{k=1}^{N} y_{k-1} y_{k-n} \\ \vdots & & & \vdots \\ \sum_{k=1}^{N} y_{k-n} x_{k-1} & \sum_{k=1}^{N} y_{k-n} y_{k-1} & \cdots & \sum_{k=1}^{N} y_{k-n}^2 \end{pmatrix} \qquad (2.7-7)$$

where n is an assumed order for the system and N is the number of data points. If the data is noise free and n^* is the "true" order of the system, then Q_n will become singular for all $n > n^*$ [21], and

$$\text{Rank}[Q_n] = \left\{ \begin{matrix} = & 2n \\ = & n+n^* \end{matrix} \right\} \text{ for } n \left\{ \begin{matrix} \leq \\ > \end{matrix} \right\} n^* \qquad (2.7-8)$$

Hence, Q_n has the following properties:

$$\det[Q_n] = \left\{ \begin{matrix} \neq & 0 \\ = & 0 \end{matrix} \right\} \text{ for } n \left\{ \begin{matrix} \leq \\ > \end{matrix} \right\} n^* \qquad (2.7-9)$$

For an arbitrary value of N and an assumed value of n, the ratio

$$D_n = \frac{\det[Q_n]}{\det[Q_{n+1}]} \qquad (2.7-10)$$

is calculated for succeeding model orders $n+1, \ldots, n^*, \ldots, n_{\max}$. If the value of D_n exhibits a distinct increase compared to D_{n-1}, then n corresponds approximately to n^*. In the presence of noise however, the $\text{Det}[Q_n]$ is usually non-zero for $n > n^*$. Assuming that the additive noise to the input and output is Gaussian and white, and the noise to signal ratio is larger than 5%, for a system with order greater than 5, then the modified product moment matrix $\hat{Q}_n$ given by

$$\hat{Q}_n = Q_n - \sigma^2 R \qquad (2.7-11)$$

is used in place of (2.7-7) where $\sigma^2 R$ is the estimated covariance matrix of the measurement noise.

A ratio test of

$$\hat{D}_n = \frac{\det[\hat{Q}_n]}{\det[\hat{Q}_{n+1}]} \qquad (2.7-12)$$

has proved its effectiveness for noise-to-signal ratio of up to 30% [20]. A further improvement may still be obtained using the ratio

$$\tilde{D}_n = \frac{\det[\tilde{P}_n]}{\det[\tilde{Q}_n]} \qquad (2.7-13)$$

where $\tilde{P}_n$ is the lower $(2n+1) \times (2n+1)$ corner of $\hat{Q}_n$, and $\tilde{Q}_n$ is the lower $2n \times 2n$ corner of $\hat{Q}_n$.

In practice, where the measurement noise is nonwhite, the enhanced PMM given by

$$\check{Q}_n = Q_n - \sum_n \qquad\qquad (2.7-14)$$

is used. An estimate of $\sum_n$, the measurement noise contributions to the PMM, is obtained by first collecting measurements from the system when the input to the system is identically zero. Denoting the input measurement noise by n_x and the output measurement noise by n_y, then $\sum_n$ is computed as

$$\sum_n = Q_n|\, y = n_y, x = n_x$$

The $\check{Q}$ product moment matrix henceforth referred to as enhanced product moment matrix (EPMM) will reduce to the formulations (2.7-7) and (2.7-11) depending upon the nature of noise in the data. The EPMM, although computationally less efficient, provides a more accurate assessment of measurement noise, and consequently, gives a better estimate of the system order.

An alternate representation of PMM is given as follows:

$$Q_n = E[a_n a_n^T] \qquad\qquad (2.7-15)$$

where

$$a_n^T = [x_0\ y_0\ x_1\ y_1 \ldots x_{n-1} y_{n-1}]$$

and E is the statistical expectation operation. We will refer to Equation (2.7-15) as the stochastic representation of PMM and the Equations (2.7-7), (2.7-11) and (2.7-14) as the deterministic representations of PMM. The implementations for each of the above representations are discussed next.

2.7.3 Deterministic Implementation

The deterministic product moment matrices henceforth referred to as PMMD and given in Equations (2.7-7), (2.7-11) and (2.7-14) require the processing of the raw input and output data. The performance of the PMMD algorithm is first evaluated by processing a single data window of length 32768 points shown in Figures 2.7-1 to 2.7-4. The data is obtained from the simulation of a truncated state space modal model of the facility. The subroutine MODEL in Fig. 2.7-6 is used with white noise input to produce output data. The process is repeated for models of different orders.

The results from three case studies with simulated data are summarized in Table 2.7-1. For this simulation, a plant with 4 modal frequencies is used, where 2 modes lie between 0 and 1 Hz, and 2 modes lie between 1 and 3 Hz. In Case Study 1, the plant is excited by a 0-1 Hz input thereby exciting only the lower 2 modes. In Case Study 2, the plant is excited by a 1-3 Hz input signal thereby exciting only the higher 2 modes. In Case Study 3 the plant is excited by a 0-3 Hz input, thereby exciting all 4 modes. For convenience, the data for Case Study 3 is depicted in more detail in Figures 2.7-1 through 2.7-5.

43

The determinant values for the PMMD algorithm are given in Table 2.7-1 for various assumed model orders, for the various cases mentioned above. It is seen that the PMM determinant values for n>4 show small variations about zero. Hence, there is no clear point at which the determinant vanishes in the PMMD algorithm (results for the stochastic algorithm PMMS will be discussed in the next section). In this study, a threshold of value 0.1% of the first determinant is used beyond which the determinant is assumed zero. With this value, the estimated model order in Case Study 1 is $n = 2$, in Case Study 2 is $n = 3$, and in Case Study 3 is $n = 4$. Clearly, these values underestimate the expected model orders of $n^* = 4$, $n^* = 4$, and $n^* = 8$, respectively. It should be noted that changing the threshold value will change the estimated model order. The present choice of 0.1% of the first determinant was found to consistently underestimate the model order and was useful to initialize the sequential curve fitting approach. In general, however, more work needs to be done to establish reasonable threshold values for the PMM algorithms based on objective criteria.

2.7.4 Stochastic Implementation

When the underlying dynamical process is stationary [22], the correlations have the form:

$$
\begin{aligned}
E[x_i y_j] &= R_{xy}(j - i) \\
E[x_i x_j] &= R_{xx}(j - i) = R_{xx}(i - j) \\
E[y_i y_j] &= R_{yy}(j - i) = R_{yy}(i - j)
\end{aligned}
\qquad (2.7-16)
$$

Then by assuming that the process is ergodic, temporal averages are equivalent to ensemble averages, and the product moment matrix given in (2.7-7) has the simple analytical form:

$$
\lim_{N \to \infty} Q(N, n) = Q_*(n)
\qquad (2.7-17)
$$

$$
Q_*(n) =
\begin{bmatrix}
Q_*^{(1,1)} & \cdots & Q_*^{(1,n)} \\
\vdots & & \vdots \\
Q_*^{(n,1)} & \cdots & Q_*^{(n,n)}
\end{bmatrix}
\qquad (2.7-18)
$$

$$
Q_*^{(i,j)} =
\begin{bmatrix}
R_{xx}(j - i) & R_{yx}(j - i) \\
R_{xy}(j - i) & R_{yy}(j - i)
\end{bmatrix}
\qquad ((2.7-19)
$$

44
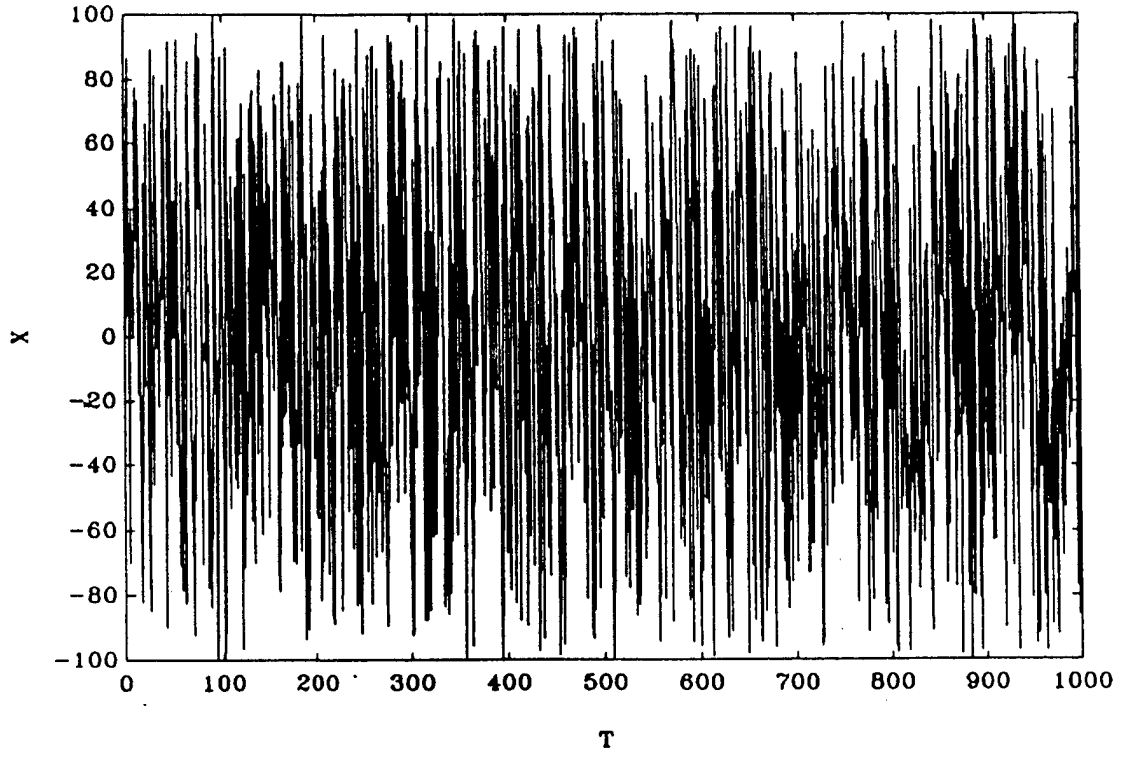
Fig. 2.7-1 Wide-Band Input Data.
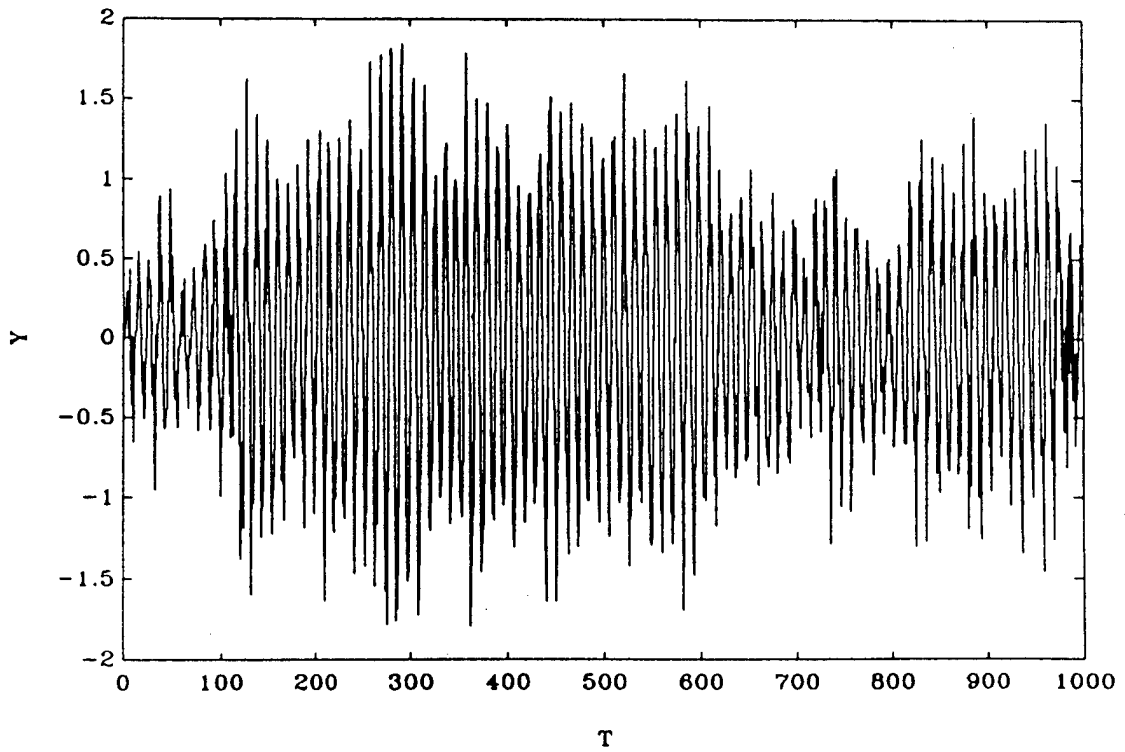

Fig. 2.7-2 System Response to Wide-Band Input.

45
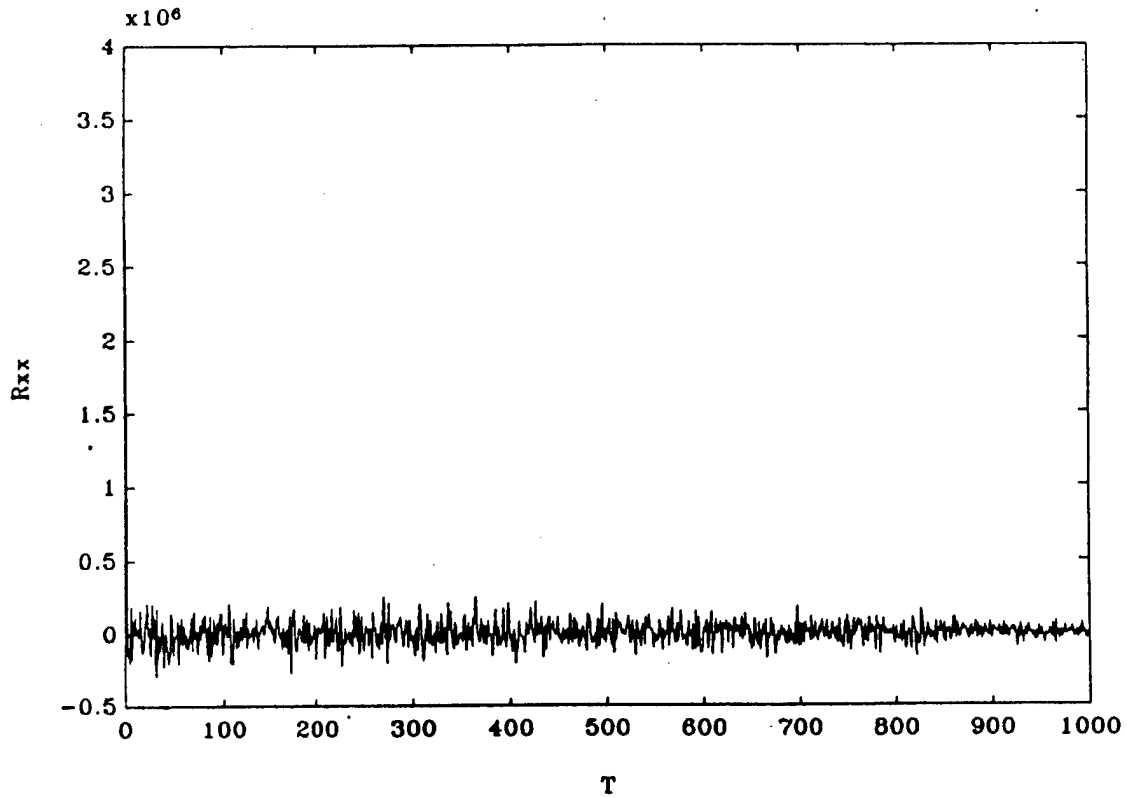
Fig. 2.7-3 Input Auto-Correlation.
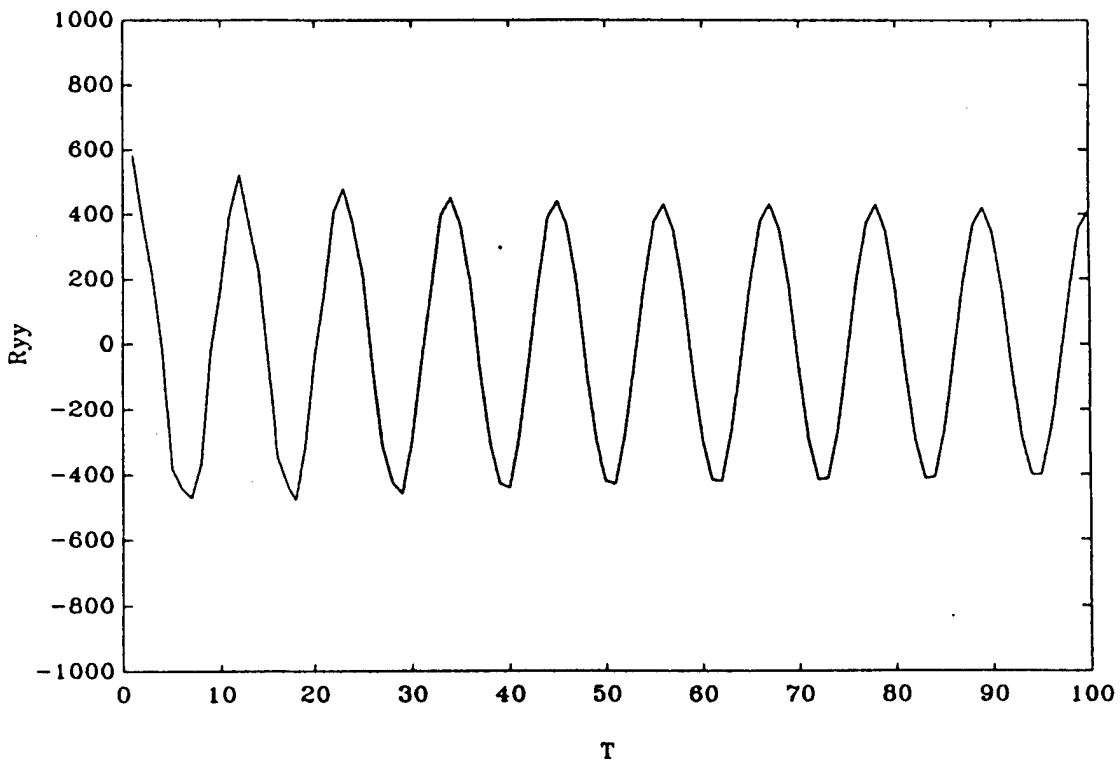
Fig. 2.7-4 Output Auto-Correlation.

46
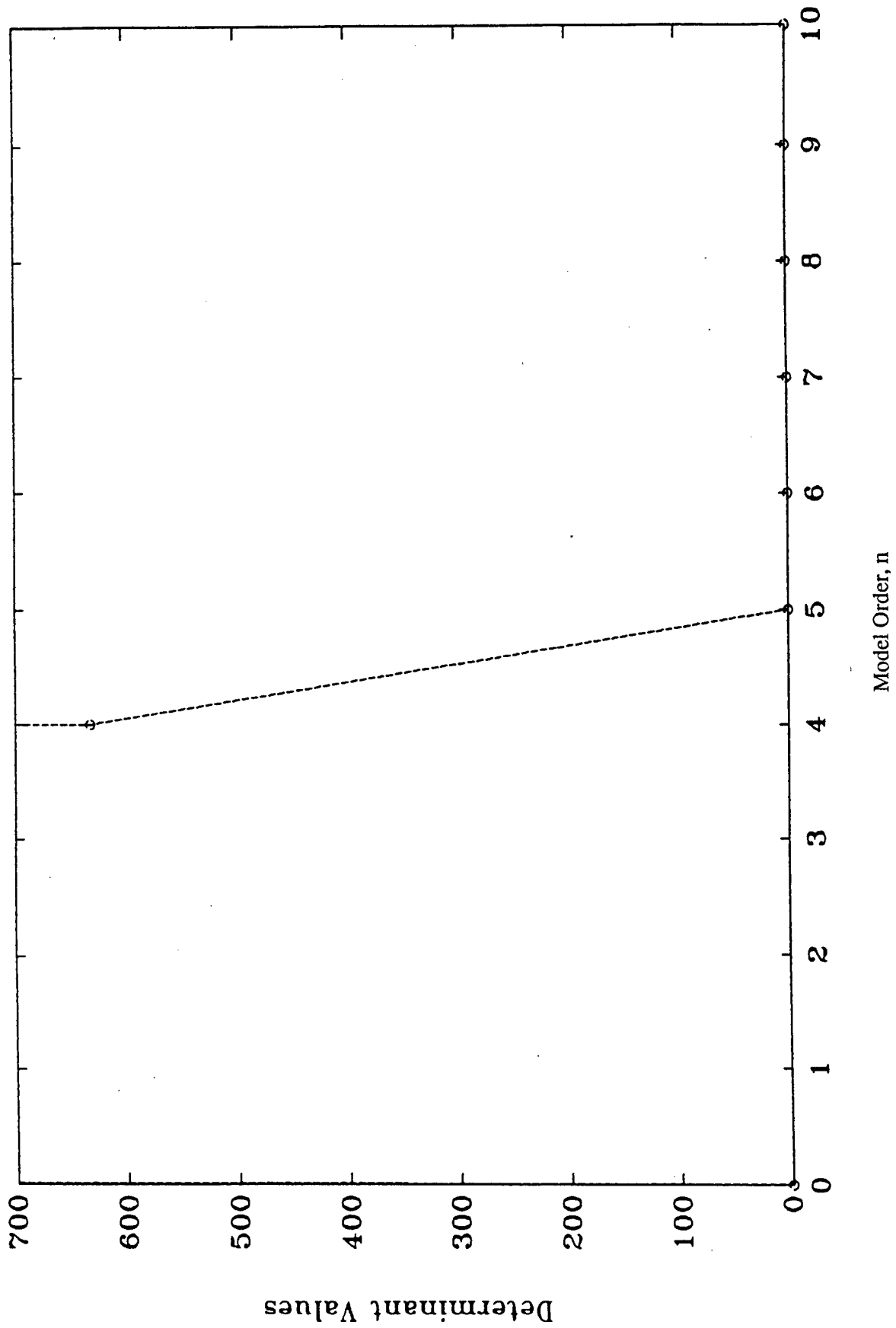
Fig. 2.7-5 PMMD Test for A System with Four Modes ($n^* = 8$).

Model Order, n

Determinant Values

Table 2.7-1 Summary of Case Studies.

Case Study	True Model	Model Order, n	Determinants	
			PMMD	PMMS
1	2 modes (0 – 1 Hz) $n^* = 4$	1 2 3 4	20968.58 21547.40 5.282252 4.444×10^{-8}	20973.97 22613.65 -212.7306 -3.56189×10^{-2}
2	2 modes (1 – 3 Hz) $n^* = 4$	1 2 3 4	97.44894 408.6275 3.533490 7.725×10^{-4}	97.432160 396.85710 -71.81800 0.9212800
3	4 modes (0 – 3 Hz) $n^* = 8$	1 2 3 4 5 6	47056.85 810270.8 156066.3 632.4109 1.3230×10^{-2} 9.0740×10^{-10}	47068.91 830226.7 -47932.89 -600815.9 466950.9 -4786.113

48

```fortran
      SUBROUTINE MODEL(N,X1,X2,U,Y)
C
C

      DIMENSION B(10),C(10),FREQ(10),X1(1),X2(1)
C
C     DEFINITIONS:
C         N=NUMBER OF MODES
C         X1=NVECTOR OF MODAL AMPLITUDES
C         X2=NVECTOR OF MODAL VELOCITIES
C         U=SCALAR INPUT
C         Y=SCALAR OUTPUT
C         B=NVECTOR,INPUT INFLUENCE COEFF.
C         C=NVECTOR,OUTPUT INFLUENCE COEFF.
C         ZETA=SCALAR X MODAL DAMPING
C
C     SISO HUB TO FEED TRANSFER FUNCTION
C     ASSUMES 3.3LB BOOM MASS
C     SAMPLE&HOLD INPUT
C     IDEAL SAMPLED OUTPUT
C
      DATA B/.0943,-.0129,.274,.368,0.,0.,0.,0.,0.,0./
      DATA C/-.319,2.97,.238,.403,0.,0.,0.,0.,0.,0./
      DATA FREQ/.0745,.307,.713,2.60,0.,0.,0.,0.,0.,0./
      DATA T/.03/,ZETA/.007/,PI/3.1415927/
C
C

      Y=0.
      DO 10 I=1,N
      WI=2.*PI*FREQ(I)
      R=EXP(-ZETA*WI*T)
      S=SQRT(1.-ZETA**2.)
      THETA= ACOS(S)
      WN= WI*S
      CS= COS(WN*T)
      SN=SIN(WN*T)
      Z1= (R/S)*(COS(WN*T-THETA)*X1(I)+SN*X2(I)/WI)
      Z2=R/S*(COS(WN*T+THETA)*X2(I)-WI*SN*X1(I))
      D=ZETA/S
      E=B(I)/WI**2.
      Z1=Z1+E*(1.-R*(CS+D*SN))*U
      X2(I)=Z2+E*R*WI*SN*U/S
      X1(I)=Z1
      Y=C(I)*Z1+Y
   10 CONTINUE
      RETURN
      END
```

Fig. 2.7-6 Subroutine MODEL used for Generating System Response.

This explicitly gives the product moment matrix without requiring any additional processing of the input and output data. Thus when correlations are available under these circumstances, the product moment matrix test can be constructed with considerable fewer arithmetic operations than those required by the algorithm outlined in the previous section. The key practical issues are the validity of the assumptions regarding stationarity and ergodicity of the signals and the means for calculating the correlation functions based on finite-time data lengths.

Results of the three case studies with simulated data are summarized in Table 2.7-1. The case studies themselves have been described in more detail in the previous section on the PMMD algorithm. Hence, this discussion will focus on results for the PMMS algorithm. It is seen from Table 2.7-1 that the determinant values of the PMMS algorithm become negative for certain model orders. At first thought this seems somewhat remarkable. However, this is easily explained by the fact that the positivity of the product moment matrix is destroyed by the finite-time estimation of the auto- and cross-covariances in eqns. (2.7-18) and (2.7-19). Note that this is never a problem in PMMD algorithm, since the product moment matrix (2.7-7) is defined as a sum of outer-products.

The above numerical example indicates that 30 minutes of experiment time is not sufficiently long enough to ensure convergence of the correlations required to accurately describe the product moment matrix. This also indicates that the PMMD is inherently more reliable for experiments on short horizons. It is interesting to note that the orders at which the PMMS determinant go negative in Table 2.7-1 roughly correspond to the system orders as predicted by the PMMD algorithm. There may still be some additional useful interpretations of the results given by PMMS algorithm. This is an area for further investigations.

2.7.5 Case Study With Experimental Data

The subroutines PMMD, PMMDN, PMMDE, and PMMS in Figures 2.7-7 and 2.7-8 have been integrated into the experiment software and were used for various identification experiments. The model order determination menu is given as follows.

MENU (4,4,5)

PRODUCT MOMENT TEST PARAMETERS

```
0 - Exit
111 - PARAM(111)  8      ; NHAT = upper bound on # structural modes
112 - PARAM(112)  0.1    ; SIGPMM = environmental noise sigma
                                 ≥ 0 PMMD
                                 = 2 PMMDN
                                 = 3 PMMDE
113 - PARAM(113)  0      ; IDEC = decimation factor
```

114 - PARAM(114)   1   ; ISD - Choose alg. (0- PMMD's, 1- PMMS)
115 - PARAM(115)   32000   ; NDATA = # time data points (PMMD's only)

The choice of PMM routines is based on the experimenter's assessment of the measurement noise. If data is noise free, then PMMD is used with SIGPMM set to zero. For white Gaussian uncorrelated input and output noise, PMMD is used with values of SIGPMM chosen as an approximation to the noise variance. If the measurement noise is colored and significant, the PMMDN will provide an estimate of the autocovariance of the measurement noise. The PMMDE will use the noise file to modify the "noisy" PMM and will subsequently use the enhanced PMM to estimate the model order.

As the first step for the determination of the model order, the measurement noise observed at the input and output is stored in a system file. The PMM test parameters are set to ISD=0, NHAT=20, and SIGPMM=-1. This enables PMMDN to be called, and the noise file processed for the computation of $\sum_n$. For a particular identification experiment, a value for the system order will be assumed, i.e., NHAT $\leq$ 20. SIGPMM is set to -2 for the PMMDE algorithm to process the input-output data making use of the processed noise file without any assumptions on the nature of measurement noise. The PMMD and PMMDE have essentially the same structure; except that for the PMMD algorithms the measurement noise is assumed white. An estimate of the variance of the measurement noise SIGPMM is provided from the noise file, and can also be separately estimated from the PMMDN subroutine. PMMD computes the model order, while SIGPMM is chosen arbitrarily by the experimenter. The PMMDE uses the noise statistics and modifies the PMMD matrix, where it assumes that the measurement noise is Gaussian and white. The PMMDE makes no assumptions on the nature of the measurement noise and appropriately takes out the contribution of the noise from the PMM matrix. If the noise file is not available (e.g., a separate experiment for noise determination was not performed), the PMMDE can provide an assessment of the noise contained in the data by computing the dynamics of PMM matrix for NHAT=20. A search will be performed to find the smallest eigenvalue of the product moment matrix which is attributed to the contributions of the measurement noise. This value will subsequently be used as the variance of the measurement noise and will then be input to the PMMD.

The PMM algorithms are used for the following identification experiments. A wideband input signal is applied to the two hub axis and the system response is observed through the two collocated hub sensors and the levitator sensor. The experiments are repeated when a narrow band signal of 0-3 Hz is applied to one of the hub axis. A total of 32768 data points are processed. Figure 2.7-9 shows measured input-output data and Figure 2.7-10 shows the PMM test results. Using 0.1% of the first determinant as a threshold for determinant of the PMM as discussed earlier, all versions of the PMM tests consistently indicate an order estimate of 4 for the system model. The levitator data shown in Figure 2.7-11 is almost noise free and gives an estimate of 3 as shown in Figure 2.7-12. A hub sensor data taken on other axis indicates that system has an order 4, using PMMDE and PMMD for SIGPMM=0.01 and SIGPMM=0.0, as shown in Figures 2.7-13

and 2.7-14. The narrow band experiment shown in Figures 2.7-15 and 2.7-16 indicates an order of 3. Note that the PMM algorithm is applicable to systems with modes which are excited due to persistently exciting inputs. The PMMS test did not however produce meaningful experimental results, essentially due to the stationarity and ergodicity assumptions on the signals in the formulation of the PMMS algorithm. The practical value of the stochastic implementation (PMMS) may also depend on reliable means for calculating the correlation functions. The PMMS approach can however substantially reduce the computational requirements for accurately identifying the system model order. The sensitivity of the stochastic product moment matrix to the breakdown of the necessary statistical assumptions requires further investigations.

```
      SUBROUTINE PMMDE(NHAT,NDATA,U,Y,DET,DETR)
C
C.    NAME: PMMDE         (8/3/88)
C
C     PURPOSE: TO COMPUTE AND CARRY OUT THE ENHANCED PRODUCT MOMENT
C              MATRIX TEST (DETERMINISTIC CASE / DOUBLE PRECISION)
C
C     INPUTS:
C          NHAT : INITIAL ESTIMATE OF SYSTEM ORDER (<=20)
C          NDATA : NUMBER OF DATA POINTS
C          U : INPUT DATA
C          Y : OUTPUT DATA
C
C     OUTPUTS:
C          DET(.) : DETERMINANT VALUES
C          DETR(.) : DETERMINANT RATIOS [DETER(I)=DET(I)/DET(I+1)]
C
C     AUXILLARY :
C          QMAT(.,..) : 2*NHAT x 2*NHAT ENHANCED PRODUCT MOMENT MATRIX
C
C     PARAMETER (NDIM=20)
C
      REAL*4 DET(*),DETR(*),U(*),Y(*)
      REAL*8 H(2*NDIM,2*NDIM),G(2*NDIM,2*NDIM),QMAT(2*NDIM,2*NDIM)
      REAL*8 QK(2*NDIM,2*NDIM),R(2*NDIM,2*NDIM),D(2*NDIM,2*NDIM)
      REAL*8 E(2*NDIM,2*NDIM)
      REAL*8 DETM1,DETM2,MIND,SIGMA2
      REAL*8 TOTAL1,TOTAL2,TEMP1,TEMP2,STORE1
      INTEGER NUMBER,CUTE,POS1,POS2,SPOT1,SPOT2,COUNT,KOUNT,K
      INTEGER NHAT,NDATA
C
C---------------------------------------------------------------------
C     BEGIN TO COMPUTE AND SET UP PRODUCT MOMENT MATRIX.
C---------------------------------------------------------------------
C
      SPOT1=-1
      SPOT2=0
      DO 10 CUTE=1,NHAT
           SPOT1=SPOT1+2
           SPOT2=SPOT2+2
           POS1=-1
           POS2=0
           DO 20 Q=1,NHAT
                TOTAL1=0
                TOTAL2=0
                DO 30 K=1,NDATA+1
                COUNT=K-CUTE
                KOUNT=K-Q
                IF (KOUNT.LT.0) THEN
                          TEMP1=0
                          TEMP2=0
                    ELSE
                          TEMP1=U(KOUNT)
                          TEMP2=Y(KOUNT)
```

Fig. 2.7-7 Subroutine PMMDE Used for Deterministic Implementations.

```
                        ENDIF
                        IF (COUNT.LT.0) THEN
                                    STORE1=0
                            ELSE
                                    STORE1=U(COUNT)
                        ENDIF
                        TOTAL1=TOTAL1+STORE1*TEMP1
                        TOTAL2=TOTAL2+STORE1*TEMP2
30                      CONTINUE
                        POS1=POS1+2
                        POS2=POS2+2
                        QMAT(SPOT1,POS1)=TOTAL1
                        QMAT(SPOT1,POS2)=TOTAL2
20              CONTINUE
                POS1=-1
                POS2=0
                DO 40 Q=1,NHAT
                        TOTAL1=0
                        TOTAL2=0
                    DO 50 K=1,NDATA+1
                        COUNT=K-CUTE
                        KOUNT=K-Q
                        IF (KOUNT.LT.0) THEN
                                    TEMP1=0
                                    TEMP2=0
                            ELSE
                                    TEMP1=U(KOUNT)
                                    TEMP2=Y(KOUNT)
                        ENDIF
                        IF (COUNT.LT.0) THEN
                                    STORE1=0
                            ELSE
                                    STORE1=Y(COUNT)
                        ENDIF
                        TOTAL1=TOTAL1+STORE1*TEMP1
                        TOTAL2=TOTAL2+STORE1*TEMP2
50                  CONTINUE
                    POS1=POS1+2
                    POS2=POS2+2
                    QMAT(SPOT2,POS1)=TOTAL1
                    QMAT(SPOT2,POS2)=TOTAL2
40              CONTINUE
10      CONTINUE
        DO 110 I=1,NHAT*2
            DO 109 J=1,NHAT*2
                QMAT(I,J)=QMAT(I,J)/NDATA
                    QK(I,J)=QMAT(I,J)
109         CONTINUE
110     CONTINUE
C------------------------------------------------------------
C       COMPUTE ESTIMATE OF NOISE VARIANCE SCALE FACTOR
C------------------------------------------------------------
        CALL TRED2(QMAT,2*NHAT,2*NDIM,D,E)
        CALL TQLI(D,E,2*NHAT,2*NDIM)
```

Fig. 2.7-7 Subroutine PMMDE Used for Deterministic Implementations (continued).

```
      CALL TRED2(QMAT,2*NHAT,2*NDIM,D,E)
      CALL TQLI(D,E,2*NHAT,2*NDIM)
      SIGMA2=MIND(D,2*NHAT)
C---------------------------------------------------------
C     SETUP ENHANCED PRODUCT MOMENT MATRIX
C---------------------------------------------------------
      CALL RNOISE(R,2*NHAT)
      DO 79 I=1,2*NHAT
         DO 69 J=1,2*NHAT
            QMAT(I,J)=QK(I,J)-SIGMA2*R(I,J)
 69      CONTINUE
 79   CONTINUE
      DO 60 I=1,NHAT -1
C---------------------------------------------------------------
C     SET UP THE (N) AUXILIARY MATRIX AS N VARIES FROM 1 TO QDIM.
C---------------------------------------------------------------
         DO 70 J=1,2*I
            DO 80 K=1,2*I
               H(J,K)=QMAT(J,K)
 80         CONTINUE
 70      CONTINUE
C---------------------------------------------------------
C     SET UP THE   (N+1) MATRIX.
C---------------------------------------------------------
         DO 90 J=1,2*I+2
            DO 100 K=1,2*I+2
               G(J,K)=QMAT(J,K)
 100        CONTINUE
 90      CONTINUE
         CALL DETERM(H,2*I,DETM1)
         CALL DETERM(G,2*I+2,DETM2)
         DET(I)=DETM1
         DETR(I)=DETM1/DETM2
 60   CONTINUE
      DET(NHAT)=DETM2
      RETURN
      END
C-------------------------------------------------------------------
C     SUBROUTINE TO FIND DETERMINANT.
C-------------------------------------------------------------------
      SUBROUTINE DETERM(A,SIZE,DETM)
      PARAMETER (NDIM=20)
      REAL*8 A(2*NDIM,2*NDIM),B(2*NDIM,2*NDIM),DETM,TEMP,VALUE
      INTEGER I,J,K,L,M,N,COUNT,SIZE
C     -------------------------------
C     COPY INTO WORKING FILE.
C     -------------------------------
      DO 356 I=1,SIZE
         DO 357 J=1,SIZE
            B(I,J)=A(I,J)
 357     CONTINUE
 356  CONTINUE
```

Fig. 2.7-7 Subroutine·PMMDE Used for Deterministic Implementations (continued).

```fortran
C-------------------------------------------------
C      BEGIN LOOP TO FIND PIVOT ELEMENT .
C-------------------------------------------------
       COUNT=0
       DO 364 K=1,SIZE
               DO 365 J=K+1,SIZE
C-------------------------------------------------------
C      IF PIVOT ELEMENT IS SMALLER THEN SWITCH ROW.
C-------------------------------------------------------
                         IF (ABS(B(K,K)).LT.ABS(B(J,K))) THEN
                              COUNT=COUNT+1
                              DO 368 I=1,SIZE
                                    TEMP=B(J,I)
                                    B(J,I)=B(K,I)
                                    B(K,I)=TEMP
 368                          CONTINUE
                         ENDIF
 365               CONTINUE
C-----------------------------------------------
C      ZERO OUT THE FIRST COLUMN.
C-----------------------------------------------
                   DO 377 M = K + 1,SIZE
C                        IF (B(K,K).EQ.0.AND.B(M,K).EQ.0) THEN
C                              VALUE=0
C                           ELSE
                                 VALUE=B(M,K)/B(K,K)
C                           ENDIF
                           DO 379 N=1,SIZE
                                 B(M,N)=B(M,N)-VALUE*B(K,N)
 379                       CONTINUE
 377               CONTINUE
 364       CONTINUE
C-------------------------------------------------------------------
C      CALCULATE DETERMINANT BY MULTIPLYING THE DIAGONAL ELEMENTS.
C-------------------------------------------------------------------
       DETM=1.0D0
       DO 388 K=1,SIZE
               DETM=DETM*B(K,K)
 388   CONTINUE
       DETM=DETM*((-1)**COUNT)
       END
C
C
C
C

       SUBROUTINE TRED2(A,N,NP,D,E)
       REAL*8 A(NP,NP),D(NP),E(NP)
       IF(N.GT.1)THEN
         DO 18 I=N,2,-1
           L=I-1
           H=0.
           SCALE=0.
           IF(L.GT.1)THEN
             DO 11 K=1,L
```

Fig. 2.7-7 Subroutine PMMDE Used for Deterministic Implementations (continued).

```
                    SCALE=SCALE+ABS(A(I,K))
11                CONTINUE
                  IF(SCALE.EQ.0.)THEN
                     E(I)=A(I,L)
                  ELSE
                     DO 12 K=1,L
                        A(I,K)=A(I,K)/SCALE
                        H=H+A(I,K)**2
12                   CONTINUE
                     F=A(I,L)
                     G=-SIGN(SQRT(H),F)
                     E(I)=SCALE*G
                     H=H-F*G
                     A(I,L)=F-G
                     F=0.
                     DO 15 J=1,L
c Following line is needed to compute eigenvectors.
c                       A(J,I)=A(I,J)/H
                        G=0.
                        DO 13 K=1,J
                           G=G+A(J,K)*A(I,K)
13                      CONTINUE
                        IF(L.GT.J)THEN
                           DO 14 K=J+1,L
                              G=G+A(K,J)*A(I,K)
14                         CONTINUE
                        ENDIF
                        E(J)=G/H
                        F=F+E(J)*A(I,J)
15                   CONTINUE
                     HH=F/(H+H)
                     DO 17 J=1,L
                        F=A(I,J)
                        G=E(J)-HH*F
                        E(J)=G
                        DO 16 K=1,J
                           A(J,K)=A(J,K)-F*E(K)-G*A(I,K)
16                      CONTINUE
17                   CONTINUE
                  ENDIF
               ELSE
                  E(I)=A(I,L)
               ENDIF
               D(I)=H
18          CONTINUE
         ENDIF
c Following line is needed to compute eigenvectors.
c        D(1)=0.
         E(1)=0.
         DO 23 I=1,N
c From here to .........
c           L=I-1
c           IF(D(I).NE.0.)THEN
c              DO 21 J=1,L
```

Fig. 2.7-7 Subroutine PMMDE Used for Deterministic Implementations (continued).

57

```
c              G=0.
c              DO 19 K=1,L
c                G=G+A(I,K)*A(K,J)
c19            CONTINUE
c              DO 20 K=1,L
c                A(K,J)=A(K,J)-G*A(K,I)
c20            CONTINUE
c21          CONTINUE
c          ENDIF
c to here is needed to compute eigenvectors.
          D(I)=A(I,I)
c From here......
c          A(I,I)=1.
c          IF(L.GE.1)THEN
c            DO 22 J=1,L
c              A(I,J)=0.
c              A(J,I)=0.
c22          CONTINUE
c          ENDIF
c to here is needed to compute eigenvectors.
23      CONTINUE
        RETURN
        END
c
c
c
c
c
c

        SUBROUTINE TQLI(D,E,N,NP)
        REAL*8 D(NP),E(NP)
        IF (N.GT.1) THEN
          DO 11 I=2,N
            E(I-1)=E(I)
11        CONTINUE
          E(N)=0.
          DO 15 L=1,N
            ITER=0
1           DO 12 M=L,N-1
              DD=ABS(D(M))+ABS(D(M+1))
              IF (ABS(E(M))+DD.EQ.DD) GO TO 2
12          CONTINUE
            M=N
2           IF(M.NE.L)THEN
              IF(ITER.EQ.30)PAUSE 'too many iterations'
              ITER=ITER+1
              G=(D(L+1)-D(L))/(2.*E(L))
              R=SQRT(G**2+1.)
              G=D(M)-D(L)+E(L)/(G+SIGN(R,G))
              S=1.
              C=1.
              P=0.
              DO 14 I=M-1,L,-1
                F=S*E(I)
```

Fig. 2.7-7 Subroutine PMMDE Used for Deterministic Implementations (continued).

58

```
                B=C*E(I)
                IF(ABS(F).GE.ABS(G))THEN
                   C=G/F
                   R=SQRT(C**2+1.)
                   E(I+1)=F*R
                   S=1./R
                   C=C*S
                ELSE
                   S=F/G
                   R=SQRT(S**2+1.)
                   E(I+1)=G*R
                   C=1./R
                   S=S*C
                ENDIF
                G=D(I+1)-P
                R=(D(I)-G)*S+2.*C*B
                P=S*R
                D(I+1)=G+P
                G=C*R-B
c From here to ........
c               DO 13 K=1,N
c                  F=Z(K,I+1)
c                  Z(K,I+1)=S*Z(K,I)+C*F
c                  Z(K,I)=C*Z(K,I)-S*F
c13              CONTINUE
c here is needed to compute eigenvectors.
14              CONTINUE
                D(L)=D(L)-P
                E(L)=G
                E(M)=0.
                GO TO 1
            ENDIF
15        CONTINUE
      ENDIF
      RETURN
      END
c
c
c
```

Fig. 2.7-7 Subroutine PMMDE Used for Deterministic Implementations (continued).

```
      SUBROUTINE PMMS(NHAT,IDEC,SIGPMM,SDATA,DET,DETR)
C
C     NAME: PMMS        (2/22/88)
C
C     PURPOSE: TO CARRY OUT PRODUCT MOMENT MATRIX TEST
C              (STOCHASTIC CASE / DOUBLE PRECISION)
C     INPUTS:
C        NHAT : UPPER BOUND FOR DIMENSION OF SYSTEM (<=20)
C        IDEC : INCREMENT FOR LAGS (=0, NOMINALLY)
C        SIGPMM : MAGNITUDE OF ERROR SIGNAL (=0., NOMINALLY)
C        SDATA(.,..) : CORRELATIONS
C                    (SDATA(2,N) : RUU(N-1)
C                     SDATA(3,N) : RYY(N-1)
C                     SDATA(4,N) : RUY(N-1)
C                     SDATA(20,N) : RYU(N-1))
C     OUTPUTS:
C       DET(.) : DETERMINANT VALUES
C       DETR(.) : DETERMINAT RATIOS [DETR(I)=DET(I)/DET(I+1)]
C
C     AUXILLARY:
C        QMAT(.,..) : 2*NHAT x 2*NHAT PRODUCT MOMENT MATRIX
C
C     PARAMETER (NDIM=20)
C
C
      INTEGER NHAT,IDEC
      REAL*4 SIGPMM,SDATA(22,*), DET(*),DETR(*)
      REAL*8 H(2*NDIM,2*NDIM),G(2*NDIM,2*NDIM)
      REAL*8 QMAT(2*NDIM,2*NDIM)
      REAL*8 DETM1,DETM2
C
C
      ISCALE=IDEC+1
      DO 100 I=1,NHAT
      IU=2*(I-1)+1
      IY=IU+1
C
C     INSERT DIAGONAL BLOCK
C
      QMAT(IU,IU)= SDATA(2,1)
      QMAT(IU,IY)= SDATA(4,1)
      QMAT(IY,IU)= SDATA(4,1)
      QMAT(IY,IY)= SDATA(3,1)
C
C
          DO 50 J=(I+1),NHAT
          JU=2*(J-1)+1
          JY=JU+1
C
C     INSERT UPPER TRIANGULAT BLOCK
C
          IDIF=(J-I)*ISCALE + 1
          QMAT(IU,JU)= SDATA(2,IDIF)
```

Fig. 2.7-8 Subroutine PMMS Used for Stochastic Implementations.

60

```
              QMAT(IU,JY)= SDATA(20,IDIF)
              QMAT(IY,JU)= SDATA(4,IDIF)
              QMAT(IY,JY)= SDATA(3,IDIF)
C
C             INSERT LOWER TRIANGULAR BLOCK
C
              QMAT(JU,IU)= QMAT(IU,JU)
              QMAT(JY,IU)= QMAT(IU,JY)
              QMAT(JU,IY)= QMAT(IY,JU)
              QMAT(JY,IY)= QMAT(IY,JY)
C
C
  50          CONTINUE
 100      CONTINUE
C
C
          DO 110 I1=1,2*NHAT
          QMAT(I1,I1) = QMAT(I1,I1) + SIGPMM
 110      CONTINUE
C
C
          DO 150 I=1,(NHAT-1)
C
--------------------------------------------------------------
C             SET UP THE (N) AUXILIARY MATRIX AS N VARY FROM 1 TO
QDIM.
C
--------------------------------------------------------------
              DO 160 J=1,2*I
                  DO 170 K=1,2*I
                      H(J,K)=QMAT(J,K)
 170              CONTINUE
 160          CONTINUE
C             ---------------------------------
C             SET UP THE (N+1) MATRIX
C             ---------------------------------
              DO 180 J=1,2*I+2
                  DO 190 K=1,2*I+2
                      G(J,K)=QMAT(J,K)
 190              CONTINUE
 180          CONTINUE
              CALL DETERM(H,2*I,DETM1)
              CALL DETERM(G,2*I+2,DETM2)
              DET(I)=DETM1
              DETR(I)=ABS(DETM1/DETM2)
 150      CONTINUE
          DET(NHAT)=DETM2
          RETURN
          END
```

Fig. 2.7-8 Subroutine PMMS Used for Stochastic Implementations (continued).
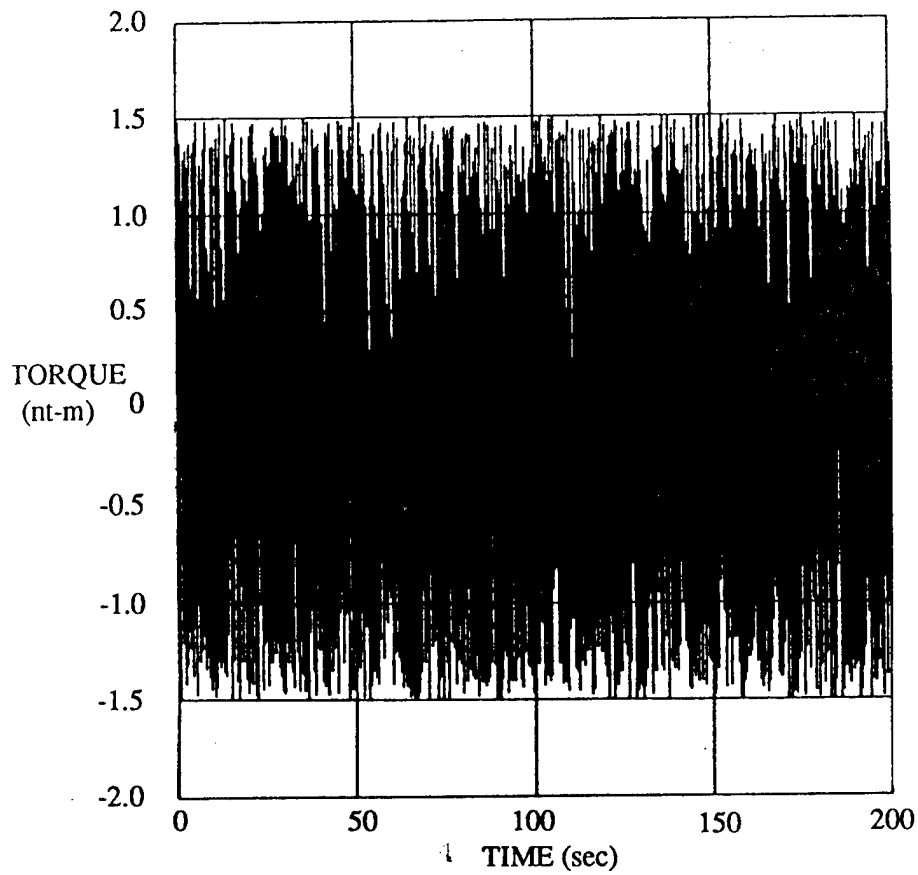
(a) Input Data
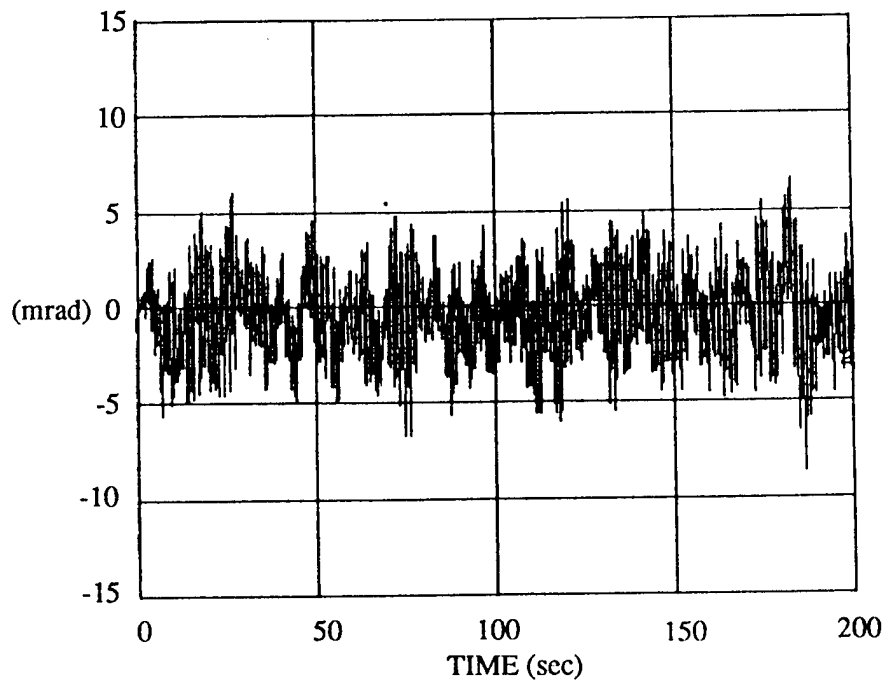
(b) Output Data

Fig. 2.7-9 Wide-Band Experiment Data (a) Input Data, (b) Hub Sensor Output Data.
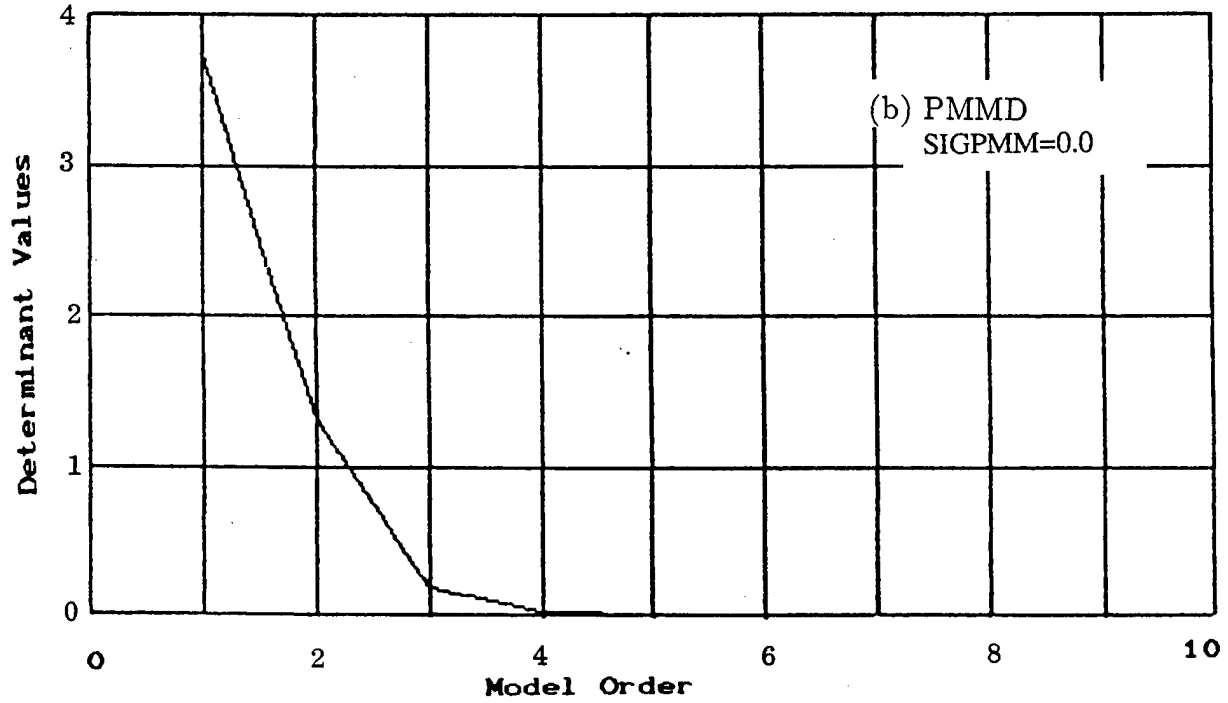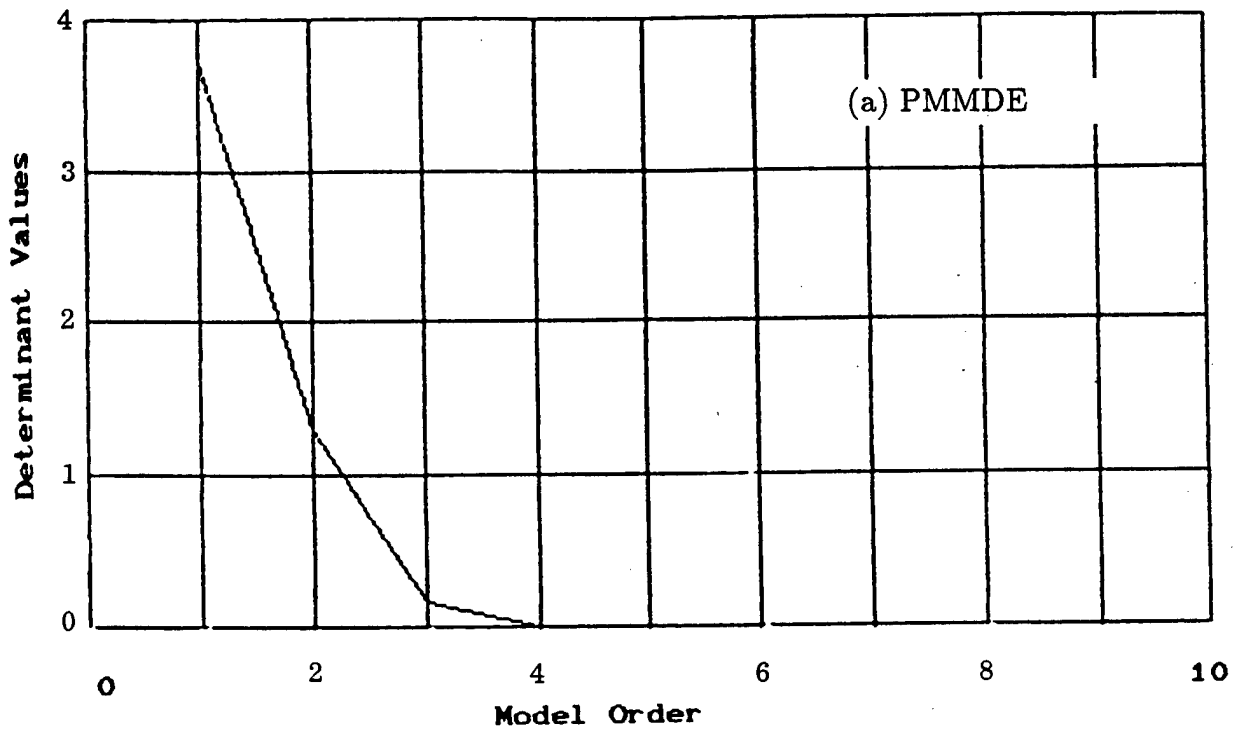
Fig. 2.7-10 The PMM Determinant Tests Using Wide-Band Data
(a) PMMDE, (b) PMMD, SIGPMM=0.0.

63
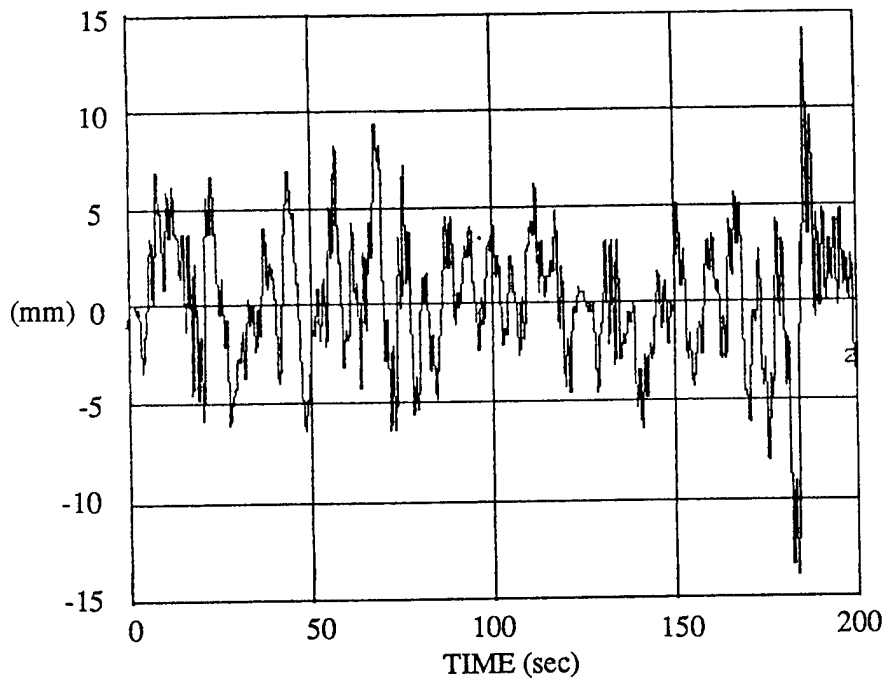
Fig. 2.7-11 System Response Using Levitator Sensor.
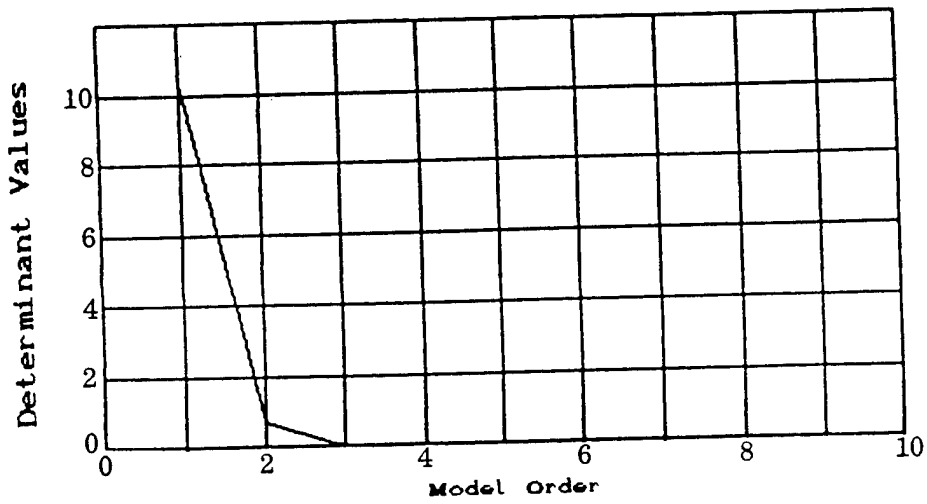
Fig. 2.7-12 The PMMD Determinant Result Using Levitator Data, with SIGPMM=0.0.

64
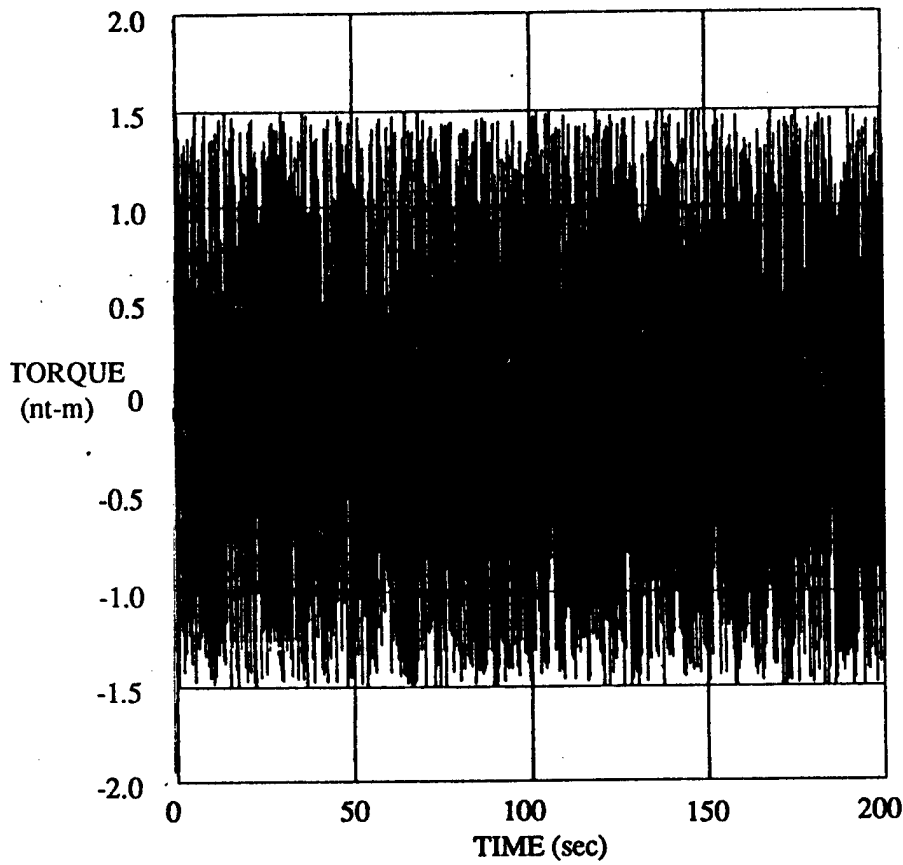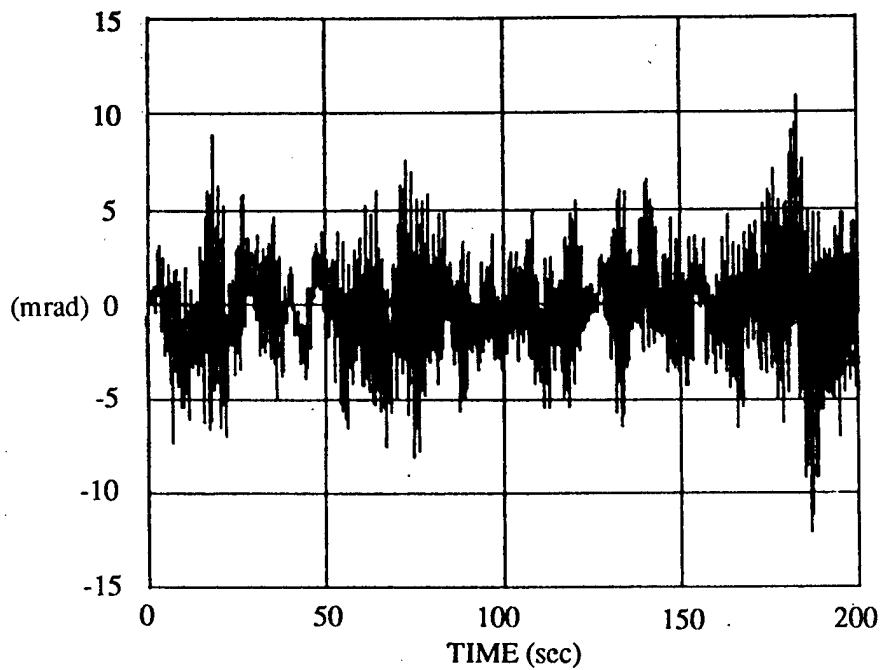
(a) Input Data

(b) Output Data

Fig. 2.7-13 Wide-Band Experiment Data of A different Axis
(a) Input Data, (b) Hub Sensor Output Data.

65
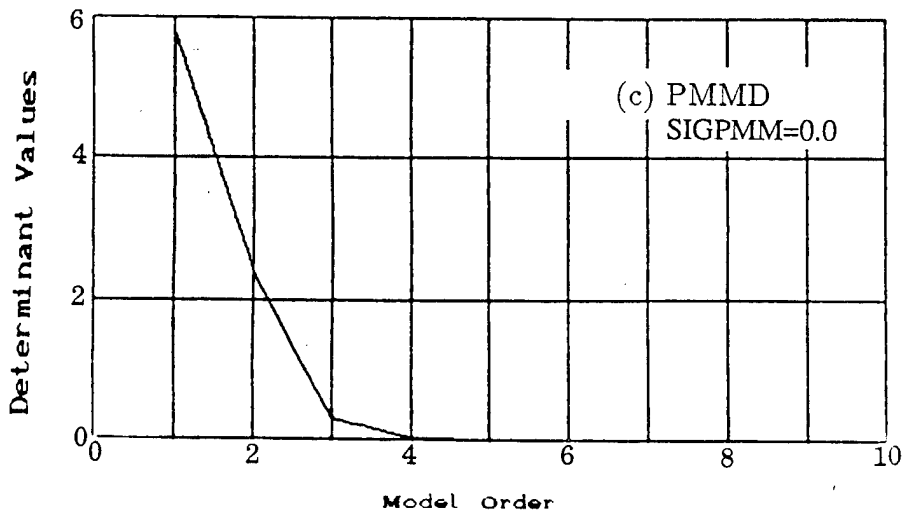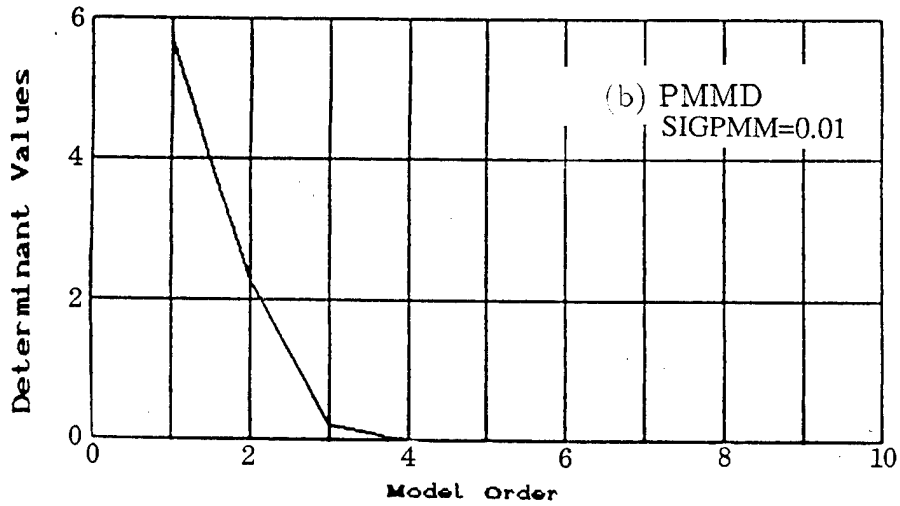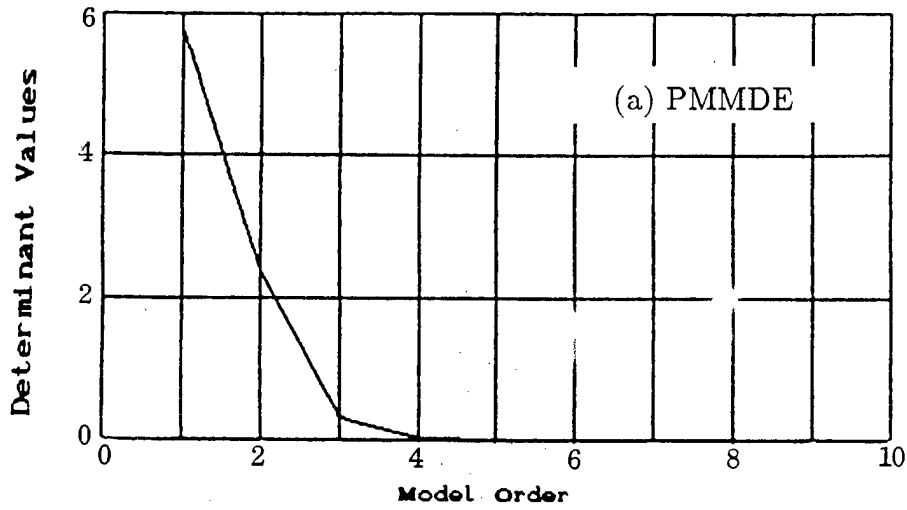
Fig. 2.7-14 The PMM Determinant Tests Using a Different Axis Data

(a) PMMDE, (b) PMMD, with SIGPMM=0.01, (c) PMMD, with SIGPMM=0.
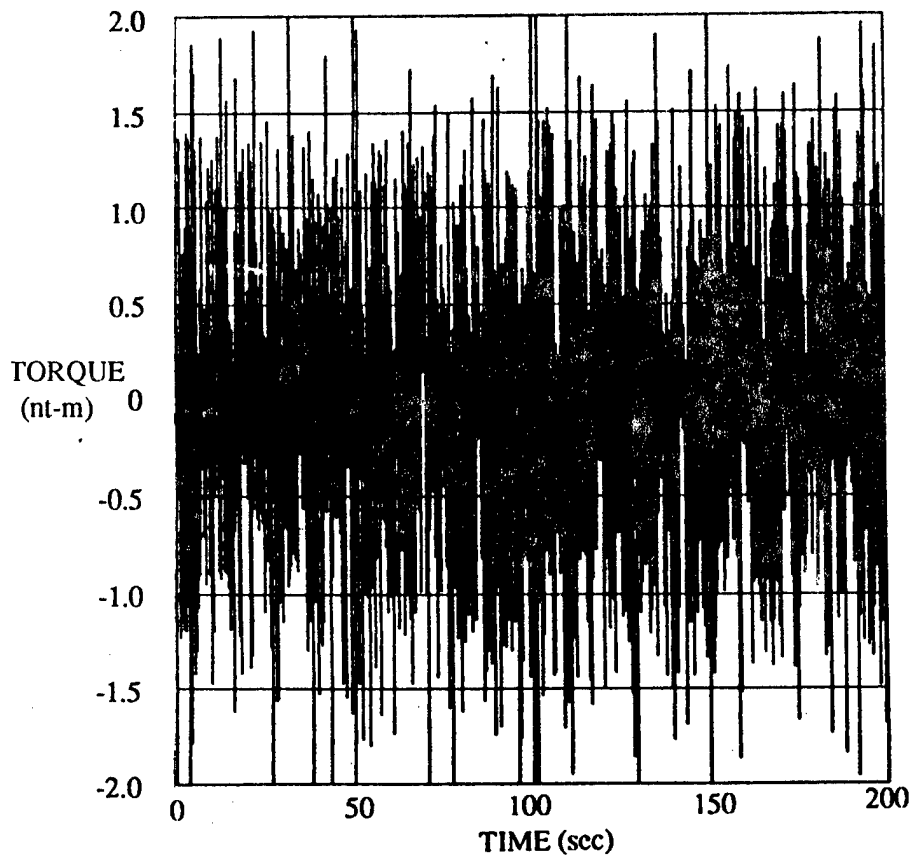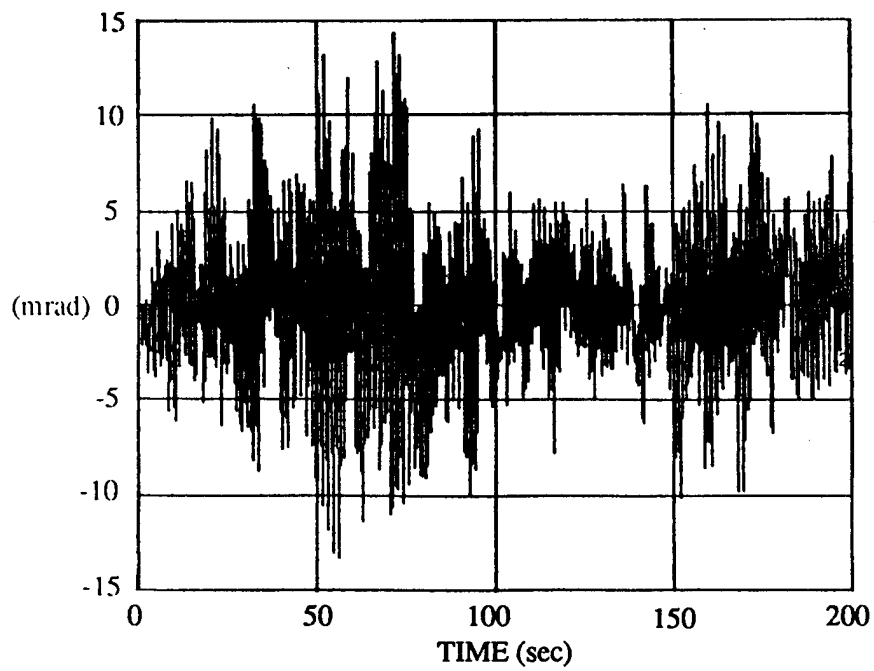
(a) Input Data

(b) Output Data

Fig. 2.7-15 Narrow-Band Experiment Data (a) Input Data,
(b) Hub Sensor Output Data.

67
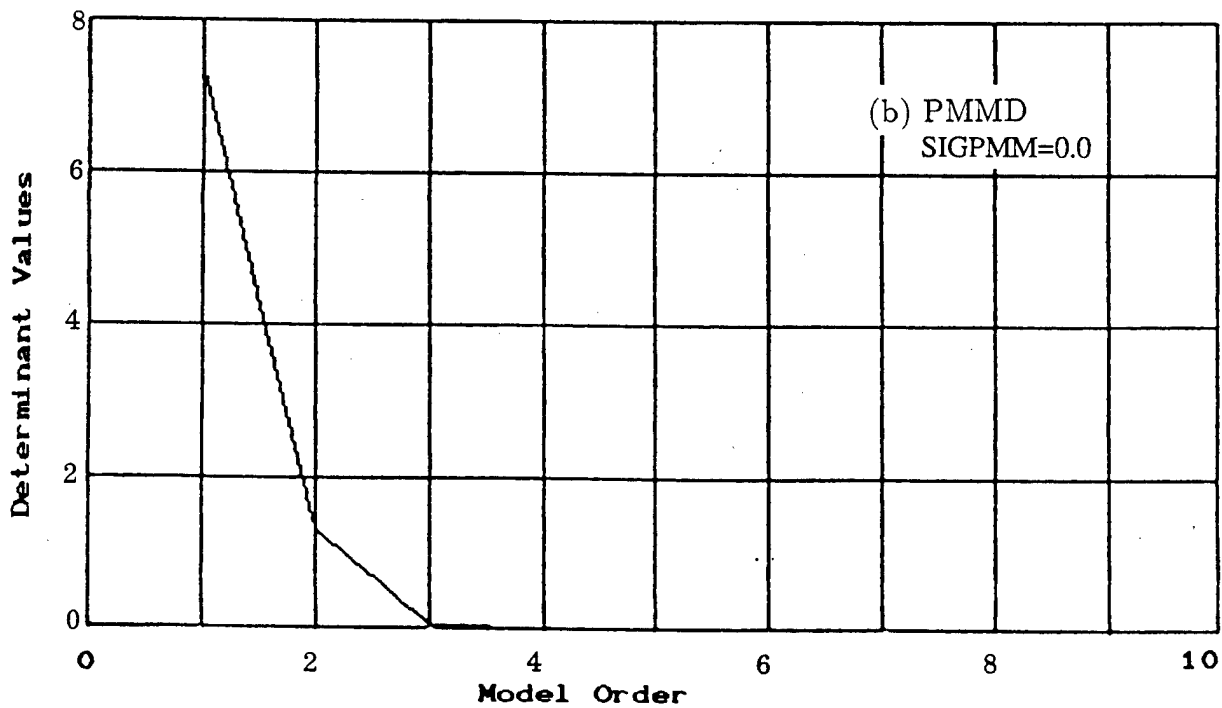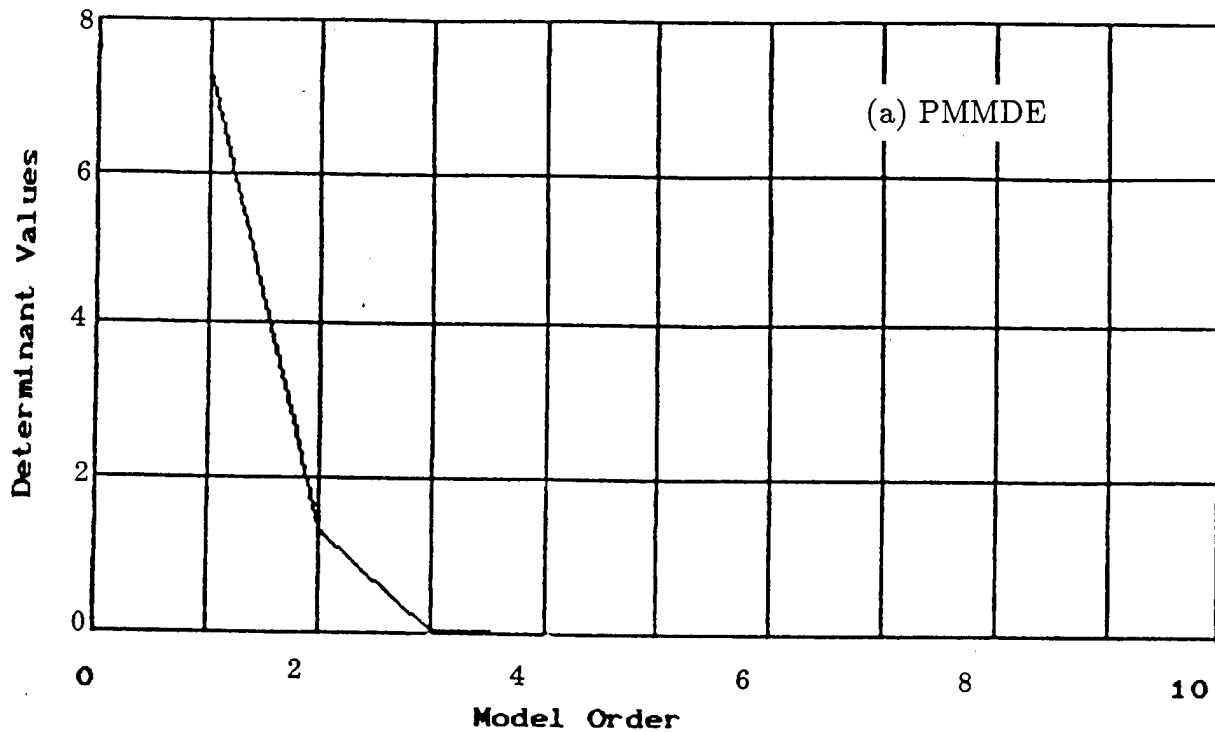
Fig. 2.7-16 The PMM Determinant Results Using Narrow-Band Data
(a) PMMDE, (b) PMMD, with SIGPMM=0.0.

2.8 Spectral Estimation Process

2.8.1 Introduction

In this section, a description is given of the spectral estimation process used for non-parametric transfer function identification. The role of spectral estimation in the overall identification process has been depicted earlier in Figure 1.1-1. The major portion of the developmental effort surrounded hosting the computer program CMPSE, taken from the IEEE Digital Signal Processing software collection [28]. The routine CMPSE is used to implement periodogram and correlation methods for power spectrum estimation of various quantities involving the plant input and output sequences.

2.8.2 Background

The basic idea of nonparametric identification of a transfer function via spectral estimation is very simple — given a measured wide-sense stationary input sequence $\{u(kT)\}$ and a measured output sequence $\{y(kT)\}$, the (digital) plant transfer function $p(\exp{(iwT)})$ enjoys the relationship [10][22],

$$p\left(\exp(iwT)\right)P_{uu}(w) = P_{uy}(w) \quad , \tag{2.8-1}$$

where

$$P_{uu}(w) = \sum_{k} R_{uu}(k)\exp(-iwkT) \quad , \tag{2.8-2}$$

$$P_{uy}(w) = \sum_{k} R_{uy}(k)\exp(-iwkT) \quad , \tag{2.8-3}$$

$$R_{uu}(k) = E\left[u\left((k+\ell)T\right)u(\ell T)\right] \tag{2.8-4}$$

$$R_{uy}(k) = E\left[u\left((k+\ell)T\right)y(\ell T)\right] \tag{2.8-5}$$

Thus, given sufficient power in the input, a determination of the transfer function can be made via (2.8-1). We also note the useful relationship involving the gain of the transfer function

$$|p\left(\exp(iwT)\right)|^{2}P_{uu}(w) = P_{yy}(w) \tag{2.8-6}$$

where

$$P_{yy}(w) = \sum_{k} R_{yy}(k)\exp(-iwkT)$$

$$R_{yy}(k) = E\left[y\left(k+\ell)T\right)y(\ell T)\right] \tag{2.8-7}$$

Relations (2.8-1)–(2.8-7) require the computation of R_{uu}, R_{yy}, R_{uy} and P_{uu}, P_{yy}, P_{uy}. The software program CMPSE performs all of these computations, i.e., estimates both the covariance and spectral functions. The precise procedure used by CMPSE is outlined in Figure 2.8-1.

69

2.8.3 Integration with System Software

The program CMPSE has been integrated as a subroutine into the experiment software, and spectral estimation can be performed via experiment menu. The spectral estimation menu is given as,

```
MENU (4,4,4)
SPECTRAL ESTIMATION PARAMETERS
0 — Exit              ;
81 — PARAM(81) 4096.  ;  MSE = window section size (2^n)
82 — PARAM(82) 32768. ;  NSE = total # analysis samples
83 — PARAM(83) 1.     ;  MODE = mode of operation
84 — PARAM(84) 1.     ;  IWIN = window type
85 — PARAM(85) 2048.  ;  LSE = # correlation values used
86 — PARAM(86) 4096.  ;  NFFT = FFT size
```

Here, the variables MSE, NSE and LSE correspond exactly to the quantities M, N and L, respectively in Figure 2.8-1. The quantities R_{uu}, R_{yy}, R_{uy}, P_{uu}, P_{yy}, P_{uy} and $h = \frac{P_{uy}}{P_{yy}}$ are all computed by the experiment software using the spectral estimation parameters specified in the menu. These computed quantities are stored in the SDATA array (see [14]) for further use.

As an example, the nominal values in the menu are set to perform spectral estimation by partitioning 32768 data points into 16 overlapping windows of 4096 data points each, retaining only 2048 lags of the correlations produced at the intermediate stage.

2.9 Transfer Function Curve Fit

2.9.1 Introduction

Once the plant has been identified nonparametrically and a frequency domain description is available, a parametric representation of the transfer function can be found by curve fitting. In this section, a curve fitting algorithm is discussed which estimates transfer function coefficients from frequency domain data. An iterative reweighting technique is introduced to remove the high frequency emphasis and assure minimum variance estimation.

Some background on the transfer function curve fit is given in Sect. 2.9.2. In Sect. 2.9.3 the curve fit is formulated as a weighted linear least squares problem. A natural question which arises is how to choose the weighting appropriately to achieve a good fit. For this purpose, an iterative reweighting technique is discussed in Sect. 2.9.4 which removes high frequency emphasis, and assures minimum variance estimation. Some discussion of robust factorization of polynomials is included in Sect. 2.9.5 to support the determination of frequencies and dampings from the estimated denominator polynomial coefficients. The various algorithms and subroutines developed to support the transfer function curve fit were integrated into the experiment software. A discussion of how they are invoked using menu selection is outlined in Sect. 2.9.6. The overall approach is demonstrated using

70

1) Partition N data points into K overlapping windows of size M
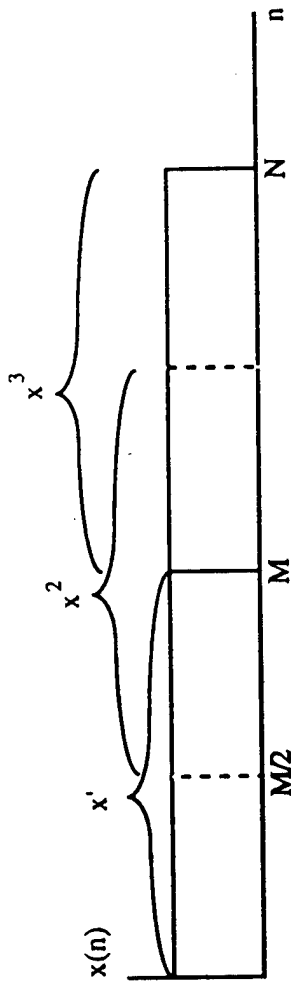
2) Compute K (M-pt)FFTs

$$J_M^{(i)}(\omega) = \frac{1}{M}\left|\sum_{n=0}^{M-1} x^i(n)\, e^{-j\omega n}\right|^2 \qquad i = 1,\ldots,K$$

3) Average in frequency domain

$$J(\omega) = \frac{1}{K}\sum_{i=1}^{K} J_M^{(i)}(\omega)$$

4) Compute IFFT of average

$$R_{xx}(m) = IFFT\{J(\omega)\}$$

5) Retain only L lags (symmetrize for autocorrelations only)

$$\tilde{R}_{xx}(m) = \begin{cases} R_{xx}(m) & 0 \le m \le L-1 \\ R_{xx}(M-m) & M-L+1 \le m \le M-1 \\ 0 & \text{Otherwise} \end{cases}$$

6) Compute NFFT-point FFT (NFFT $\ge$ 2*L-1)

$$P_{xx}(\omega) = \sum_{n=0}^{NFFT-1} R_{xx}(n)\, e^{-j\omega n}$$

Fig. 2.8-1 Outline of Computations Performed by Subroutine CMPSE.

experimental data in Sect. 2.9.7, where it is seen that the iterative reweighting technique tends to fit the high frequencies best initially, and then extend the accuracy of the fit down towards the low frequencies as the iterative process continues. Some remarks on the general relevance of these methods to the on-orbit identification are noted in Sect. 2.9.8.

2.9.2 Background

Assume a transfer function $p(\cdot)$ is of order n

$$p(z) = b(z)/a(z) \qquad (2.9-1)$$

with a, b polynomials of degree $\leq n$, and a monic. Then, with

$$a(z) = z^n + \sum_{j=0}^{n-1} a_j z^j$$

$$b(z) = \sum_{j=0}^{n} b_j z^j$$

(2.9-1) is equivalent to

$$\sum_{j=0}^{n-1} p(z) a_j z^j - \sum_{j=0}^{n} b_j z^j = -p(z) z^n \qquad (2.9-2)$$

For $\{z_i\}_{i=1}^{M}$ introduce the matrix $Z = \{Z_{ij}\} \epsilon R^{M \times (n+1)}$ such that

$$Z_{ij} = z_i^{j-1} \; ; \quad i = 1, \ldots, M \; ; \quad j = 1, \ldots, n+1$$

and let $Z^0 \triangleq \{Z$ with the $n+1^{st}$ column deleted$\}$. Let $D = \text{diag}[p(z_1), \ldots, p(z_M)]$, and denote the "data" vector by $y = [p(z_1) z_1^n, \ldots, p(z_M) z_M^n]^T$.

Equation (2.9-2) then has the compact representation

$$(DZ^0 - Z)\binom{\underline{a}}{\underline{b}} = -y \qquad (2.9-3)$$

where

$$\underline{a} = [a_0, \ldots, a_{n-1}]^T$$

$$\underline{b} = [b_0, \ldots, b_n]^T$$

2.9.3 Frequency Weighted Curve Fitting Algorithm

The curve fitting problem is to estimate the vectors $\underline{b}$ and $\underline{a}$ given D, Z and y (where (2.9-3) is in general not an equality due to errors). A straightforward approach is to use a weighted least squares solution. However, a realizable approximation to the transfer function requires that 1) the polynomial $a(z)$ and $b(z)$ have real coefficients, and 2) $b(z)$ is stable. We shall enforce constraint 1) and dispense with 2) (although we will monitor the roots of b). It is noted in the discrete-time formulation used here, that the regression matrix is based on the functions $\{e^{ij\omega T}\}_{j=0}^{n}$ which form an orthogonal set on the interval $\frac{-\pi}{T} \leq \omega \leq \frac{\pi}{T}$. Hence, there is no need to utilize Chebychev polynomials or other class orthogonal polynomials for the curve fit as recommended in continuous-time formulations of the problem [25].

72

To put (2.9-3) into real form, we just equate real and imaginary parts. Using standard notation (for $z = x + iy$, write $z_R = x$ and $z_I = y$), we obtain the $2M \times (2n + 1)$ system

$$\begin{pmatrix} D_R Z_R^0 - D_I Z_I^0 & -Z_R \\ D_I Z_R^0 + D_R Z_I^0 & -Z_I \end{pmatrix} \begin{pmatrix} \underline{a} \\ \underline{b} \end{pmatrix} = \begin{pmatrix} y_R \\ y_I \end{pmatrix} \qquad (2.9-4a)$$

Eq. (2.9-4a) leads to the weighted least squares problem

$$\min_{x \in \mathcal{R}^{2n+1}} |Ax - b|_W \qquad (2.9-4b)$$

where the proper matrix and vector identifications are made, and W is a user specified weighting matrix. We note that the matrix W can be used to distinguish the quality of different information sources (e.g., sine-dwell data vs. spectral estimation data), it can be used to obtain local 2nd order fits around resonances, or it can be used to reduce the inherent high frequency emphasis in the curve fit. The choice of W to ensure minimum variance estimation will be treated in Sect. 2.9.4.

The vector b and matrix A are formed in the following manner. Given

(1) Sampling interval T

(2) Discrete frequencies $\{f_j\}_{i=1}^M$ (in Hz)

(3) Transfer function data

$$\left\{ p(e^{2\pi i T f_j}) \right\}_{j=1}^M = \{p(j)\}_{j=1}^M$$

we obtain the ij^{th} component of Z as

$$Z_{ij} = z_i^{j-1} = e^{2\pi i f_i T(j-1)}$$

so that

$$(Z_R)_{ij} = \cos 2\pi f_i T(j-1) \qquad (2.9-5)$$
$$(Z_I)_{ij} = \sin 2\pi f_i T(j-1) \qquad (2.9-6)$$

In particular we can obtain

$$y_R(i) = p_R(i) \cos 2\pi f_i T n - p_I(i) \sin 2\pi f_i T n \qquad (2.9-7)$$
$$y_I(i) = p_R(i) \sin 2\pi f_i T n + p_I(i) \cos 2\pi f_i T n \qquad (2.9-8)$$

Hence, for $1 \leq i \leq M$, the components of b in (2.9-4b) are given as

$$b_i = -y_R(i), \qquad (2.9-9)$$

and for $M + 1 \leq i \leq 2M$,

$$b_i = -y_I(i - M). \qquad (2.9-10)$$

To form A in (2.9-4b) we have for $1 \leq i \leq M, 1 \leq j \leq n$

$$A_{ij} = p_R(i)(Z_R)_{ij} - p_I(i)(Z_I)_{ij}; \qquad (2.9-11)$$

73

for $1 \leq i \leq M$, $n+1 \leq j \leq 2n+1$

$$A_{ij} = -(Z_R)_{ij};$$ (2.9 − 12)

for $M+1 \leq i \leq 2M$, $1 \leq j \leq j$,

$$A_{ij} = p_{\mathcal{I}}(i-M)(Z_R)_{i-M,j} + p_R(i-M)(Z_{\mathcal{I}})_{i-M,j} ;$$ (2.9 − 13)

for $M+1 \leq i \leq 2M$, $n+1 \leq j \leq 2n+1$

$$A_{ij} = -(Z_{\mathcal{I}})_{i-M,j-n}$$ (2.9 − 14)

To incorporate a (diagonal) weighting matrix W indicated in (2.9-4b) into the above it is sufficient to premultiply A by $W^{\frac{1}{2}}$ and b by $W^{\frac{1}{2}}$, since

$$\langle Ax - b, W(Ax - b)\rangle = \langle W^{\frac{1}{2}}Ax - W^{\frac{1}{2}}b, W^{\frac{1}{2}}Ax - W^{\frac{1}{2}}b \rangle$$

Thus when $W = \text{diag}\,(\mathrm{w}_1^2, \ldots \mathrm{w}_{2M}^2)$, we take $A_{ij} \rightarrow \mathrm{w}_i A_{ij}$ and $b \rightarrow \mathrm{w}_i b_i$.

The Fortran subroutine CRVFT in Figure 2.9-1 was developed to implement the least squares solution to (2.9-4a). In particular, CRVFT sets up A and b as in (2.9-9)-(2.9-14) and then calls subroutines HFTI, H12 and DIFF from the Lawson and Hanson software [4]. For convenience, subroutines HFTI, H12 and DIFF are included in Figure 2.9-1 since some modification was required to assure successful operations. The Lawson and Hanson routines make use of Householder transformations to robustly compute the least squares solution with possibly deficient pseudorank (see Chapter 14 of [4]). Robustness to deficient pseudorank is important in the present application since model order is not clearly defined when fitting experimental data.

CRVFT also makes use of the subroutine A2FR for robustly factorizing the a(z) polynomial to determine frequency and damping estimates. A2FR is a special purpose subroutine discussed in more detail in Sect. 2.9.5.

2.9.4 Iterative Reweighting for Minimum Variance Estimation

In this section, the weighting matrix W is chosen to guarantee a minimum variance estimate of the parameter vector x, assuming that noise on the spectral estimate is additive, equal, and uncorrelated at all frequencies. In this case, the choice of W is plant dependent, leading to an overall nonlinear estimation problem. The nonlinear estimation problem is solved using an iterative reweighting process.

In the approach put forth here, a complex valued noise $e(z)$ is assumed to be additive and independent at each point $z_k = \exp(i\omega_k T)$, $k = 1, \ldots, M$ and such that

$$p(z_k) = \frac{b(z_k)}{a(z_k)} + e(z_k)$$ (2.9 − 15)

$$e(z_k) = e_R(z_k) + i e_{\mathcal{I}}(z_k)$$

74

```
C        THE CURVE FIT ALGORITHM
C        SUBROUTINE CRVFT(M,N,FSTART,FSTOP,IFLAG,TAU,NDF,KRANK,RESFREQ,
C       *ZETA,RNUM,DNOMR,ROOTS,GAINEST,PHASEST,GAINEROR)
         REAL*8 A(500,31), B(500,1),G(31),FSTART,FSTOP
         REAL*8 FREQ(500), TFIM(500), TFRE(500),H(31)
         REAL*8 W(500), RNORM(1),RNUM(15),GAINEST(200),PHASEST(200)
         REAL*8 GAINEROR(200),DNOMR(15),DFREQ
         COMPLEX*16 DNOM(15),ROOTS(32), HTRU,HEST,HST
         REAL*8 D,DD,THETA(14),RESFREQ(20),ZETA(20),VAL,TAU,X,Y,Z
         LOGICAL POLISH
         INTEGER IP(31), IFLAG
C        N=MODORD
C        M=DATALENGTH
C        D=SAMPLINT
         IFLAG=1    .
         NDF=1
         TAU=.0000000000000001
         M=15
         N=2
         MDA=500
         MDB=500
         D=1.D0/30.D0

         OPEN(UNIT=2,FILE='TFDATA.DAT',STATUS='OLD')
         DO 1 I=1,M
            READ(2,*) X,Y,Z
            FREQ(I)=X
            TFRE(I)=Y
            TFIM(I)=Z
1        CONTINUE
         FSTART=.0D0
         FSTOP=   .2D0
            IF(IFLAG. EQ. 0) GO TO 11
            DFREQ= FREQ(3)-FREQ(2)
            NSTART=IFIX(FSTART/DFREQ)+1
            NSTOP=IFIX(FSTOP/DFREQ)+1
            NSTART1=NSTART-1
            NSTOP1=NSTOP+1
         DO 13 I=1,NSTART1
            W(I)=0.0
13       CONTINUE
         DO 14 I=NSTART,NSTOP
            W(I)=1.0
14       CONTINUE
         DO 15 I=NSTOP1,M
            W(I)=0.0
15       CONTINUE
         GO TO 12
11       CONTINUE
         DO 10 I=1,M
            W(I)=1.0
10       CONTINUE
12       CONTINUE
```

Fig. 2.9-1 Curve Fit Subroutine CRVFT and Supporting Subroutines HFTI, H12, & DIFF.

```
C      SETTING PROPER DIMENSIONS FOR A MATRIX AND B VECTOR
       N1=N+1
       NN1=2*N+1
       M1=M+1
       MM=2*M
       NN=2*N

C      FILLING OUT WEIGHTING MATRIX W

       DO 20 I=M1,MM
       IM=I-M
       W(I)=W(IM)
 20    CONTINUE
       PI=3.14159265

C      COMPUTING NORTHWEST BLOCK OF "A" MATRIX

       DO 100 I=1,M
          DO 110 J=1,N
           VAL=2.0*PI*FREQ(I)*D*(J-1)
           A(1,J)=TFRE(I)*COS(VAL)-TFIM(I)*SIN(VAL)
 110   CONTINUE
 100   CONTINUE

C      COMPUTING NORTHEAST BLOCK OF "A" MATRIX

       DO 101 I=1,M
          DO 111 J=N1,NN1
           JN=J-N
           A(I,J)=-COS(2.0*PI*FREQ(I)*D*(JN-1))
 111    CONTINUE
 101   CONTINUE

C      COMPUTING SOUTHWEST BLOCK OF "A" MATRIX

       DO 102 I=M1,MM
          DO 112 J=1,N
           IM=I-M
           VAL=2.0*PI*FREQ(IM)*D*(J-1)
           A(I,J)=TFIM(IM)*COS(VAL)+TFRE(IM)*SIN(VAL)
 112   CONTINUE
 102   CONTINUE

C      COMPUTING SOUTHEAST BLOCK OF "A" MATRIX

       DO 103 I=M1,MM
          DO 113 J=N1,NN1
           IM=I-M
           JN=J-N
           A(I,J)=-SIN(2.0*PI*FREQ(IM)*D*(JN-1))
 113   CONTINUE
 103   CONTINUE
```

Fig. 2.9-1 Curve Fit Subroutine CRVFT and Supporting Subroutines HFTI, H12, & DIFF (continued).

```
C       COMPUTING UPPER BLOCK OF "B" VECTOR
        DO 200 I=1,M
         VAL=2.0*PI*FREQ(I)*D*N
         B(1,1)=-TFRE(I)*COS(VAL)+TFIM(I)*SIN(VAL)
  200   CONTINUE

C       COMPUTING LOWER BLOCK OF "B" VECTOR
        DO 300 I=M1,MM
         IM=I-M
         VAL=2.0*PI*FREQ(IM)*D*N
         B(1,1)=-TFRE(IM)*SIN(VAL)-TFIM(IM)*COS(VAL)
  300   CONTINUE

C       FORM "A" MATRIX AND "B" VECTOR FOR WEIGHTED LEAST SQUARES PROBLEM
        DO 310 I=1,MM
           DO 311 J=1,NN1
            A(I,J)=W(I)*A(I,J)
  311   CONTINUE
           B(I,1)=W(I)*B(I,1)
  310   CONTINUE
C       DO 400 I=1,MM
C          A(I,NN1)=0.0
C400    CONTINUE
C       CHECK ENTRIES OF "A" MATRIX
C        DO 400 I=1,MM
C           DO 401 J=1,NN1
C            PRINT, A(I,J)
C401    CONTINUE
C400    CONTINUE

C       CHECK ENTRIES OF "B" VECTOR

C       DO 410 I=1,MM
C        PRINT, B(I,1)
  410   CONTINUE

        NB=1
        CALL HFTI(A,MDA,MM,NN1,B,MDB,NB,TAU,KRANK,RNORM,H,G,IP)
C       PRINT, KRANK
C       PRINT SOLUTION VECTOR CONTAINING COEFFICIENTS OF DENOMINATOR AND
C       NUMERATOR POLYNOMIALS
        DO 500 I=1,N
         DNOM(I)= B(I,1)
  500   CONTINUE
        DNOM(N1)=(1.0,0.0)
        DO 501 I=1,N1
         NI=N+I
         RNUM(I)=B(NI,1)
  501   CONTINUE
        N2=N1+1
        DO 510 I=N2, 15
         DNOM(I)=0.0
         RNUM(I)=0.0
  510   CONTINUE
```

Fig. 2.9-1 Curve Fit Subroutine CRVFT and Supporting Subroutines HFTI, H12, & DIFF (continued).

```
      PRINT, (RNUM(1), I=1,15)

      DO 511 I=1,15
        DNOMR(1)= REAL(DNUM(I))
511   CONTINUE

      PRINT, (DNOMR(1), I=1,15)

      DO 512 I=1,N
        NI=N-I+1
        THETA(I)=DNOMR(NI)
512   CONTINUE

C     DETERMINING RESONANCES OF THE SYSTEM

      DD=D
      CALL A2FR(THETA,N,NDF,RESFREQ,ZETA,DD,ROOTS)
C     CALL ZROOTS(DNOM,N,ROOTS,POLISH)
      DO 610 I=N1,14
        ROOTS(I)=0.0
610   CONTINUE
      PRINT, (ROOTS(I), I=1,14)
      NI2=N/2
      PRINT, (RESFREQ(1), ZETA(1), I=1,NI2)
C     FIND RMS ERROR OF CURVE FIT ALGORITHM

      CALL COMPR(D,M,N1,FREQ,TFRE,TFIM,RNUM,DNOM,GAINEROR,GAINEST,
     *PHASEST)


      PRINT, (GAINEROR(I), I=1,M)
      PRINT, (GAINEST(1), I=1,M)
      PRINT, (PHASEST(I), I=1,M)

      END
```

Fig. 2.9-1 Curve Fit Subroutine CRVFT and Supporting Subroutines HFTI, H12, & DIFF
            (continued).

```
      SUBROUTINE HFTI (A,MDA,M,N,B,MDB,NB,TAU,KRANK,RNORM,H,G,IP)
C     C.L.LAWSON AND R.J.HANSON, JET PROPULSION LABORATORY, 1973 JUN 12
C     TO APPEAR IN 'SOLVING LEAST SQUARES PROBLEMS', PRENTICE-HALL, 1974
C          SOLVE LEAST SQUARES PROBLEM USING ALGORITHM, HFTI.
C
      REAL*8 A(MDA,N),B(MDB,N),H(N),G(N),RNORM(N)
      INTEGER IP(N)
      REAL*8 SM,DZERO,FACTOR,HMAX,TMP,SM1,TAU
      SZERO=0.
      DZERO=0.D0
      FACTOR=0.001
      HMAX=0.0
      LOGICAL IFLAG
      IFLAG = .TRUE.
      CALL UNDER0(IFLAG)
C
      K=0
      LDIAG=MIN0(M,N)
      IF (LDIAG.LE.0) GO TO 270
          DO 80 J=1,LDIAG
          IF (J.EQ.1) GO TO 20
C
C     UPDATE SQUARED COLUMN LENGTHS AND FIND LMAX
C        ..
          LMAX=J
              DO 10 L=J,N
              H(L)=H(L)-A(J-1,L)**2
              IF (H(L).GT.H(LMAX)) LMAX=L
   10         CONTINUE
          IF(DIFF(HMAX+FACTOR*H(LMAX),HMAX)) 20,20,50
C
C     COMPUTE SQUARED COLUMN LENGTHS AND FIND LMAX
C        ..
   20     LMAX=J
              DO 40 L=J,N
              H(L)=0.
                  DO 30 I=J,M
   30             H(L)=H(L)+A(I,L)**2
              IF (H(L).GT.H(LMAX)) LMAX=L
   40         CONTINUE
          HMAX=H(LMAX)
C        ..
C     LMAX HAS BEEN DETERMINED
C
C     DO COLUMN INTERCHANGES IF NEEDED.
C        ..
   50     CONTINUE
          IP(J)=LMAX
          IF (IP(J).EQ.J) GO TO 70
              DO 60 I=1,M
              TMP=A(I,J)
              A(I,J)=A(I,LMAX)
   60         A(I,LMAX)=TMP
          H(LMAX)=H(J)
```

Fig. 2.9-1 Curve Fit Subroutine CRVFT and Supporting Subroutines HFTI, H12, & DIFF (continued).

```
C
C        COMPUTE THE J-TH TRANSFORMATION AND APPLY IT TO A AND B.
C     ..
   70        CALL H12 (1,J,J+1,M,A(1,J),1,H(J),A(1,MIN(J+1,N)),1,MDA,N-J)
   80        CALL H12 (2,J,J+1,M,A(1,J),1,H(J),B,1,MDB,NB)
C
C        DETERMINE THE PSEUDORANK, K, USING THE TOLERANCE, TAU.
C     ..
             DO 90 J=1,LDIAG
             IF (ABS(A(J,J)).LE.TAU) GO TO 100
   90        CONTINUE
       K=LDIAG
       GO TO 110
  100  K=J-1
  110  KP1=K+1
C
C        COMPUTE THE NORMS OF THE RESIDUAL VECTORS.
C
       IF (NB.LE.0) GO TO 140
           DO 130 JB=1,NB
           TMP=SZERO
           IF (KP1.GT.M) GO TO 130
               DO 120 I=KP1,M
  120              TMP=TMP+B(I,JB)**2
  130      RNORM(JB)=SQRT(TMP)
  140  CONTINUE
C                                              SPECIAL FOR PSEUDORANK = 0
       IF (K.GT.0) GO TO 160
       IF (NB.LE.0) GO TO 270
           DO 150 JB=1,NB
               DO 150 I=1,N
  150              B(I,JB)=SZERO
       GO TO 270
C
C        IF THE PSEUDORANK IS LESS THAN N COMPUTE HOUSEHOLDER
C        DECOMPOSITION OF FIRST K ROWS.
C     ..
  160  IF (K.EQ.N) GO TO 180
           DO 170 II=1,K
           I=KP1-II
  170      CALL H12 (1,I,KP1,N,A(I,1),MDA,G(I),A,MDA,1,I-1)
  180  CONTINUE
C
C
       IF (NB.LE.0) GO TO 270
           DO 260 JB=1,NB
C
C        SOLVE THE K BY K TRIANGULAR SYSTEM.
C     ..
               DO 210 L=1,K
               SM=DZERO
               I=KP1-L
               IF (I.EQ.K) GO TO 200
               IP1=I+1
```

Fig. 2.9-1 Curve Fit Subroutine CRVFT and Supporting Subroutines HFTI, H12, & DIFF (continued).

```
                   DO 190 J=IP1,K
  190                  SM=SM+A(I,J)*DBLE(B(J,JB))
  200              SM1=SM
  210              B(I,JB)=(B(I,JB)-SM1)/A(I,I)
C  .
C      COMPLETE COMPUTATION OF SOLUTION VECTOR.
C      ..
              IF (K.EQ.N) GO TO 240
                  DO 220 J=KP1,N
  220              B(J,JB)=SZERO
                  DO 230 I=1,K
  230              CALL H12 (2,I,KP1,N,A(I,1),MDA,G(I),B(1,JB),1,MDB,1)
C                  .
C      RE-ORDER THE SOLUTION VECTOR TO COMPENSATE FOR THE
C      COLUMN INTERCHANGES.
C      ..
  240              DO 250 JJ=1,LDIAG
                  J=LDIAG+1-JJ
                  IF (IP(J).EQ.J) GO TO 250
                  L=IP(J)
                  TMP=B(L,JB)
                  B(L,JB)=B(J,JB)
                  B(J,JB)=TMP
  250              CONTINUE
  260          CONTINUE
C      ..
C      THE SOLUTION VECTORS, X, ARE NOW
C      IN THE FIRST  N  ROWS OF THE ARRAY B(,).
C
  270 KRANK=K
      RETURN
      END
```

Fig. 2.9-1 Curve Fit Subroutine CRVFT and Supporting Subroutines HFTI, H12, & DIFF (continued).

```
C     SUBROUTINE H12 (MODE,LPIVOT,L1,M,U,IUE,UP,C,ICE,ICV,NCV)
C     C.L.LAWSON AND R.J.HANSON, JET PROPULSION LABORATORY, 1973 JUN 12
C     TO APPEAR IN 'SOLVING LEAST SQUARES PROBLEMS', PRENTICE-HALL, 1974
C
C     CONSTRUCTION AND/OR APPLICATION OF A SINGLE
C     HOUSEHOLDER TRANSFORMATION..      Q = I + U*(U**T)/B
C
C     MODE    = 1 OR 2   TO SELECT ALGORITHM  H1  OR  H2 .
C     LPIVOT IS THE INDEX OF THE PIVOT ELEMENT.
C     L1,M   IF L1 .LE. M   THE TRANSFORMATION WILL BE CONSTRUCTED TO
C            ZERO ELEMENTS INDEXED FROM L1 THROUGH M.   IF L1 GT. M
C            THE SUBROUTINE DOES AN IDENTITY TRANSFORMATION.
C     U(),IUE,UP   ON ENTRY TO H1 U() CONTAINS THE PIVOT VECTOR.
C                  IUE IS THE STORAGE INCREMENT BETWEEN ELEMENTS.
C                                      ON EXIT FROM H1 U() AND UP
C            CONTAIN QUANTITIES DEFINING THE VECTOR U OF THE
C            HOUSEHOLDER TRANSFORMATION.   ON ENTRY TO H2 U()
C            AND UP SHOULD CONTAIN QUANTITIES PREVIOUSLY COMPUTED
C            BY H1.   THESE WILL NOT BE MODIFIED BY H2.
C     C()    ON ENTRY TO H1 OR H2 C() CONTAINS A MATRIX WHICH WILL BE
C            REGARDED AS A SET OF VECTORS TO WHICH THE HOUSEHOLDER
C            TRANSFORMATION IS TO BE APPLIED.   ON EXIT C() CONTAINS THE
C            SET OF TRANSFORMED VECTORS.
C     ICE    STORAGE INCREMENT BETWEEN ELEMENTS OF VECTORS IN C().
C     ICV    STORAGE INCREMENT BETWEEN VECTORS IN C().
C     NCV    NUMBER OF VECTORS IN C() TO BE TRANSFORMED. IF NCV .LE. 0
C            NO OPERATIONS WILL BE DONE ON C().
C
      SUBROUTINE H12 (MODE,LPIVOT,L1,M,U,IUE,UP,C,ICE,ICV,NCV)
      REAL*8 U(IUE,M),  C(*),CL,CLINV,SM1,UP,ONE
      REAL*8 SM,B
      ONE=1.
C
      IF (0.GE.LPIVOT.OR.LPIVOT.GE.L1.OR.L1.GT.M) RETURN
      CL=ABS(U(1,LPIVOT))
      IF (MODE.EQ.2) GO TO 60
C                                  ****** CONSTRUCT THE TRANSFORMATION. ******
         DO 10 J=L1,M
   10    CL=AMAX1(ABS(U(1,J)),CL)
      IF (CL) 130,130,20
   20 CLINV=ONE/CL
      SM=(DBLE(U(1,LPIVOT))*CLINV)**2
         DO 30 J=L1,M
   30    SM=SM+(DBLE(U(1,J))*CLINV)**2
C                                  CONVERT DBLE. PREC. SM TO SNGL. PREC. SM1
      SM1=SM
      CL=CL*SQRT(SM1)
      IF (U(1,LPIVOT)) 50,50,40
   40 CL=-CL
   50 UP=U(1,LPIVOT)-CL
      U(1,LPIVOT)=CL
      GO TO 70
```

Fig. 2.9-1 Curve Fit Subroutine CRVFT and Supporting Subroutines HFTI, H12, & DIFF (continued).

82

```
C            ****** APPLY THE TRANSFORMATION  I+U*(U**T)/B  TO C. ******
C
   60 IF (CL) 130,130,70
   70 IF (NCV.LE.0) RETURN
      B=DBLE(UP)*U(1,LPIVOT)
C                       B  MUST BE NONPOSITIVE HERE.  IF B = 0., RETURN.
C
      IF (B) 80,130,130
   80 B=ONE/B
      I2=1-ICV+ICE*(LPIVOT-1)
      INCR=ICE*(L1-LPIVOT)
          DO 120 J=1,NCV
          I2=I2+ICV
          I3=I2+INCR
          I4=I3
          SM=C(I2)*DBLE(UP)
              DO 90 I=L1,M
              SM=SM+C(I3)*DBLE(U(1,I))
   90         I3=I3+ICE
          IF (SM) 100,120,100
  100     SM=SM*B
          C(I2)=C(I2)+SM*DBLE(UP)
              DO 110 I=L1,M
              C(I4)=C(I4)+SM*DBLE(U(1,I))
  110         I4=I4+ICE
  120     CONTINUE
  130 RETURN
      END



      DOUBLE PRECISION FUNCTION DIFF(X,Y)
C     C.L.LAWSON AND R.J.HANSON, JET PROPULSION LABORATORY, 1973 JUNE 7
C     TO APPEAR IN 'SOLVING LEAST SQUARES PROBLEMS', PRENTICE-HALL, 1974
      REAL*8 X,Y
      DIFF=X-Y
      RETURN
      END
```

Fig. 2.9-1 Curve Fit Subroutine CRVFT and Supporting Subroutines HFTI, H12, & DIFF
(continued).

Here, the real and imaginary parts of e are statistically independent, and are distributed as $p(e_R) = N(0, \sigma^2)$ and $p(e_\mathcal{I}) = N(0, \sigma^2)$, respectively; and $e(z_j)$ is independent of $e(z_k)$ for $j \neq k$.

Rearranging (2.9-15) gives the M complex equations,

$$p(z_k)z_k^n = \sum_{j=0}^{n} b_j z_k^j - \sum_{j=0}^{n-1} a_j p(z_k) z_k^j + a(z_k)e(z_k) \qquad (2.9-16)$$

which can be put into a complex matrix form analogous to (2.9-3),

$$(DZ^0 - Z)\begin{pmatrix} \underline{a} \\ \underline{b} \end{pmatrix} = -y + \mathcal{A}E \qquad (2.9-17)$$

where $\mathcal{A} = \mathrm{diag}[a(z_1), \dots, a(z_M)]$ and $E = [e(z_1), \dots, e(z_M)]^T$.

Converting (2.9-17) to real form by equating the real and imaginary parts gives the noisy generalization of (2.9-4)

$$\begin{pmatrix} D_R Z_r^0 - D_\mathcal{I} Z_\mathcal{I}^0 & -Z_R \\ D_\mathcal{I} Z_R^0 - D_R Z_\mathcal{I}^0 & -Z_\mathcal{I} \end{pmatrix} \begin{pmatrix} \underline{a} \\ \underline{b} \end{pmatrix} = \begin{pmatrix} y_R \\ y_\mathcal{I} \end{pmatrix} + v \qquad (2.9-18)$$

where the subscript notations "R" and "$\mathcal{I}$" are used to denote the real and imaginary parts, respectively, of the indicated quantities. Using matrix notation the equation (2.9-18) can be put into the equivalent form,

$$Ax = b + v \qquad (2.9-19)$$

where the noise vector v has the following properties,

$$v = \begin{pmatrix} \mathcal{A}_R E_R - \mathcal{A}_\mathcal{I} E_\mathcal{I} \\ \mathcal{A}_\mathcal{I} E_R + \mathcal{A}_R E_\mathcal{I} \end{pmatrix} \qquad (2.9-20a)$$

$$E[v] = 0 \qquad (2.9-20b)$$

$$Cov[v] = \sigma^2 \begin{pmatrix} \mathcal{A}^*\mathcal{A} & 0 \\ 0 & \mathcal{A}^*\mathcal{A} \end{pmatrix} \triangleq V \qquad (2.9-20c)$$

It is well known that the minimum variance estimator of x in (2.9-19) is given by solving the least squares problem,

$$\min_x |Ax - b|_W \qquad (2.9-21)$$

where the matrix W is chosen as the inverse of the noise covariance [29]

$$W = V^{-1} \qquad (2.9-22)$$

It is noted that the optimal weighting W in (2.9-22) is a function of plant parameters (i.e., the $\{a_j\}$ in particular) and will not be known a priori. Hence, the following iterative scheme is used,

84

0. Assume $\sigma = 1$

1. Set $W = I$

2. Estimate x from (2.9-21)

3. Calculate $(\mathcal{A}^*\mathcal{A})^{-1} = \mathrm{diag}\left[\left|\frac{1}{a(z_1)}\right|^2, \ldots, \left|\frac{1}{a(z_M)}\right|^2\right]$ and V^{-1} using estimated $\{a_j\}$ and smooth as a function of frequency

4. Set $W = V^{-1}$ and go to 2.

The smoothing in 3. is introduced to enhance convergence of the relaxation algorithm to a global minimum. Without smoothing, resonances estimated early in the iterative process are overemphasized in subsequent curve fits by the $\left|\frac{1}{a(z)}\right|$ weighting and hence tend to become premature fixed points of iterative optimization procedure. Smoothing is introduced to avoid this phenomenon.

Two subroutines given in Figure 2.9-2 were developed to perform the weighting and smoothing tasks. The $\left|\frac{1}{a(z)}\right|$ weighting is performed by the subroutine WEIGHT which simply substitutes values into the $a(z)$ polynomial. The smoothing is performed by a subroutine WSMOOTH which lowpass filters forward in frequency (i.e., treating the frequency axis as if it were a time axis), and then backwards in frequency (i.e., noncausally) using a first order lowpass filter with filter constant SF.

As an example, consider the $a(z)$ polynomial specified by the following coefficients,

$$a_{15} = -.1433157023880846\mathrm{D}02$$
$$a_{14} = .9771317541274720\mathrm{D}02$$
$$a_{13} = -.4206232200907015\mathrm{D}03$$
$$a_{12} = .1279287523027041\mathrm{D}04$$
$$a_{11} = -.2914512176210783\mathrm{D}04$$
$$a_{10} = .5144460500626343\mathrm{D}04$$
$$a_{9} = -.7176063793295143\mathrm{D}04$$
$$a_{8} = .7994218683170717\mathrm{D}04$$
$$a_{7} = -.71359051162079569\mathrm{D}04$$
$$a_{6} = .5087115810204192\mathrm{D}04$$
$$a_{5} = -.2866020585540510\mathrm{D}04$$
$$a_{4} = .1251072967803763\mathrm{D}04$$
$$a_{3} = -.4091056752151899\mathrm{D}03$$
$$a_{2} = .9452747852297180\mathrm{D}02$$
$$a_{1} = -.13791312576272273\mathrm{D}02$$
$$a_{0} = .9573564792851850\mathrm{D}0$$

A plot of $\left|\frac{1}{a(z)}\right|$ is shown in Fig. 2.9-3 with several different values of smoothing factors.

```
C          THIS ROUTINE TESTS SUBROUTINE WEIGHT
           REAL*8 FREQ(400),WS95(400),WS9(400),WS8(400),WS7(400),
          @ A(16),T,W(400),FDEL,SF
           OPEN(9,FILE='WTST.M',STATUS='OLD')
           OPEN(10,FILE='WTST1.M',STATUS='OLD')
C          POLYNOMIAL FROM 8 MODE LSTST SIMULATION (16 SIG DIGITS)
           A(1)=-.1433157023880846D02
           A(2)= .9771317541274720D02
           A(3)=-.4206232200907015D03
           A(4)= .1279287523027041D04
           A(5)=-.2914512176210783D04
           A(6)= .5144460500626343D04
           A(7)=-.7176063793295143D04
           A(8)= .7994218683170717D04
           A(9)=-.7135905162079569D04
           A(10)= .5087115810204192D04
           A(11)=-.2866020585540510D04
           A(12)= .1251072967803763D04
           A(13)=-.4091056752151899D03
           A(14)= .9452747852297180D02
           A(15)=-.1379131257627273D02
           A(16)= .9573564792851850D0
C          NOTE THAT A(0) WOULD EQUAL 1
           T=.03D0
           FDEL=.01D0
           N=16
           DO 10 I=1,400
           FREQ(I)=FDEL*DBLE(I)
           CALL WEIGHT(FREQ(I),A,N,T,W(I))
     10 CONTINUE
           MW=400
           SF=.95
           CALL WSMOOTH(W,MW,WS95,SF)
           SF=.9
           CALL WSMOOTH(W,MW,WS9,SF)
           SF=.8
           CALL WSMOOTH(W,MW,WS8,SF)
           SF=.7
           CALL WSMOOTH(W,MW,WS7,SF)
           DO 20 I=1,400
           WRITE(9,50) FREQ(I),W(I),WS95(I)
           WRITE(10,60) WS9(I),WS8(I),WS7(I)
     20 CONTINUE
     50 FORMAT(1X,E12.6,2X,E12.6,2X,E12.6)
     60 FORMAT(1X,E12.6,2X,E12.6,2X,E12.6)
           STOP
           END
C
C

           SUBROUTINE WSMOOTH(W,MW,WS,SF)
C          THIS ROUTINE SMOOTHS VECTOR W=1/A
C          W - WEIGHTING VECTOR TO BE SMOOTHED
C          MW - SIZE OF W
C          WS - SMOOTHED WEIGHTING
```

Fig. 2.9-2 The Subroutines WEIGHT & WSMOOTH with Calling Routine for Test.

```
C     SF - SMOOTHING FACTOR (O<SF<1 , O-MINIMUM, 1-MAXIMUM)
C          .95 NOMINAL
      REAL*8 W(*),WS(*),WSC(2000),SF
C     SMOOTH CAUSALLY
      WSC(1)=1.DO
      DO 10 I=1,MW-1
      WSC(I+1)= SF*WSC(I)+(1.DO-SF)*W(I)
   10 CONTINUE
C     SMOOTH ANTICAUSALLY
      WS(MW)=WSC(MW)
      DO 20 I=1,MW-1
      WS(MW-I)=SF*WS(MW-I+1)+(1.DO-SF)*WSC(MW-I+1)
   20 CONTINUE
      RETURN
      END




      SUBROUTINE WEIGHT(FREQ,A,N,T,W)
C     THIS ROUTINE DETERMINES THE CURVE FIT WEIGHT W AT FREQUENCY
C     FREQ GIVEN DENOMINATOR POLYNOMIAL A
C
C     FREQ - (I) FREQUENCY OF WEIGHT TO BE DETERMINED
C     A  - (I) POLYNOMIAL 1+A(1)/Z+A(2)/Z**2+...+A(N)/Z**N
C     T  - (I) SAMPLING PERIOD
C     W  - (O) CURVE FIT WEIGHT
C
C
      REAL*8  FREQ,T,A(*),AREAL,AIMAG,AMODULUS,W,EPS,ANORM,FNORM
      DATA PI/3.14159265358979323846426433DO/,EPS/1.D-15/
      DATA FNORM/.0001/
      AREAL=1.DO
      DO 10 I=1,N
      AREAL=AREAL+A(I)*DCOS(DBLE(I)*2.*PI*FREQ*T)
   10 CONTINUE
      AIMAG=0.DO
      DO 20 I=1,N
      AIMAG=AIMAG+A(I)*DSIN(DBLE(I)*2.*PI*FREQ*T)
   20 CONTINUE
      AMODULUS=DSQRT(AREAL**2+AIMAG**2)
C     COMPUTE NORMALIZATION BY FNORM AMPLITUDE
      AREAL=1.DO
      DO 30 I=1,N
      AREAL=AREAL+A(I)*DCOS(DBLE(I)*2.*PI*FNORM*T)
   30 CONTINUE
      AIMAG=0.DO
      DO 40 I=1,N
      AIMAG=AIMAG+A(I)*DSIN(DBLE(I)*2.*PI*FNORM*T)
   40 CONTINUE
      ANORM=DSQRT(AREAL**2+AIMAG**2)
C     COMPUTE WEIGHT W
      W=ANORM/(AMODULUS+EPS)
      RETURN
      END
```

Fig. 2.9-2 The Subroutines WEIGHT & WSMOOTH with Calling Routine for Test (continued).

The plot is generated by using the testing program in Figure 2.9-2 which calls subroutines WEIGHT and WSMOOTH. Some empirical results indicate that the algorithm above can be used with the smoothing factor fixed at $SF = .95$, and iterated until convergence is observed in x.

2.9.5 Robust Root Solver

Once the transfer function coefficients are estimated, one can determine the resonant frequencies and dampings by factorizing the $a(z)$ polynomial into complex conjugate root pairs. Although this approach is simple in principle, we found that the calculation in practice is laden with numerical difficulties. We briefly describe an investigation into the numerical properties of sampled resonance systems and the development of special purpose software subroutine A2FR to overcome the problem.

The root sensitivity problem has been well-studied in the numerical analysis literature [18]. Assuming that the roots are on the unit circle, a bound on the root perturbation is given in Figure 2.9-4. In particular, the sensitivity of the jth root is inversely proportional to the "product of the secants" from roots i (i not equal to j) directed towards root j. Hence, if there are any "short secants" pointing to the jth root, the jth root will be very sensitive to perturbations in the a(z) coefficients.

Simply stated, root sensitivity problems occur when there are short secants in the pole location diagram. As depicted in Figure 2.9-5, the root sensitivity problem can be minimized by a judicious choice of sampling period and bandwidth over which the resonances of the a(z) polynomial lie. In general, for sampled resonance systems, short secants arise in the following situations

1) a(z) is a high order polynomial

2) the lowest frequency mode is heavily sampled (e.g., more than 20 samples per cycle)

3) modes appear near the Nyquist fold over frequency

4) the "difference frequencies" between closely spaced modes are heavily sampled.

In the present study, the sensitivity was due to situation (2) above, i.e., a heavily sampled low frequency mode. Due to the extreme sensitivity in the low frequency root, standard root solving software would typically misinterpret the low frequency conjugate root pair as two real roots – one inside and one outside the unit circle. This led to an ambigious low frequency estimate and considerable error in the remaining frequency estimates.

The special purpose subroutine A2FR, given in Figure 2.9-6, was written to factorize the $a(z)$ polynomial in the presence of root sensitivity due to oversampled low frequency modes, and then convert the results to frequency and damping estimates. The routine A2FR works by first extracting NDF (Number of Difficult to Find) low frequency conjugate root pairs using Bairstows method and then passing the remaining deflated polynomial to a standard root solving routine based on Laguerre's method (with polishing) to finish the job. When the polynomial factorization is complete, the A2FR routine converts the complex conjugate roots of $a(z)$ to frequency and damping estimates.
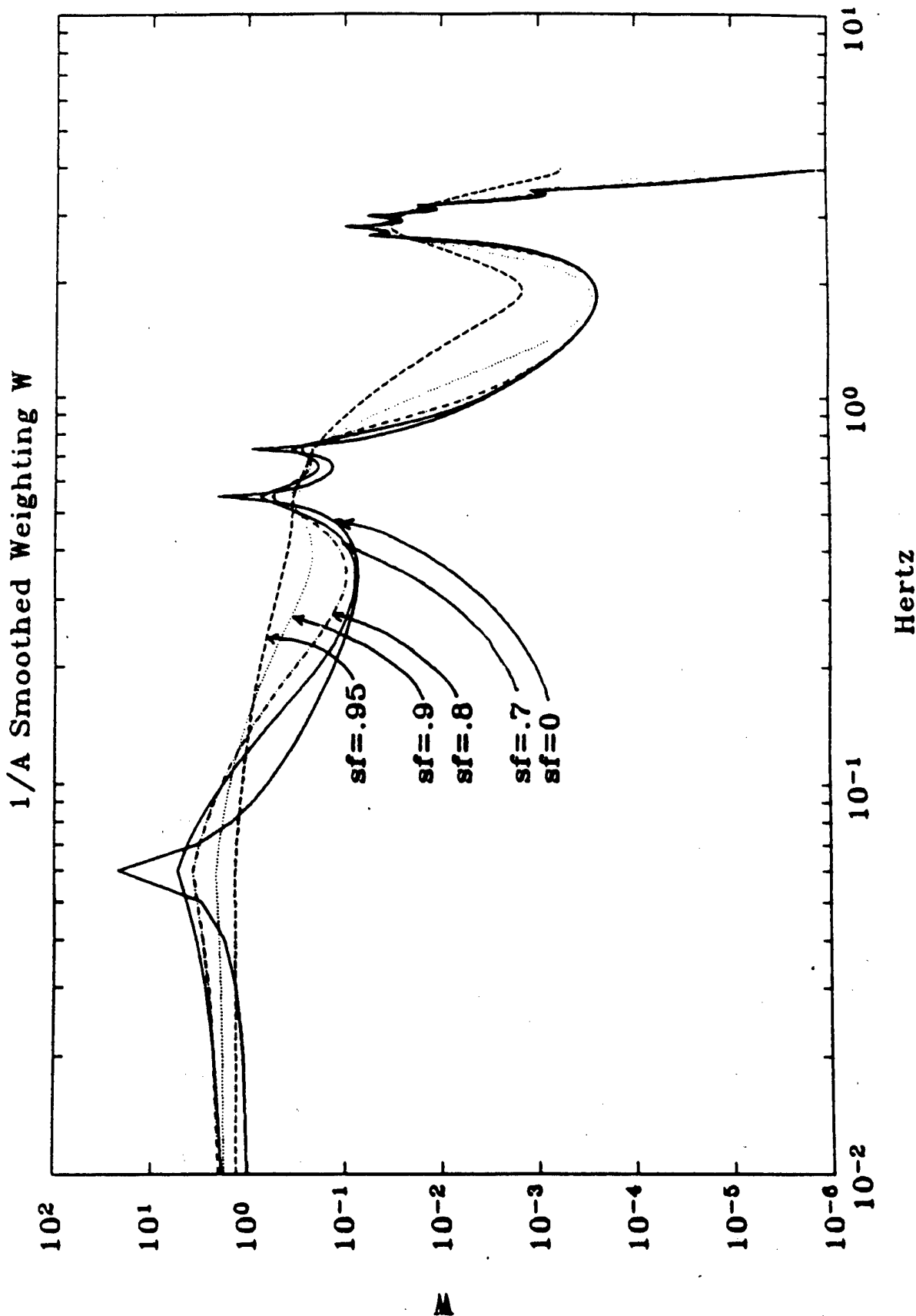
Fig. 2.9-3 Plot of $\left|\frac{1}{a(e^{j2\pi fT})}\right|$ Weighting with Various Values of Smoothing Factor.

- • DISCRETE TRANSFER FUNCTION: $\quad G(z) = \dfrac{B(z)}{A(z)}$

$A(z) = z^n + a_1 z^{n-1} + \ldots + a_n$

ROOTS ON UNIT CIRCLE: $\quad z_i = e^{j\omega_i T} \quad i = 1, \ldots, n$

$T \triangleq$ SAMPLING PERIOD

z_i COMPLEX CONJUGATE PAIRS

ASSUME RELATIVE PERTURBATION:

$$\left| \frac{\delta a_i}{a_i} \right| \leq \epsilon \quad \text{FOR } i = 1, \ldots, n$$

THEN

$$\left| \frac{\delta z_j}{z_j} \right| \leq \frac{\sum\limits_{k=1}^{n} |a_k|\,\epsilon}{\prod\limits_{i \neq j} s_{ij}}$$

s_{ij} IS SECANT FROM ω_i TO ω_j
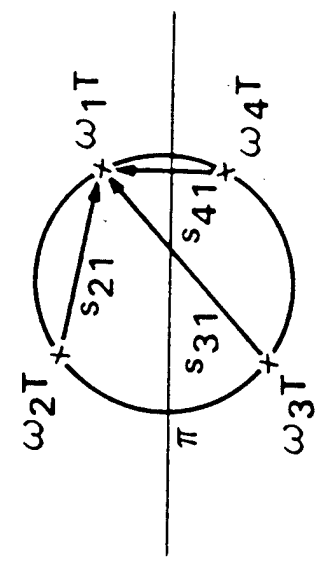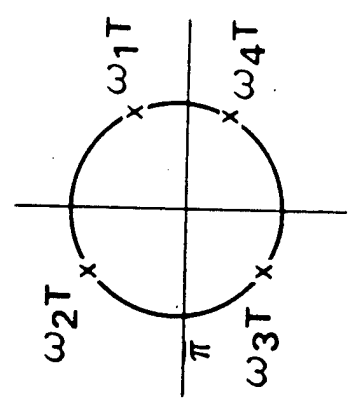
Fig. 2.9-4 Root Sensitivity in terms of Pole Locations.

90

$$\left| \frac{\delta z_j}{z_j} \right| \leq \frac{\displaystyle\sum_{k=1}^{n} |a_k| \epsilon}{\displaystyle\prod_{i \neq j} s_{ij}} \Bigg\} \text{ ROOT SENSITIVITY}$$

- AVOID ESTIMATING TOO MANY MODES AT ONE TIME

- OPTIMAL T FOR ONE MODE IS GIVEN BY $\omega T = \dfrac{\pi}{2}$ i.e., 4 SAMPLES/CYCLE
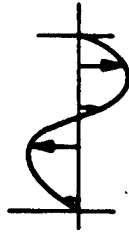
- AVOID OVERSAMPLING LOW FREQUENCY MODES

$$\frac{b_1 z + b_0}{z^2 - 2\cos\omega T\, z + 1} \approx \frac{b_1 z + b_0}{z^2 - 2(1 - \omega^2 T^2) z + 1}$$

$\omega = (2\pi)(.01)$
$T = 0.1$
$\omega^2 T^2 = 0.00004$

- AVOID MODES NEAR FOLD-OVER FREQUENCY

- AVOID MODES CLOSE TO EACH OTHER

IN GENERAL, CHOOSE T TO KEEP ROOTS AWAY FROM ± 1 AND AWAY FROM EACH OTHER
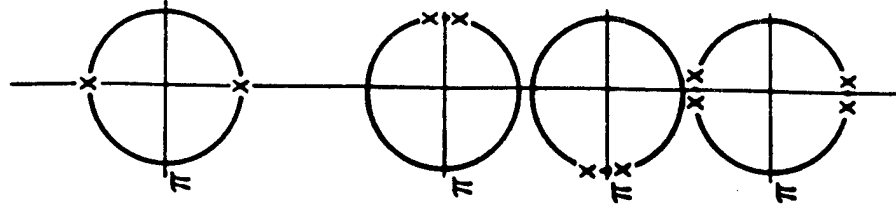
Fig. 2.9-5 Typical Root Sensitivity Problems Arising from Sampled Resonant Systems.

```
C      FILE: A2FR.FOR
C
C      THIS ROUTINE CALLS ZROOTS
C
C      SUBROUTINE A2FR(THETA,NA,NDF,FREQ,ZETA,T)
C
C      THIS ROUTINE ACCEPTS THE ARMA COEFFICIENTS AND RETURNS FREQ
C      (HERTZ) AND DAMPING ESTIMATES. ONLY THE DENOMINATOR COEFFS
C      IN THETA ARE USED.THIS IS A ROBUSTIFIED VERSION OF A2F.FOR
C      WHICH INCORPORATES BAIRSTOWS METHOD TO EXTRACT HARD TO DETERMINE
C      LOW FREQUENCY ROOTS.
C
C      THETA      VECTOR OF ARMA OR ARMAX COEFFICIENTS SUCH THAT THETA(I)=
C                 AI I=1,...,NA;   WHERE A(Z**-1)Y=B(Z**-1)U+C(Z**-1)E AND
C                 A(Z**(-1))=1+A1*Z**(-1)+...+ANA*Z**(-NA)
C      NA         ORDER OF POLYNOMIAL A(Z**(-1)) --DIVISIBLE BY 2
C      NDF        NUMBER OF DIFFICULT TO FIND ROOT PAIRS
C      FREQ       NA/2 VECTOR OF MODAL FREQ IN HERTZ
C      ZETA       NA/2 VECTOR OF MODAL DAMPING
C      T          SAMPLING PERIOD IN SECS
C
C
C
      REAL*8 THETA(*),FREQ(*),ZETA(*),P(33),PD(33),RD(33),
     * PQUAD(3),B(16),C(16),T,PI,RR,RI,W,Z,EPS,DISC
      COMPLEX*16 A(33),ROOTS(32),R
      LOGICAL FLAG
      DATA PI/3.1415927/,EPS/1.0D-30/
      CALL DVCHK(FLAG)
      NAP=NA+1
      NAPP=NAP
C
C      LOAD VECTOR P IN REVERSE ORDER
      P(NAP)=1.
      DO 5 I=1,NA
      P(NA-I+1)=THETA(I)
    5 CONTINUE
      IF(NDF.EQ.0) GO TO 8
C
C      FACTOR OUT NDF DIFFICULT TO FIND ROOT PAIRS WITH BAIRSTOWS METHOD
C      PROBLEM ROOT PAIRS ASSUMED TO BE NEAR Z=1+0i
C      (IE, SAMPLED LOW FREQ MODES)
      N3=3
      DO 6 I=1,NDF
      B(I)=-2.D0
      C(I)=1.D0
C      DETERMINE QUADRATIC FACTOR & PUT INTO PQUAD
      CALL DQROOT(P,NAPP,B(I),C(I),EPS)
      PQUAD(3)=1.D0
      PQUAD(2)=B(I)
      PQUAD(1)=C(I)
C      DIVIDE P BY PQUAD & PUT RESULT INTO PD
      CALL DPOLDIV(P,NAPP,PQUAD,N3,PD,RD)
C      LOAD PD INTO P
```

Fig. 2.9-6 Subroutine A2FR for Robust Polynomial Factorization and Supporting Sub-routines DQROOT, DPOLYDIV, LAGUERD, and ZROOTSD.

```fortran
      DO 7 J=1,NAPP
      P(J)=PD(J)
    7 CONTINUE
      NAPP=NAPP-2
    6 CONTINUE
      IF(NAPP.EQ.1) GO TO 11
C
C     LOAD VECTOR A AND CONVERT TO COMPLEX
    8 A(NAPP)=DCMPLX(1.,0.)
      DO 10 I=1,NAPP-1
      A(I)=DCMPLX(P(I),0.)
   10 CONTINUE
C
      MNAPP=NAPP-1
      CALL ZROOTS(A,MNAPP,ROOTS,.TRUE.)
   11 CONTINUE
C
C     AUGMENT ROOTS(I) WITH PROBLEM ROOTS FORMED FROM B&C
      DO 15 I=1,NDF

      DISC=-B(I)**2+4*C(I)
      IF(DISC.GE.0.D0) GO TO 14
C     IF ROOTS ARE REAL PUT AT Z=1+0i
      B(I)=-2
      DISC=0.D0
   14 ROOTS(NA+2*I-2*NDF)=DCMPLX(-B(I)/2.D0,DSQRT(DISC)/2.D0)
   15 CONTINUE
C
C     CONVERT ROOTS TO FREQ & ZETA VALUES
C
      NA2=NA/2
      DO 20 I=1,NA2
      PRINT *, ROOTS(2*I-1), ROOTS(2*I)
      R=ROOTS(2*I)
      Q=REAL(R)
      RR=DBLE(Q)
      RI=DIMAG(R)
      IF(DABS(RR).LE.1.D-30) RR=DSIGN(1.D-30,RR)
      W=DATAN2(RI,RR)/T
      W=DABS(W)
      Z=RR**2+RI**2
      Z=DLOG(Z)
      IF(W.LE.1.D-30) W=DSIGN(1.D-30,W)
      ZETA(I)=-Z/(2.*W*T)
      FREQ(I)=W/(2.*PI)
   20 CONTINUE
      RETURN
      END
C
C
```

Fig. 2.9-6 Subroutine A2FR for Robust Polynomial Factorization and Supporting Subroutines DQROOT, DPOLYDIV, LAGUERD, and ZROOTSD (continued).

```fortran
      SUBROUTINE DQROOT(P,N,B,C,EPS)
      PARAMETER (NMAX=33,ITMAX=1000,TINY=1.0D-30)
      REAL*8 P(*),Q(NMAX),D(3),REM(NMAX),QQ(NMAX),S,R,
     * SC,RC,SB,RB,DIV,DELB,DELC,B,C,EPS
      D(3)=1.
      DO 12 ITER=1,ITMAX
        D(2)=B
        D(1)=C
        CALL DPOLDIV(P,N,D,3,Q,REM)
        S=REM(1)
        R=REM(2)
        CALL DPOLDIV(Q,N-1,D,3,QQ,REM)
        SC=-REM(1)
        RC=-REM(2)
        DO 11 I=N-1,1,-1
          Q(I+1)=Q(I)
11      CONTINUE
        Q(1)=0.
        CALL DPOLDIV(Q,N,D,3,QQ,REM)
        SB=-REM(1)
        RB=-REM(2)
        DIV=1./(SB*RC-SC*RB)
        DELB=(R*SC-S*RC)*DIV
        DELC=(-R*SB+S*RB)*DIV
        B=B+DELB
        C=C+DELC
        IF((ABS(DELB).LE.EPS*ABS(B).OR.ABS(B).LT.TINY)
     *       .AND.(ABS(DELC).LE.EPS*ABS(C)
     *       .OR.ABS(C).LT.TINY)) RETURN
12    CONTINUE
C      PAUSE 'too many iterations in QROOT'
      RETURN
      END
C
C

      SUBROUTINE DPOLDIV(U,N,V,NV,Q,R)
      REAL*8 U(*),V(*),Q(*),R(*)
      DO 11 J=1,N
        R(J)=U(J)
        Q(J)=0.
11    CONTINUE
      DO 13 K=N-NV,0,-1
        Q(K+1)=R(NV+K)/V(NV)
        DO 12 J=NV+K-1,K+1,-1
          R(J)=R(J)-Q(K+1)*V(J-K)
12      CONTINUE
13    CONTINUE
      R(NV)=0.
      RETURN
      END
```

Fig. 2.9-6 Subroutine A2FR for Robust Polynomial Factorization and Supporting Subroutines DQROOT, DPOLYDIV, LAGUERD, and ZROOTSD (continued).

```
C         THIS FILE CONTAINS SUBROUTINES TO FIND THE ROOTS OF
C         POLYNOMIALS OF DEGREE M HAVING TERMS A(I)X**(I-1) I=1,
C         ...,M+1. SUBROUTINE ZROOTS CALLS LAGUER FOR EACH NEW
C         ROOT UNTIL ALL ROOTS ARE FOUND AND THEN SORTS ALL ROOTS
C         BY THEIR REAL PARTS. TOP LEVEL SUBROUTINE IS ZROOTS.
C         ALL VECTORS AND ARITHMETIC IS COMPLEX.
C
          SUBROUTINE LAGUER(A,M,X,EPS,POLISH)
C         NOTE: SML & CML ADDED TO AVOID DIVIDE BY ZERO
C
          REAL*8 EPS,TINY,DXOLD,YY,ZZ,CDX,SML
          COMPLEX*16 A(*),X,DX,X1,B,D,F,G,H,SQ,GP,GM,G2,ZERO,XX,WW,CML
          LOGICAL POLISH,FLAG
          PARAMETER (ZERO=(0.D0,0.D0),TINY=1.D-15,MAXIT=100)
          DATA SML/1.D-100/
          CALL UNDFL(FLAG)
          CML=(1.D-100,1.D-100)
          IF (POLISH) THEN
             DXOLD=CDABS(X)
             NPOL=0
          ENDIF
          DO 12 ITER=1,MAXIT
             B=A(M+1)
             D=ZERO
             F=ZERO
             DO 11 J=M,1,-1
                F=X*F+D
                D=X*D+B
                B=X*B+A(J)
11           CONTINUE
             IF(CDABS(B+CML).LE.TINY) THEN
                DX=ZERO
             ELSE IF(CDABS(D).LE.TINY.AND.CDABS(F).LE.TINY)THEN
                DX=DCMPLX(CDABS((B+CML)/(A(M+1)+CML))**(1./M),0.D0)
             ELSE
                G=D/(B+CML)
                G2=G*G
                H=G2-2.*F/(B+CML)
             XX=(M-1)*(M*H-G2)
             YY=DABS(REAL(XX))
             ZZ=DABS(DIMAG(XX))
             IF(YY.LT.TINY.AND.ZZ.LT.TINY) THEN
                SQ=ZERO
             ELSE IF (YY.GE.ZZ) THEN
                WW=(1.D0/(YY+SML))*XX
                SQ=DSQRT(YY+SML)*CDSQRT(WW)
             ELSE
                WW=(1.D0/(ZZ+SML))*XX
                SQ=DSQRT(ZZ)*CDSQRT(WW)
             ENDIF
                GP=G+SQ
                GM=G-SQ
                IF(CDABS(GP).LT.CDABS(GM)) GP=GM
                DX=M/GP
```

Fig. 2.9-6 Subroutine A2FR for Robust Polynomial Factorization and Supporting Sub-
      routines DQROOT, DPOLYDIV, LAGUERD, and ZROOTSD (continued).

```
            ENDIF
            X1=X-DX
            IF(X.EQ.X1)RETURN
            X=X1
            IF (POLISH) THEN
               NPOL=NPOL+1
               CDX=CDABS(DX)
               IF(NPOL.GT.9.AND.CDX.GE.DXOLD)RETURN
               DXOLD=CDX
            ELSE
               IF(CDABS(DX).LE.EPS*CDABS(X))RETURN
            ENDIF
  12     CONTINUE
         RETURN
         END
C
         SUBROUTINE ZROOTS(A,M,ROOTS,POLISH)
         REAL*8 EPS
         PARAMETER (EPS=1.D-6,MAXM=101)
         COMPLEX*16 A(*),ROOTS(*),AD(MAXM),X,B,C
         LOGICAL POLISH,FLAG
         CALL OVEFL(FLAG)
         DO 11 J=1,M+1
            AD(J)=A(J)
  11     CONTINUE
         DO 13 J=M,1,-1
            X=DCMPLX(0.D0,0.D0)
            CALL LAGUER(AD,J,X,EPS,.FALSE.)
            IF(DABS(DIMAG(X)).LE.2.*EPS**2*DABS(REAL(X)))
   1        X=DCMPLX(REAL(X),0.D0)
            ROOTS(J)=X
            B=AD(J+1)
            DO 12 JJ=J,1,-1
               C=AD(JJ)
               AD(JJ)=B
               B=X*B+C
  12        CONTINUE
  13     CONTINUE
         IF (POLISH) THEN
            DO 14 J=1,M
               CALL LAGUER(A,M,ROOTS(J),EPS,.TRUE.)
  14        CONTINUE
         ENDIF
         DO 16 J=2,M
            X=ROOTS(J)
            DO 15 I=J-1,1,-1
               IF(REAL(ROOTS(I)).LE.REAL(X))GO TO 10
               ROOTS(I+1)=ROOTS(I)
  15        CONTINUE
            I=0
  10        ROOTS(I+1)=X
  16     CONTINUE
         RETURN
         END
```

Fig. 2.9-6 Subroutine A2FR for Robust Polynomial Factorization and Supporting Subroutines DQROOT, DPOLYDIV, LAGUERD, and ZROOTSD (continued).

A general discussion of Bairstow's method and Laguerre's method is beyond the scope of this report, but can be found in [2]. Briefly, Bairstow's method estimates quadratic factors of a polynomial using a Newton-Raphson (N-R) iteration, deflating the polynomial after each quadratic factor is found. Because a N-R iteration is used, Bairstow's method can find roots to an arbitrary degree of accuracy, but requires a good initial guess for each root pair being extracted. In A2FR, the Newton Raphson iteration of Bairstow's method is conveniently initialized at complex $1 + i0$ since heavily sampled low frequency modes are known to lie in this vicinity a-priori. After all difficult to find root pairs have been extracted, the deflated polynomial is passed to a general root solving routine based on Laguerre's method. In contrast to Bairstow's method, Laguerre's method does not require any initial guess and can easily find the remaining roots. Hence, by using Bairstow's method in conjunction with Laguerre's method, the problem roots in the vicinity of $1 + i0$ to be found with an arbitrary degree of accuracy and the adverse effect of coefficient perturbations due to subsequent polynomial deflation is minimized.

In A2FR, the quadratic factors of Bairstow's method are extracted using the subroutine DQROOT, polynomial deflation is performed by the polynomial division routine DPOLDIV, and the standard root solver based on Laguerre's method is implemented using routines LAGUERD and ZROOTSD. The subroutines DQROOT, DPOLYDIV, LAGUERD, and ZROOTSD are based on routines found in Numerical Recipes [2], and are included in Figure 2.9-6 for convenience.

2.9.6 Integration with System Software

A curve fitting subroutine based on the above theory has been integrated into the experiment software. A curve fit is specified by the experiment menu as follows:

```
MENU (4,4,6)
TRANSFER FUNCTION CURVE FIT PARAMETERS
0 — Exit                       ;
121 — PARAM(121) 1000.    ;   MTFCF = # data points to be read in
122 — PARAM(122) 8.       ;   NTFCF = order of fitted model (2×#modes)
124 — PARAM(124) 0.       ;   FSTART = start freq band (Hz)
125 — PARAM(125) 0.       ;   FSTOP = stop freq band (Hz)
126 — PARAM(126) 1.       ;   ITFCF = data type flag
                          ;   1 - spec. est.
                          ;   2 - sindwell
                          ;   3 - compute TF
                          ;   4 - compute YERR, YEST, PUE, PEE
                          ;   5 - append SINFIL with data in FREQ, TFRE, and TFIM
                          ;   6 - calc Re and Im of TREF
                          ;   7 - calc modulus (TREF-TF) and store in SDATA (20)
128 — PARAM(128)          ;   ICFFIL sine-dwell data storage file
129 — PARAM(129) 1.E-15 ;   TAU = threshold for singular values
130 — PARAM(130) 1.       ;   SF = smoothing factor for 1/A weighting
191 — PARAM(191) 1.       ;   NDF = # difficult to find root pairs
```

Here, the quantities MTFCF and NTFCF correspond, respectively, to M and n from this section. The quantities FSTART and FSTOP specify data in a particular frequency band, and can be used to "window" the data if desired. The data type flag ITFCF indicates the type of data to be used in the curve fit (i.e., spectral estimation data, sine-dwell data), and the type of computation to be performed (i.e., transfer function curve fit, output error computation, etc.). If sine-dwell data is used, the storage file number is indicated by ICFFIL. The value TAU is a threshold on the singular values in a robust least squares inversion routine taken from [4]. The quantity NDF specifies the number of root pairs near complex $(1 + 0i)$ which must be carefully removed by a robust root solving routine discussed in Sect. 2.9.5. The quantity SF is the smoothing factor for the reweighting defined earlier in Sect. 2.9.4. The choice SF=1 defuses the smoothing process in case smoothing is not desired (e.g., for the initial curve fit).

As an example, the nominal values in MENU (4,4,6) are set to fit a four mode model using 1000 points of spectral estimation data between 0 and 5 Hz. The choice NDF=1 corresponds to a single heavily sampled low frequency mode which would cause numerical problems if not specified to the robust root solver.

2.9.7 Case Study with Experimental Data

The curve fit algorithm with iterative reweighting is demonstrated in this section using real experimental data taken from the JPL/AFAL ground test structure. The input excitation is chosen as white noise, uniformly distributed between ±1.5. The experimental constants are given by

Sampling time $T = .05$ sec
Total Run Time = 1638.4 sec
Total Number of Samples = 32768
Actuator Number =HA41
Sensor Number =HA51

The spectral estimation was performed with the following parameters,

NSE=32768
MSE=4096
LSE=2048
NFFT=4096

The transfer function Bode plot, as obtained by the spectral estimation technique outlined in Section 2.8 is shown in Figure 2.9-7. It is desired to curve fit this data using the iterative algorithm outlined above.
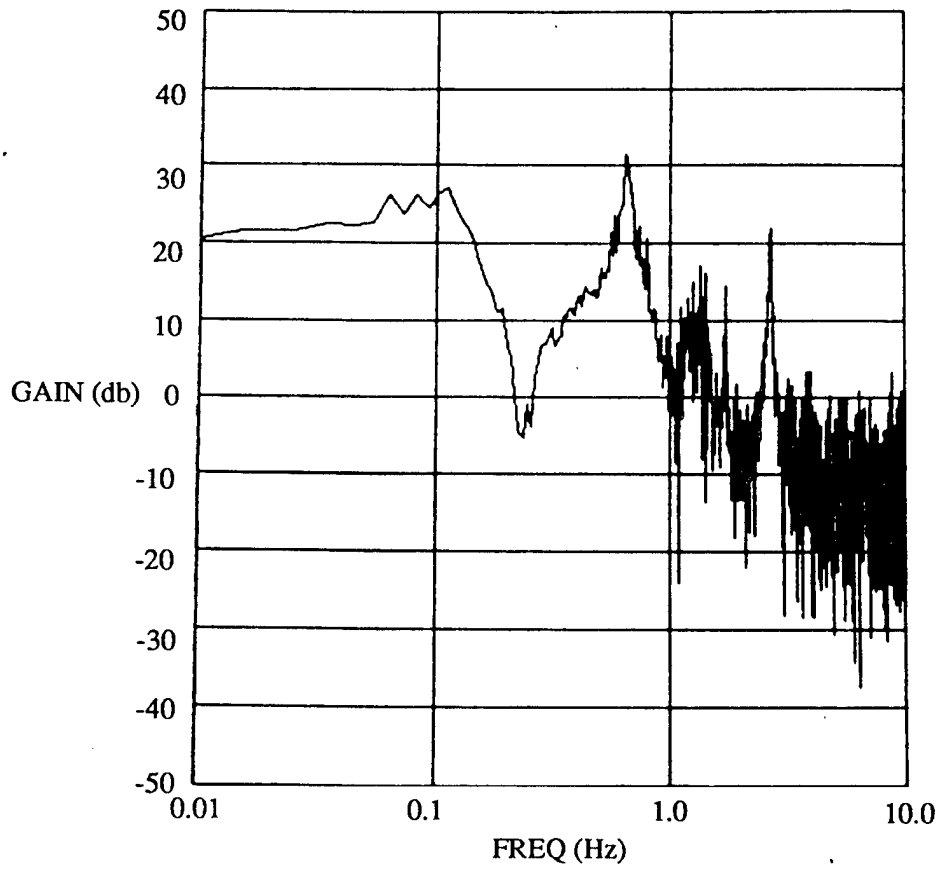
Fig. 2.9-7 Transfer Function Estimate $|h(e^{i2\pi ft})|$ Using Spectral Estimation.

Iteration #1.

The parameters of the curve fit in MENU(4,4,6) set initially as

TRANSFER FUNCTION CURVE FIT PARAMETERS

121	6.24000E+02	;MTFCF
122	8.00000E+00	;NTFCF
123	0.00000E+00	;ERROR
124	0.00000E+00	;FSTART
125	3.00000E+00	;FSTOP
126	1.00000E+00	;ITFCF
127	0.00000E+00	;KRANK
128	1.00000E+00	1.0;ICFFIL
129	1.00000E-14	TAU
130	1.00000E+00	;SF
191	1.00000E+00	;NDF

It is noted that the curve fit is based on a 4 mode model using data between 0 and 3Hz, and the smoothing factor for the initial fit is chosen as $SF = 1$. The results of the curve fit are plotted in Figure 2.9-8a, and are superimposed, for convenience, on the original data in Figure 2.9-8b. The actual estimated parameters are given as

RESFREQ	ZETA
2.68482562323547	6.935074494025807E-003
1.93615032936596	6.311028753404398E-002
0.885720297246297	0.150087235080724
0.371661120928969	0.417671952251777

RNUM	DNOMR
2.667572791224959E-002	0.763734578745717
-0.347097718143222	-5.44834387164698
1.45759741919601	17.7130844726174
-3.23332172396834	-34.3104984507499
4.43825412037593	43.3387487650913
-3.9988235177777	-36.5781889577652
2.37004790953087	20.1594579615938
-0.863238306715730	-6.63772897717782
0.151221467231719	1.00000000000000

Here, RNUM and DNOMR are the estimated coefficients of the $b(z)$ and $a(z)$ polynomials, respectively, and RESFREQ and ZETA are the frequency and damping estimates obtained from robustly factorizing the $a(z)$ polynomial as discussed in Sect. 2.9.5. It is seen from Figure 2.9-8 that there is excellent agreement between the data and fit above 2 Hz, but that matching at lower frequencies is poor. Hence, the estimation process will continue.
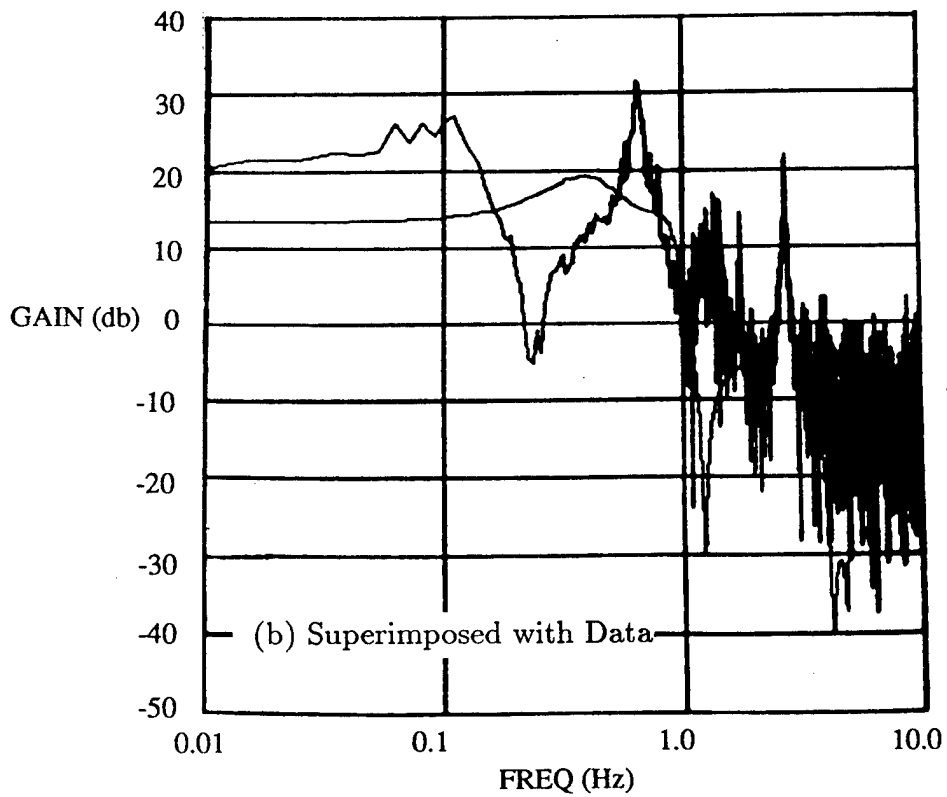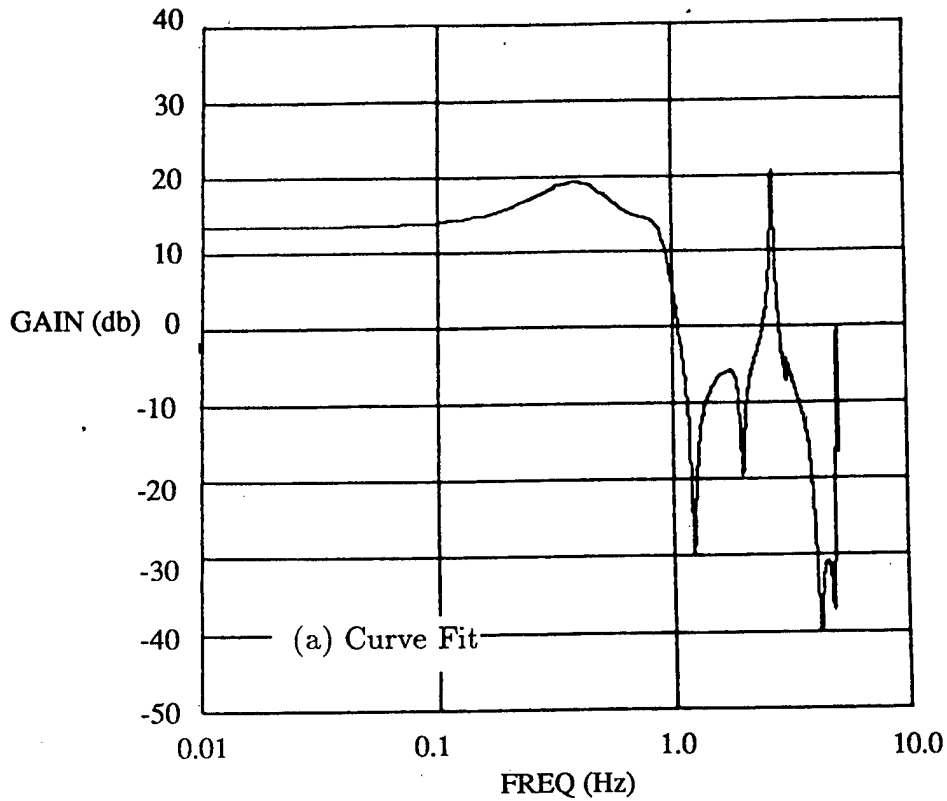
Fig. 2.9-8 Transfer Function Curve Fit $|\hat{p}(e^{i2\pi ft})|$

Iteration #1   (a) Curve Fit, (b) Superimposed with Data

101

Iteration # 2

Using the iterative reweighting technique outlined in Sect. 2.9.4, the next curve fit is performed using a smoothing factor of $SF = .95$. The results are plotted in Figure 2.9-9a and again superimposed in Figure 2.9-9b on the original data. The numerical estimates are given as

RESFREQ	ZETA
2.67833403534730	6.743402652914477E-003
1.52929655464298	2.193933717986753E-002
0.661894271068050	3.243351469997596E-002
0.117973948317708	0.666134888026146

RNUM	DNOMR
0.3908633303376424	0.909104562067029
-2.55846947265990	-6.50146641694411
7.58086971124726	21.0232212659114
-13.2924226437306	-40.2392885081865
15.1209267366128	49.9367819618536
-11.4811860318949	-41.1700641283635
5.72380975367326	22.0156214697750
-1.72964961944145	-6.97389788048100
0.245362156074281	1.00000000000000

It is seen from Figure 2.9-9 that there is now excellent agreement above .6 Hz, but that matching at lower frequencies can still be improved. Hence, the algorithm is iterated several more times with $SF = .95$ until convergence is obtained. The numerical results of each iteration are given below.

Iteration #3

RESFREQ	ZETA
2.67494555948228	7.292945787501519E-003
1.42044285989733	1.421410134099574E-002
0.652000477405587	3.616030864378409E-002
0.112126702597779	0.187788619317773

RNUM	DNOMR
0.451866816901085	0.948392472337719
-2.90399258429018	-6.77436268461013
8.43230707071977	21.8557127336814
-14.4448183355408	-41.6943553559408
15.9844659934227	51.5202812955275
-11.7378635967656	-42.2472480498091
5.61674353878678	22.4398859374651
-1.61446747935643	-7.04829952012047
0.215838388194334	1.00000000000000
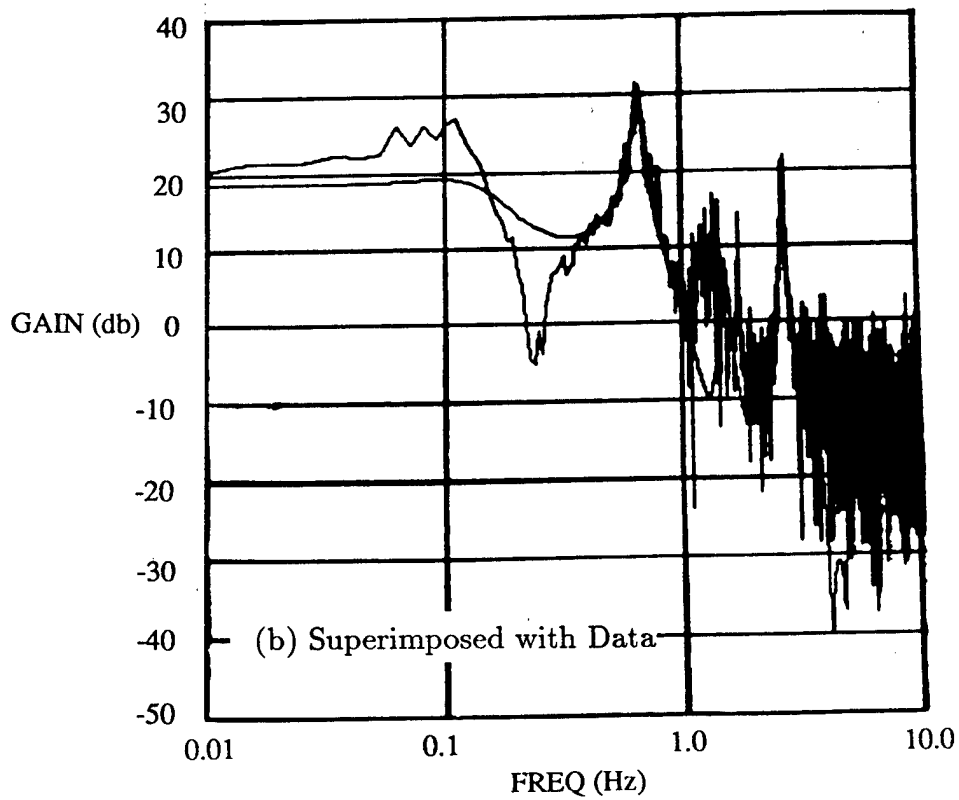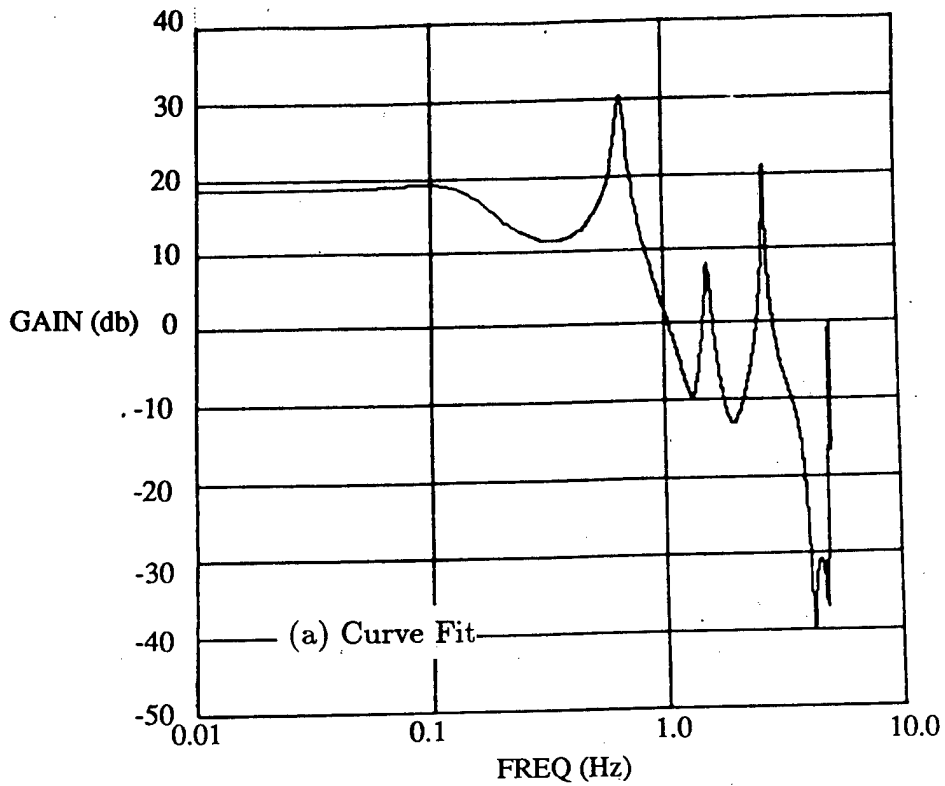
Fig. 2.9-9 Transfer Function Curve Fit $|\hat{p}(e^{i2\pi ft})|$

Iteration #2 (a) Curve Fit, (b) Superimposed with Data

103

Iteration #4

RESFREQ	ZETA
2.67244274573406	8.043442648885062E-003
1.37368405071712	6.083223897629544E-003
0.650697334494611	3.676059230245317E-002
0.113624972759847	0.187885600551214

RNUM	DNOMR
0.564465111689107	0.953896928083314
-3.67715141674060	-6.82162600740708
10.8156714810019	22.0201656815095
-18.7713591868752	-42.0088045568720
21.0575938714166	51.8858247894536
-15.6766485282723	-42.5087101042217
7.59283238335803	22.5467635992743
-2.19888013024134	-7.06750378380504
0.293553767381303	1.00000000000000

Iteration #5

RESFREQ	ZETA
2.67000344968331	8.661824648985038E-003
1.36503621372472	2.852985277743727E-003
0.650898737237889	3.649211408759811E-002
0.113752209047907	0.187209240934942

RNUM	DNOMR
0.620050521065320	0.955727252779591
-4.05379320351566	-6.83604326246442
11.9600934637594	22.0685276317073
-20.8177087689239	-42.0999803778184
23.4204459743473	51.9911986695610
-17.4833116486189	-42.5836361923464
8.48593235745119	22.5770818495063
-2.45947866118802	-7.07286809407923
0.327846632983107	1.00000000000000

Iteration #6

RESFREQ	ZETA
2.66805278162247	9.106929382103085E-003
1.36538370108693	2.080171882987349E-003
0.650973772558464	3.625769369271443E-002
0.113672074464551	0.187020739578903

RNUM	DNOMR
0.632729530860752	0.955769181570290
-4.14029191297692	-6.83691284755813
12.2229201436413	22.0731578480721
-21.2857696801876	-42.1116511860108
23.9585495503371	52.0075271406141
-17.89467751605791	-42.5967401687734
8.69104205997418	22.5827586986245
-2.52062878723200	-7.07390220335866
0.336200798463567	1.00000000000000

Iteration #7

RESFREQ	ZETA
2.66707318851004	9.324617160475453E-003
1.36684763433731	1.866356076126991E-003
0.650979720293050	3.615786199199247E-002
0.113609290131807	0.186962373900882

RNUM	DNOMR
0.632708417037254	0.955649495444489
-4.14004342220431	-6.83615573469628
12.2205087377552	22.0713709245612
-21.2768652375020	-42.1097199081578
23.9423126322335	52.0067354919846
-17.8783080294831	-42.5969203807879
8.68184619846102	22.5829986807213
-2.51802028534971	-7.07395210430566
0.335937543624198	1.00000000000000

Iteration #8

RESFREQ	ZETA
2.66655390594996	9.436688140356413E-003
1.36826802072691	1.748379226851594E-003
0.650969019868184	3.609426691662075E-002
0.113560798772055	0.186911130483292

RNUM	DNOMR
0.630693351011426	0.955602326539438
-4.12632650759666	-6.83569727762743
12.1777329263034	22.0698564192642
-21.1973057233994	-42.1071692879014
23.8464168652950	52.0041759001754
-17.8022221830550	-42.5952787150502
8.64336256751223	22.5823435683768
-2.50677161079163	-7.07382646418624
0.334496910752865	1.00000000000000

Iteration #9

RESFREQ	ZETA
2.66641966397125	9.465197767070372E-003
1.36907192858008	1.723490367847868E-003
0.650957713446217	3.608219499836319E-002
0.113543739190183	0.186901052427773

RNUM	DNOMR
0.628755173654102	0.955584624204267
-4.11297395457326	-6.83543633680460
12.1361329730733	22.0687930612142
-21.1205589928004	-42.1050173618617
23.7546781645900	52.0016102497990
-17.7295652305880	-42.5933971051415
8.60622066954573	22.5815446169944
-2.49560103918734	-7.07367527419586
0.332988873991462	1.00000000000000

Iteration #10

RESFREQ	ZETA
2.66649774162126	9.448392713026308E-003
1.36933858301979	1.743956549354619E-003
0.650951071231850	3.609648855785963E-002
0.113547277009458	0.186909849416950

RNUM	DNOMR
0.627724705347606	0.955587543452579
-4.10580524597273	-6.83536011134953
12.1138119966461	22.0683132651731
-21.0796328485946	-42.1038096724405
23.7060644648940	51.9999523834919
-17.6911021199320	-42.5920742667560
8.58638153302003	22.5809629484524
-2.48949866324928	-7.07356561266829
0.332132846135351	1.00000000000000

It is noted that convergence to approximately 3 significant digits in the transfer function coefficients and approximately 5 significant digits in the frequency estimates is obtained after 10 iterations. The results of the last iteration are plotted in Figure 2.9-10a and in superimposed form in Figure 2.9-10b. It is seen that agreement over all frequencies is good. A magnitude plot of the transfer function curve fit error is given in Figure 2.9-11, where it is seen that the maximum errors are approximately 10dB down from the signal levels at the corresponding frequencies.

2.9.8 General Remarks

The lessons learned while developing and testing the algorithms of this section can be summarized as follows,

1) Curve-fitting based on the equation error least squares approach has an inherent high frequency emphasis which must be removed before accurate fits are possible. This is performed in our software using an original iterative reweighting algorithm to establish minimum variance estimation. This reweighting approach was seen to work very well on the actual experimental data with little human intervention required. However, we note the next lesson.

2) The present methodology is not yet fully automated, since there is still some judgment needed in specifying the model order for the curve fit, and in determining the smoothing factor for the iterative reweighting. Presently, there is on-going work on both of these issues.
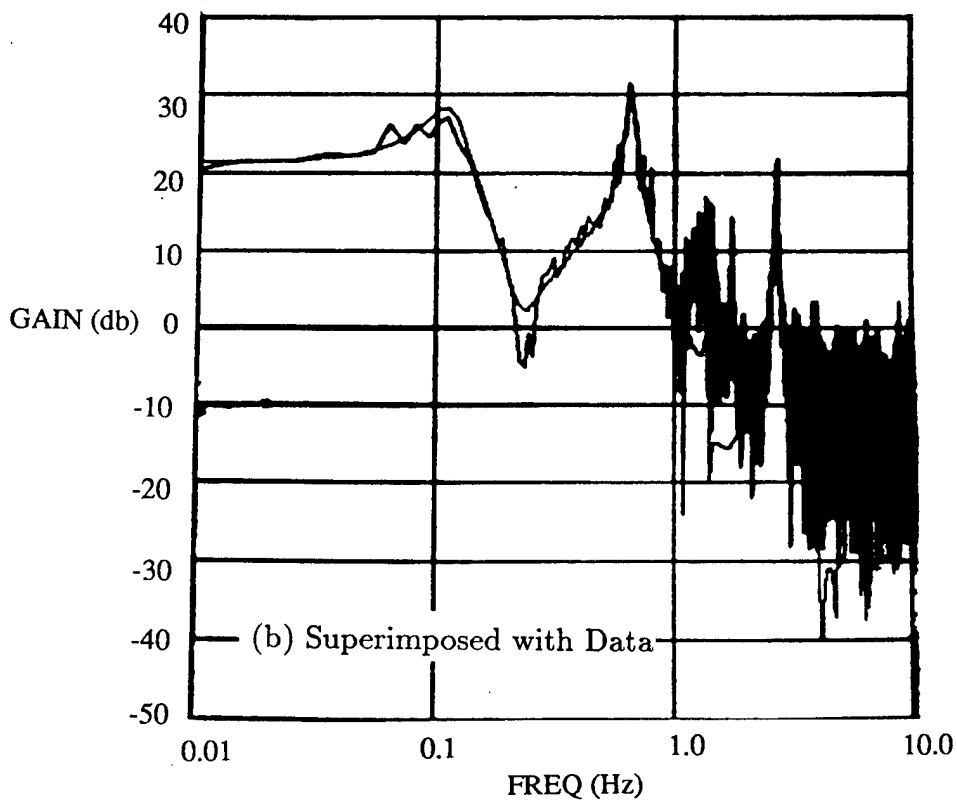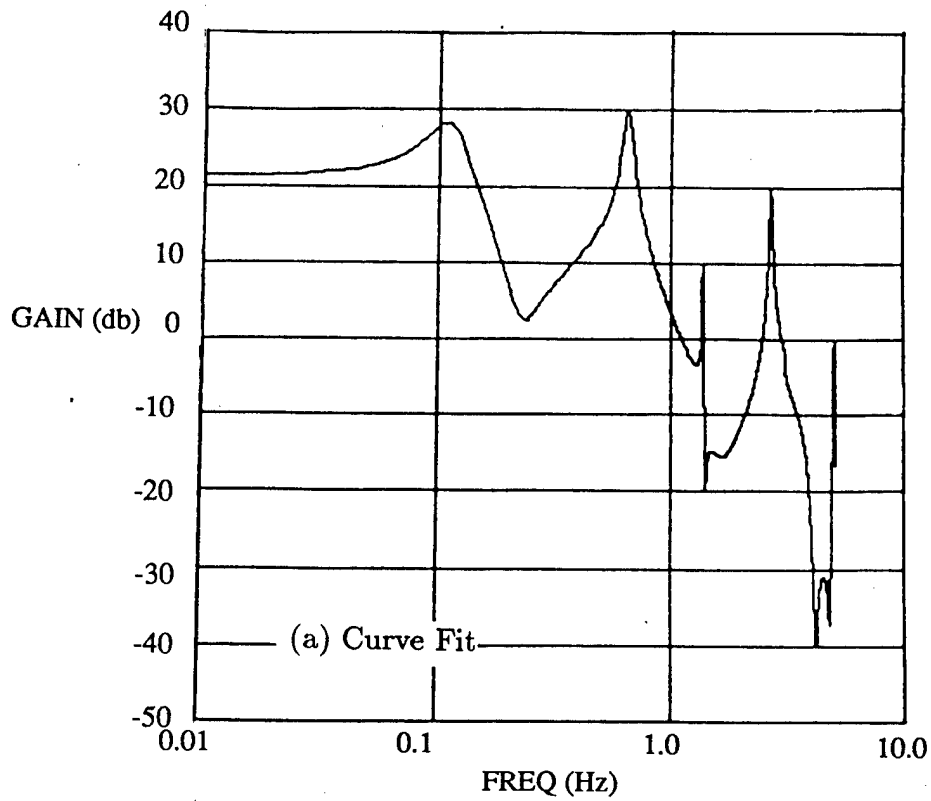
Fig. 2.9-10 Transfer Function Curve Fit $|\hat{p}(e^{i2\pi ft})|$

Iteration #10   (a) Curve Fit, (b) Superimposed with Data
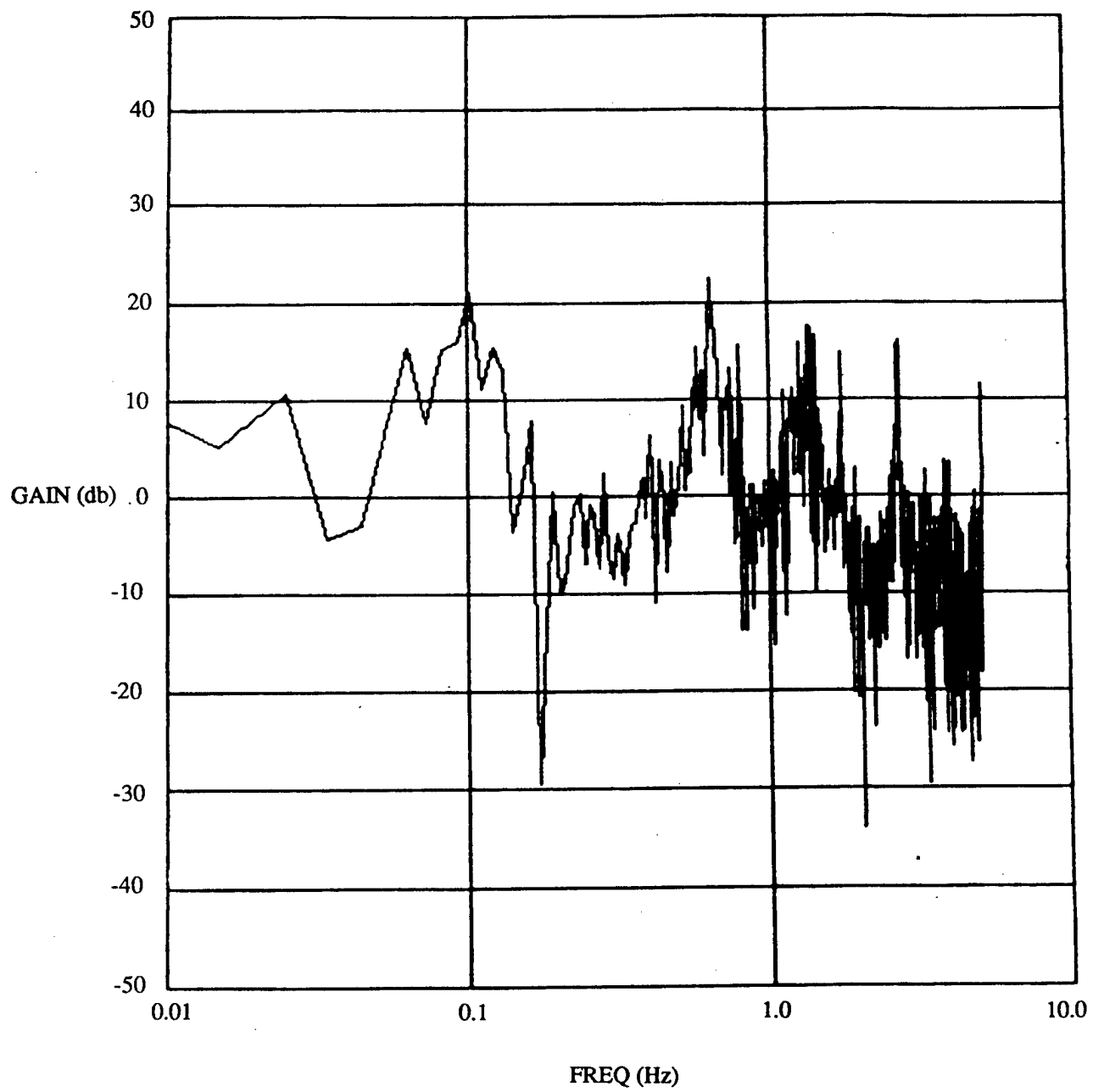
Fig. 2.9-11 Transfer Function Curve Fit Error $|h - \hat{p}|$.

3) When modes are close together with respect to the sampling frequency, or when there is a low frequency mode which is heavily sampled there are numerical problems in determining the polynomial roots and estimating frequencies. This problem arose in the present effort and required special software to be developed to remove the low frequency mode.

4) The length of the experiment appears to be driven by the frequency of the lowest mode. Two basic problems associated with accurately estimating and fitting the low frequency mode are poor resolution due to the sparseness of FFT data points in the vicinity of the low frequency mode (i.e., for a given FFT frequency spacing, the smallest number of data points fall on the lowest mode) and the large variance of the spectral estimate. Of course in spectral estimation, resolution and variance one can always be traded off against the other by adequate choice of data windowing. However, the only method to resolve both problems is by going to a longer experiment time. We were forced to go to a longer experiment time (i.e., (.05 secs)(32768) = 1638 secs = 27.3 minutes) to resolve the mode and curve fit it satisfactorily.

2.10 Output Error Analysis

2.10.1 Introduction

The analysis and design of robust controllers requires more information about the plant than simply a nominal estimate of the plant transfer function. Information is also required concerning the uncertainty in the nominal estimate, or more generally, the identification of a model set within which the true plant is known to lie.

Precisely how to go about identifying model set membership to best support robust control design is not known, and in fact, is presently an active area of research. For the present effort we have chosen to use a simple but useful characterization of the model uncertainty based on the output error. This is essentially a characterization of the additive uncertainty in the plant model, and has found considerable use in robust control analysis and synthesis [24].

2.10.2 Background

Consider the single-input single-output plant p with transfer function spectral estimate $h = P_{uy}/P_{uu}$ where u and y are the input and output of the plant. Assume that an identified parametric model $\widehat{p}$ is produced as a result of system identification efforts. The additive uncertainty $(\delta_m = p - \widehat{p})$ in this work is then estimated as the quantity Δ, where,

$$\Delta = P_{ue}/P_{uu} \qquad (2.10-1)$$

where $e = y - \widehat{y}$ is the output error. A simple method to generate Δ is

1) Run an experiment with wideband excitation input u to plant p yielding output y

2) Apply the identification techniques to obtain the identified parametric model $\widehat{p}$

3) Compute the output $\widehat{y}$ of the identified model $\widehat{p}$ subjected to the same input u

110

4) Compute output error $e = y - \widehat{y}$

5) Compute Δ by cross spectral analysis,

$$\Delta = P_{ue}/P_{uu}$$

In principle, this approach has the added advantage that system and measurement noise uncorrelated with u will not affect the estimate of Δ.

Motivated by simplicity, it is very tempting to dispense with the above procedure, and estimate the additive uncertainty directly by the curve fit error τ where,

$$\tau = h - \widehat{p} \qquad (2.10 - 2)$$

However, τ in eqn.(2.10-2) is generally a much worse estimate of δ_m than Δ in eqn.(2.10-1). This will be demonstrated both analytically and by numerical example in Sect. 2.10.3.

The usefulness of the output error for LSS robust control design has been considered earlier by Kosut in [12]. The discussion here will closely follow his presentation.

Let S denote the set of stable single-input single-output rational transfer functions (rational in the delay variable z^{-1}). A compensator C is said to stabilize plant p if the following three transfer functions are in S:

$$C/(1 + pC)$$
$$1/(1 + pC)$$
$$p/(1 + pC)$$

Then we have the following result

Theorem 1

(i) Stabilization

If $p \in S$ then C stabilizes p if and only if $C = Q(1 - pQ)^{-1}$ for some $Q \in S$

(ii) Robustness

If $p = \hat{p} + \delta_m$, and if some compensator $\hat{C}$ stabilizes $\hat{p}$, then it also stabilizes p if and only if,

$$\delta_m(1 + \delta_m\hat{Q})^{-1} \in S \qquad (2.10 - 3)$$

where
$$\hat{Q} = \hat{C}(1 + \hat{p}\hat{C})^{-1} \in S$$

Part (i) of this result says that a plant is open-loop stable, then the set of all rational compensators that stabilize p, denoted by $S(p)$, is given by
$$S(p) = \{Q(1 - pQ)^{-1} : Q \in S\}$$

111

Hence, any stabilizing controller must produce a Q which is in S, and conversely.

Part (ii) of the result gives conditions on when the controller $\hat{C}$ designed for nominal plant $\hat{p}$ is robustly stable to a plant perturbation δ_m. Here, the nominal plant $\hat{p}$ and perturbation δ_m can be unstable. However, when $\delta_m \in S$ condition (2.10-3) reduces to

$$(1 + \delta_m \hat{Q})^{-1} \in S$$

a sufficient condition for which is that,

$$\|\delta_m(e^{j\omega T})\| \leq \frac{1}{\|\hat{Q}(e^{j\omega T})\|} for \ \ all \ \ \omega \in [-\infty, \infty] \qquad (2.10-4)$$

Note that $\hat{Q}$ can be computed directly from $\hat{p}$ and $\hat{C}$, and δ_m can be approximated by $\Delta = P_{ue}/P_{uu}$. Hence, (2.10-4) is a simple condition to check for stability robustness of a specified controller. The use of this condition for robust control synthesis is outlined in Fig. 2.10-1 where it is embedded into an iterative design methodology. The idea behind the iterative approach is to design a sequence of controllers (robust in some sense) with increasingly good performance until the robust stability condition is violated. Any of a number of existing robust design techniques can be used for this purpose.

2.10.3 Numerical Example

It was mentioned earlier in Sect. 2.10.1 that of the two plausible methods for estimating the additive uncertainty, the quantity Δ in eqn.(2.10-1) is a much better estimate than τ in eqn.(2.10-2). Some insight can be gained by considering the diagram of Figure 2.10.2. In order to aid the discussion, a (ficticious) quantity $\hat{h}$ which is the cross-spectral estimate of the predicted output $\hat{y} = \hat{p}u$ with u (here u is assumed to be the same as used in the physical experiment) is defined, i.e.,

$$\hat{h} = P_{u\hat{y}}/P_{uu} \qquad (2.10-5)$$

Using eqn.(2.10-5), eqn.(2.10-1) can be written as

$$\Delta = P_{ue}/P_{uu} = P_{uy}/P_{uu} - P_{u\hat{y}}/P_{uu} = h - \hat{h} \qquad (2.10-6)$$

The fact that τ and Δ are estimates of the additive uncertainty δ_m can be seen more clearly by rearranging eqns. (2.10-2) and (2.10-6), respectively, to give,

$$\tau = (h - p) + (p - \hat{p}) = \epsilon + \delta_m \qquad (2.10-7)$$

$$\Delta = (h - p) - (\hat{h} - \hat{p}) + (p - \hat{p}) = \epsilon - \hat{\epsilon} + \delta_m \qquad (2.10-8)$$

where,

Fig. 2.10-1 Functional Flow Diagram for On-Orbit ID and On-line Robust Controller Redesign.

Flow diagram contents:

ID

$\hat{p}, \delta_m(\omega)$

CHOOSE NOMINAL WEIGHTS q, r

ROBUST CONTROL REDESIGN $C(\hat{p}, q, r, s)$

ROBUSTLY STABLE ? $\|Q\|\delta_m(\omega) \leq 1$

INCREASE ROBUSTNESS WEIGHTING r

NOMINAL PERFORMANCE SATISFACTORY ?

IMPLEMENT $C(\hat{p}, q, r, s)$

INCREASE PERFORMANCE WEIGHTING q
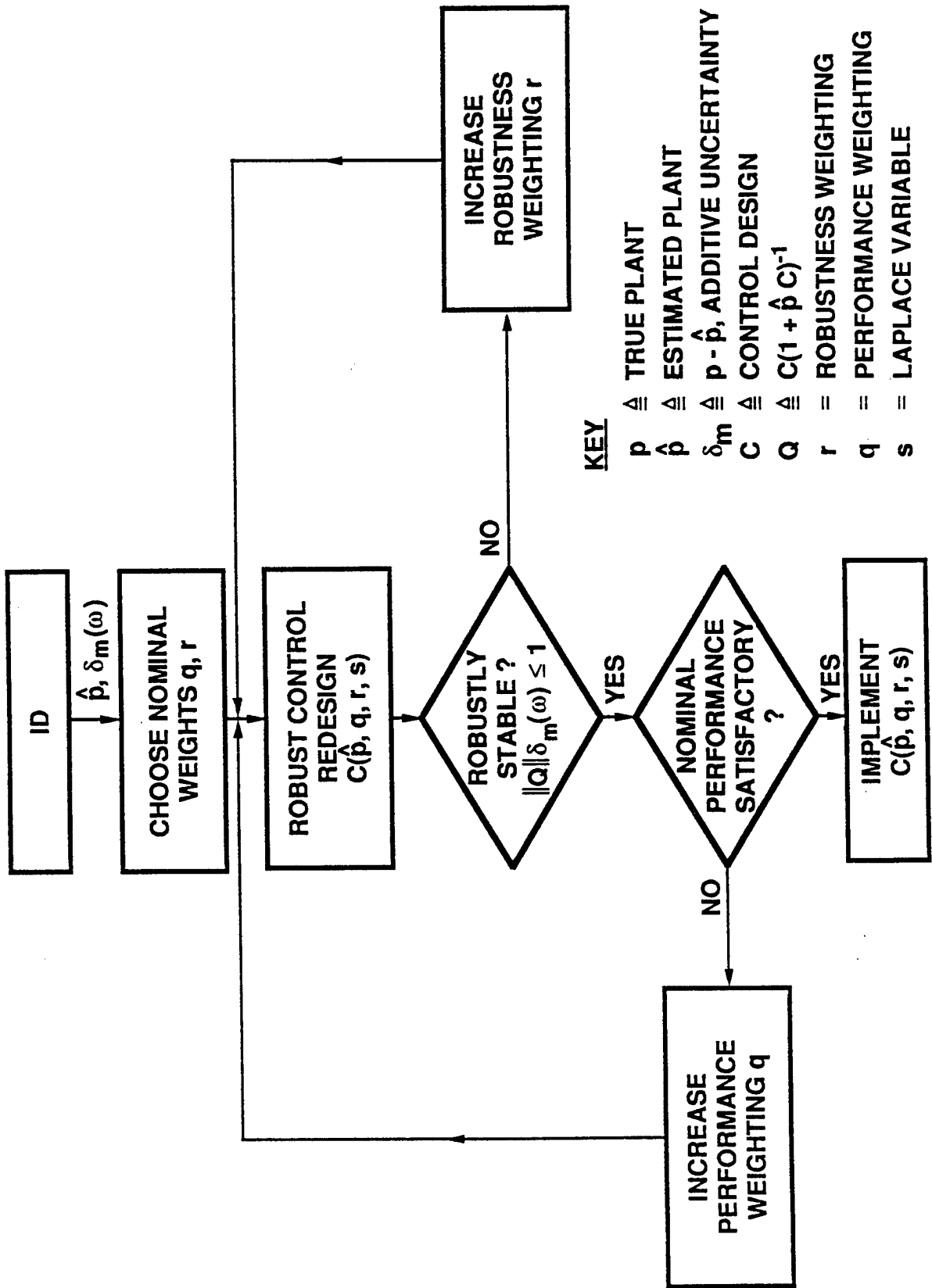
KEY

p	$\triangleq$	TRUE PLANT
$\hat{p}$	$\triangleq$	ESTIMATED PLANT
δ_m	$\triangleq$	$p - \hat{p}$, ADDITIVE UNCERTAINTY
C	$\triangleq$	CONTROL DESIGN
Q	$\triangleq$	$C(1 + \hat{p} C)^{-1}$
r	=	ROBUSTNESS WEIGHTING
q	=	PERFORMANCE WEIGHTING
s	=	LAPLACE VARIABLE

113

EXACT ADDITIVE
UNCERTAINTY

p

δ_m

$\hat{p}$

ϵ

$\hat{\epsilon}$

Translation due to
the same input/output
generation and
spectral analysis
processes

CURVE FIT
ERROR
$\tau = h - \hat{p}$

h

Δ

ADDITIVE
UNCERTAINTY
ESTIMATE

$\hat{h}$

Fig. 2.10-2 Estimation of the Additive Uncertainty δ_m.

$$\epsilon = h - p \qquad\qquad (2.10-9)$$

$$\hat{\epsilon} = \hat{h} - \hat{p} \qquad\qquad (2.10-10)$$

It is emphasized that eqns. (2.10-9) and (2.10-10) are precisely the errors incurred from using spectral estimation to estimate quantities p and $\hat{p}$, respectively. This relationship is depicted schematically in Figure 2.10-2. The reason that Δ is a much better estimate of δ_m than τ is easilty seen from the variance of the estimates. Assuming negligible bias on the spectral estimation errors (2.10-9) and (2.10-10), it follows from (2.10-7) and (2.7-8) that,

$$Var[\tau] = Var[\epsilon] \qquad\qquad (2.10-11)$$

$$Var[\Delta] = Var[\epsilon] - 2Cov[\epsilon\hat{\epsilon}] + Var[\hat{\epsilon}] \qquad\qquad (2.10-12)$$

Assume for the moment that the estimate of the plant is very precise, i.e., $\hat{p} = p$. Then $\epsilon = \hat{\epsilon}$ and it follows that,

$$Var[\tau] = Var[\epsilon]$$

$$Var[\Delta] = 0$$

Clearly, Δ is a much better estimator of δ_m than τ in this case. In the experimental case where p is close to but not equal to $\hat{p}$, by continuity ϵ will be strongly correlated with $\hat{\epsilon}$ and the negative term in eqn. (2.10-12) will reduce the variance of the estimate significantly over (2.10-11). Hence, the quantity Δ will generally be a much more accurate estimate of the additive uncertainty δ_m than τ.

Results from a simulation example are presented to illustrate these concepts. Figure 2.10-3 shows the transfer function spectral estimate of the plant $h = P_{uy}/P_{uu}$. Figure 2.10-4 shows the identified parametric model $\hat{p}$. The gain of the transfer function curve fit error $\tau = h - \hat{p}$ is shown in figure 2.10-5. The output error $e = y - \hat{y}$ is shown in figure 2.10-6. The estimate $\Delta = P_{ue}/P_{uu}$ is shown in figure 2.10-7. As this is a simulation example, the actual plant p is known. The exact additive uncertainty δ_m is determined and plotted in figure 2.10-8. It can be seen that Δ constitutes a very good approximation of δ_m, much better than τ. In fact, the transfer function error τ is much larger than Δ or δ_m, by up to 30 db for low frequency values.
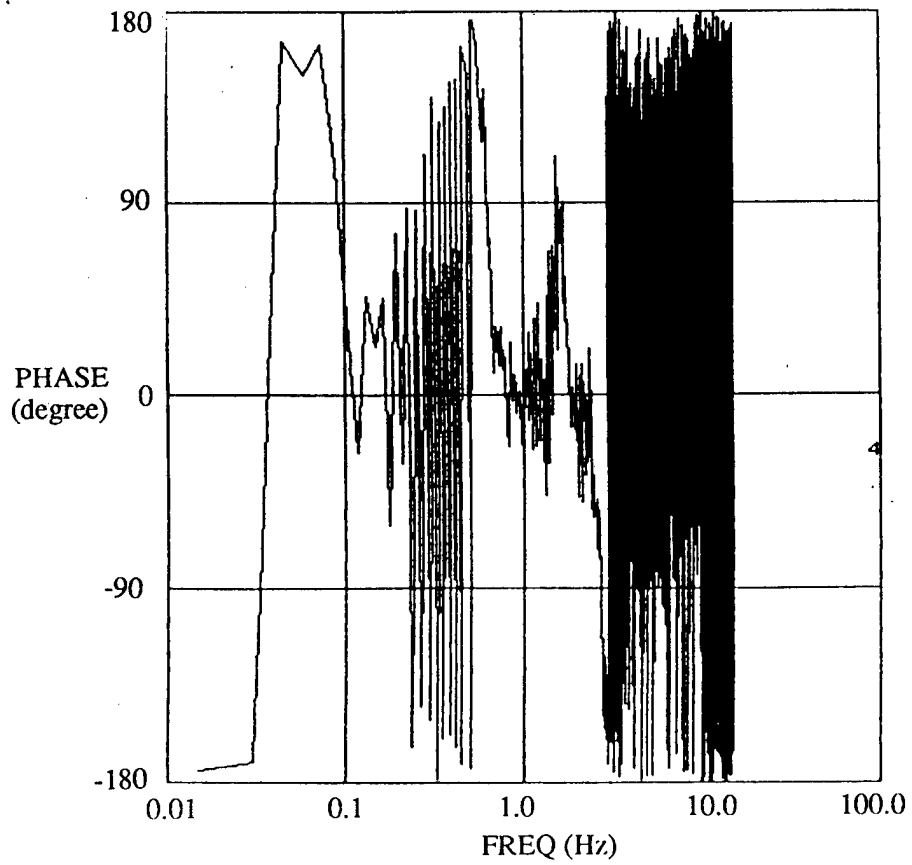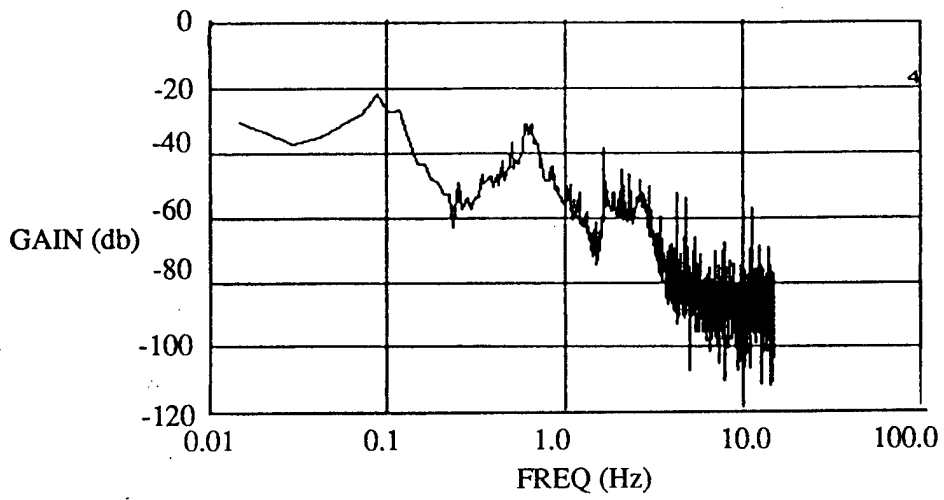
Fig. 2.10-3 Transfer Function Spectral Estimate $h = P_{uy}/P_{uu}$.

116
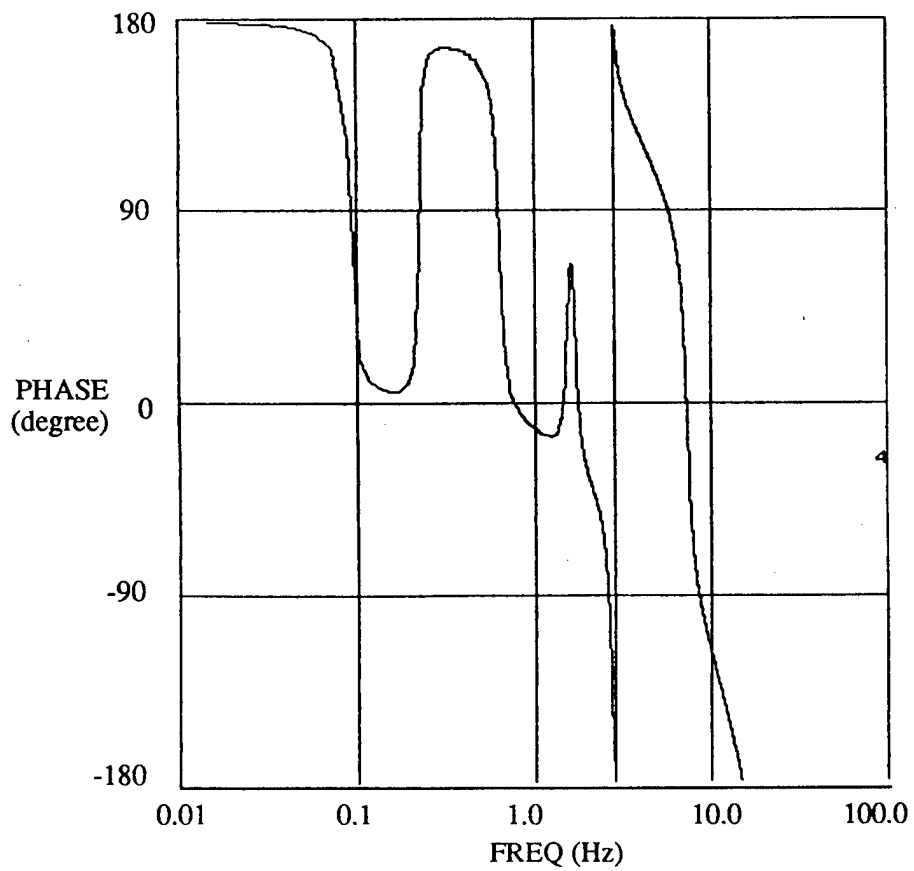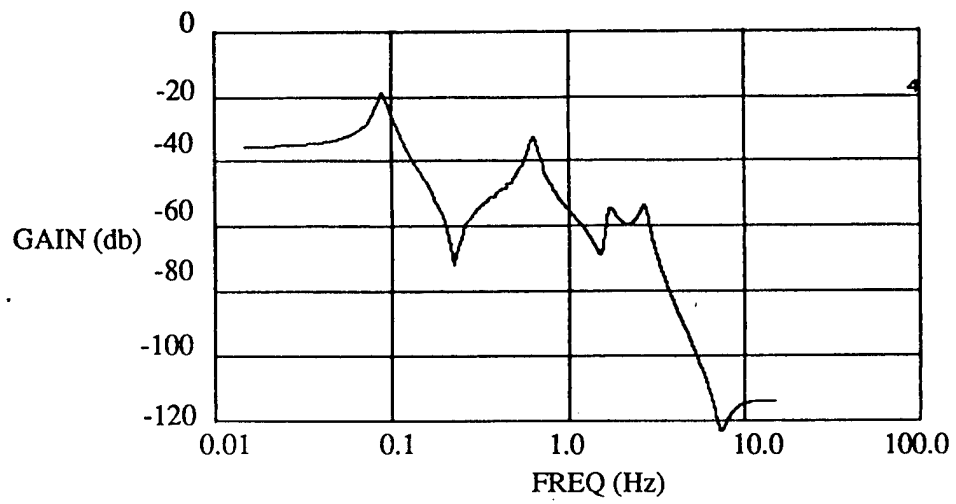
Fig. 2.10-4 Identified Parametric Model $\hat{p}$.
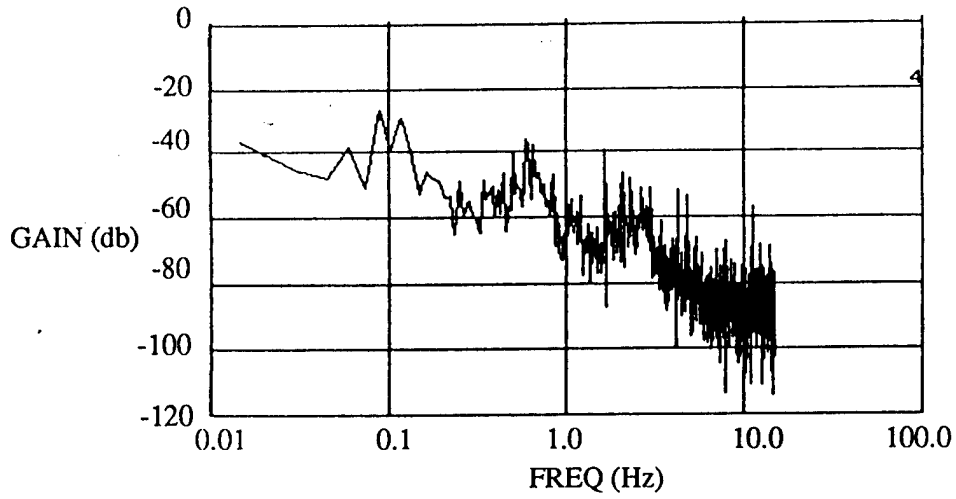
Fig. 2.10-5 Transfer Function Curve Fit Error $\tau = h - \hat{p}$.
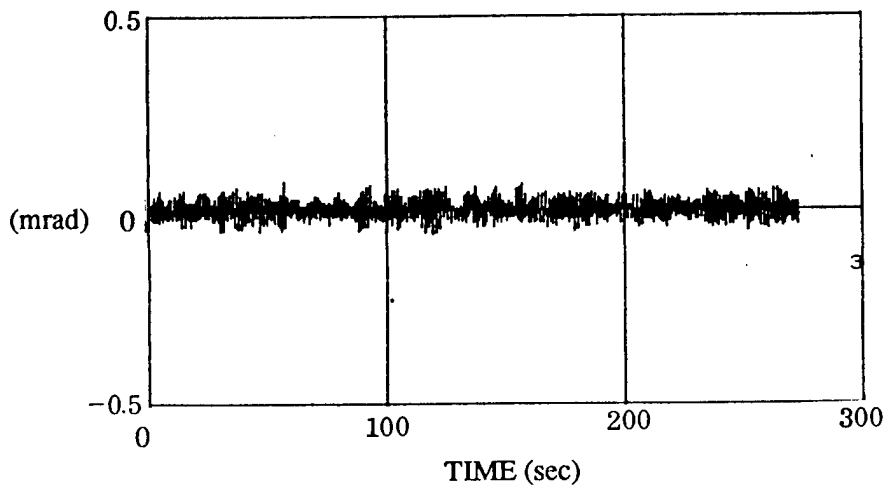
Fig. 2.10-6 Output Error $e = y - \hat{y}$, where $\hat{y} = \hat{p}u$ is the Computed Output of the Identified Parametric Model $\hat{p}$ Subjected to u.

118
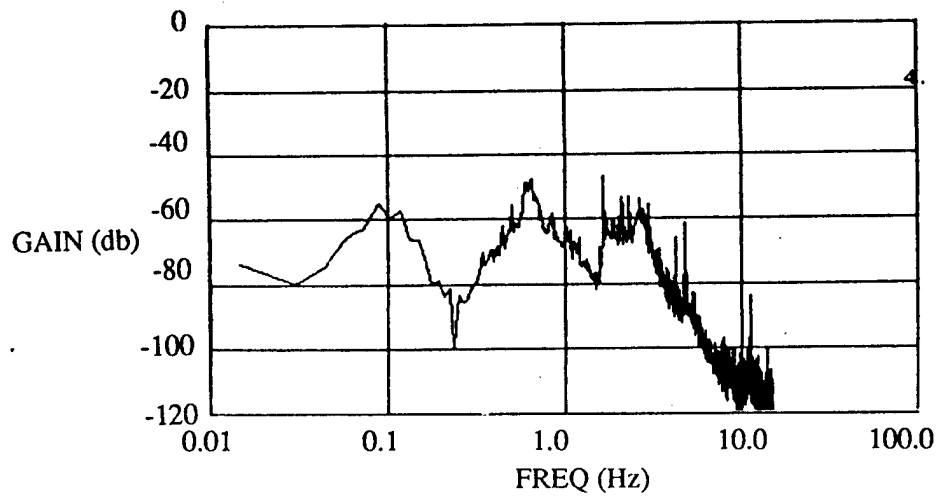
Fig. 2.10-7 The Additive Uncertainty Estimate $\Delta = P_{ue}/P_{uu}$.
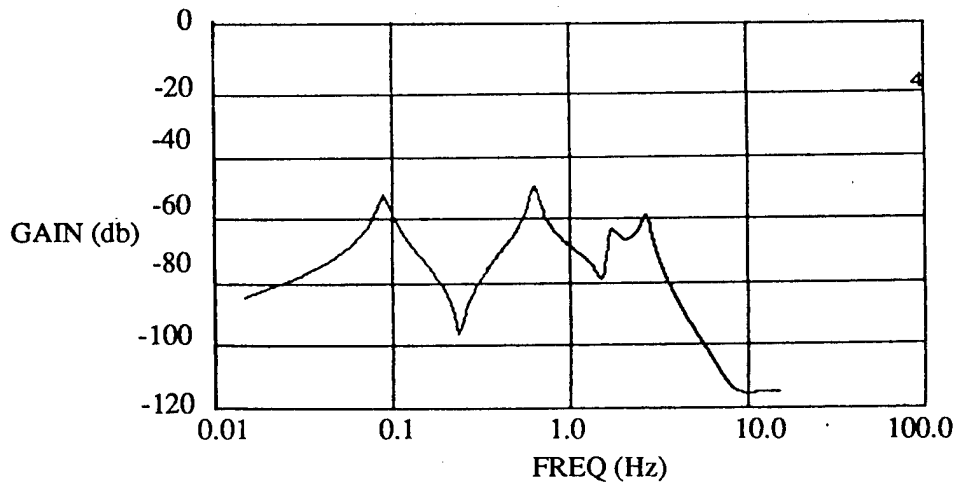
Fig. 2.10-8 The Exact Additive Uncertainty δ_m.

119

Figure 2.10-9 shows a second identified parametric model $\hat{p}'$ for the plant through a different process. Figure 2.10-10 presents the output error e' which indicates that this second model identified is not as good as the first one. This is reflected in figure 2.10-11 which shows the additive uncertainty $\Delta' = P_{ue'}/P_{uu}$ for this case. The uncertainty Δ' is larger than Δ by as much as 30 db for the lowest frequency mode. However, the transfer function error τ' for this case in Figure 2.10-12 is not too much different with that of figure 2.10-5. The curve fit errors, τ and τ', are dominated by the translation vector due to processing and is not a sensitive measure of the modelling performance. The additive uncertainty Δ is defined as the measure of model uncertainty for later analysis.

2.10.4 Integration With System Software

The output error analysis can be performed in the experiment software under the menu of transfer function curve fitting:

```
MENU (4,4,6)
TRANSFER FUNCTION CURVE FIT PARAMETERS
0 — Exit                     ;
121 — PARAM(121) 1000.   ;   MTFCF = # data points to be read in
122 — PARAM(122) 8.      ;   NTFCF = order of fitted model (2×#modes)
124 — PARAM(124) 0.      ;   FSTART = start freq band (Hz)
125 — PARAM(125) 0.      ;   FSTOP = stop freq band (Hz)
126 — PARAM(126) 1.      ;   ITFCF = data type flag
                         ;   1 - spec. est.
                         ;   2 - sindwell
                         ;   3 - compute TF
                         ;   4 - compute YERR, YEST, PUE, PEE
                         ;   5 - append SINFIL with data in FREQ, TFRE, and TFIM
                         ;   6 - calc Re and Im of TREF
                         ;   7 - calc modulus (TREF-TF) and store in SDATA (20)
128 — PARAM(128)         ;   ICFFIL sine-dwell data storage file
129 — PARAM(129) 1.E-15 ;   TAU = threshold for singular values
130 — PARAM(130) 1.      ;   SF = smoothing factor for 1/A weighting
191 — PARAM(191) 1.      ;   NDF = # difficult to find root pairs
```

After an identified parametric model is obtained, setting ITFCF=4 in the TRANSFER FUNCTION CURVE FITTING mode of operation then calls for the computation of $\hat{y}$, stored in array YEST, the output error e, stored in YERR, the cross spectral density P_{ue}, stored in PUE, and the power spectral density of e, P_{ee}, stored in PEE. Though not specified, the additive uncertainty Δ is also computed as P_{ue}/P_{uu}. The parameters adopted for spectral analysis here are the ones set for SPECTRAL ESTIMATION (refer to section 2.8) at this time. When needed, the arrays YEST and YERR, containing $\hat{y}$ and e, can be swapped with the content of y by running the DATA COMPOSITION mode of operation with IDC set at 4 and 5 respectively.
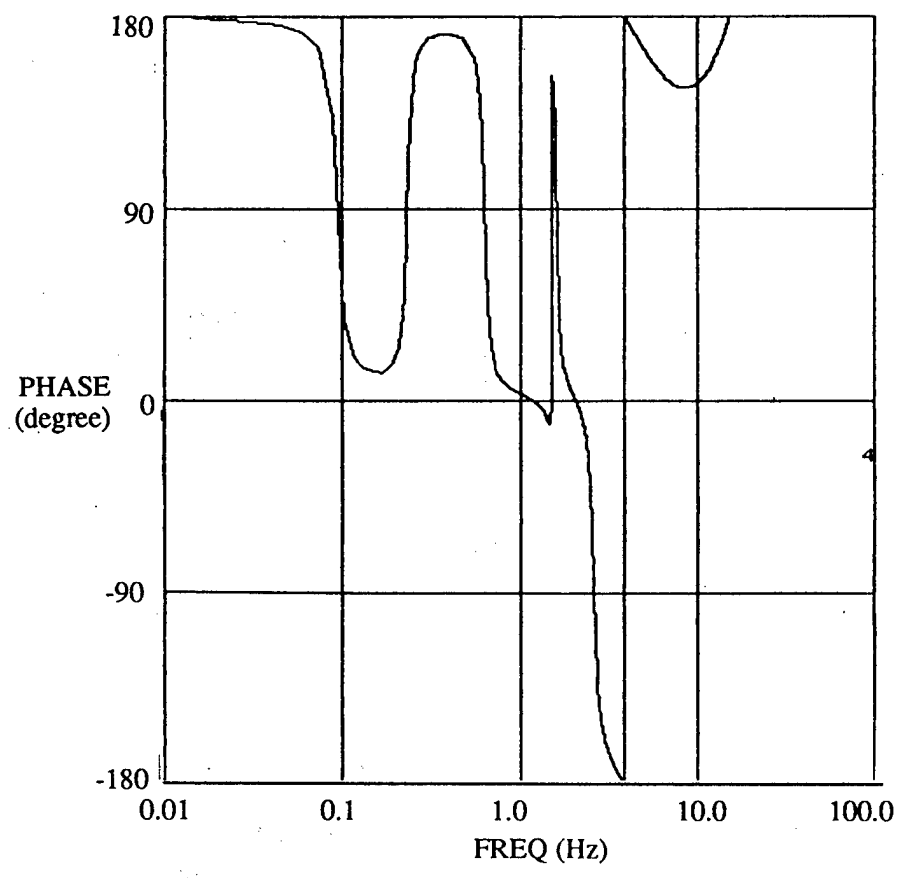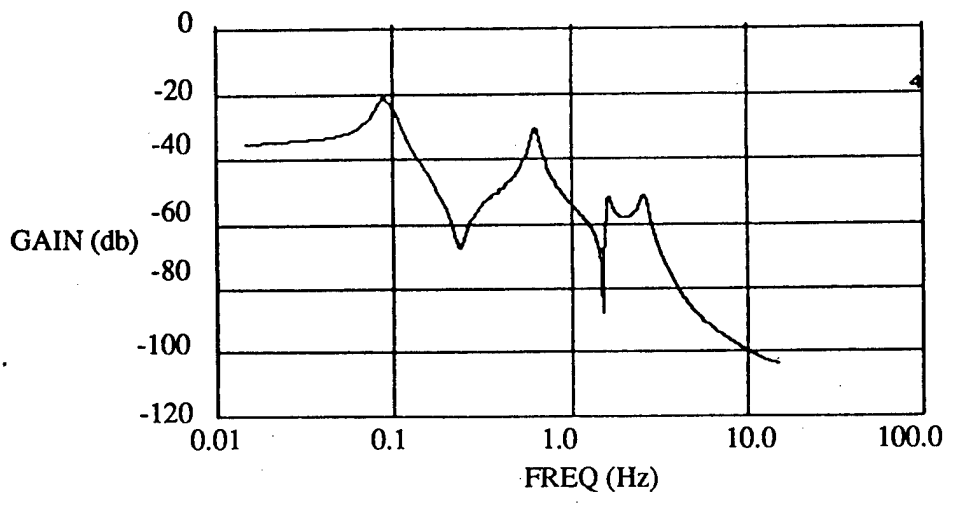
Fig. 2.10-9 A Second Identified Parametric Model $\widehat{p}'$.
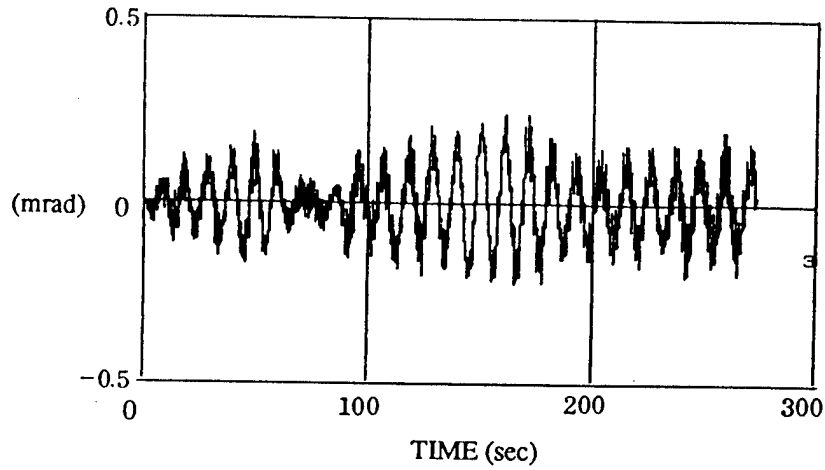
Fig. 2.10-10 Output Error $e' = y - \widehat{y}'$, where $\widehat{y}' = \widehat{p}'u$ is the Computed Output of the Second Identified Parametric Model $\widehat{p}'$ Subjected to u.
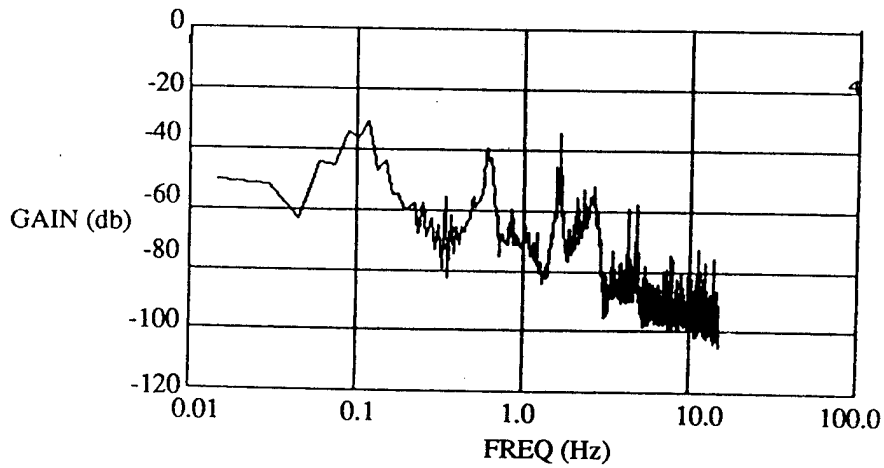
Fig. 2.10-11 Additive Uncertainty Estimate $\Delta' = P_{ue'}/P_{uu}$ For the Second Identified Parametric Model.
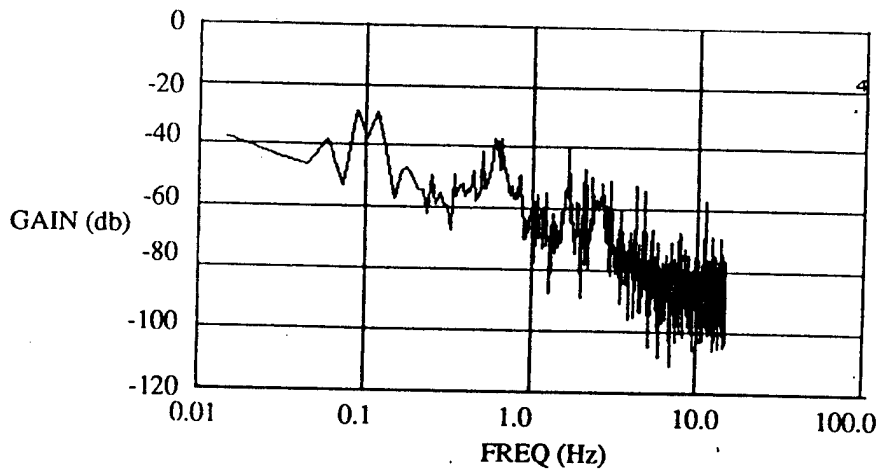
Fig. 2.10-12 Transfer Function Curve Fit Error $\widehat{r}' = h - \widehat{p}'$ for the Second Identified Parametric Model.

122

Chapter 3. EXPERIMENT RESULTS

3.1 Introduction

This Chapter details the experimental results obtained through implementation of the integrated ID software to the testbed structure. Several investigations utilizing wideband, narrowband, and sine-dwell excitations were performed. Areas of investigation included reduced order model identification, residual mode excitation and analysis, system nonlinearity, and noise anomaly. The results enabled a better understanding and characterization of the structure, and demonstrated the performance and versatility of the software algorithms.

This chapter is organized as follows: The next section, titled "On-orbit Scenarios," deals with the "would be" scenarios of on-orbit and automated system model identification. It is divided into four subsections. Section 3.2.1 describes the procedures adopted in this analysis to perform system model determination based on experimental data. Section 3.2.2 presents the identification results obtained via wideband excitations implemented through different sensor and actuator instrumentations. Some characterization of the testbed structure is also discussed. Sections 3.2.3 and 3.2.4 present the results of investigating the system with narrowband excitation and data composition, respectively.

The identified models obtained through the automated procedures in section 3.2.1 constitute the "reduced order" models determined according to the numerical precision of the algorithms, i.e., some "weak" modes will not be included in this identified model. Section 3.3 describes the excitation and evaluation of these so-called residual modes for better understanding of their dynamics. Two residual modes are studied. Results and analysis are given in section 3.3.1, for the first residual mode, and section 3.3.2, for the second one.

The linear (or nonlinear) properties of the structure were investigated and are presented in section 3.4. Both wideband and sine-dwell excitations were used to characterize the nonlinearity of the testbed structure. Respective results are given in section 3.4.1 and 3.4.2. A nominal set of parameter values was adopted for the present analysis. The effects of variation of some of the parameters, namely, the spectral estimation parameter and smoothing factor, on the identification results and performance are presented in two subsections of section 3.5.

Initial experimentation on the testbed structure revealed that the hub sensors were contaminated with appreciable colored noise of approximately 6 Hz frequency. As a result, analog filters were put into the system to remedy the situation. Discussion of this problem as well as comparisons of experimental results using noisy and improved sensors are presented in the final section.

3.2 On-orbit Scenarios

3.2.1 Automated Identification of Reduced Order System Model

As discussed in Chapter 1, on-orbit autonomous system identification constitutes an important element in future large space structure development and deployment. Demonstration of such capability is therefore the intent of these first experiments. A system of automated procedures was developed which would systematically execute various algorithms of the integrated ID software to yield an identified model for the system based on its excitation and response, in absence of any decision from expert systems such as analysts or operators. These automated identification procedures were based on experiences gained in simulation studies of the ID software and yielded reasonably good results for the physical experiments.

Figure 3.2-1 shows the automated identification procedures adopted for the present experiments. The input u and output y are fed into the algorithms for spectral estimation and the PMM test. The spectral estimation algorithm computes the input and output auto- and cross-correlations, power spectral densities (PSDs), and P_{uy}/P_{uu}. The quantity P_{uy}/P_{uu} provides an estimate of the system Bode Plot and is termed the transfer function spectral estimate (TFSE) h. The PMM test yields the estimated system model order, m_o, which is the estimate of the number of states in the system as reflected by its input and output. The identification process that follows involves initializing a certain modal order n for the system based on the PMM result, curve fitting P_{uy}/P_{uu} by a transfer function of the assumed order, and evaluating the quality of the curved fitted model via output error analysis. This process is then repeated for the assumed modal order of $n + 1$. Output error analysis results of the curve fitted models are compared. If the performances are comparable, the adopted model will be the one with the modal order n. If not, the identification process is again repeated for assumed modal order of $n + 2$, after which the performances of the curve fitted models of assumed modal order $n + 1$ and $n + 2$ are compared. The process of incrementing assumed modal order and comparing output error performances is continued until the performances are comparable, in which case the curve fitted model with the smaller assumed order is adopted as the identified parametric model. Note that except for the PMM algorithm the system order is given in terms of the modal order which is the number of modes in the system. A system with a modal order n has a model order of $2 * n$ in state space representation.

Several details of the present procedures are noted:

1. The initial modal order estimate n assumed for the system could well be assigned as 1. The PMM algorithm is included here to facilitate a closer initial model (and hence, modal) order estimate and to enable saving of computational efforts. Based on the PMM model order estimate m_o, the system modal order estimate n is initialized in the procedures as $m_o/2$ or the next higher integer. Generation of the PMM model estimate m_o from experiment data is based on the 0.1% criterion which means using 0.1% of the first determinant as the threshold value. Determinant values lying below the threshold value are regarded as zeros. As was discussed in Section 2.7, this criterion is shown through simulation and experiment examples to have a tendency to underestimate the

order of the "best" model which minimizes the output error. More efficient methods for model order estimation remain to be investigated.

2. The curve fitting process is not straightforward by itself. As depicted in the figure, it involves initially performing curve fitting of the TFSE $h = P_{uy}/P_{uu}$ with smoothing factor $SF = 1.0$ which amounts to uniform weighting of the spectral data (W=I in eqn. (2.9-21)). This yields a first estimation of the system model of the assumed modal order. This first estimate, however, inevitably emphasizes high frequency modes as there are more data corresponding to high frequency modes than low frequency ones. It is therefore necessary to curve fit h again, this time with $SF = 0.9$. This utilizes a non-uniform weighting (W$\neq$I) emphasizing the low frequency data, computed based on the first estimate (see Steps 0 through 4 in Section 2.9.4). With SF remains at 0.9, this updated estimate forms the basis for generating yet another non-uniform weighting for the next curve fitting of h. The process is continued until finally the system model estimates converge. The converging estimate is then adopted as the curve fitted model of the assumed order. The present work does not specifically set a percentage margin for model estimate convergence though it can certainly do so without difficulties. From experiences, convergence to high accuracy is reached after performing six or seven curve fitting trials on h.

3. The output error analysis is carried out after the curve fitted model of the assumed model order is reached. It includes computation of the output $\hat{y}$ of the curve fitted model subjected to the same input u, the output error $e = y - \hat{y}$, and the additive uncertainty spectral estimate $\Delta = P_{ue}/P_{uu}$. Naturally, smaller values for P_{ue}/P_{uu} imply a better estimate of the system model. The adopted procedure takes the maximum gain of Δ as an indication of the performance or quality of the curve fitted model.

4. After completing the processes of curve fitting and output error analysis for the assumed modal orders of n and $n + 1$, the maximum gains of Δ are compared. If there is an appreciable improvement (i.e., reduction of maximum Δ gain) in the assumed modal order case, the process is conducted with an assumed modal order of $n + 2$ after which maximum values of Δ are compared for the assumed modal order of $n + 1$ and $n + 2$. If not, the curve fitted model corresponding to the smaller modal order will be taken as the identified parametric model, and its additive uncertainty spectral estimate Δ would give a frequency domain measure of its ability to approximate the actual system. The identified parametric model is thus the curve fitted model of the lowest assumed modal order that yields the best possible performance. To quantify, the present procedures considered an approximate 10% reduction as an appreciable improvement.

The adoption in the procedures of the 0.1% criterion for PMM model order estimation, a starting modal order estimate of $n = m_o/2$ or the next higher integer, smoothing factor $SF = 0.9$ for subsequent curve fitting, and the 10% margin for output error performance improvement were derived from trials. For the present experiment, they yielded reasonable results. Different values, however, can be adopted for other experiments. For example, if there is a concern about the PMM estimate of the model order a more or less conservative modal order of n may be initialized for the identification process. As a final note, it has
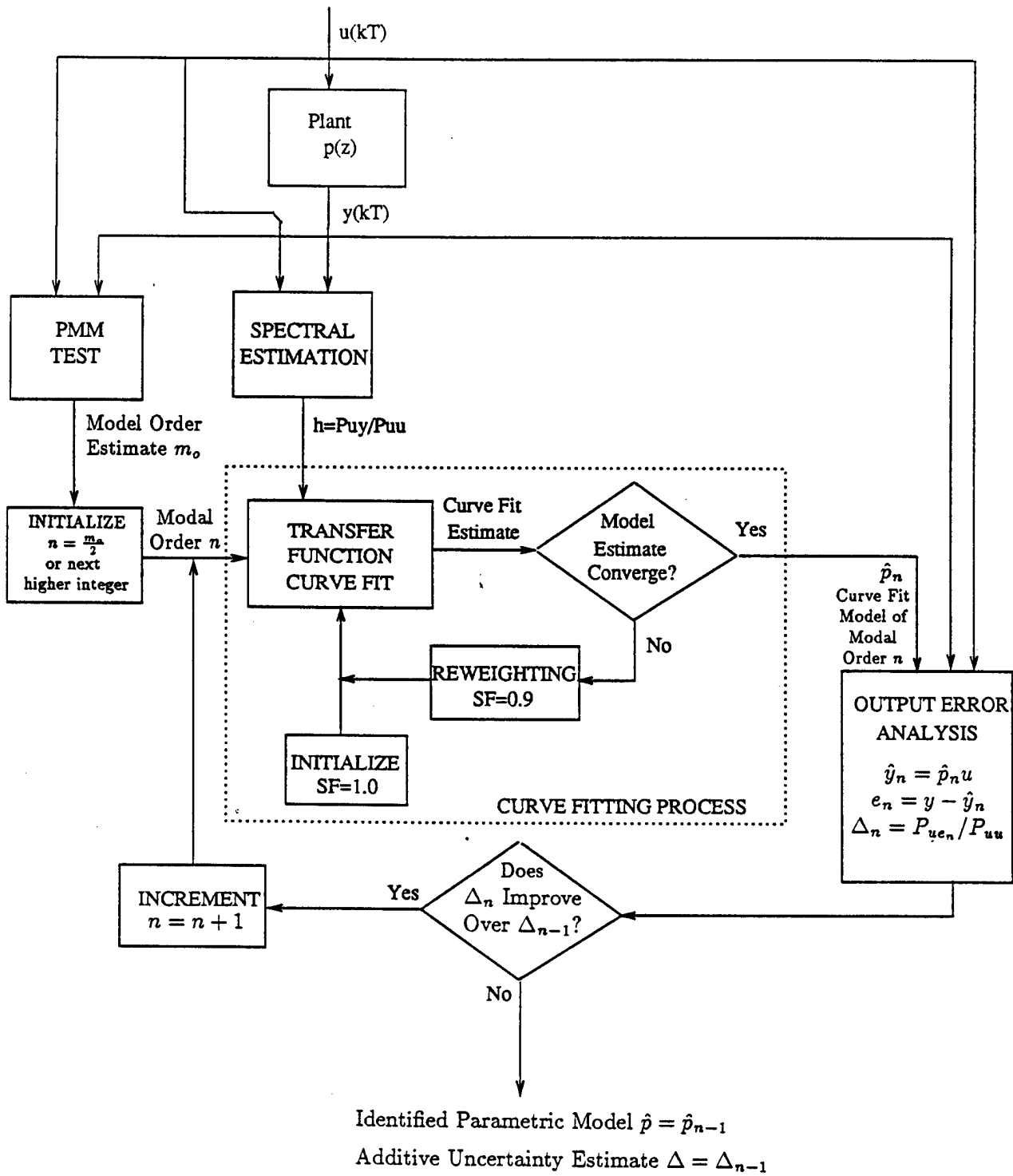
Fig. 3.2-1 The Automated Identification Procedures.

126

been observed that for the case where the assumed modal order is too large, the extra mode(s) in the curve fitted model would move under the shadow of a dominant mode, and for some values of SF this mode(s) may become unstable. The adopted value of $SF = 0.9$ yielded stable curve fitted models even when the assumed modal order is excessive.

3.2.2 Wideband Excitation (0-10 Hz)

Wideband excitation experiments utilize as inputs uniformly distributed random number sequences. Experiments were performed about the 1-7 axis and 4-10 axis of the structure utilizing their respective hub actuator and sensor. Experiments were also performed for the 4-10 axis using the hub actuator and levitator sensor. For all experiments described in this section, the sampling frequency was 20 Hz. The experiment time was 1638.4 sec, amounting to a data sequence of 32768 for u and y. The amplitude of the input was 1.5 nt-m, out of a full range of 2 nt-m.

3.2.2.1 The 1-7 Axis — Hub Actuator/Hub Sensor

This section presents the wideband excitation results of the 1-7 axis of the structure using the hub actuator HA10 and sensor HS1. The final result is an identified parametric model which is in fact a reduced order model for the 1-7 axis at the selected input/output points. As this section also serves to illustrate for the first time the automated identification procedures described in the previous section, presentation will be detailed.

The input and output data of the experiment are presented first. Figure 3.2-2 shows the time history of u for 200 sec. Figure 3.2-3 shows the time history of y for 200 sec, and figure 3.2-4 shows the same for 40 sec. The adopted parameters for spectral estimation were MSE=2048, NSE=32768, LSE=1024, and NFFT=2048. Physical interpretation of these parameters will be given in section 3.5.1. The autocorrelation and PSD of u, R_{uu} and P_{uu}, are shown in figures 3.2-5 and 3.2.6. The autocorrelation, R_{uu}, closely resembles a Δ-function. The PSD P_{uu} shows that u has uniform power density for all frequencies up to 10 hz, half of the sampling frequency. The whiteness of the input is thus verified. The PSD of the output, P_{yy}, is shown in figure 3.2-7. The PSD of the input/output cross-correlation, P_{uy}, is presented in figure 3.2-8. The gain and phase of the TFSE, $h = P_{uy}/P_{uu}$, is shown in figure 3.2-9. These figures all indicate the existence of five modes with approximate frequencies 0.1 Hz, 0.6 Hz, 1.7 Hz, 2.6 Hz, and 5 Hz. For convenience, they will from now on be designated as the 1st, 2nd, 3rd, 4th, and 5th modes of the system. Among them, the 2nd mode is the most dominant, followed by the 1st and 4th mode.

Figure 3.2-10 shows the PMM test results generated with the PMMDE algorithm which takes into account the presence of sensor noise through the construction of a noise file. In this experiment where the analog filters are in place, the noise level is minimal. A representative time history of the noise in the hub sensor HS1 is given in figure 3.2-11. Another way of approximating the effect of the noise through the use of a diagonal noise matrix is also possible with the algorithm PMMD, in which case an assumed parameter SIGPMM is used to model the strength of the noise. As the noise is small in the present setup, PMMDE results match closely to that of PMMD with SIGPMM=0. Detail descriptions of these PMM algorithms can be found in section 2.7. The PMM test of figure 3.2-10 indicates an estimated model order of $m_o = 4$ according to the 0.1% criterion.

127
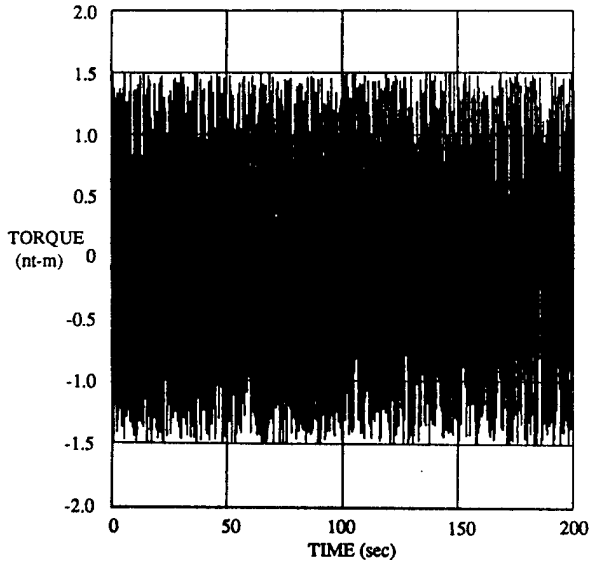
Fig. 3.2-2 Wideband Excitation Input u.
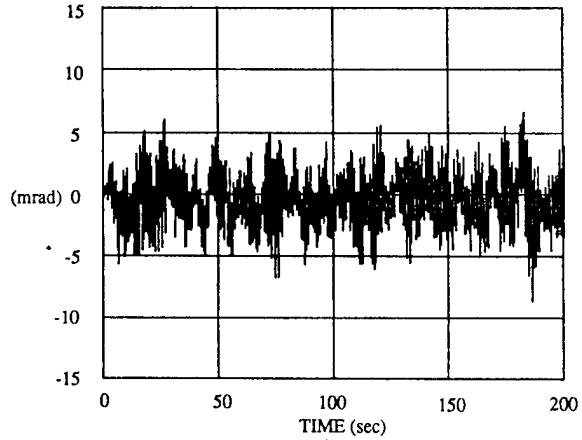
Fig. 3.2-3 Output Response y at Hub Sensor HS1 for the 1-7 Axis Hub Actuator/Hub Sensor Wideband Excitation Case.
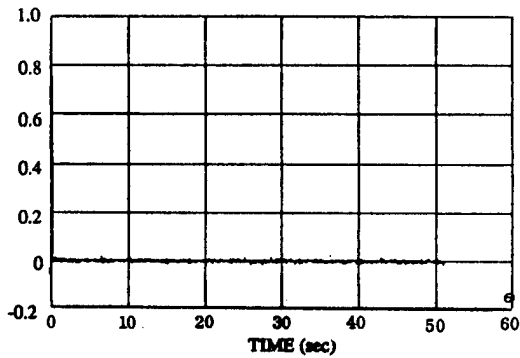
Fig. 3.2-5 Auto-Correlation R_{uu} for the 1-7 Axis Hub Actuator/Hub Sensor Wideband Excitation Case.
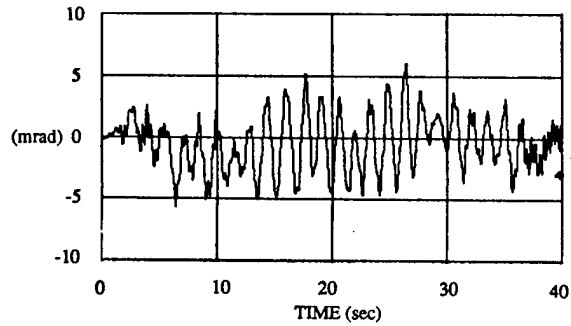
Fig. 3.2-4 Expanded view of Output Response y at Hub Sensor HS1 for the 1-7 Axis Hub Actuator/Hub Sensor Wideband Excitation Case.
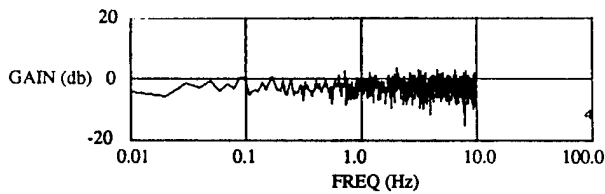
Fig. 3.2-6 Power Spectral Density P_{uu} for the 1-7 Axis Hub Actuator/Hub Sensor Wideband Excitation Case.
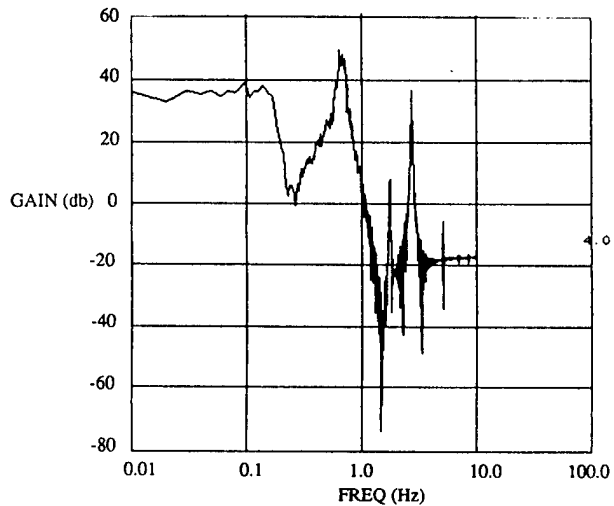
Fig. 3.2-7 Power Spectral Density P_{yy} for the 1-7 Axis Hub Actuator/Hub Sensor Wideband Excitation Case.

128
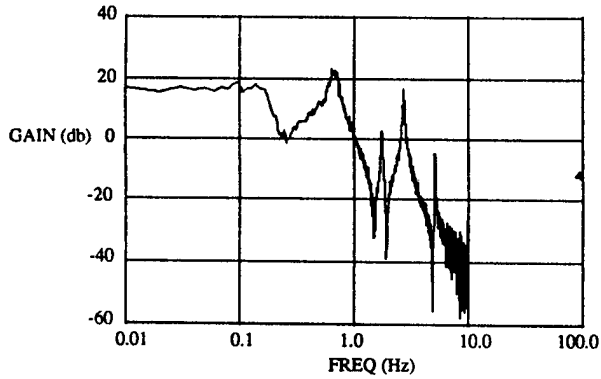
Fig. 3.2-8 Cross Spectral Density P_{uy} for the 1-7 Axis Hub Actuator/Hub Sensor Wideband Excitation Case.
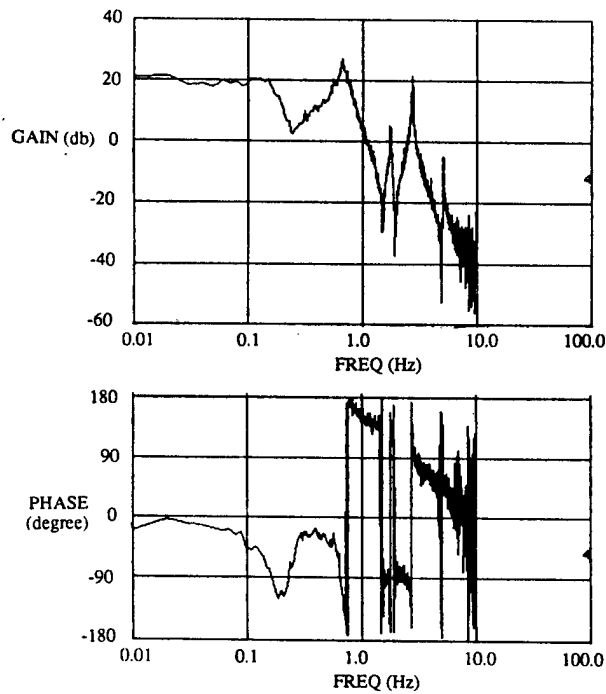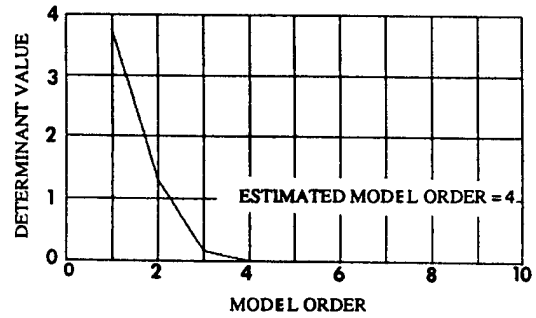
Fig. 3.2-10 PMM TEST Determinant Plot for the 1-7 Axis Hub Actuator/Hub Sensor Wideband Excitation Case.
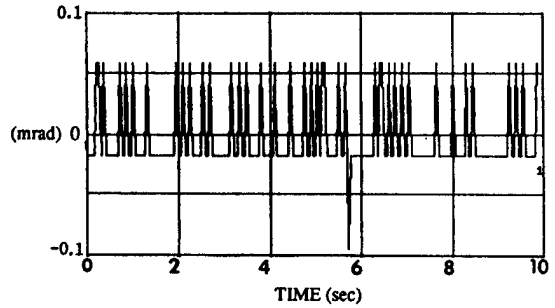
Fig. 3.2-11 Sensor Noise of Hub Sensor HS1.

Fig. 3.2-9 Bode Plot of Transfer Function Spectral Estimate $h = P_{uy}/P_{uu}$ for the 1-7 Axis Hub Actuator/Hub Sensor Wideband Excitation Case.

129

Following the automated identification procedures, a curve fitted model of assumed modal order $n = m_o/2$ and its corresponding output error are to be generated first. The curve fitting process is presented in figure 3.2-12. It shows the sequence of curve fitting computations until convergence of the estimates. The gains of the estimate transfer functions are shown on the left column and their modal data of frequency and damping coefficients on the right. The first estimate in figure 3.2-12 was generated with $SF = 1.0$. All others were generated with $SF = 0.9$. The full range of h was used for curve fitting as this was a wideband experiment. The process was terminated when the frequency and damping values converged to reasonably high accuracy. The convergent estimate constitutes the curve fitted model for the assumed modal order of 2.

The curve fitted model is shown in more detail in figure 3.2-13. It yields two modes of frequencies 0.658 Hz and 2.67 Hz, and damping coefficients 0.062 and 0.00858. They correspond to the 2nd and 4th mode of the system. The other modes were not fitted. Figure 3.2-14 shows the output error $e = y - \widehat{y}$ where $\widehat{y}$ is the output of the curve fitted model of figure 3.2-13 subjected to the same input u of figure 3.2-2. The error e clearly indicates the presence of the 1st mode which is the most dominant of the unfitted modes. Figure 3.2-15 shows the additive uncertainty $\Delta = P_{ue}/P_{uu}$. At the identified modal frequency of 0.658 Hz and 2.67 Hz, the values of Δ are roughly 20 db down from that of h in figure 3.2-9. The dynamics of the actual system at those frequencies are being modelled to roughly 10% by the curve fitted model. Since the 1st mode was not fitted, the additive uncertainty Δ is just about the same as h at around 0.1 Hz. As a result, the maximum value 19.7 db of Δ occurs at this frequency. The overall characterization of the output error for the curve fitted model of assumed modal order 2 is therefore 19.7 DB.

Next in the identification process is the curve fitting of a model of assumed modal order 3. Figure 3.2-16 shows the sequence of curve fitting computations until convergence of the model estimates. Again, the first computation used even weighting ($SF = 1$) over the full range (0-10 Hz). Subsequent computations used $SF = 0.9$ and emphasized the low frequency portion of the spectrum. Convergence occurs after six computations and agreement was within 0.1%. It is interesting to note that the 1st mode of 0.126 Hz gradually came in as the third curve fitted mode during later computations. Figure 3.2-17 shows the converged curve fitted model and modal data. The identified modes are of frequencies 0.126 Hz, 0.666 Hz, and 2.68 Hz, and of damping coefficients 0.32, 0.0564, and 0.00746. Figure 3.2-18 shows the computed output $\widehat{y}$ of the curve fitted model subjected to actual input u. The computed output $\widehat{y}$ is in good agreement to the actual output y of figure 3.2-3. Their difference, $e = y - \widehat{y}$, is shown in figure 3.2-19. Improvement of figure 3.2-19 over figure 3.2-14 is obvious as e now has a smaller error component of the 1st mode, resulting in smaller error amplitude. The power spectral density of e, P_{ee}, is shown in figure 3.2-20. Its values at the identified modal frequencies are more than 20 db smaller than that of P_{yy}. Figure 3.2-21 shows the additive uncertainty $\Delta = P_{ue}/P_{uu}$ for this case. It is well to point out that both figures 3.2-20 and 3.2.21 show that error values due to the unfitted 3rd and 5th modes are small relative to that of the fitted modes. The overall modelling error is actually dominated by that of the fitted modes. Figure 3.2-21 also shows that as the 1st mode was being fitted, appreciable reduction of Δ values at around 0.1 Hz occurs. The maximum value for Δ is 11.7 db for this case.
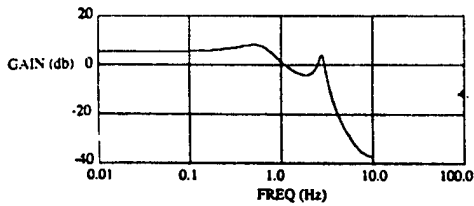
FREQUENCY (Hz) DAMPING COEFFICIENT

2.77261266156980 6.3046012638226798E-002
0.544297524656172 0.498984177906475
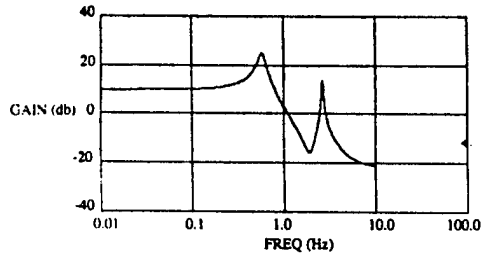
FREQUENCY (Hz) DAMPING COEFFICIENT

2.61839204924477 1.618360912108759E-002
0.576783748717076 8.539393877961064E-002
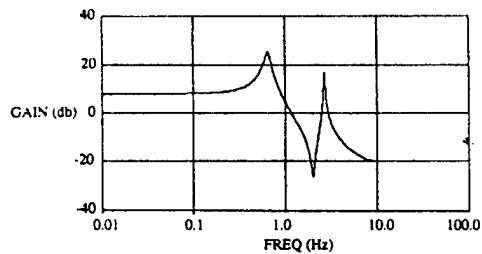
FREQUENCY (Hz) DAMPING COEFFICIENT

2.65447548506786 1.207177116297930E-002
0.646572757735625 6.452945554951449E-002

FREQUENCY (Hz) DAMPING COEFFICIENT
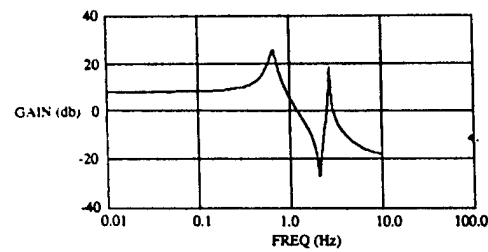
2.66932971561153 9.399741757787631E-003
0.657328032548153 6.238109589887664E-002

FREQUENCY (Hz) DAMPING COEFFICIENT
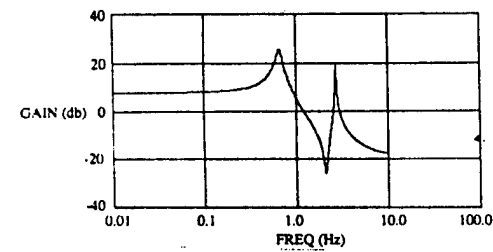
2.67286715616988 8.721196104445417E-003
0.658164134873697 6.209696553163501E-002
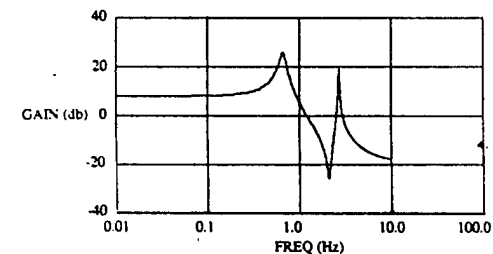
FREQUENCY (Hz) DAMPING COEFFICIENT

2.67357372387997 8.581899063477488E-003
0.658223313716739 6.206129006158552E-002

Fig. 3.2-12 Curve Fit Computation Sequence of Assumed Modal Order 2 for the 1-7 Axis Hub Actuator/Hub Sensor Wideband Excitation Case.

131
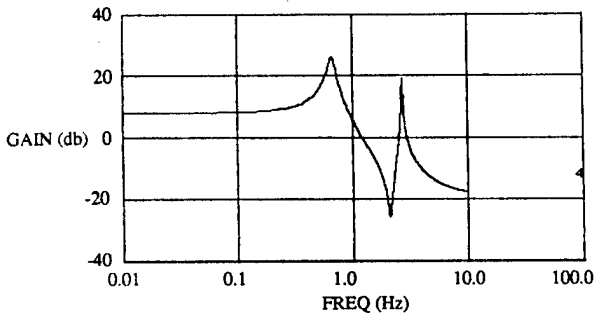
| FREQUENCY (Hz)	DAMPING COEFFICIENT
2.67357372387997	8.581899063477488E-003
0.658223313716739	6.206129006158552E-002
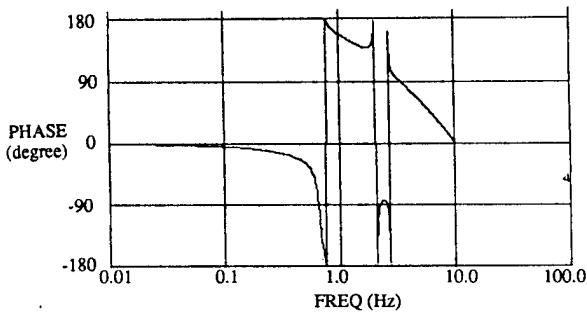
NUMERATOR COEFFICIENT	DENOMINATOR COEFFICIENT
0.312020163531875	0.960709423525656
-0.663882539984430	-3.19663009282870
0.592590948272135	4.52167744297748
-0.183373428311394	-3.26787606861032
1.177304334795010E-002	1.00000000000000

Fig. 3.2-13 Curve Fitted Model of Assumed Modal Order 2 for the 1-7 Axis Hub Actuator/Hub Sensor Wideband Excitation Case.
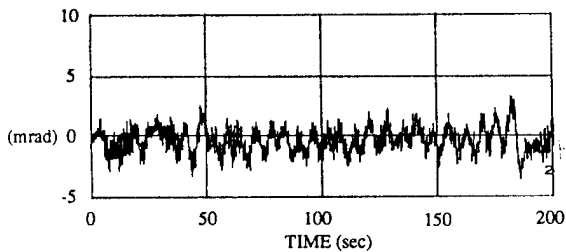
Fig. 3.2-14 Output Error e of the Curve Fitted Model of Modal Order 2 for the 1-7 Axis Hub Actuator/Hub Sensor Wideband Excitation Case.
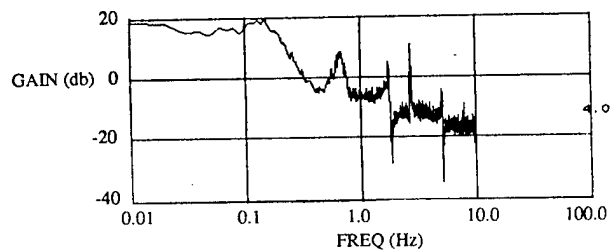

Fig. 3.2-15 Additive Uncertainty $\Delta = P_{u\epsilon}/P_{uu}$ of the Curve Fitted Model of Modal Order 2 for the 1-7 Axis Hub Actuator/Hub Sensor Wideband Excitation Case.

132
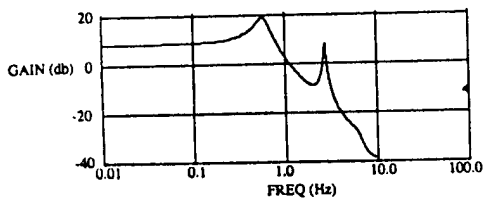
FREQUENCY (Hz)	DAMPING COEFFICIENT
6.09273148886673	0.230345283476510
2.70231638944101	2.124657733586369E-002
0.573309816710884	0.150249546786903
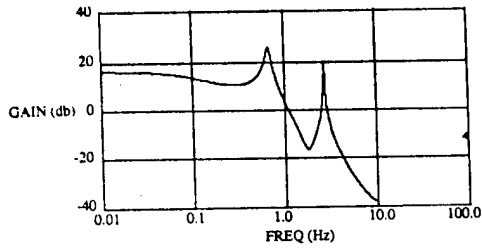
FREQUENCY (Hz)	DAMPING COEFFICIENT
2.68455566147251	7.336731109033750E-003
1.591549430918954E-031	5.573001269356036E+029
0.669624939276309	5.293868778443579E-002
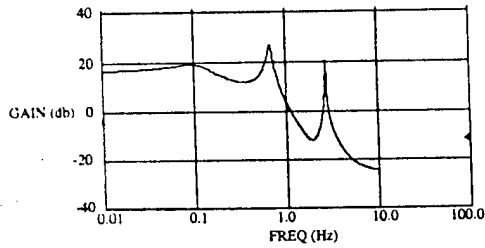
FREQUENCY (Hz)	DAMPING COEFFICIENT
2.68374112431432	6.970855409447972E-003
0.673297583562017	4.840727225347798E-002
8.786731359565073E-002	0.683650226421350
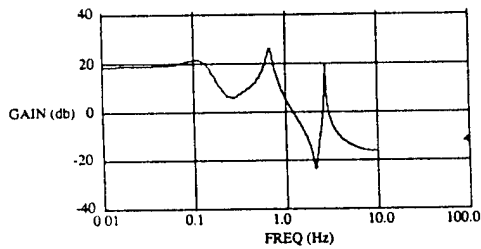
FREQUENCY (Hz)	DAMPING COEFFICIENT
2.67977818191846	7.383879223568065E-003
0.666673673023243	5.576513737790320E-002
0.120506206172285	0.343510981811264
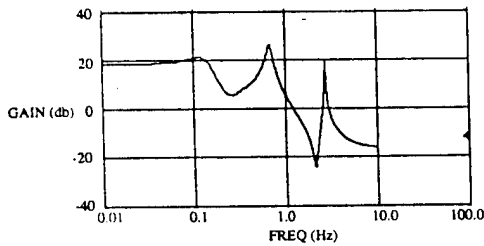
FREQUENCY (Hz)	DAMPING COEFFICIENT
2.67949932476461	7.451970668916287E-003
0.665875280963602	5.631088443539669E-002
0.125560808644870	0.325992694683059
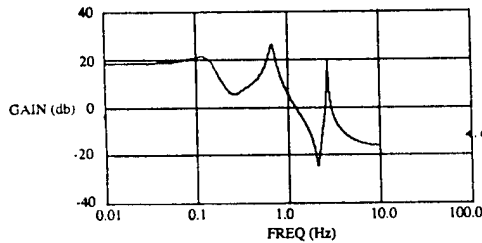
FREQUENCY (Hz)	DAMPING COEFFICIENT
2.67948325976869	7.455106884985409E-003
0.665841662834349	5.637050655021455E-002
0.126133832248622	0.321990607752176
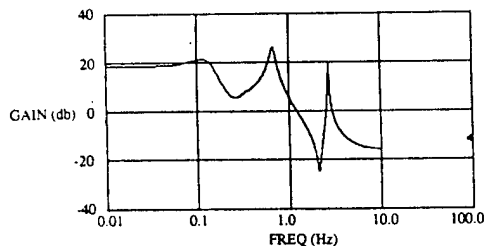
FREQUENCY (Hz)	DAMPING COEFFICIENT
2.67947979531002	7.455688479968888E-003
0.665833758767297	5.638073958690457E-002
0.126221370924959	0.321593752253260

Fig. 3.2-16 Curve Fit Computation Sequence of Assumed Modal Order 3 for the 1-7 Axis Hub Actuator/Hub Sensor Wideband Excitation Case.

133
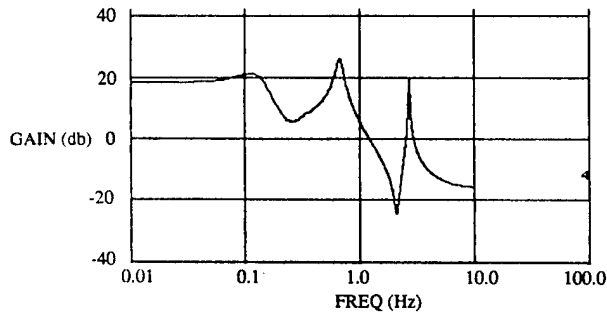
FREQUENCY (Hz)	DAMPING COEFFICIENT
2.67947979531002	7.455688479968888E-003
0.665833758767297	5.638073958690457E-002
0.126221370924959	0.321593752253260
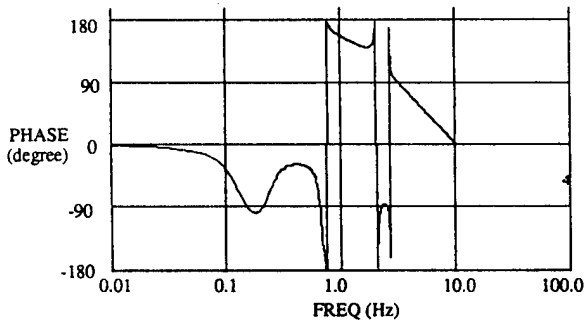
NUMERATOR COEFFICIENT	DENOMINATOR COEFFICIENT
0.320966042381471	0.940217486158167
-1.36548397182586	-5.02484609753407
2.47189012820007	11.6932837265819
-2.40972743286449	-15.3041033197454
1.30449312904019	11.9260009762582
-0.366718798654619	-5.23050364369577
4.498048323998861E-002	1.00000000000000

Fig. 3.2-17 Curve Fitted Model of Assumed Modal Order 3 for the 1-7 Axis Hub Actuator/Hub Sensor Wideband Excitation Case.
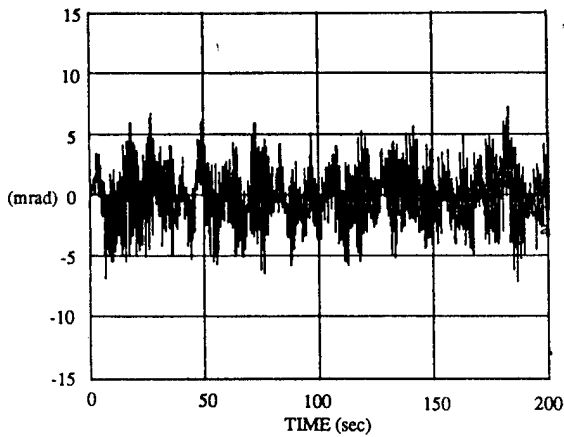
Fig. 3.2-18 Computed Response $\hat{y}$ of the Curve Fitted Model of Modal Order 3 Subjected to Actual Input u for the 1-7 Axis Hub Actuator/Hub Sensor Wideband Excitation Case.

Fig. 3.2-19 Output Error $e = y - \hat{y}$ of the Curve Fitted Model of Modal Order 3 for the 1-7 Axis Hub Actuator/Hub Sensor Wideband Excitation Case.
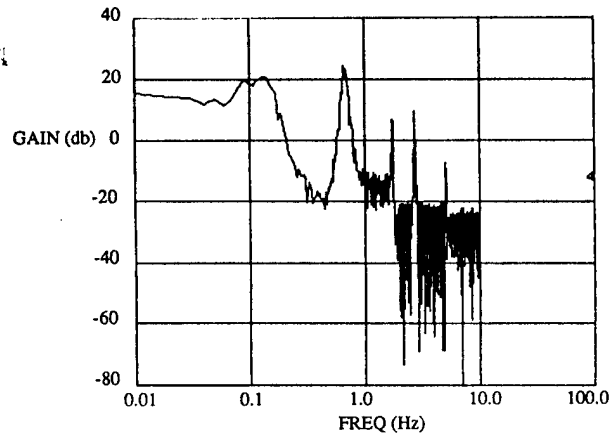
Fig. 3.2-20 Output Error Power Spectral Density P_{ee} of the Curve Fitted Model of Modal Order 3 for the 1-7 Axis Hub Actuator/Hub Sensor Wideband Excitation Case.
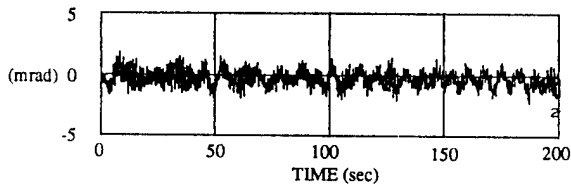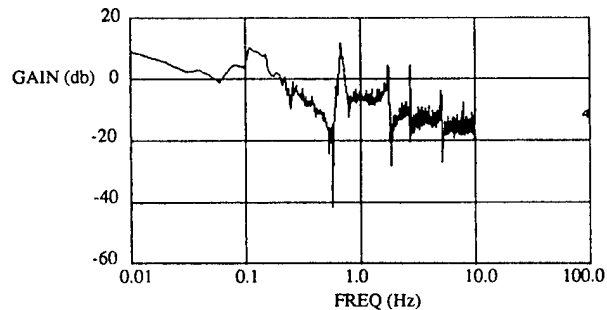
Fig. 3.2.21 Additive Uncertainty $\Delta = P_{ue}/P_{uu}$ of the Curve Fitted Model of Modal Order 3 for the 1-7 Axis Hub Actuator/Hub Sensor Wideband Excitation Case.

134

The curve fitted model of 3 modes represents an appreciable improvement over that of 2 modes. Accordingly, curve fitting is to be performed for the assumed modal order of 4. Figure 3.2-22 shows the sequence of computations until convergence of the model estimates assuming a system modal order of 4. As for the case of curve fitting 3 modes, the 1st mode emerges gradually in later computations. The additional curve fitted mode briefly modelled the 5th mode in the first few computations and then drifted to the low end of the spectrum. The convergent curve fitting model is shown in figure 3.2-23. The additional curve fitted mode appears as a spike near the peak of the 2nd mode. The output error $e = y - \hat{y}$ and the additive uncertainty Δ are shown in figure 3.2-24 and 3.2.25. As compared to figure 3.2-19, the output error e here shows an component around 0.7 Hz which resulted from the additional curve fitted mode. Similarly, the additive uncertainty shows that the additional curve fitted mode causes increased error around that frequency, and results in a maximum value of roughly 20 db for Δ. As such, the curve fitted model of assumed modal order of 4 did not show appreciable improvement over that of 3. The automated identification procedures thus adopted the curve fitted model of assumed modal order of 3 as the identified parametric model for the system.

It may appear puzzling that the automated procedures manage to yield an identified parametric model of only 3 modes while 5 modes were apparent from the transfer function spectral estimate. To make sense out of this, notice that most of the modelling errors as reflected by P_{ee} and Δ are due mainly to the low frequency modes. For the case of curve fitting 3 modes, the peak values of Δ corresponding to the 1st and 2nd modes are both around 11 db, while that for the two unfitted modes are approximately 5 and -5 db. This explains why, in the event of curve fitting 4 modes, the additional curve fitted mode gradually moves to the low end of the spectrum: the algorithm is attempting to achieve a better fit of the low frequency modes. The algorithm will not attempt to curve fit the previously unfitted modes as doing so does not effectively improve the fitting performance. In this sense, the identified parametric model constitutes a "reduced-order" model of the system determined according to the curve fitting accuracy of the algorithms.

3.2.2.2 The 4-10 Axis — Hub Actuator/Hub sensor

This section presents the wideband excitation experiments about the 4-10 axis. The corresponding hub torquer HA1 and hub angular sensor HS10 were used for instrumentation. The automated identification procedures as depicted in figure 3.2-1 were applied. Only the most pertinent results are presented here as the identification process was detailed and demonstrated. In section 1.3.7, the finite element model yielded slightly different frequencies for the 1-7 and 4-10 axis because of the non-symmetry of the hub. This is to be studied here via comparing experiment results for the axes.

For better comparison with previous results, the experiment utilized as wideband excitation input the same u as for the 1-7 axis depicted in figure 3.2-2. The response y is shown in figure 3.2-26 and 3.2.27 for the time spans of 200 sec and 40 sec, respectively. It exhibits an appreciable difference in excursion amplitude compared to that of figure 3.2-3 and 3.2.4. Slight differences in frequencies and phases are also noticed. More detail is observed through frequency domain analysis. The power spectral density of y, P_{yy}, is shown in figure 3.2-28. It shows general similarity with that of the 1-7 axis except that the

FREQUENCY (Hz)   DAMPING COEFFICIENT
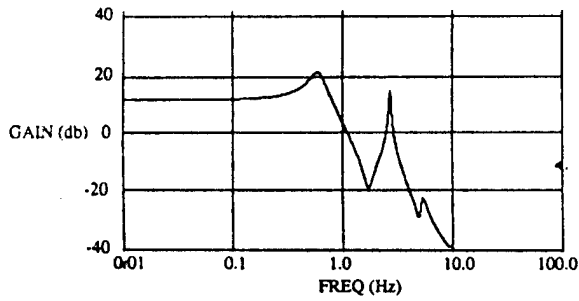
FREQUENCY (Hz)	DAMPING COEFFICIENT
5.23199388717009	5.121825772798859E-002
1.591549430918954E-031	1.192421384596419E+031
2.68384837823232	1.441252388330066E-002
0.602809317719666	0.141949435520156
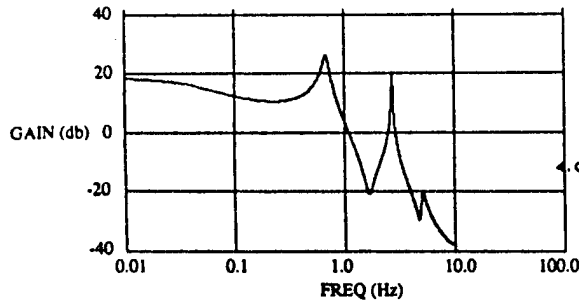
FREQUENCY (Hz)	DAMPING COEFFICIENT
5.04668970079038	3.587594581114825E-002
2.68458643858335	7.578245368033839E-003
0.671880931806730	5.628051916202454E-002
1.591549430918954E-031	0.000000000000000E+000
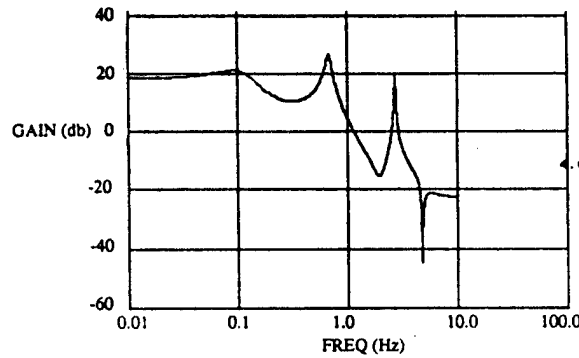
FREQUENCY (Hz)	DAMPING COEFFICIENT
4.62571216138996	7.683595664729868E-002
2.68279218848472	7.210596651427745E-003
0.671305413296539	5.018773928276232E-002
9.749527655753007E-002	0.461473412053191
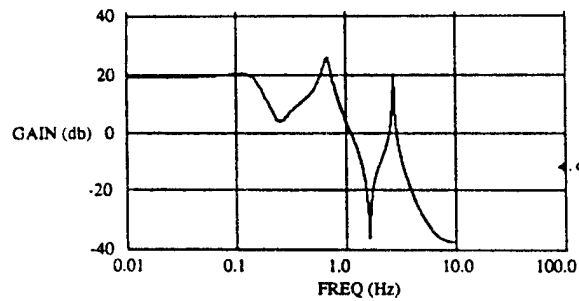
FREQUENCY (Hz)	DAMPING COEFFICIENT
1.08392505708326	1.63316193826968
2.68539916950740	7.689569377247765E-003
0.669816596969127	6.266209452729296E-002
0.134345679861717	0.399926240247065
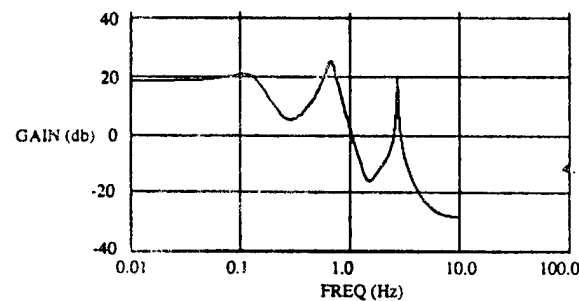
FREQUENCY (Hz)	DAMPING COEFFICIENT
2.68493031906658	7.252493083880330E-003
0.664880605199422	0.378664510239611
0.667276374992109	8.379202563686924E-002
0.117324196277108	0.397237547430677

Fig. 3.2-22 Curve Fit Computation Sequence of Assumed Modal Order 4 for the 1-7 Axis Hub Actuator/Hub Sensor Wideband Excitation Case.

136
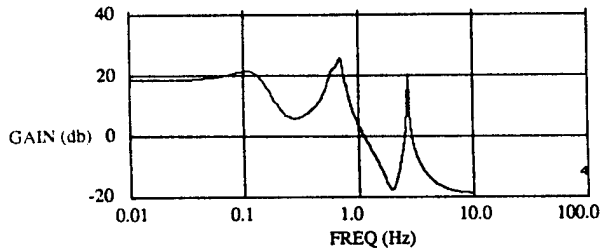
FREQUENCY (Hz)	DAMPING COEFFICIENT
2.68224206259022	7.108778602775563E-003
0.691915236571891	5.389418326664784E-002
0.582845229360586	8.610220247370114E-002
0.118738489443827	0.349062604837694
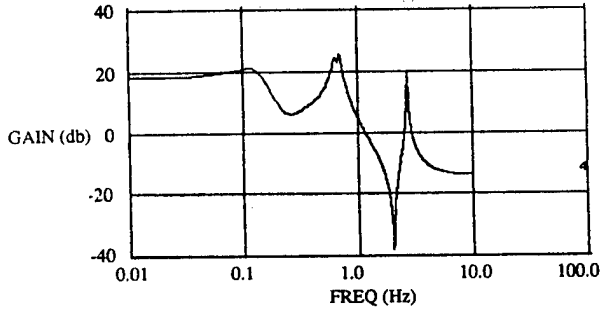
FREQUENCY (Hz)	DAMPING COEFFICIENT
2.67913008236319	7.543119371811425E-003
0.691262316305582	3.350324065298275E-002
0.635876414062383	4.281088965012490E-002
0.123672342574965	0.327669532772886
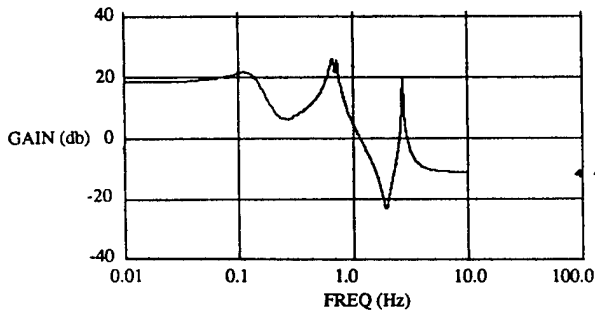
FREQUENCY (Hz)	DAMPING COEFFICIENT
2.67655823180426	8.115211291375983E-003
0.656466837071705	4.798142304462239E-002
0.708809387151656	1.646800979048205E-002
0.123997486906250	0.311175604085290
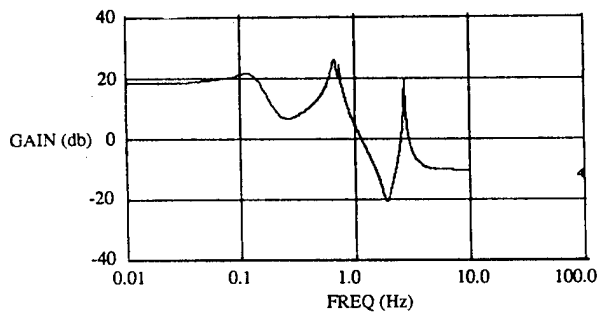
FREQUENCY (Hz)	DAMPING COEFFICIENT
2.67543208605083	8.407124489999427E-003
0.660169763452212	5.067081901374012E-002
0.723227592424732	1.156125776942770E-002
0.123990037807602	0.309313299238841

Fig. 3.2-22 Curve Fit Computation Sequence of Assumed Modal Order 4 for the 1-7 Axis Hub Actuator/Hub Sensor Wideband Excitation Case (Continued).
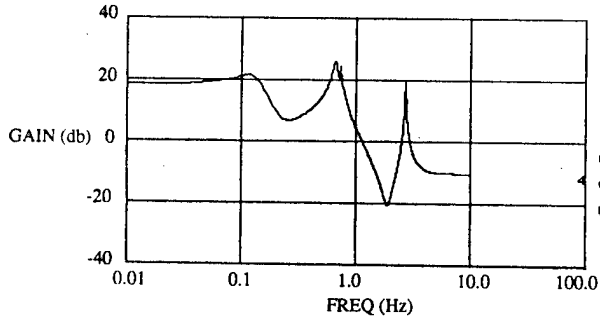
137

FREQUENCY (Hz)	DAMPING COEFFICIENT
2.67543208605083	8.407124489999427E-003
0.660169763452212	5.067081901374012E-002
0.723227592424732	1.156125776942770E-002
0.123990037807602	0.309313299238841
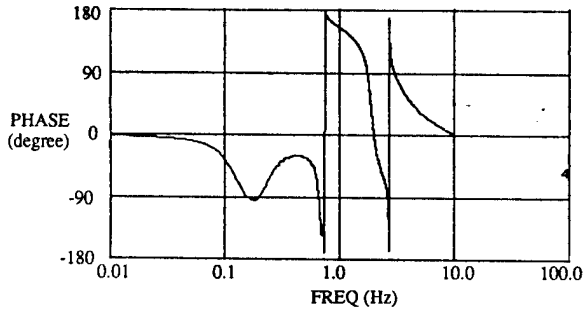
NUMERATOR COEFFICIENT	DENOMINATOR COEFFICIENT
0.456809175894412	0.937534768389485
-2.99070932786709	-6.84200767260182
8.74239587730392	22.3900734843272
-14.9464937736064	-43.0712885664923
16.3993665838491	53.4114623349233
-11.8739985019578	-43.7640375290563
5.57274674583309	23.1177488845066
-1.56243700381428	-7.17948333638930
0.202339519404172	1.00000000000000

Fig. 3.2-23 Curve Fitted Model of Assumed Modal Order 4 for the 1-7 Axis Hub Actuator/Hub Sensor Wideband Excitation Case.
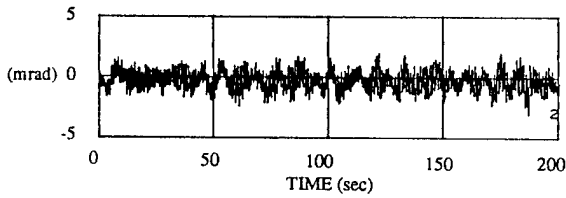
Fig. 3.2-24 Output Error $e = y - \hat{y}$ of the Curve Fitted Model of Modal Order 4 for the 1-7 Axis Hub Actuator/Hub Sensor Wideband Excitation Case.
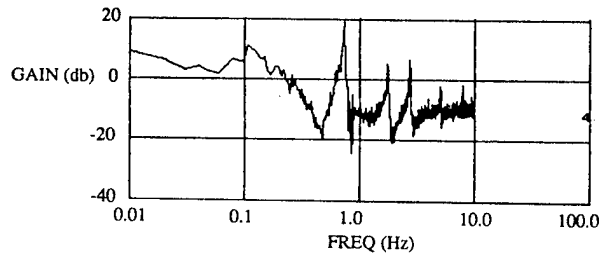
Fig. 3.2.25 Additive Uncertainty $\Delta = P_{ue}/P_{uu}$ of the Curve Fitted Model of Modal Order 4 for the 1-7 Axis Hub Actuator/Hub Sensor Wideband Excitation Case.

138

resonance peak corresponding to the 2nd mode now sits at roughly 40 db as compared to 35 db before. Peak values for other modes are approximately the same. Higher excursion amplitude exhibited here is thus due mainly to the larger component of the dominant 2nd mode. This could not have been caused by a scaling difference in the hub actuators. The gain and phase of the transfer function spectral estimate $h = P_{uy}/P_{uu}$ are presented in figure 3.2-29. Again, it is similar to that of figure 3.2-9 except that the 2nd mode exhibits a slightly higher peak.

Figure 3.2-30 plots the PMM determinant values as a function of the model order. The PMM test result is quite similar to that of the 1-7 axis. It is obtained using the algorithm PMMDE. A representative time history of the noise as observed at the hub sensor HS10 is shown in figure 3.2-31. Same as for the 1-7 axis, the PMM test yields a model order estimate of 4 for this axis with the 0.1% criterion.

The automated identification procedures were applied as before with similar results: curve fitting and output error analysis were performed for the assumed modal orders of 2, 3, and 4. Output error analysis results were compared. As no appreciable improvement in modelling performance was observed for the cases of curve fitting 3 and 4 modes, the curve fitted model of 3 modes was adopted as the identified parametric model. In the following, only the pertinent 3 mode curve fitting result is presented.

Figure 3.2-32 shows the sequence of curve fitting computations performed on the TFSE h. Again, the first computation used $SF = 1.0$ for equal weighting. Subsequent computations used $SF = 0.9$, and implicitly emphasized lower frequency spectral data. At convergence, the modal parameters varied by less than 0.3%. Figure 3.2-33 shows the gain and phase of the curve fitted model and modal data. The identified frequencies and damping coefficients are 0.114 Hz, 0.637 Hz, and 2.57 Hz, and 0.4, 0.0364, and 0.00604, respectively. These values confirm the slight nonsymmetry of the two axes. The 1st mode differs by 10% in frequency value and is 25% more damped here than the other axis. The 2nd mode modal frequency differs by 5% but is 40% less damped here. This accounts for the higher P_{yy} peak and hence stronger response of the mode, constituting the major difference in dynamics response of the two axis. The 3rd mode differs in frequency by 4% and is 20% less damped than the other axis. Table 3.2.1 tabulates the modal frequency values of the 1st, 2nd, and 4th modes for the two axes as determined from finite element modelling method and experiment results. The two sets of results agree exceptionally well for the 4th mode and resonably well for the others. In general, the experimental results confirm that the 4-10 axis have smaller frequency values than the 1-7 axis.

Figure 3.2-34 shows the computed output $\hat{y}$ of the identified parametric mode subjected to the actual input u. The error $e = y - \hat{y}$ is shown in figure 3.2-35. It has comparable amplitude as that for the 1-7 axis even though the output y here has a larger excursion amplitude. The power spectral density of e, P_{ee}, is given in figure 3.2-36. Compared with P_{yy}, it shows a 20 db drop of power in the 1st modal component and a 30 db drop in the 2nd and 4th modal components. This indicates that the dominant modal dynamics of the system are being well approximated. The modelling performance here is roughly the same as that of the 1-7 axis. The additive uncertainty $\Delta = P_{ue}/P_{uu}$ is shown in figure 3.2-37. The maximum gain value, which is adopted as the overall characterization of the

139

modelling performance, is 11.38 db, nearly the same as the 1-7 axis. Again, the 3rd and 5th modes, apparent in figure 3.2-29, are not fitted here. The PSD P_{ee} and additive uncertainty P_{ue}/P_{uu} both show that modelling error resulted from these unfitted modes are small compared to that from curve fitting the 1st and 2nd modes. As such, curve fitting assuming a modal order of 4 results in the additional curve fitted mode gradually drifting to low frequency spectrum for better fitting in that region. Such observations are the same as the 1-7 axis.

As a conclusion, the identification results for the two axes agree reasonably with finite element predictions. Experimental results for the two axis agreed to within 4 - 10% for modal frequency values. Compared to the 1-7 axis, the damping coefficient for the 1st mode of the 4-10 axis is 20% more damped, and those for the 2nd and 4th mode are respectively 20% to 25% less damped. A stronger response in the 2nd mode dynamics is therefore effected for the 4-10 axis. These differences characterized the slight non-symmetry of the two axes.

3.2.2.3 The 4-10 Axis — Hub Actuator/Levitator Sensor

The experiment of the previous section is repeated except that instead of using the hub angular sensor data, observations from the outer levitator sensor on rib#1, LO1, were examined. The previous section served to characterize the testbed structure via observing at the hub position of the orthogonal axis. This section tends to characterize the structure via observing at the hub and the outer rib levitator position for the same axis. Again, as the identification procedure has been discussed, only the most relevant identification results are shown here.

The input of this experiment is the same as that of the previous section which is as shown in figure 3.2-2. Figure 3.2-38 and 3.2.39 show the time histories of the levitator output y for 200 sec and 40 sec. They clearly lack the higher frequency components as compared to the hub sensor data in figure 3.2-26 and 3.2.27. This is further illustrated in figure 3.2-40 which shows the PSD of y and Figure 3.2-41 which shows the gain and phase of the TFSE P_{uy}/P_{uu}. Unlike the hub observations, the 1st mode is now the most dominant, followed by the 2nd mode. The higher frequency modes are greatly diminished. The fact that levitator sensors are not effective in observing higher frequency modes is expected. As a result of the levitator counterweights, nodal points of structural modes tend to be located close to the levitating positions, making the levitator sensors less effective, especially in observing high frequency modes. The PMM test results are shown in figure 3.2-42. As there is zero noise observed for the sensor, the results were generated using the algorithm PMMD with SIGPMM=0.0. The PMM test results indicate an approximate model order of 3 with the 0.1% criterion.

The automated procedure thus calls for curve fitting with an initial model order of 2, and then 3, and so on. No improvement in modelling performance was observed for the curve fit models of assumed modal orders 2 and 3. The curve fitted model of 2 modes was thus adopted as the identified parametric model for this case. Such results are no surprise as P_{uy}/P_{uu} in figure 3.2-41 shows that the 1st and 2nd modes are appreciably

140
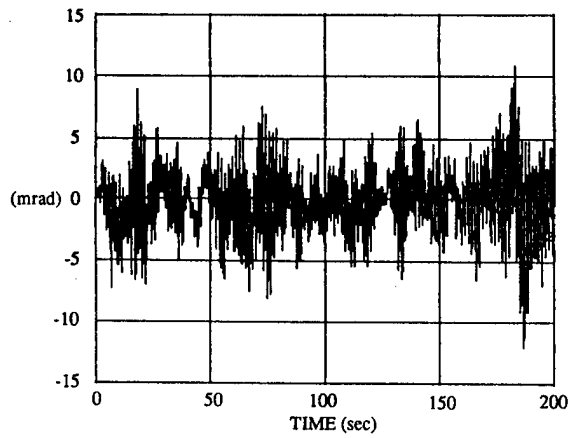
Fig. 3.2-26 Output Response y at Hub Sensor HS10 for the 4-10 Axis Hub Actuator/Hub Sensor Wideband Excitation Case.
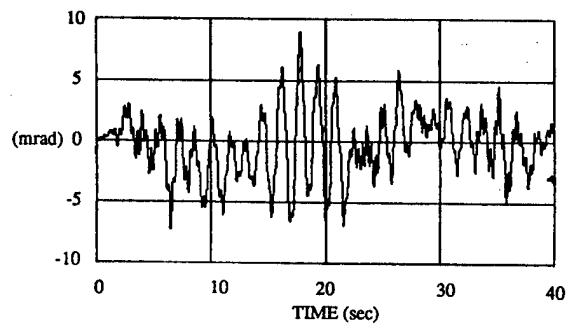
Fig. 3.2-27 Expanded view of Output Response y at Hub Sensor HS10 for the 4-10 Axis Hub Actuator/Hub Sensor Wideband Excitation Case.
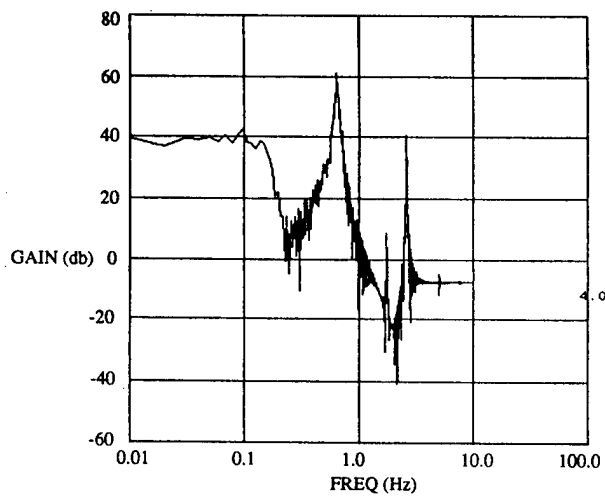

Fig. 3.2-28 Power Spectral Density P_{yy} for the 4-10 Axis Hub Actuator/Hub Sensor Wideband Excitation Case.

141
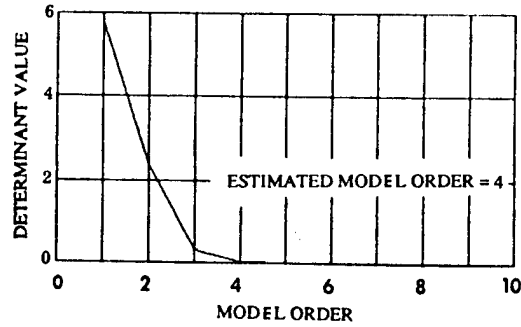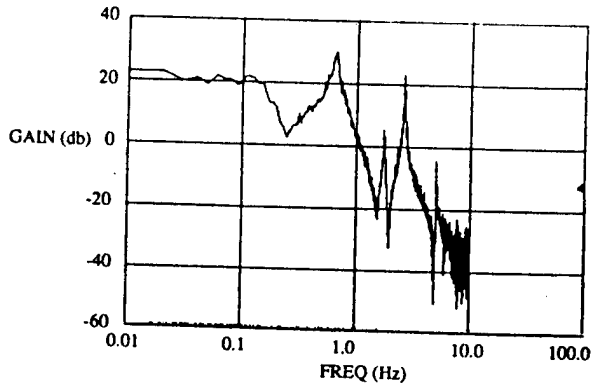
Fig. 3.2-30 PMM TEST Determinant Plot for the 4-10
Axis Hub Actuator/Hub Sensor Wideband
Excitation Case.
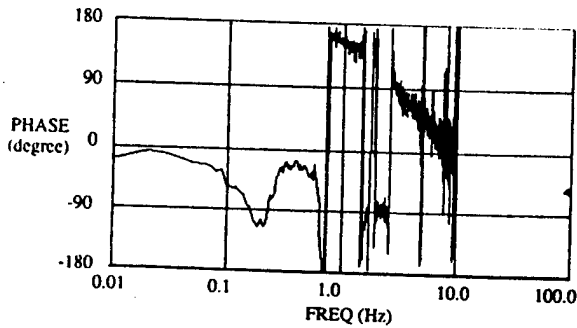
Fig. 3.2-29 Bode Plot of Transfer Function Spectral Estimate $h = P_{uy}/P_{uu}$ for the 4-10 Axis Hub
Actuator/Hub Sensor Wideband Excitation
Case.
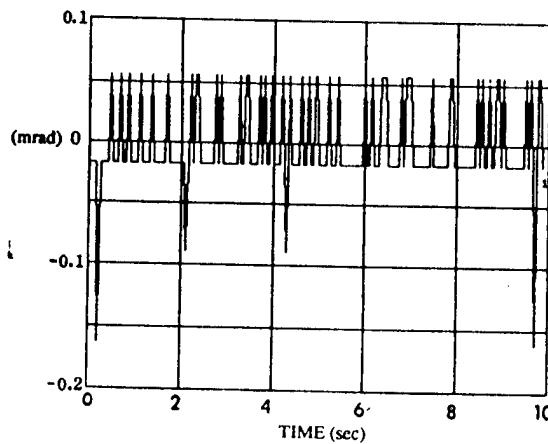
Fig. 3.2-31 Sensor Noise of Hub Sensor HS10.

Table 3.2-1
Comparison of Finite Element Modelling (FEM) and
Experiment Results for Boom-Dish Modal Frequencies.

Mode Number	The 1-7 Axis		The 4-10 Axis	
	FEM Result	Experiment Result	FEM Result	Experiment Result
1	0.091	0.126	0.091	0.114
2	0.628	0.666	0.616	0.637
4	2.682	2.68	2.577	2.57
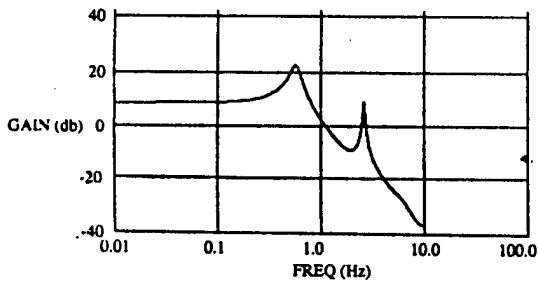
142

FREQUENCY (Hz)	DAMPING COEFFICIENT
6.74372615630164	0.294804242241718
2.69063086962966	1.886665092010740E-002
0.569302248325097	0.102227184314484
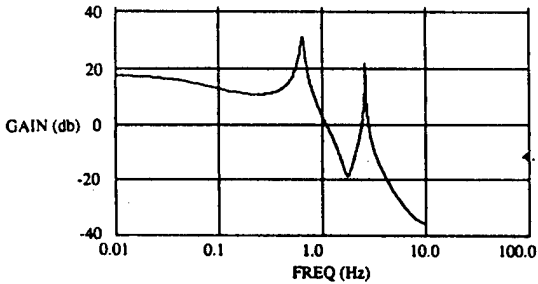
FREQUENCY (Hz)	DAMPING COEFFICIENT
2.57485292621491	6.010316454259838E-003
1.591549430918954E-031	3.466381283365332E+029
0.638600283416937	3.614834659835230E-002
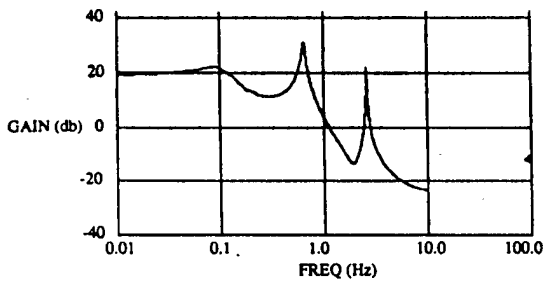
FREQUENCY (Hz)	DAMPING COEFFICIENT
2.57396009741196	5.646150203739603E-003
0.639310446700395	3.314971127914047E-002
9.055101939839522E-002	0.469761090417009
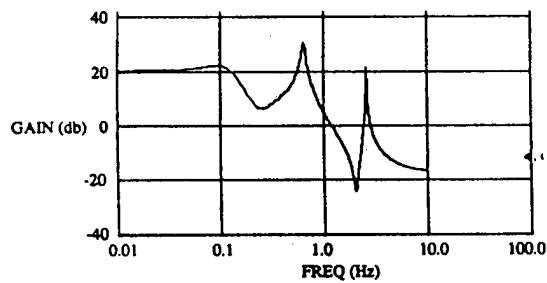
FREQUENCY (Hz)	DAMPING COEFFICIENT
2.57118501813782	6.031738854103093E-003
0.636692072398986	3.630040909311377E-002
0.111304915112333	0.422023916637950
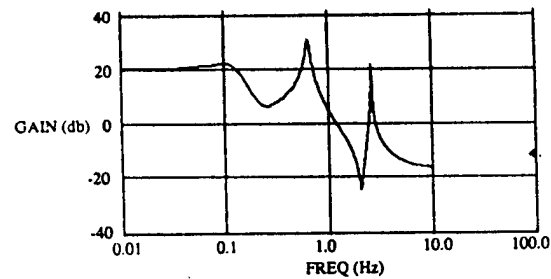
FREQUENCY (Hz)	DAMPING COEFFICIENT
2.57118815539440	6.041210055508633E-003
0.636653780610485	3.639334570166898E-002
0.113424081595023	0.401622291577043
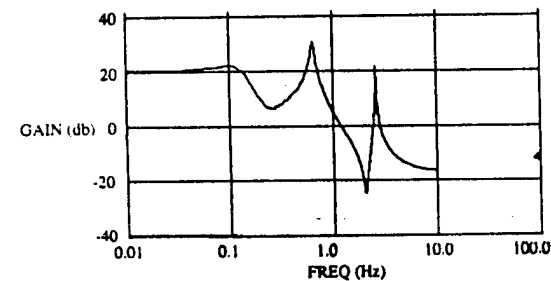
FREQUENCY (Hz)	DAMPING COEFFICIENT
2.57117709973122	6.042845974054128E-003
0.636639669353661	3.641059295623022E-002
0.113709508062294	0.400310467878806

Fig. 3.2-32 Curve Fit Computation Sequence of Assumed Modal Order 3 for the 4-10 Axis Hub Actuator/Hub Sensor Wideband Excitation Case.

143

FREQUENCY (Hz)	DAMPING COEFFICIENT
2.57117709973122	6.042845974054128E-003
0.636639669353661	3.641059295623022E-002
0.113709508062294	0.400310467878806
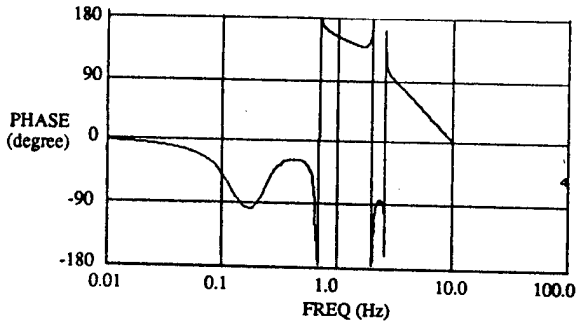
NUMERATOR COEFFICIENT	DENOMINATOR COEFFICIENT
0.313828565339137	0.948448754545826
-1.34219134539618	-5.11306033857448
2.43393981621130	11.9651322910484
-2.36853003555418	-15.6773058544137
1.27677741665536	12.1685830156099
-0.356802485010616	-5.29176230790066
4.333607662209583E-002	1.00000000000000

Fig. 3.2-33 Curve Fitted Model of Assumed Modal Order 3 (which is the Identified Parametric Model) for the 4-10 Axis Hub Actuator/Hub Sensor Wideband Excitation Case.
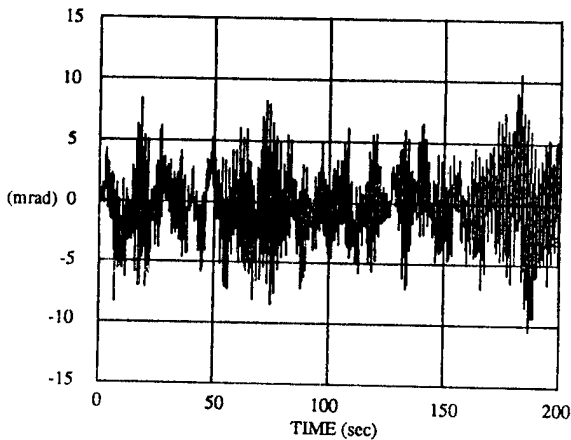

Fig. 3.2-34 Identified Parametric Model Response $\hat{y}$ to Actual Input u for the 4-10 Axis Hub Actuator/Hub Sensor Wideband Excitation Case.
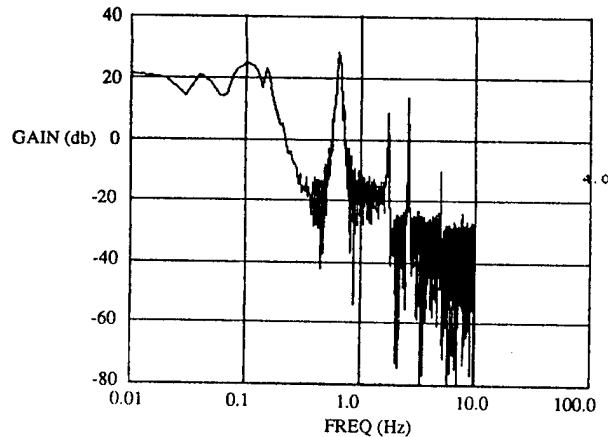

Fig. 3.2-36 Output Error Power Spectral Density P_{ee} of the Identified Parametric Model for the 4-10 Axis Hub Actuator/Hub Sensor Wideband Excitation Case.
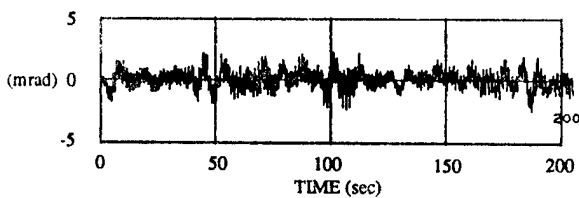

Fig. 3.2-35 Output Error $e = y - \hat{y}$ of the Identified Parametric Model for the 4-10 Axis Hub Actuator/Hub Sensor Wideband Excitation Case.
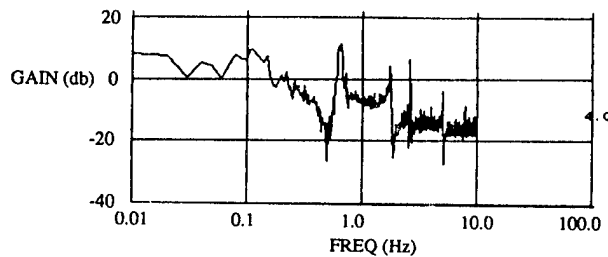
Fig. 3.2-37 Additive Uncertainty $\Delta = P_{ue}/P_{uu}$ of the Identified Parametric Model for the 4-10 Axis Hub Actuator/Hub Sensor Wideband Excitation Case.

144
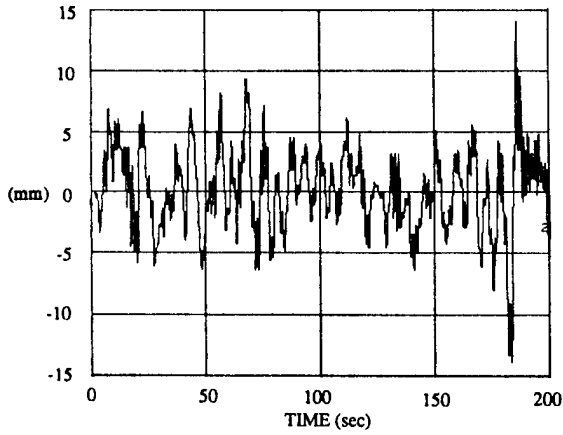
Fig. 3.2-38 Output Response y at Levitator Sensor LO1 for the 4-10 Axis Hub Actuator/Levitator Sensor Wideband Excitation Case.
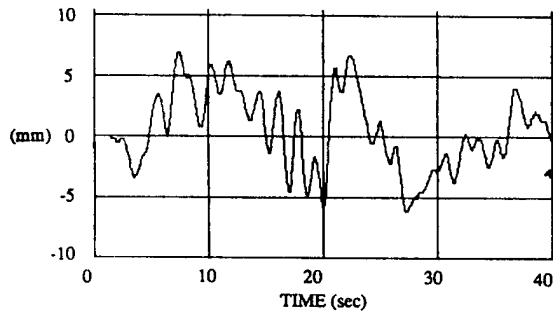
Fig. 3.2-39 Expanded view of Output Response y at Levitator Sensor LO1 for the 4-10 Axis Hub Actuator/Levitator Sensor Wideband Excitation Case.
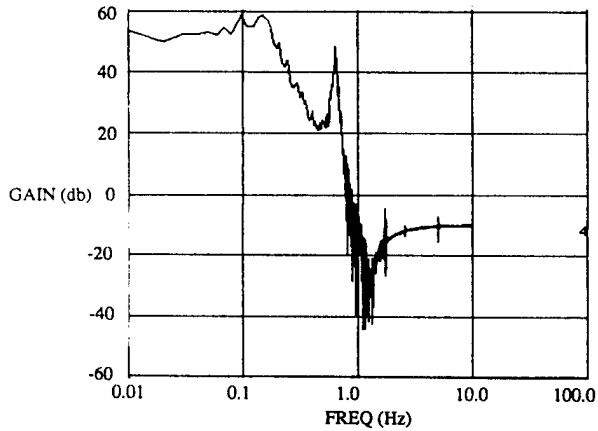
Fig. 3.2-40 Power Spectral Density P_{yy} for the 4-10 Axis Hub Actuator/Levitator Sensor Wideband Excitation Case.
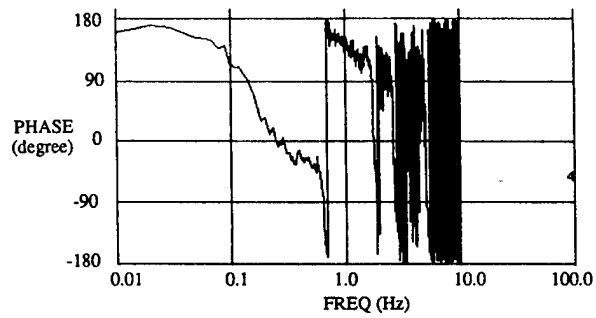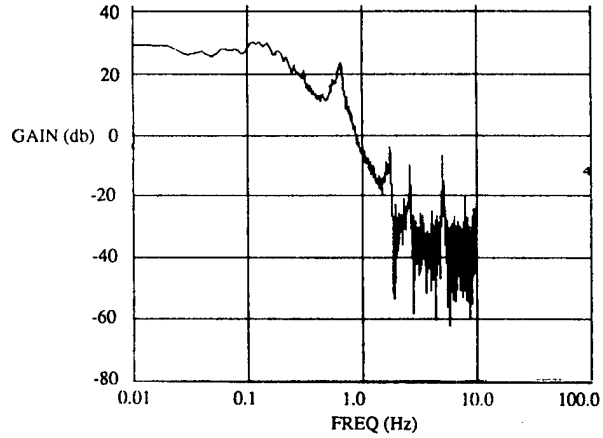
Fig. 3.2-41 Bode Plot of Transfer Function Spectral Estimate $h = P_{uy}/P_{uu}$ for the 4-10 Axis Hub Actuator/Levitator Sensor Wideband Excitation Case.
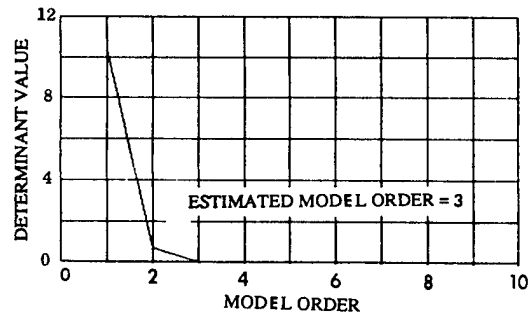
Fig. 3.2-42 PMM TEST Determinant Plot for the 4-10 Axis Hub Actuator/Levitator Sensor Wideband Excitation Case.

145

more dominant over the rest. Curve fitting the high frequency modes in the present case would not efficiently improve the identification performance which is dominated by the fitting error of the 1st and 2nd modes.

Curve fitting results assuming a modal order of 2 are now presented. Figure 3.2-43 shows the sequence of computations of the system model transfer function estimates. As before, the 1st mode came into prominence gradually during later computations emphasizing low frequency spectral data. At convergence, subsequent frequency values and damping coefficients vary less than 0.3%. Figure 3.2-44 shows the transfer function of the converged curve fitted model.

The computed output $\hat{y}$ of the identified parametric model subject to the same input is given in figure 3.2-45 and $e = y - \hat{y}$ is given in figure 3.2-46. P_{ee}, the spectral density of e, is shown in figure 3.2-47. The seemingly larger output error for the present case is dominated by the fitting error of the 1st mode. The frequency resolution adopted for present analysis was around 0.01 Hz, roughly 10% of the frequency of the 1st mode. Hence, out of the 1024 spectral data points of P_{uy}/P_{uu}, there were only twenty or so corresponding to the 1st mode. This caused difficulties in curve fitting the 1st mode. The present identification procedures utilized a non-uniform weighting emphasizing the low frequency spectral region to achieve curve fitting this 1st mode. Unavoidably, appreciable fitting error for the 1st mode was induced in the process. It is important to point out that appreciable fitting error for the 1st mode was similarly induced for previous hub angular sensor cases, except that here it is much more apparent as the 1st mode was the most dominating component in the levitator sensor output.

The additive uncertainty, estimated by $\Delta = P_{ue}/P_{uu}$, is shown in figure 3.2-48. Errors corresponding to the 1st mode contributed the maximum value of P_{ue}/P_{uu} at 16 db. The identified modes were of frequencies 0.134 Hz and 0.637 Hz and of damping coefficients 0.39 and 0.041. Compared with the identified parametric modes of section 3.2.3, the results showed a reasonable match of frequency and damping values except for the frequency of the 1st mode which is 20% off. This is probably due to the appreciable curve fitting error for the 1st mode in the two cases. Also, the relatively large damping coefficient gave rise for this mode a flat resonance in the transfer function. This contributed further to a possible mismatch of the spectral data and curve fit. As a final note, the unfitted modes contributed smaller curve fitting errors than those due to the fitting of the 1st and 2nd modes, which was why the algorithms avoided fitting them in the first place.

3.2.3 Narrowband Excitation (0-3 Hz)

In this and the next section, the techniques of narrowband excitation and data composition are presented. Working together, these techniques allowed data from different spectral region of interest to be generated and combined for analysis. The narrowband excitation technique is presented first. As was discussed before, narrowband excitation concentrated the available actuation power for structural excitation within a narrow spectral range, leading to an improvement in signal to noise ratio in the observations and hence, better curve fitting results. This is useful when only a narrow range of frequency spectrum is of interest or when attempts are being made to enable excitation of otherwise difficult-

146
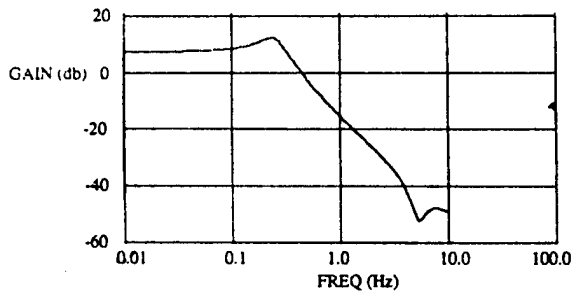
FREQUENCY (Hz)	DAMPING COEFFICIENT
4.26130744911608	0.911425788287989
0.239357655862265	0.316552471008934
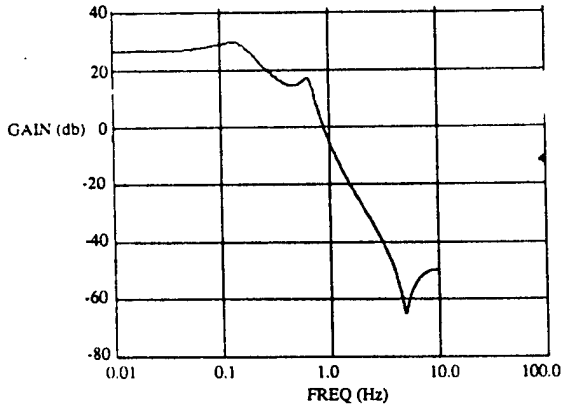
FREQUENCY (Hz)	DAMPING COEFFICIENT
0.642860272080362	0.107086625374627
0.135905862464804	0.429866752474150
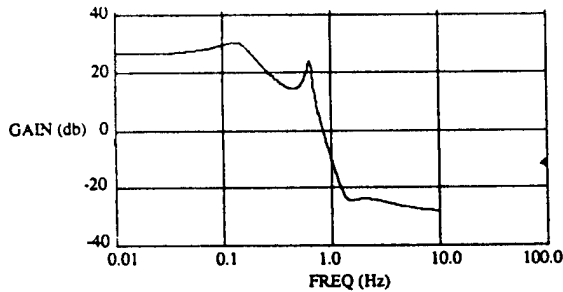
FREQUENCY (Hz)	DAMPING COEFFICIENT
0.633459336744205	4.244614840871643E-002
0.133866402720678	0.391164024171868
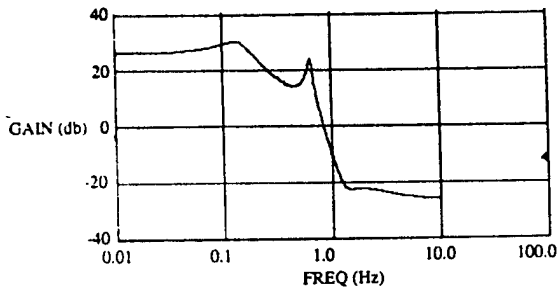
FREQUENCY (Hz)	DAMPING COEFFICIENT
0.636997027548176	4.034609661619287E-002
0.133927976211006	0.389903863088258
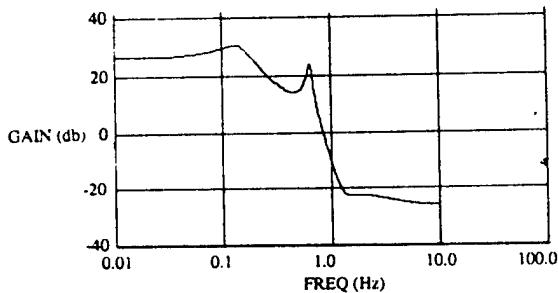
FREQUENCY (Hz)	DAMPING COEFFICIENT
0.637140938295392	4.053421127951689E-002
0.133905708176015	0.389785868932030

Fig. 3.2-43 Curve Fit Computation Sequence of Assumed Modal Order 2 for the 4-10 Axis Hub Actuator/Levitator Sensor Wideband Excitation Case.
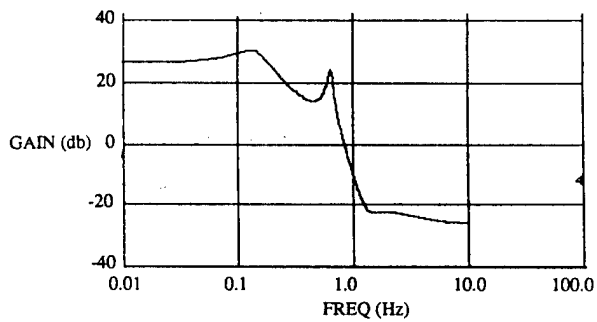
147

FREQUENCY (Hz)	DAMPING COEFFICIENT
0.637140938295392	4.053421127951689E-002
0.133905708176015	0.389785868932030
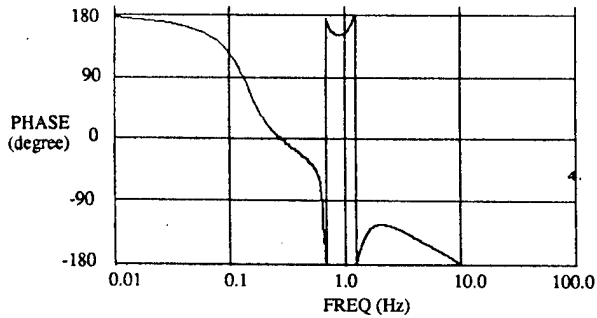
NUMERATOR COEFFICIENT	DENOMINATOR COEFFICIENT
-8.057486105796713E-002	0.952160407377924
0.251603498461151	-3.81559449798919
-0.294751432421448	5.77347503719817
0.144793889592196	-3.90996139267422
-2.273219235793110E-002	1.00000000000000

Fig. 3.2-44 Curve Fitted Model of Assumed Modal Order 2 (which is the Identified Parametric Model) for the 4-10 Axis Hub Actuator/Levitator Sensor Wideband Excitation Case.
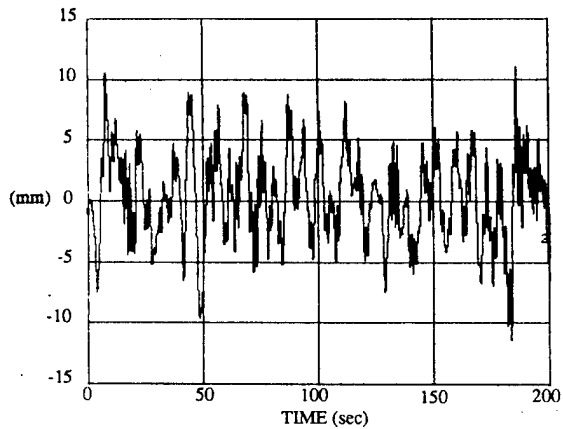
Fig. 3.2-45 Identified Parametric Model Response $\hat{y}$ to Actual Input u for the 4-10 Axis Hub Actuator/Levitator Sensor Wideband Excitation Case.
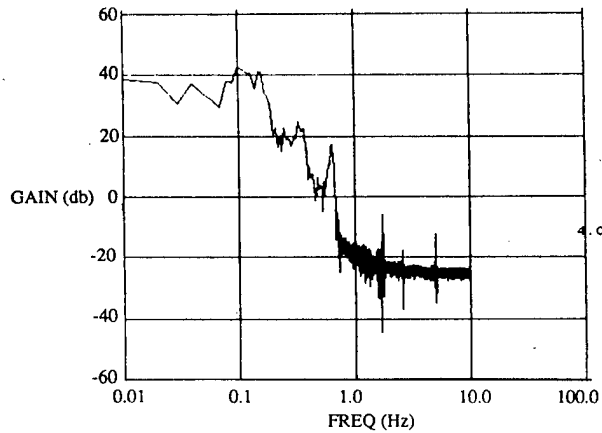
Fig. 3.2-47 Output Error Power Spectral Density P_{ee} of the Identified Parametric Model for the 4-10 Axis Hub Actuator/Levitator Sensor Wideband Excitation Case.
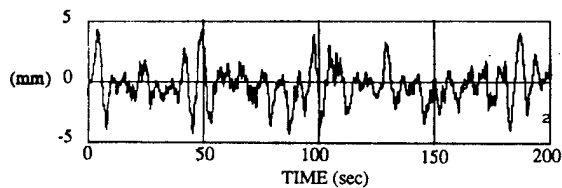
Fig. 3.2-46 Output Error $e = y - \hat{y}$ of the Identified Parametric Model for the 4-10 Axis Hub Actuator/Levitator Sensor Wideband Excitation Case.
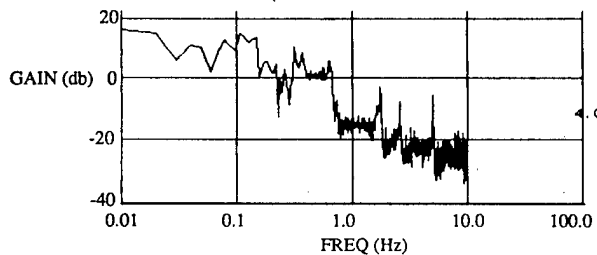
Fig. 3.2.48 Additive Uncertainty $\Delta = P_{ue}/P_{uu}$ of the Identified Parametric Model for the 4-10 Axis Hub Actuator/Levitator Sensor Wideband Excitation Case.

148

to-excite mode(s). As an example to demonstrate the technique, this section describes a narrowband experiment and its identification results. The frequency range of interest is from 0 to 3 Hz. The experiment was performed on the 4-10 axis of the structure using the hub torquer HA1 and hub angular sensor HS10, the same axis and instrumentation as in section 3.2.2.2. The 0-3 Hz filter was designed based on the following parameters:

ITYPE=1 (low Pass)
IAPRO=1 (Butterworth)
NDEG=12
EDEG=0.2
FR(1)=3.0
FR(2)=3.5
ADELP=0.02
ADELS=0.01
NBFIL=1.0

As such, the low pass filter has a transfer function magnitude which starts to roll off at 3 Hz, arriving at cutoff at 3.5 Hz. The filter coefficients are stored as the first filter coefficient storage file 'filcoe1.dat'. The parameters Fr(3) and Fr(4) are irrelevant as the filter is a lowpass one.

The parameters set for the narrowband experiment were WBMEAN=0.0 and WBSTAN=1.5, which were the same as for the previous wideband experiments. The other parameters were PER=66.7 and NBFIL=1.0. NBFIL=1.0 implied reading in the filter coefficients from the first storage file which is where the intend filter was stored. PER=66.7 dictated that the narrowband experiment utilized 66.7% of the actuation energy in the wideband case. This value of PER ensured that the hub torquer not be commanded for actuation beyond its maximum power. Compared with the wideband experiment, the present narrowband experiment thus concentrated 66.7% of the actuation power into a 30% (0-3 Hz out of 10 Hz) of the full range. This amounted to a factor of 2 increase in excitation power density.

Figure 3.2-49 and 3.2.50, respectively, present the 200 sec time histories of the narrowband experiment input u and output y. The autocorrelation of u at zero lag, $R_{uu}(0)$, was determined to be 0.509 for this case, while it was 0.75 before for the wideband excitation case. As $R_{uu}(0)$ is a measure of the total integrated power of the spectrum, it confirmed the fact that only 66.7% of actuation power in the wideband experiment was used for this experiment. The PSD of u, P_{uu}, is given in figure 3.2-51. It showed a drastic rolloff of input power at 3 Hz, indicating clearly that the filter design and implementation were as desired. The PSD of y, P_{yy}, is given in figure 3.2-52. Compared with figure 3.2-28, it indicated enhanced structural excitation over that of the wideband excitation case within the range of 0-3 Hz, as expected. The component of the 5th mode which is around 5 Hz is missing in P_{yy}, also as expected. Figure 3.2-53 shows the TFSE P_{uy}/P_{uu}. Only the data within the range 0-3 Hz constituted meaningful results in figure 3.2-53. Outside the range, noise dominated as there was very little input and output energy there. Figure 3.2-54 presents the PMM test results obtained using algorithm PMMDE. The estimated model order is 3 according to the 0.1% criterion.
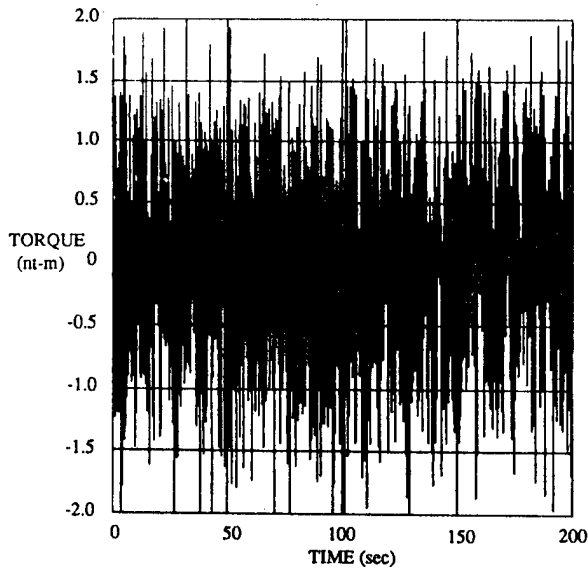
Fig. 3.2-49 Narrowband (0-3 Hz) Excitation Input.
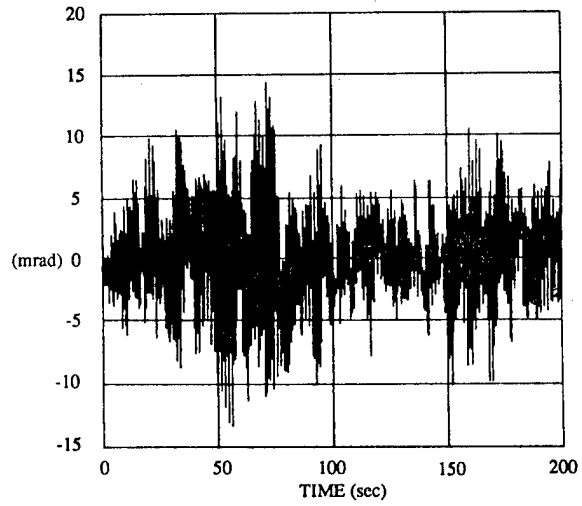
Fig. 3.2-50 Output Response y at Hub Sensor HS10 for the 4-10 Axis Hub Actuator/Hub Sensor Narrowband (0-3 Hz) Excitation Case.
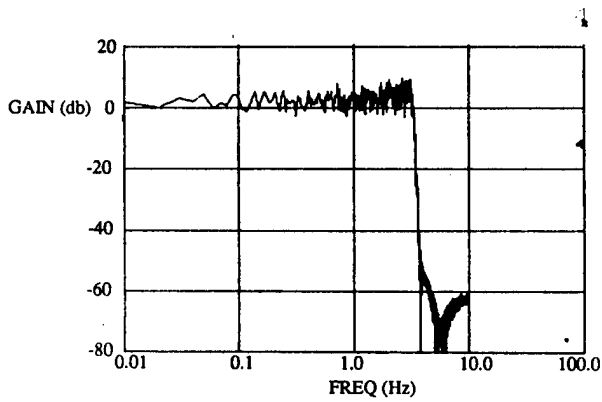
Fig. 3.2-51 Power Spectral Density P_{uu} for the 4-10 Axis Hub Actuator/Hub Sensor Narrowband (0-3 Hz) Excitation Case.
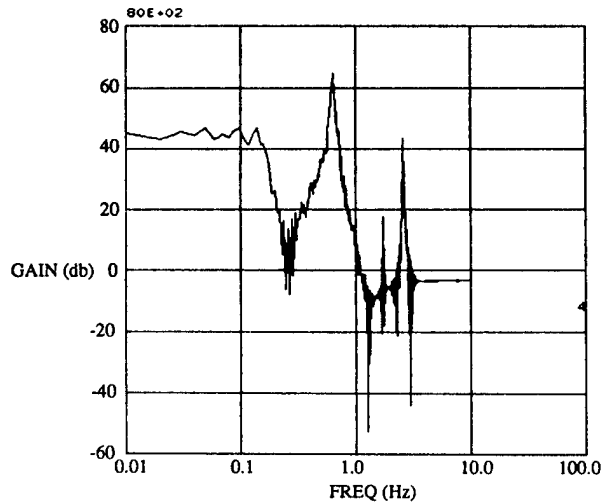
Fig. 3.2-52 Power Spectral Density P_{yy} for the 4-10 Axis Hub Actuator/Hub Sensor Narrowband (0-3 Hz) Excitation Case.

150

To see if better identification results could be obtained, the automated procedures depicted in figure 3.2-1 were applied as before, except that this time spectral data within the range 0-3 Hz were being utilized for curve fitting. The final identified parametric model is the one with an assumed modal order of 3. This identified modal order of 3 is not surpising as the difference between the present case and the wideband case is the absence of the 5th mode which is a mode that did not show up in curve fitting anyway. Figure 3.2-55 shows the sequence of curve fit computations. Convergence was reached after 5 computations and subsequent modal values agreed to within 0.1%. Again, the first computation utilized SF=1.0 for equal weighting while the rest used SF=0.9. All the time only the 0-3 Hz spectral data was processed. The 1st mode, as before, gradually came into being during later computations. Figure 3.2-56 shows the identified parametric model. Figure 3.2-57 shows the output error $e = y - \widehat{y}$, where $\widehat{y}$ is the identified parametric model output subjected to the same input u depicted in figure 3.2-49. The additive uncertainty, Δ, is given in fig 3.2.58. The output error analysis here of e and Δ did not show any observable improvement as compared to that of the wideband excitation. It seems that the wideband excitation output already enjoyed a good signal to noise ratio so that a further increase by a factor of 2, in this case, did not bring about any noticeable improvement. However, the technique of narrowband excitation capability incorporated here in the experiment software can constitute, in other circumstances, a good method of reducing the measurement noise.

3.2.4 Data Composition

Due to the finite power constraint on the actuator, the obtainable power density and frequency range of excitation are inversely proportional to each other. This section presents a technique called data composition which effectuates, after conducting several narrowband experiments covering different frequency ranges of interest, the summation of their inputs and outputs. The results would be the data of an 'effective' experiment of which the frequency range of excitation is the sum of the individual narrowband experiments. As such, an experiment of high excitation power density as well as wide frequency range can be achieved.

The technique of data composition is illustrated in this section. Data from narrowband experiments of frequency range 0-3 Hz and 3-6 Hz are added together to form that of one with 0-6 Hz as an effective frequency range of excitation. The data for the 0-3 Hz narrowband experiment are the same as that presented in the previous section. Data for the 3-6 Hz narrowband experiment are now presented. Consistent with the 0-3 Hz narrowband experiment, this 3-6 Hz narrowband experiment was performed on the same 4-10 axis and utilized the same hub actuator HA1 and sensor HS10. The filter parameters were:

ITYPE=333 (Band Pass)
IAPRO=1 (Butterworth)
NDEG=12
EDEG=0.2
FR(1)=2.5
FR(2)=3.0
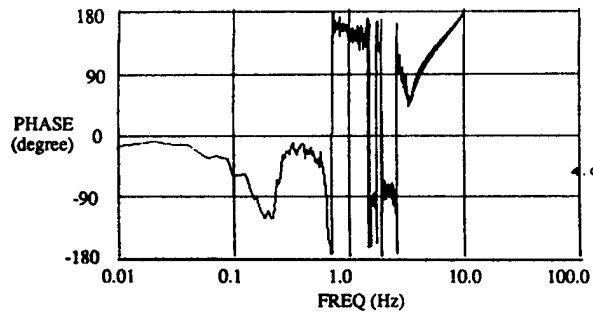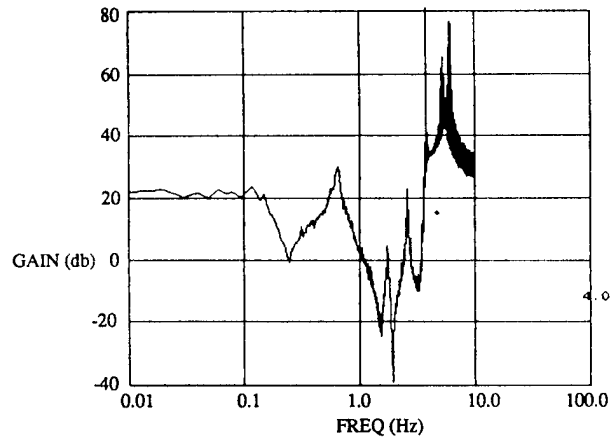
Fig. 3.2-53 Bode Plot of Transfer Function Spectral Estimate $h = P_{uy}/P_{uu}$ for the 4-10 Axis Hub Actuator/Hub Sensor Narrowband (0-3 Hz) Excitation Case.
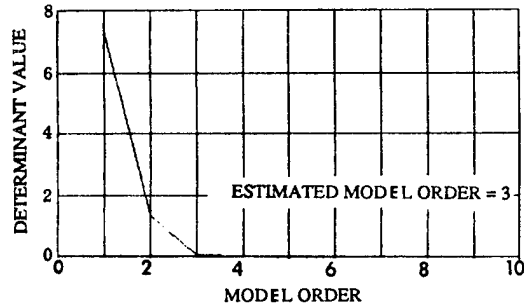
Fig. 3.2-54 PMM TEST Determinant Plot for the 4-10 Axis Hub Actuator/Hub Sensor Narrowband (0-3 Hz) Excitation Case.

152
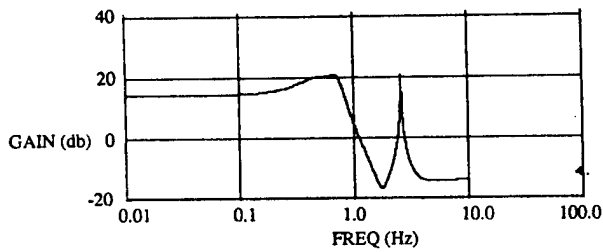
FREQUENCY (Hz)	DAMPING COEFFICIENT
2.56740246953400	6.249613328231810E-003
0.718667610725937	0.143492756239670
0.452476817781635	0.427254819356082
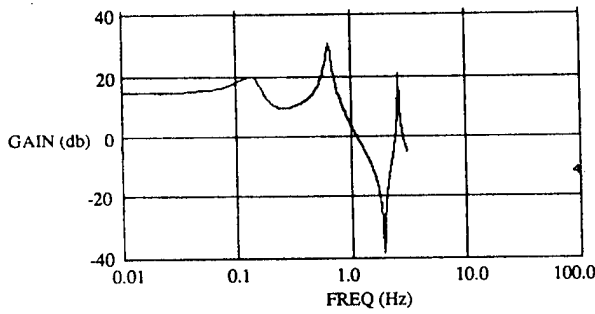
FREQUENCY (Hz)	DAMPING COEFFICIENT
2.56534881633432	7.010988318957218E-003
0.634717358193997	3.610476037658784E-002
0.138376685429615	0.215918580645229
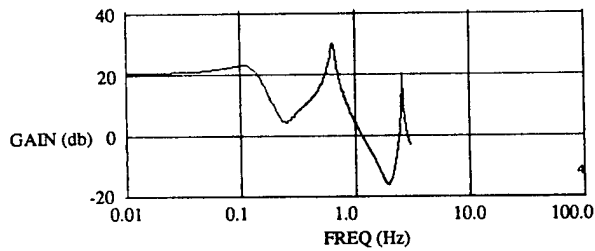
FREQUENCY (Hz)	DAMPING COEFFICIENT
2.56358445712333	7.602056609044330E-003
0.632057493141175	3.911361841740383E-002
0.119896708153327	0.361928436842128
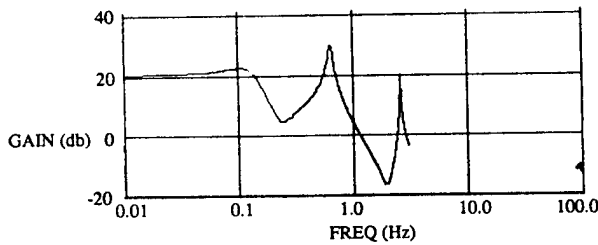
FREQUENCY (Hz)	DAMPING COEFFICIENT
2.56358579202972	7.610125292684910E-003
0.632037838244232	3.899877945327621E-002
0.117763346790050	0.366657427578757
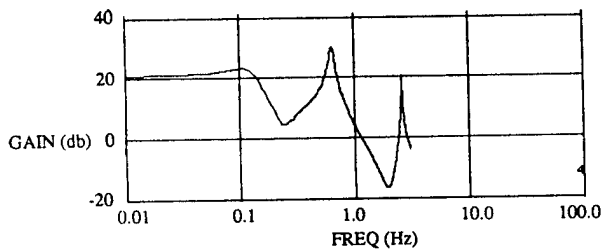
FREQUENCY (Hz)	DAMPING COEFFICIENT
2.56358370722263	7.608804875517834E-003
0.632041998399339	3.898615970482653E-002
0.117540339237004	0.368285236570123

Fig. 3.2-55 Curve Fit Computation Sequence of Assumed Modal Order 3 for the 4-10 Axis Hub Actuator/Hub Sensor Narrowband (0-3 Hz) Excitation Case.

FREQUENCY (Hz)	DAMPING COEFFICIENT
2.56358370722263	7.608804875517834E-003
0.632041998399339	3.898615970482653E-002
0.117540339237004	0.368285236570123
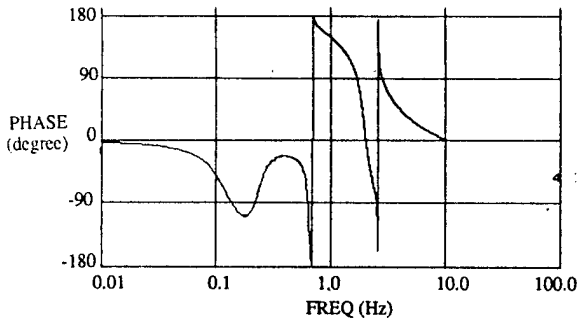
NUMERATOR COEFFICIENT	DENOMINATOR COEFFICIENT
0.556150474832277	0.946544706814846
-2.60865169349456	-5.10769098624538
5.31082193679151	11.9626948396374
-6.02879199045097	-15.6835556824229
4.03453041630456	12.1764851971016
-1.51988896118575	-5.29444165114957
0.256223708213091	1.00000000000000

Fig. 3.2-56 Curve Fitted Model of Assumed Modal Order 3 (which is the Identified Parametric Model) for the 4-10 Axis Hub Actuator/Hub Sensor Narrowband (0-3 Hz) Excitation Case.
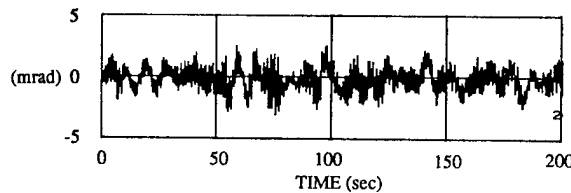
Fig. 3.2-57 Output Error $e = y - \hat{y}$ of the Identified Parametric Model for the 4-10 Axis Hub Actuator/Hub Sensor Narrowband (0-3 Hz) Excitation Case.
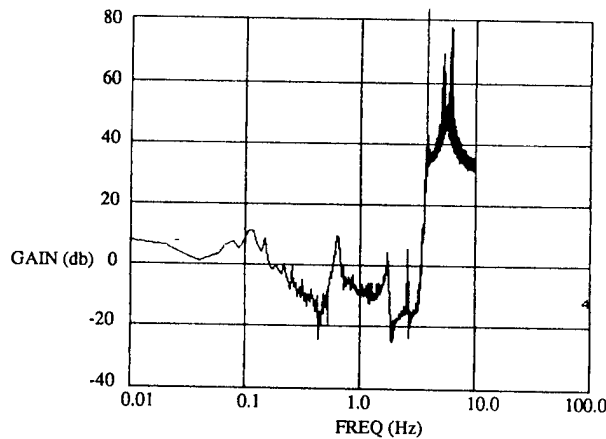
Fig. 3.2.58 Additive Uncertainty $\Delta = P_{ue}/P_{uu}$ of the Identified Parametric Model for the 4-10 Axis Hub Actuator/Hub Sensor Narrowband (0-3 Hz) Excitation Case.

154

FR(3)=6.0
FR(4)=6.5
ADELP=0.02
ADELS=0.01
IFIL=2.0

The band pass filter has its pass band located between 3 and 6 Hz, with cutoff frequency at 2.5 and 6.5 Hz. As the parameter IFIL shows, the filter coefficients were stored in the second filter coefficient storage file 'filcoe2.dat'. The parameters for this 3-6 Hz narrowband experiment were WBMEAN=0.0, WBSTAN=1.5, PER=66.7, and NBFIL=2.0. Note that they are the same as the 0-3 Hz narrowband experiment, except that NBFIL now dictated the filter coefficients be read from the second filter coefficient storage location. As compared to wideband excitation, this experiment used 66.7% of the actuation power in 30% of the frequency range for excitation, yielding a factor of 2 increase in excitation power density. This is the same as for 0-3 Hz narrowband experiment. Again, PER=66.7 ensured that the torquer was not commanded beyond its maximum output.

The input and output of the 3-6 Hz narrowband experiment are given in figure 3.2.59 and 3.2.60 for the time span of 20 sec which enabled better appreciation of the frequency components in u and y. The maximum excursion of the output in figure 3.2-60 is approximately 20 times smaller than that of the 0-3 Hz narrowband experiment in figure 3.2-50. This shows the dominant presence of 0-3 Hz component over the 3-6 Hz component in the structure dynamics. The PSDs of u and y, P_{uu} and P_{yy}, are given in figure 3.2-61 and 3.2.62. The PSD P_{uu} confirmed the validity in the design and implementation of the filter. The integrated spectral power of P_{uu} as indicated by $R_{uu}(0)$ is computed to be 0.508, again confirmed that 66.7% of the actuation power as in the wideband case was used. The PSD P_{yy} showed that though the intent was to excite the 3-6 Hz component of the structure, the first two system modes were also slightly excited because of their prominence in the dynamics. The PSD P_{yy} also indicated the more apparent excitation of the 5th mode. The strongest component in y and P_{yy}, however, is a 3 Hz component which is due to the residual resonance of the 4th mode around 2.6 Hz. The TFSE P_{uy}/P_{uu} is shown in fig. 3.2.63. Again, only the data within the pass band of 3-6 Hz are meaningful. Figure 3.2-63 clearly indicated the presence of the 5th mode around 5 Hz. The PMM test result is shown in figure 3.2-64. It yielded an estimated model order of 2 with the 0.1% criterion.

Data composition was performed adding the inputs and outputs of the 0-3 Hz and 3-6 Hz narrowband experiments together to generate the input and output of an effective 0-6 Hz experiment run. Figures 3.2-65 and 3.2-66 show, respectively, the input and output of data composition. Note that the maximum input command is now around 3.2 nt-m which is beyond the maximum actuation level of 2 nt-m. Figure 3.2-67 shows the PSD P_{uu}. It illustrated the basic idea of data composition. The input excitation constituted effectively that of a 0-6 Hz narrowband experiment. The little hump on P_{uu} near 3 Hz is due to the overlapping of the rolloff ranges of the narrowband filters. The integrated spectral power of the input excitation as indicated by $R_{uu}(0)$ is computed to be 1.01. Thus, the composed data were equivalent to concentrating 133% of the actuation power available to the wideband experiment 60% of the full frequency range. The output is very

similar to that of the 0-3 Hz narrowband experiment. This is because the output of the 3-6 Hz narrowband experiment is relatively small. The PSD of y, P_{yy}, is shown in figure 3.2-68. It indicated the presence of 5 modes, 4 from the 0-3 Hz narrowband experiment, 1 from the 3-6 Hz. The TFSE of the composed data is shown in figure 3.2-69, again showing the presence of 5 modes. By the same reasoning as before, only the spectral data within the 0-6 Hz range are meaningful.

The PMM test result for the composed data is shown in figure 3.2-70. It estimated the number of states in the system to be 4. Note that the 0-3 hz narrowband experiment alone yielded an estimated model order of 3. The added component from the 3-6 Hz narrowband excitation managed to increase the model order estimate by 1 resulting in the same estimated order as the wideband excitation case. The automated identification procedures were applied to the composed data. The identified results were very similar to the wideband experiment case. This is also expected as there had not been much improvement with the 0-3 Hz narrowband excitation data, and there should not be any with the addition of a not too significant mode in the data.

The methodology of data composition is illustrated in this section. In cases where actuation is inadequate, or when narrowband excitation is more desirable for effective dynamics observation, data composition can effectively produce a high excitation power/wide frequency range experiment run. Data generated from different experiments corresponding to the same narrowband excitation can also be composed together to enhance the signal to noise ratio.

3.3 Investigation of The Residual Modes

A 3 mode identified model was obtained based on the automated identification procedures as depicted in figure 3.2-1. Two other modes, termed the 3rd and 5th mode, were apparent in the spectral transfer function but did not appear during curve fitting computations. The reason is that they are "weak" as compared to others. The resulting identification error due to their omission was found to be small compared to the curve fitting error of the three major modes. Hence, for better performance the algorithm would rather attempt to better fit the major modes than to accommodate curve fitting the "weak" modes. As such, the automated identification procedure yields a "reduced-order" model based on the curve fitting performance of the algorithms. Using conventional terminology, modes that were not included in the "reduced-order" model are termed residual modes in contrast to retained modes for those included in the "reduced-order" model.

This section examines the residual modes which, in the present case, are the 3rd and 5th modes. Two methods were used for this investigation. The first, described in section 3.3.1, involves performing curve fitting computations on selected frequency ranges that correspond to residual modes. It yielded frequencies and damping coefficients for the residual modes. The second is the sine-dwell methodology described in section 3.3.2. It excites a particular residual mode via sinusoidal inputs. It should be pointed out that both methods can also be applied to the investigations of modes which appear during curve fitting computations. However, here they are devoted to investigating the residual modes. It is hoped that information on the residual modes adding to the "reduced-order" model
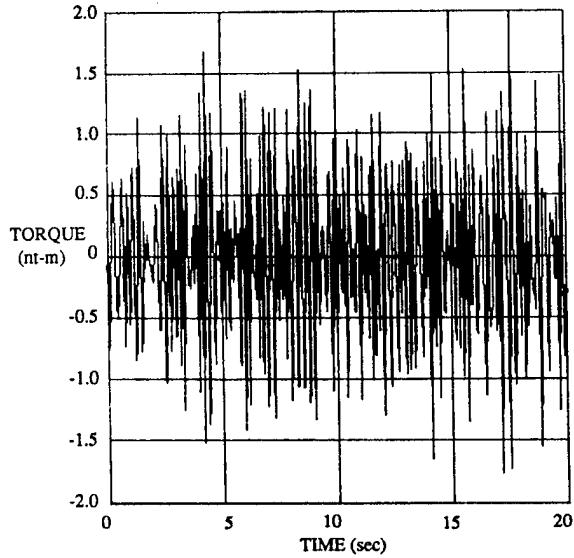
Fig. 3.2-59 Narrowband (3-6 Hz) Excitation Input.
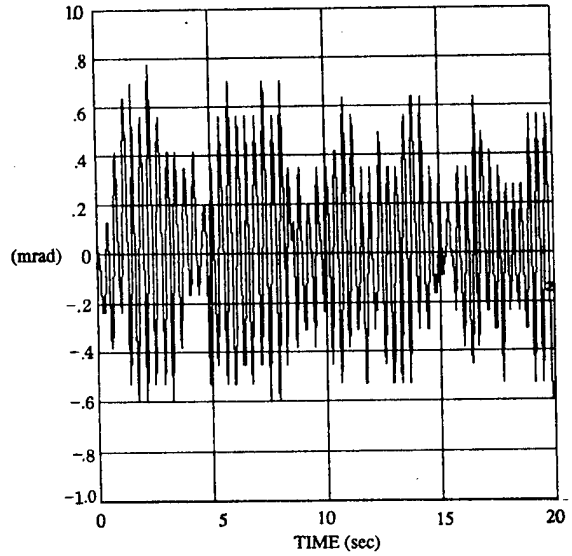
Fig. 3.2-60 Output Response y at Hub Sensor HS10 for the 4-10 Axis Hub Actuator/Hub Sensor Narrowband (3-6 Hz) Excitation Case.
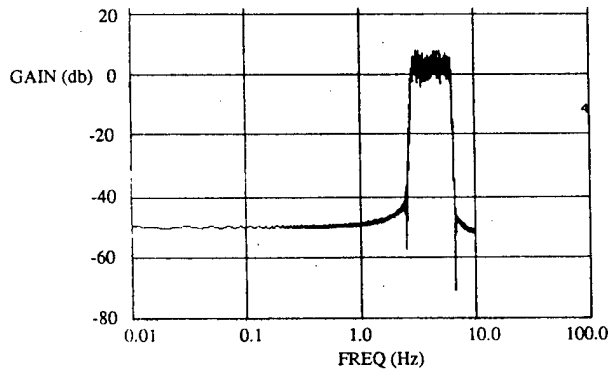
Fig. 3.2-61 Power Spectral Density P_{uu} for the 4-10 Axis Hub Actuator/Hub Sensor Narrowband (3-6 Hz) Excitation Case.
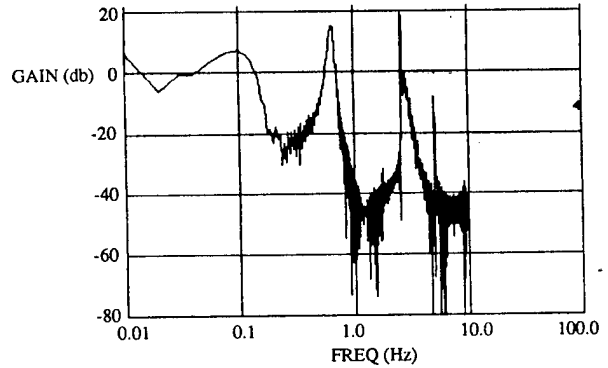
Fig. 3.2-62 Power Spectral Density P_{yy} for the 4-10 Axis Hub Actuator/Hub Sensor Narrowband (3-6 Hz) Excitation Case.
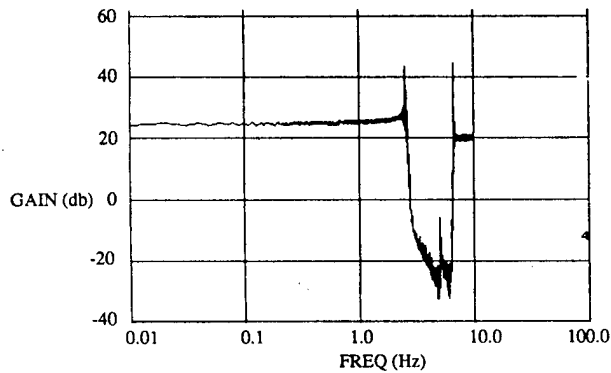
Fig. 3.2-63 Bode Plot of Transfer Function Spectral Estimate $h = P_{uy}/P_{uu}$ for the 4-10 Axis Hub Actuator/Hub Sensor Narrowband (3-6 Hz) Excitation Case.
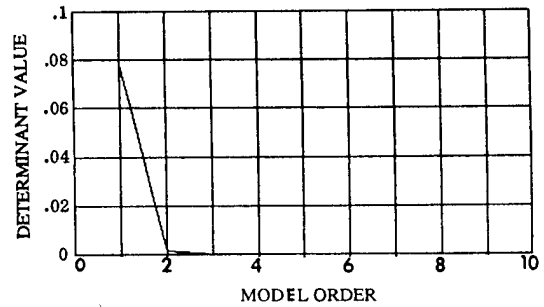
Fig. 3.2-64 PMM TEST Determinant Plot for the 4-10 Axis Hub Actuator/Hub Sensor Narrowband (3-6 Hz) Excitation Case.

157
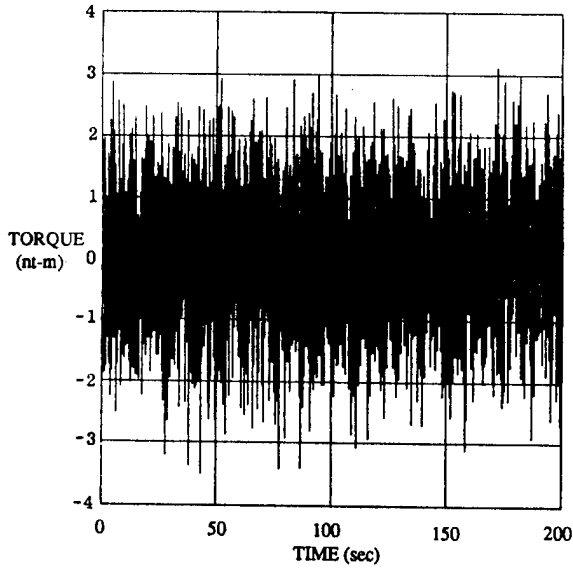
Fig. 3.2-65 Data Composition Input of (0-3 Hz) and (3-6 Hz) Narrowband Excitations.
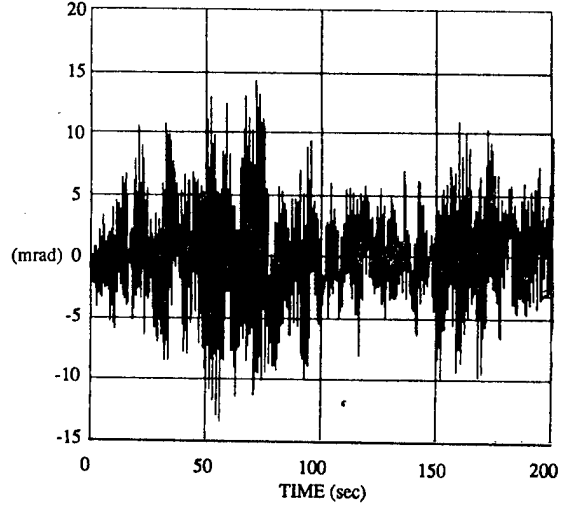
Fig. 3.2-66 Data Composition Output of (0-3 Hz) and (3-6 Hz) Narrowband Excitations.
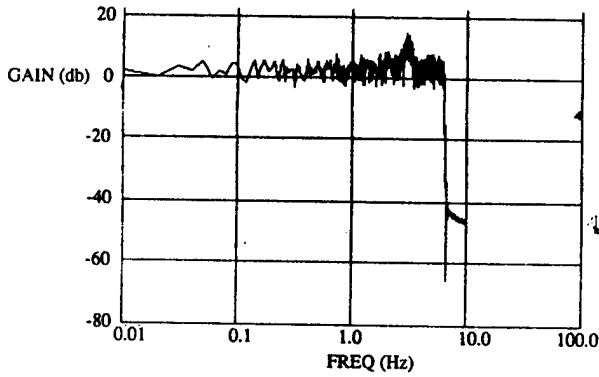
Fig. 3.2-67 Power Spectral Density P_{uu} of Data Composition Input.
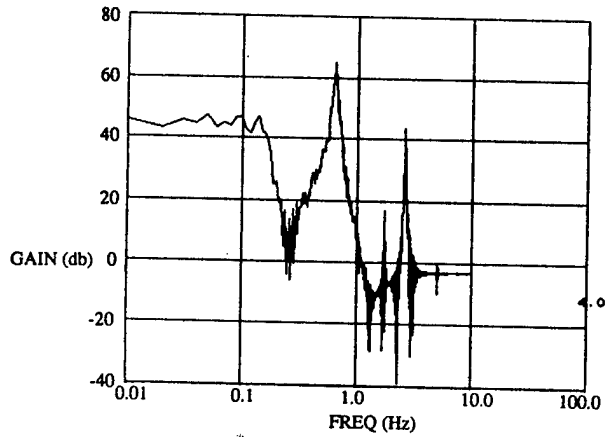
Fig. 3.2-68 Power Spectral Density P_{yy} of Data Composition Output.
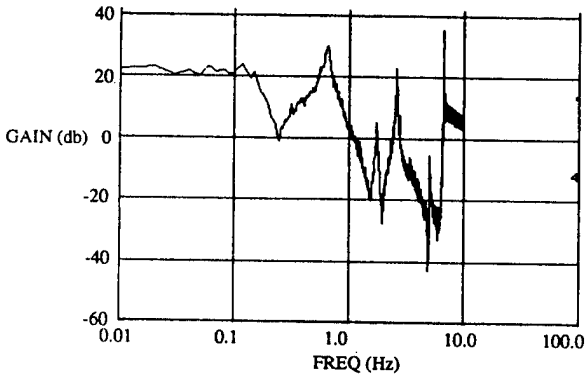
Fig. 3.2-69 Bode Plot of Transfer Function Spectral Estimate $h = P_{uy}/P_{uu}$ for Data Composition of (0-3 Hz) and (3-6 Hz) Narrowband Excitations.
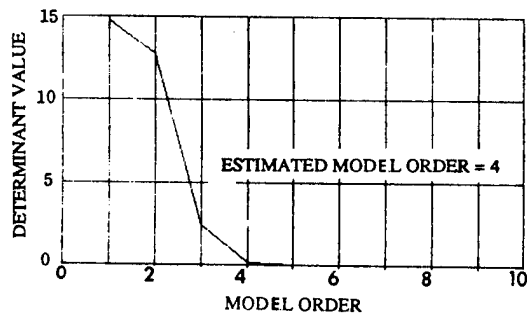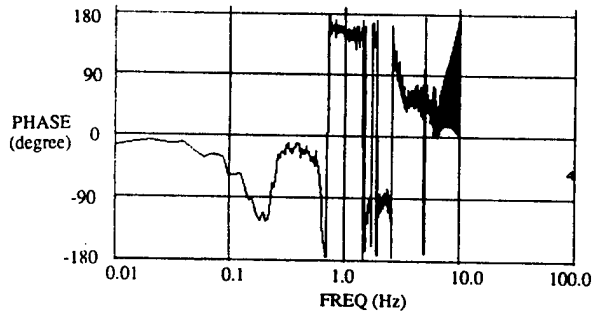
Fig. 3.2-70 PMM TEST Determinant Plot for Data Composition of (0-3 Hz) and (3-6 Hz) Narrowband Excitations.

158

will enable a better understanding of the model structure. All experiments described in this section were performed about the 4-10 axis with the hub actuator HA1 and angular sensor HS10.

3.3.1 Selective Range For Curve Fitting

The identification software developed has the capability to perform curve fitting using the spectral data of a selected frequency range. In such cases, even weighting, SF=1.0, has to be adopted. The technique here is to select the range of frequency for curve fitting close to the residual modal frequency. A narrow range about the resonance frequency of the residual mode is desired as such selection minimizes the effects of the major modes. This section utilizes narrowband excitation data for demonstration. They in general constitute a better signal to noise ratio though in the present case, selected data from wideband excitation data could be used as the noise level is small anyway.

The first residual mode to be investigated is the 3rd mode. It has a resonant frequency of roughly 1.7 Hz as indicated by the spectral transfer function obtained via 0-3 Hz narrowband excitation and depicted in figure 3.2-53. Three ranges were selected for curve fitting computations. The first was from 1.5 to 2.0 Hz. The curve fitting results showed a modal frequency of 1.719 Hz and a damping coefficient of 0.00515. A narrower second frequency range based on this information was then selected: 1.6 to 1.8 Hz. Curve fitting yielded a 1.718 Hz modal frequency with 0.0104 damping coefficient. To see if the spillover effect of the other modes has already been minimized to the limit, a third even narrower range of 1.65 to 1.75 Hz was selected for confirmation. The curve fitting computation yielded almost identical results of 1.718 Hz modal frequency and 0.01024 damping coefficient.

The curve fitted models consisting of the 3rd mode are presented in figure 3.3-1 for the three selected ranges. The phase plot is given for the third selected range only. To see how well this mode was fitted, output error analysis was performed. Figure 3.3-2 shows the time history of the computed output $\hat{y}$ of the curve fitted model corresponding to the third selected range subjected to the same input as in the narrowband experiment. It has a maximum excursion of approximately 0.4, as compared to roughly 15 for y. Contribution from the major modes to y dominated over that of the 3rd mode. The error $e = y - \hat{y}$ is shown in figure 3.3-3. Not surprisingly, e is very similar to y as $\hat{y}$ is small relatively. The PSD of e, P_{ee}, is shown in figure 3.3-4. The corresponding TFSE, $\Delta = P_{ue}/P_{uu}$, is given in figure 3.3-5. Three observations should be noted from these figures: First, the modelling of the first residual mode, or the 3rd mode, at around 1.7 Hz was quite adequate as P_{ee} and Δ both show that the corresponding modal component is being taken out. Second, e, composed mainly of modal components of the 1st, 2nd, and 4th modes, has a maximum excursion of approximately 15 and $\hat{y}$, which approximated the modal component of the 3rd mode, has a maximum displacement of around 0.4. This illustrated the relative weakness of the 3rd mode. Also, the resultant e in the 0-3 Hz narrowband excitation case as given in fig. 3.2.57 has a maximum error of 2.6, it is thus likely that the 3rd mode, of around 0.4 maximum excursion at full strength, would not show up in the "reduced-order" model. Finally, the present results indicated that curve fitting computations based on selected spectral data managed quite adequately to extract relevant information concerning the

(a)
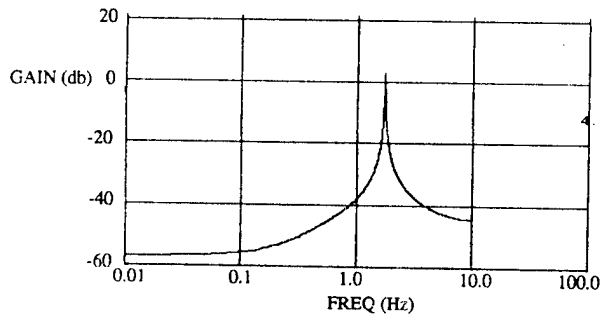
FREQUENCY (Hz)
1.71927920546976

DAMPING COEFFICIENT
5.148185168473725E-003

(b)
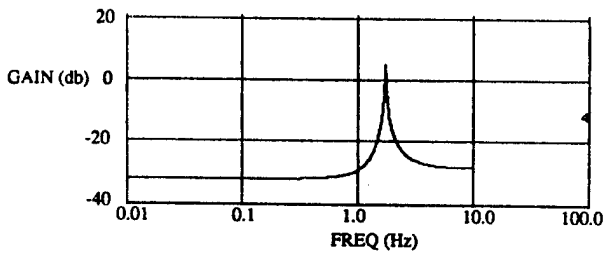
FREQUENCY (Hz)
1.71851144060777

DAMPING COEFFICIENT
1.039704242332437E-002
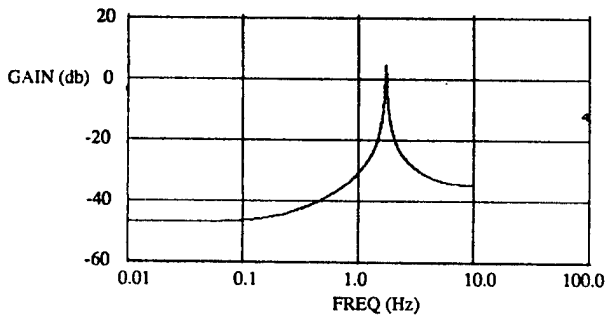
FREQUENCY (Hz)
1.71815564614365

DAMPING COEFFICIENT
1.024397455607727E-002

(c)
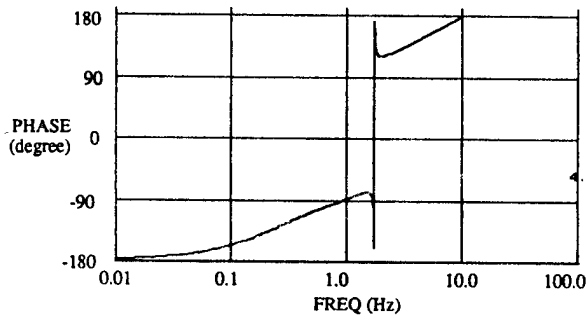
NUMERATOR COEFFICIENT
-8.281716010674900E-003
3.274240225201278E-002
-2.568733679606393E-002

DENOMINATOR COEFFICIENT
0.989002051571567
-1.70618877648530
1.00000000000000

Fig. 3.3-1 Curve Fitted Models of the 3rd Mode via Curve Fitting Computations of Selective Frequency Ranges:
(a) 1.5-2.0 Hz, (b) 1.6-1.8 Hz, (c) 1.65-1.75 Hz.

160
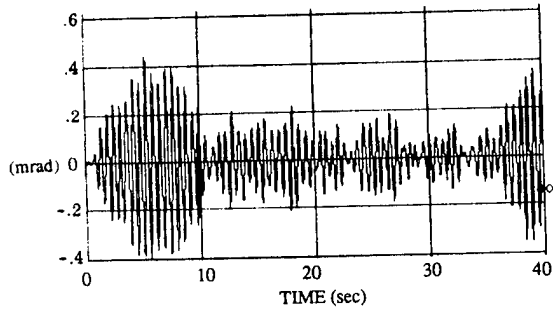
Fig. 3.3-2 The Computed Output $\widehat{y}$ of the 1.65-1.75 Hz Selected Range Curve Fitted Model.
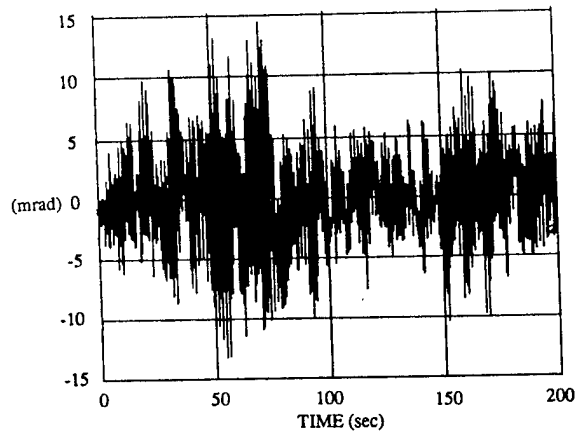
Fig. 3.3-3 The Output Error $e = y - \widehat{y}$ of the 1.65-1.75 Hz Selected Range Curve Fitted Model.
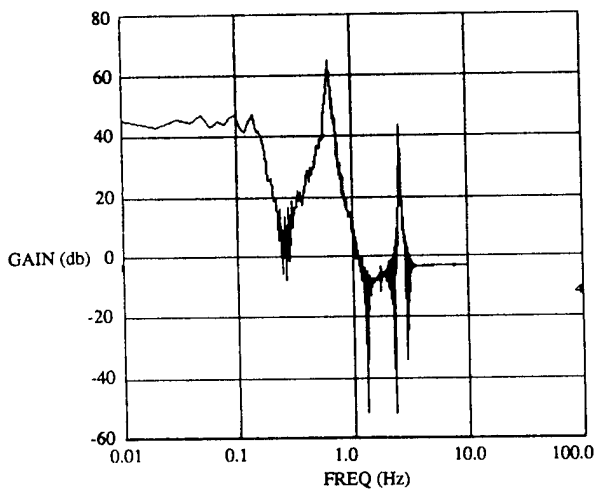
Fig. 3.3-4 Power Spectral Density P_{ee} of the Output Error of the 1.65-1.75 Hz Selected Range Curve Fitted Model.
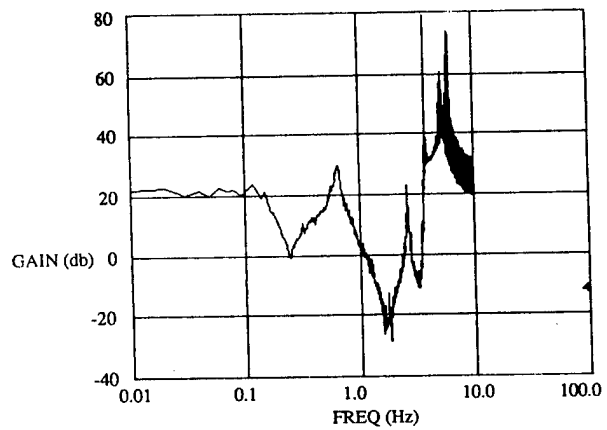
Fig. 3.3-5 Additive Uncertainty P_{ue}/P_{uu} of the 1.65-1.75 Hz Selected Range Curve Fitted Model.

161

residual mode.

The second residual mode to be investigated is the 5th mode at around 5 Hz. Spectral data were selected from a narrowband experiment having a band pass of 3-6 Hz. It should be noted that data from a different 3-6 Hz narrowband experiment than the one presented in section 3.2.3 was utilized here. The present data run still used a 20 Hz sampling frequency but lasted only 409.6 sec., with a total of 8192 input and output data recorded. It utilized a different set of parameters for its spectral estimation analysis. The reason is that for investigation of a mode at approximately 5 Hz, the frequency resolution required can be more relaxed than that of investigating a, say, 0.1 Hz mode. Previous experiments adopted a run time of 1638.4 sec. as dictated by the desired resolution for the 1st mode at 0.1 Hz. Here, a shorter run time can be afforded. The spectral estimation parameter was accordingly set as: MSE=512, NSE=8192, LSE=256, and NFFT=512. Detail discussion concerning the selection of spectral estimation parameters will be given in section 3.5.1. The instrumentation and other parameters set for the presently adopted 3-6 Hz narrowband experiment was the same as that before: hub torquer HA1 , hub sensor HS10, WBMEAN=0.0, WBSTAN=1.5, PER=66.7, and NBFIL=2.0.

Figures 3.3-6 and 3.3-7 show the 20 sec time histories of the input and output of the 3-6 Hz narrowband experiment. Maximum excursion of y is around 0.6. Figures 3.3-8 and 3.3-9 show the input and output PSDs. The input PSD P_{uu} confirms that the excitation was composed of frequency components between 3-6 Hz. The output PSD P_{yy} shows that though y apparently has an approximate 5 Hz modal component, the most dominant component is around 3 Hz which is actually due to the residual resonance of the 4th mode at 2.67 Hz. This is the same as the previous 3-6 Hz experiment described in section 3.2.4. The TFSE P_{uy}/P_{uu} is shown in figure 3.3-10. As for the narrowband experiment before, only the data within the passband is meaningful. From figure 3.3-10, the second residual mode, or the 5th mode, is apparent. Figure 3.3-11 shows the results of performing curve fitting on the spectral data of three selected ranges. The first ranged from 4 Hz to 5.5 Hz, yielding a frequency of 4.99 Hz and damping coefficient of 0.0043. Based on this, the second range is chosen to be from 4.5 Hz to 5.5 Hz, yielding a frequency of 5.033 Hz and a damping coefficient of 0.0066. The third range really narrowed down to eliminate as much as possible the residual effect of other major modes. It ranged from 4.8 Hz to 5.2 Hz and yielded a frequency of 5.03 Hz and a damping coefficient of 0.00562. Transfer functions for the curve fitted models are given in figure 3.3-11 for the selected ranges, with the phase plot included only for the third range. Several figures are given to illustrate the modelling performance. Figure 3.3-12 shows the computed output $\widehat{y}$ subjected to the same input u as in figure 3.3-6 for the 4.8-5.2 Hz selected range curve fitted model. Figure 3.3-13 shows the corresponding PSD P_{ee} of the output error $e = y - \widehat{y}$. Figure 3.3-14 shows the additive uncertainty Δ. Both P_{ee} and Δ show elimination of the mode component at around 5 Hz, indicating that identification of the residual mode has been satisfactory. $\widehat{y}$ has an amplitude of approximately 0.05, small compared with y of figure 3.3-7 which consisted mainly of the tail end of the 4th mode component. $\widehat{y}$ is even smaller compared to the combined effect of the 3 major modes which, as discussed before, summed up to a maximum excursion of the order of 15. Again, knowing the fact that fitting only the major modes would already generate an output error e of approximately 2.6 in amplitude,

162
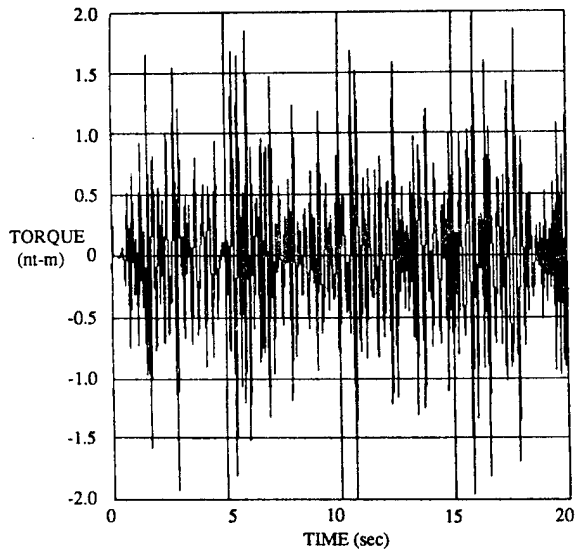
Fig. 3.3-6 Narrowband (3-6 Hz) Excitation Input.
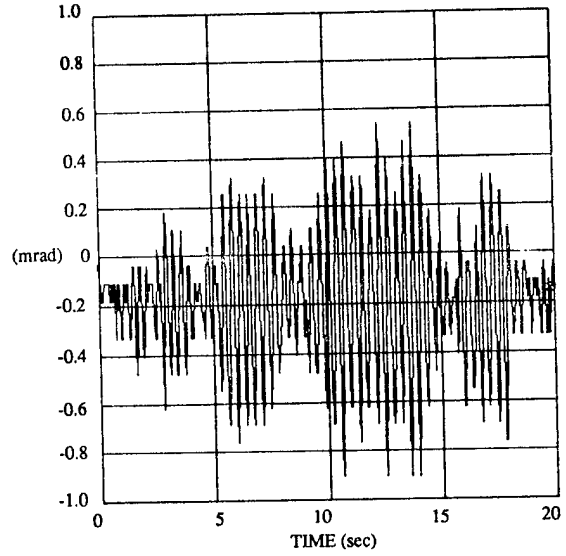
Fig. 3.3-7 Output Response of the 3-6 Hz Narrowband Excitation.
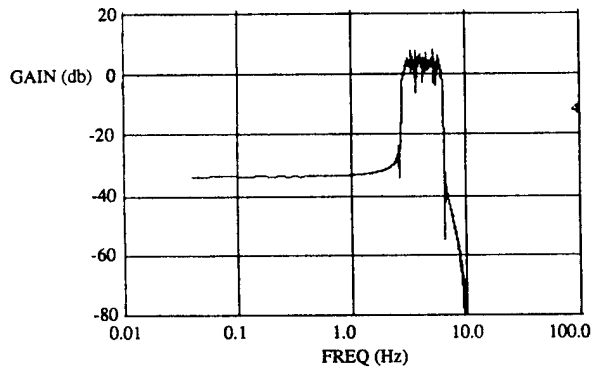
Fig. 3.3-8 Power Spectral Density P_{uu} of the 3-6 Hz Narrowband Excitation Input.
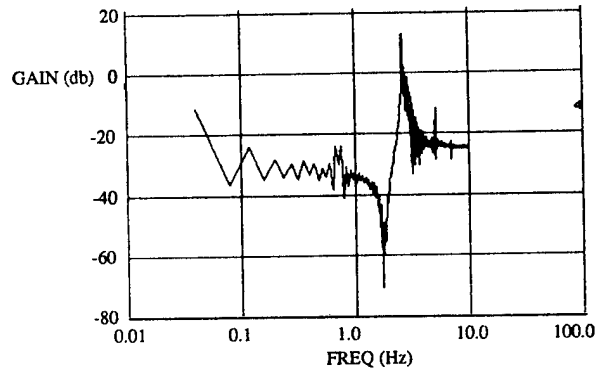

Fig. 3.3-9 Power Spectral Density P_{yy} of the 3-6 Hz Narrowband Excitation Output Response.
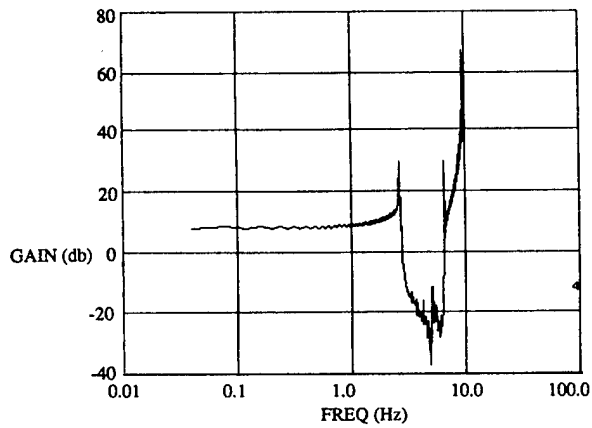

Fig. 3.3-10 Bode Plot of the Transfer Function Spectral Estimate $h = P_{uy}/P_{uu}$ of the 3-6 Hz Narrowband Excitation Experiment.

163

FREQUENCY (Hz)

4.98522342948152

DAMPING COEFFICIENT

4.295108317701316E-003

(a)
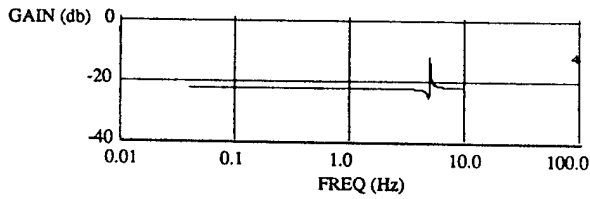
FREQUENCY (Hz)

5.03284905185639

DAMPING COEFFICIENT

6.611063446918967E-003

(b)

Fig. 3.3-12 The Computed Output $\hat{y}$ of the 4.8-5.2 Hz Selected Range Curve Fitted Model.
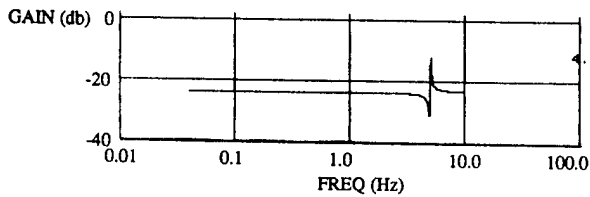
FREQUENCY (Hz)

5.02908029005084

DAMPING COEFFICIENT

5.619493054814747E-003

NUMERATOR COEFFICIENT

5.737764942000654E-002
-3.438888666685816E-003
5.449505448961031E-002

DENOMINATOR COEFFICIENT

0.982399887632248
1.810997422306237E-002
1.00000000000000

Fig. 3.3-13 Power Spectral Density P_{ee} of the Output Error of the 4.8-5.2 Hz Selected Range Curve Fitted Model.
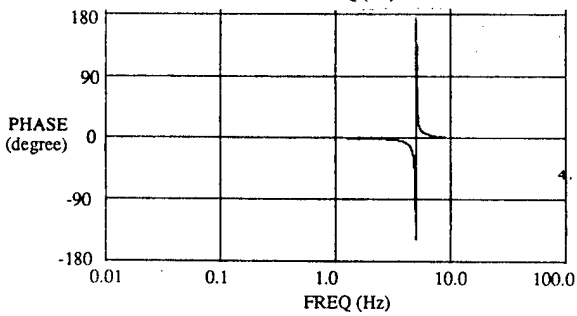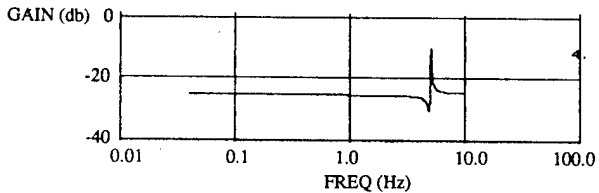
(c)

Fig. 3.3-11 Curve Fitted Models of the 5th Mode via Curve Fitting Computations of Selective Frequency Ranges: (a) 4.0-5.5 Hz, (b) 4.5-5.5 Hz, (c) 4.8-5.2 Hz.
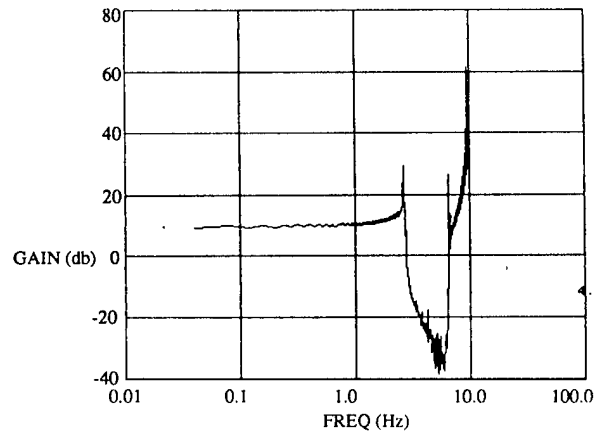
Fig. 3.3-14 Additive Uncertainty P_{ue}/P_{uu} of the 4.8-5.2 Hz Selected Range Curve Fitted Model.

164

it is understandable that the 5th mode did not show up in the curve fitting computations along with others.

The present section has demonstrated the capability of the experiment software to perform curve fitting on spectral data of selected ranges. It yields modal information of the two residual modes which are the 3rd and 5th system mode. As illustrated by output error analysis, the curve fitted results seemed to be quite adequate. In the next section, input frequency for the sine-dwell investigation of the residual modes will be selected based on this modal information. Understanding of why the residual modes did not show up in previous curve fitting computations with the major modes was also discussed here. As a final note, though it may be possible to incorporate the residual modal data into the identified "reduced-order" model, this would not help to improve the modelling performance of the identified parametric model. The modelling performance is dictated by the output error, e or $\Delta = P_{ue}/P_{uu}$, which depended heavily on the major modes.

3.3.2 Sine-Dwell Investigation

The previous section obtained modal data of the residual mode by curve fitting spectral transfer function data of selected frequency ranges. The residual modes were not physically excited and observed. The first residual mode was not observed from the output of the 0-3 Hz narrowband experiment as it was overshadowed by the presence of the three other major modes. Even for the narrowband experiment of 3-6 Hz, within which there lies only the second residual mode at around 5 Hz, the residual modal component was obscured by a 3 Hz component which was the tail end of the 4th mode at 2.67 Hz. It would seem that to clearly excite a residual mode, a very narrow filter properly set at the residual modal frequency would have to be used. Sine-dwell excitation is just such a filter carried to the limit. It utilizes the full force of the actuator to implement a sinusoidal input at a particular frequency. By scanning the sine-dwell frequency through a narrow range about the plausible residual modal frequency, resonance should occur at certain frequency which can be associated with the residual mode. In addition, by forcing the sinusoidal inputs until steady state is established, real and imaginary parts of the system transfer fucntion at that frequency can be computed, stored, and processed for curve fitting. As such, excitation of the residual mode can be physically observed and the residual modal information can be generated.

The sine-dwell investigation of the first residual mode, i.e., the 3rd system mode, is presented here. The sine-dwell parameter SAMP and TGRIM were set to be 2 nt-m and 10 sec, respectively. They reflected that the maximum actuation level of 2 nt-m and an averaging time of 10 sec are being used for the experiment. Results from previous sections indicated a frequency of approximately 1.7 Hz for this residual mode. The parameter TGRIM=10 sec thus amounted to roughly 17 cycles of modal oscillation and should be adequate for averaging. The other unassigned parameter SDFREQ which is the frequency of the sinusiodal input excitation, would take on values around 1.7 Hz. The sampling frequency was kept at 20 Hz. The total experiment run time is 200 sec which amounted to 340 cyles of the residual mode. Given the anticipated damping coefficient of the mode, this should be long enough to achieve steady state dynamics.

The following figures present data for the sine-dwell run of 1.7 Hz input excitation, i.e. SDFREQ=1.7 Hz. Figure 3.3-15 shows the sine-dwell input for 20 sec. Figures 3.3-16 and 3.3.17 show the time histories of the output for 200 sec and 50 sec, respectively. Figure 3.3-16 shows that steady state has indeed been reached. Figure 3.3-17 reveals the frequency content of the approximately 1.7 Hz component in the output. Table 3.3.1 shows the real and imaginary parts of the system transfer function as computed for the last 100 sec of the run. The values vary very little, again confirming that steady state has been achieved. Figure 3.3-18 compares the 200 sec time histories of the sine-dwell experiment outputs at input frequencies of 1.66 Hz, 1.68 Hz, 1.69 Hz, 1.70 Hz, 1.71 Hz, 1.72 Hz, and 1.74 Hz. It clearly shows a maximum output amplitude at 1.7 Hz input frequency, indicating modal resonance. The modal frequency of this residual mode must therefore be quite close to 1.7 Hz, a fact consistent with previous analysis. Table 3.3.2 listed the input sine-dwell frequencies and corresponding real and imaginary parts of the system transfer function. The phases of the transfer function as computed from the real and imaginary parts are also given. At around modal resonance of 1.7 Hz, the phase is roughly -155 degrees. The phase would have been + or -90 degrees had this been the only mode in the system. However, this is not the case and so the residual effect of other modes contributed to the phase value. Another observation from Table 3.3.2 is that the phase drops abruptly by a large amount close to 1.7 Hz, again indicating modal resonance around that frequency.

In practice, frequency selection of sine-dwell investigation is based on knowledge obtained through full range or selected range spectral transfer function curve fitting. Even so, it is not likely that the sine-dwell input frequency will be exactly on the structural modal frequency, as only so many sine-dwell experiments can be performed. One way to enable better modal identification is to implement a search routine stepping towards the frequency with the largest gain of the computed transfer function, counting that residual effects of other modes on the gain are minimal. Note that the frequency resolution for sine-dwell investigation, however, is dictated by the reciprocal of the experiment run time and the signal to noise level.

Another way to obtain more detail modal data via sine-dwell investigation is to perform curve fitting on the real and imaginary parts of the computed system transfer function. This capability was built into the present experiment software. The data in Table 3.3.2 were put into a sine-dwell data file from which they were read and processed by the curve fitting algorithm. The results are as given in figure 3.3-19 which presents the transfer function gain and phase of the curve fitted model. The frequency and damping coefficient of this first residual mode are determined to be 1.702 Hz and 0.00571. This is reasonably close to the values of 1.718 Hz and 0.01024 as identified for this mode in the previous section.

Maximum actuation level SAMP=2 nt-m is again set for the sine-dwell investigation of the second residual mode which is the 5th system mode. Other parameters were set as according to the fact that previous analysis pointed to a modal frequency of around 5 Hz for this mode. The averaging time TGRIM was set at 5 sec which amounted to averaging approximately 10 cycles of oscillations. The experiment run time remained at 200 sec to ensure steady state dynamics. Instead of 20 Hz, the sampling frequency was increased to 30 Hz, the reason being that generation of a 5 Hz sinusoidal input with a 20 Hz sampling
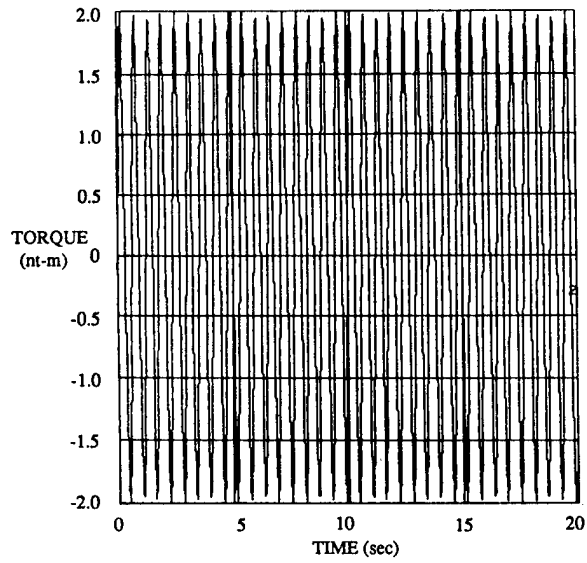
Fig. 3.3-15 Sinedwell Input Excitation for 1.7 Hz Frequency.
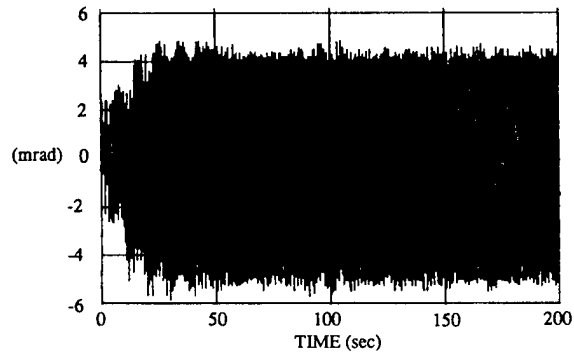
Fig. 3.3-16 Output Response at Sensor HS10 Subjected to the 1.7 Hz Sinedwell Input Excitation Implemented at Actuator HA1.
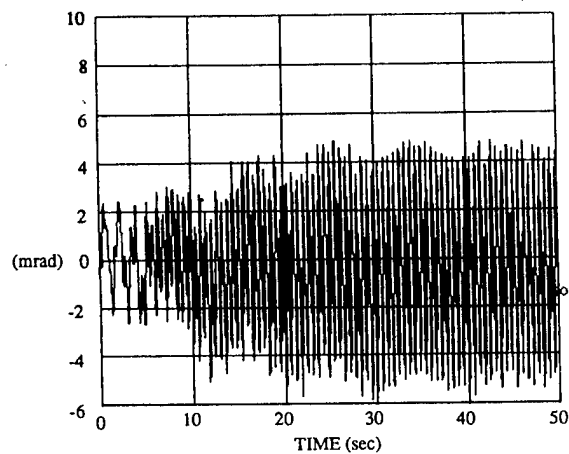

Fig. 3.3-17 Expanded View of Output Response at Sensor HS10 Subjected to 1.7 Hz Sinedwell Input Excitation at Actuator HA1.

167
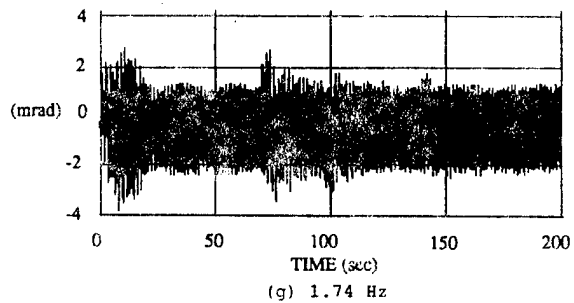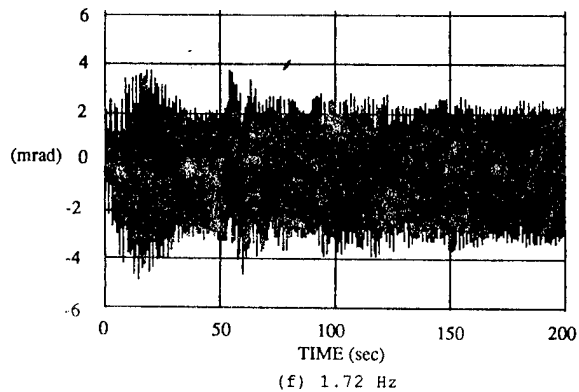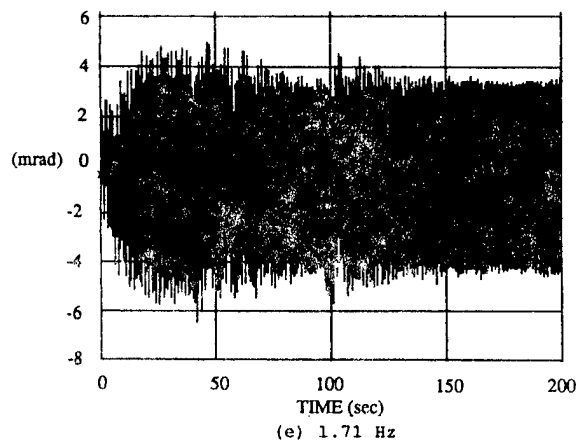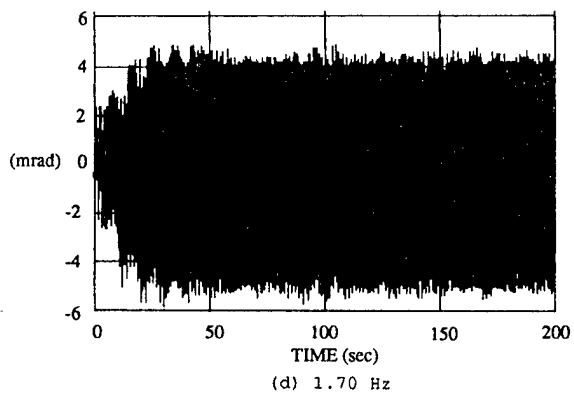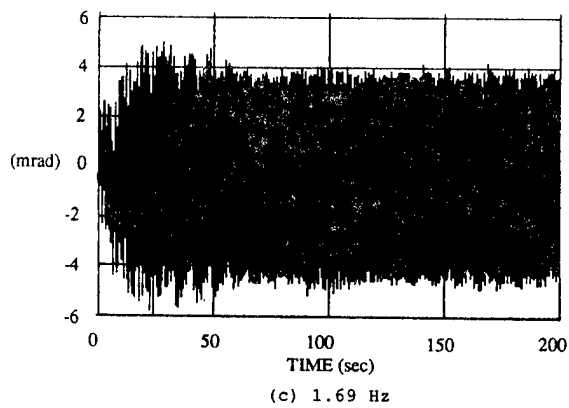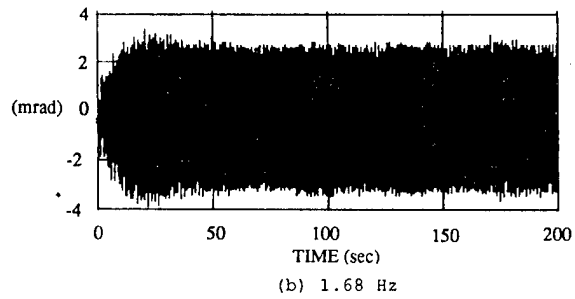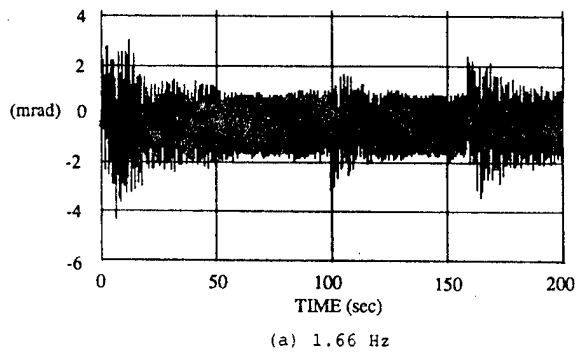
Fig. 3.3-18 Comparison of Output Responses at Sensor HS10 Subjected to Sinedwell Excitations of Frequencies (a) 1.66 Hz, (b) 1.68 Hz, (c) 1.69 Hz, (d) 1.70 Hz, (e) 1.71 Hz, (f) 1.72 Hz, and (g) 1.74 Hz at Actuator HA1.

FREQUENCY (Hz)	DAMPING COEFFICIENT
1.70152820399374	5.705027584449422E-003

NUMERATOR COEFFICIENT	DENOMINATOR COEFFICIENT
-1.041461212868897E-002	0.993919307999804
3.246150048205832E-002	-1.71575467567672
-2.747871818793629E-002	1.00000000000000
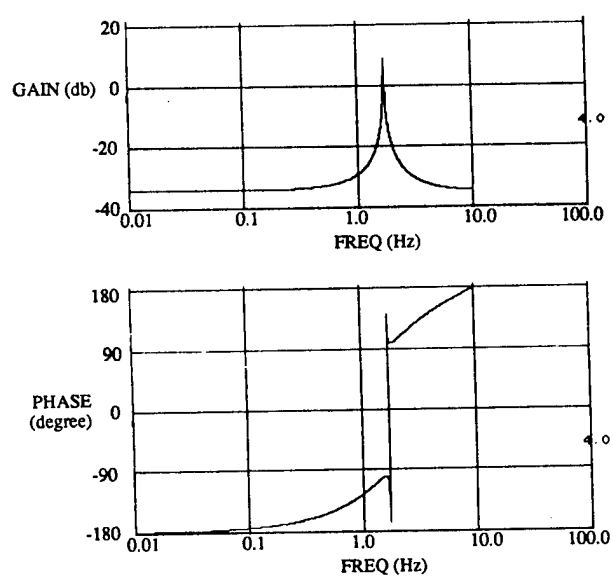
Fig. 3.3-19 Curve Fitted Model of the 3rd Mode Based
on Sinedwell Excitation Data.

169

TABLE 3.3-1
Computed Real and Imaginary Parts of System Transfer
Function For Sine-Dwell Investigation of The 3rd Mode

Time (sec)	Real Part	Imaginary Part
100	-2.05414	-0.83419
110	-2.02237	-0.88742
120	-2.00977	-0.89982
130	-2.05409	-0.81231
140	-2.04397	-0.84610
150	-2.01537	-0.89309
160	-2.00668	-0.90468
170	-2.05053	-0.81733
180	-2.03962	-0.85687
190	-2.01274	-0.90788
200	-2.00255	-0.91835

TABLE 3.3.2
System Transfer Function Computed at
Different Sine-Dwell Input Frequency

Sine-dwell Freq (Hz)	Real Part	Imaginary Part	Phase (degrees)
1.66	-0.164613	-0.587671	-105.65
1.68	-0.669877	-1.232019	-118.53
1.69	-1.271916	-1.425530	-131.74
1.70	-2.006244	-0.924542	-155.26
1.71	-1.184758	1.474806	-231.22
1.72	-0.544025	1.165272	-244.97
1.74	-0.219744	0.753130	-253.73

170

period would amount to a representation of only 4 data points per cycle which is clearly not adequate. At 30 Hz sampling frequency, the representation is better though not the best with 6 data points per cycle. Figure 3.3-20 shows the 10 sec time history of a 5 Hz sinusoidal input represented under a sampling frequency of 30 Hz. The input excitation did not reach the maximum amplitude of 2 nt-m because of the limited number of available data points. However, in order to leave adequate time for the execution of the experiment software, a higher sampling frequency is not sought. Figure 3.3-21, 3.3-22, and 3.3-23 show the results of the investigation at 5 Hz sine-dwell input frequency. They respectively show the 133 sec, 50 sec, and 20 sec time histories of the hub angular sensor subjected to a 5 Hz sinusoidal input. The figures indicated a large component of the 2nd system mode at around 0.64 Hz. Step representation of sinusoidal input as in this case inherently induced excitation of other modes in the structure and the 2nd system mode is the strongest among them. Besides the 2nd mode, however, the figures, especially figure 3.3-23, indeed indicated excitation of an approximately 5 hz mode. Presence of the 2nd modal component did not affect the calculation of the real and imaginary part of the system transfer function. This is because during the computation, only the components close the sinusoidal input frequency which is 5 Hz are being correlated to yield the results. Representations of these results for the last 66.7 sec of the experiment run are given in Table 3.3.3. They show reasonably steady state results. Figure 3.3-24 compares the 50 sec time histories of the hub sensor outputs for the sinusoidal investigations at input frequencies of 4.9 Hz, 4.95 Hz, 5 Hz, 5.05 Hz, and 5.1 Hz. It is visualized that, taking out the approximate 0.64 Hz component, modal resonance would occur at close to 5 Hz, consistent with previous analysis. Table 3.3.4 listed the computed real and imaginary parts of the system transfer function at different input frequencies. The phases are also included. Roughly, the phase goes from 156, 172, 70, 20, and 10 degrees, again showing a steep drop at around 5 Hz which indicated possible modal resonance. As for the first residual mode, more detailed modal information of the residual mode under investigation was obtained by curve fitting the data as listed in Table 3.3.4. Figure 3.3-25 shows the gain and phase of the identified model as obtained. The modal frequency is determined to be 4.99 Hz while the damping coefficient is 0.003. They are compared reasonably to the values of 5.029 Hz and 0.0056 that were determined in previous section.

3.4 Nonlinearity Investigation

This section describes the nonlinearity investigation of the structure via wideband and sine-dwell excitations. As is, the structure allows a maximum of +5 cm excursion on the ribs and +2 degree rotation on the hub. If nothing else, this will be the high bound of system linearity. Care was taken to avoid exciting the structure beyond these limits during experimentation to avoid causing any damage. In case of small excursions, effects of stiction, hysteresis, etc., are expected to come in and again make the system nonlinear. High and low bounds of linearity for the system are therefore expected. The existing finite element model of the structure generally assumed a linear range of roughly +2 cm for the rib tip and +1 degree for the hub angle with zero excursion low limit. Here, attempts were made to infer this linear range from experiments. All experiments in this section were performed about the Rib4/Rib10 axis with the hub actuator HA1.

171
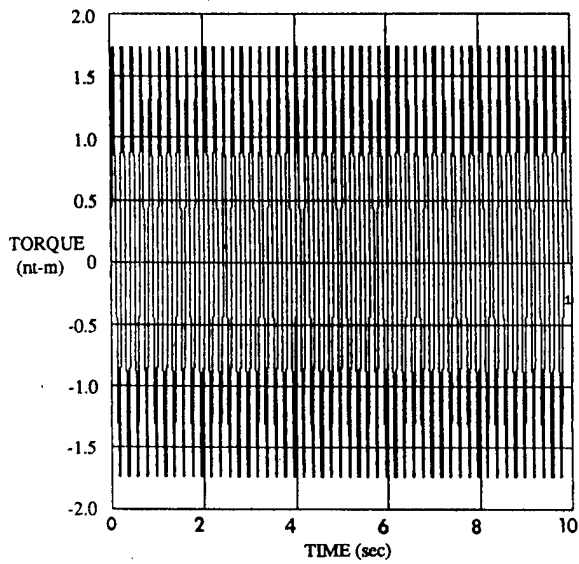
Fig. 3.3-20 Sinedwell Input Excitation for 5.0 Hz Frequency.
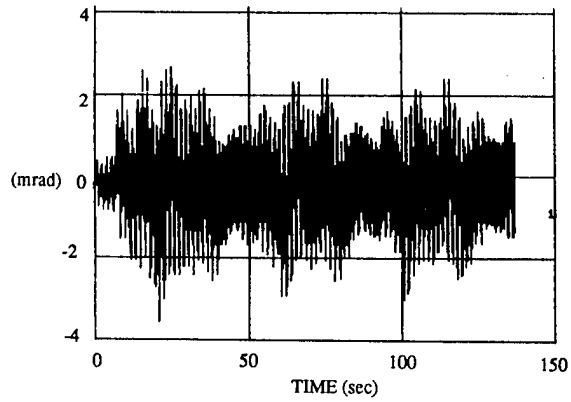
Fig. 3.3-21 Output Response at Sensor HS10 Subjected to the 5.0 Hz Sinedwell Input Excitation at Actuator HA1.
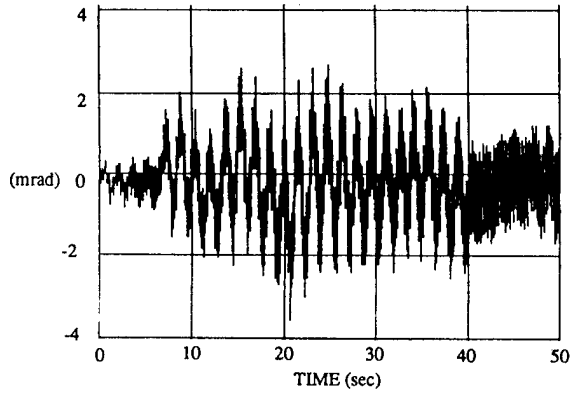

Fig. 3.3-22 Expanded View of Output Response at Sensor HS10 Subjected to 5.0 Hz Sinedwell Input Excitation at Actuator HA1.
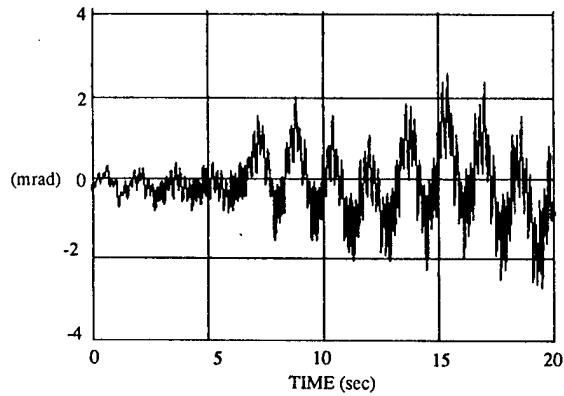

Fig. 3.3-23 Expanded View of Output Response at Sensor HS10 Subjected to 5.0 Hz Sinedwell Input Excitation at Actuator HA1.

172
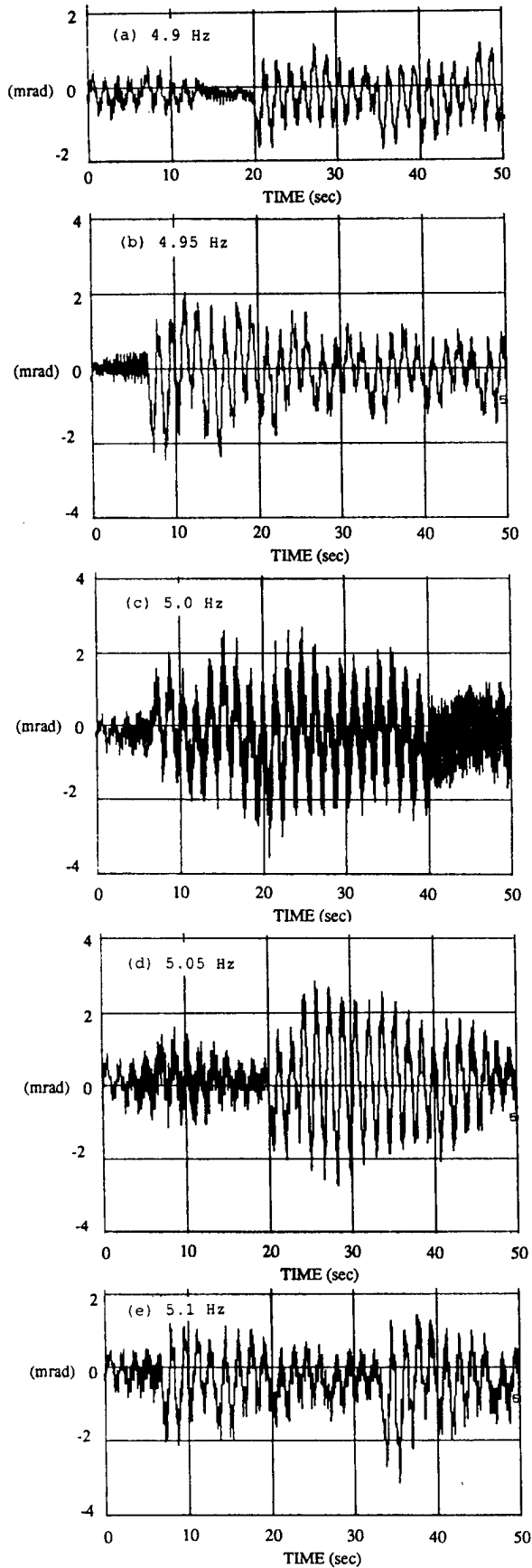
Fig. 3.3-24 Comparison of Output Responses at Sensor HS10 Subjected to Sinedwell Excitations of Frequencies (a) 4.9 Hz, (b) 4.95 Hz, (c) 5.0 Hz, (d) 5.05 Hz, and (e) 5.1 Hz at Actuator HA1.

FREQUENCY (Hz)	DAMPING COEFFICIENT
4.99429740636348	2.987333337065182E-003

NUMERATOR COEFFICIENT	DENOMINATOR COEFFICIENT
6.326907515696362E-002	0.990669520739737
-5.217465847959361E-003	-3.566241866811324E-003
6.302110962052503E-002	1.00000000000000
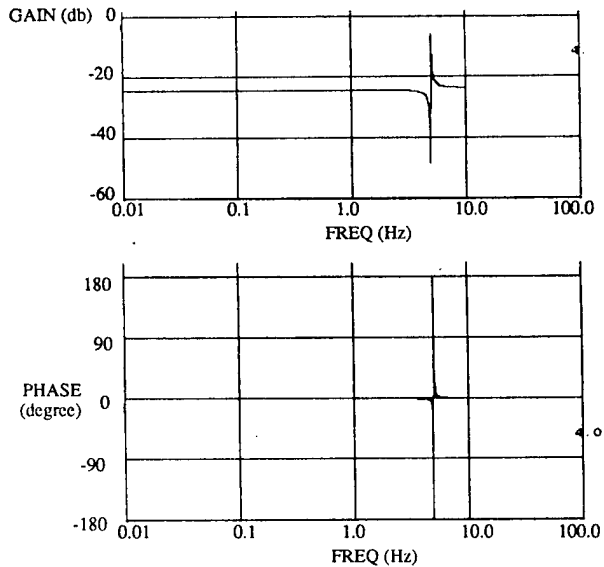
Fig. 3.3-25 Curve Fitted Model of the 5th Mode Based on Sinedwell Excitation Data.

173

TABLE 3.3-3
Computed Real and Imaginary Parts of System Transfer
Function For Sine-Dwell Investigation of The 5th Mode

Time (sec)	Real Part	Imaginary Part
133.3	0.19971	0.51614
140.0	0.22797	0.49368
146.7	0.21305	0.50273
153.3	0.20188	0.49462
160.0	0.19861	0.49020
166.7	0.21494	0.51424
173.3	0.19941	0.51791
180.0	0.22970	0.49640
186.7	0.21799	0.50005
193.3	0.19996	0.49445
200.0	0.19424	0.48952

TABLE 3.3.4
System Transfer Function Computed at
Different Sine-Dwell Input Frequency

Sine-dwell Freq (Hz)	Real Part	Imaginary Part	Phase (degrees)
4.90	-0.019156	0.0085858	155.86
4.95	-0.108024	0.0142690	172.48
5.00	0.181920	0.4877198	69.50
5.05	0.202054	0.0737014	20.04
5.10	0.130458	0.0218893	9.52

174

3.4.1 Wideband Excitation Approach

In this approach, the structure was excited at different excursion levels with wideband excitations and the output responses were observed and compared. The experiments were performed about the 4-10 axis. The hub torquer HA1 was used for input excitation. For output observation, three sensors were used: HS10, LI1, and LO1. They are, respectively, the hub angular sensor of the 4-10 axis, the inner levitator sensor on rib #1, and the outer levitator sensor on rib #1. Rib #1 is orthogonal to the 4-10 axis, structural displacements on the rib due to torquing about the axis are very observable with these sensors. Moreover, the outputs yield a good understanding of how modal displacement are being sensed along the rib.

Four experiments, gradually decreasing in input command amplitudes and hence, resultant structural excursions, were performed. The experiment run times were 40 sec. To enable effective output comparsions, the same sequences of input commands were used for all experiments, only that they are scaled by different constants. Thus, if the structure were truly linear, excursions subjected to different excitations should be scaled correspondingly.

Figure 3.4-1 shows the results of the investigation. The first column presents the input excitations of the four wideband excitations. They are the same input sequences scaled to have maximum amplitudes of 2 nt-m, 1.5 nt-m, 1.0 nt-m, and 0.5 nt-m, respectively. The second, third, and fourth columns show the corresponding structural excursions as observed in sensors HS10, LI1, and LO1. Previous results had revealed that the two modes at roughly 1.7 Hz and 5 Hz are relatively weak. This explains why only three out of the five modes are observable by the sensors as in figure 3.4-1. Referring to fig. 1.3-5, which shows the mode shapes of the boom-dish modes of the structure as generated by finite element modelling method, these three modes would be most observable with the hub angular sensor as indicated by their mode shapes. Moreover, the inner levitator sensor LI1 would not be too effective in observing the 2.7 Hz mode as it is located close to the nodal point of the mode. Similarly, the outer levitator sensor LO1, sitting near the nodal points of both the 0.64 Hz and 2.7 Hz modes, would not be effective in observing these two modes. It is also noted that, especially for experiments subjected to stronger input excitations, the excursions as observed by the levitator sensors seem to be in the opposite direction as that by the hub angular sensor. This is due to the adopted definition for positive angular rotation and rib displacement in this work, and is again consistent with the mode shape of the observed modes as given in figure 1.3-5. These observations are all reflected in figure 3.4.1. Hence, general results from the experiments seem to validate the mode shapes generated by the finite element structural model.

The second column in figure 3.4-1 is now considered in more detail. Three distinct modal components are observed during experiments subjected to relatively strong excitation. Comparison of the first two experiments reveals that, more or less, they are properly scaled. This indicates that the structure as observed by the hub angular sensor indeed behaves as a linear system at the corresponding levels of actuation and displacement. At lower actuation level, however, the 1st modal component appears to drop out leaving only the 2nd and 4th modal components. The structure therefore loses its linearity. However, these two remaining modes by themselves seem to retain linearity pretty well even to the

Output Response at Sensor HS10
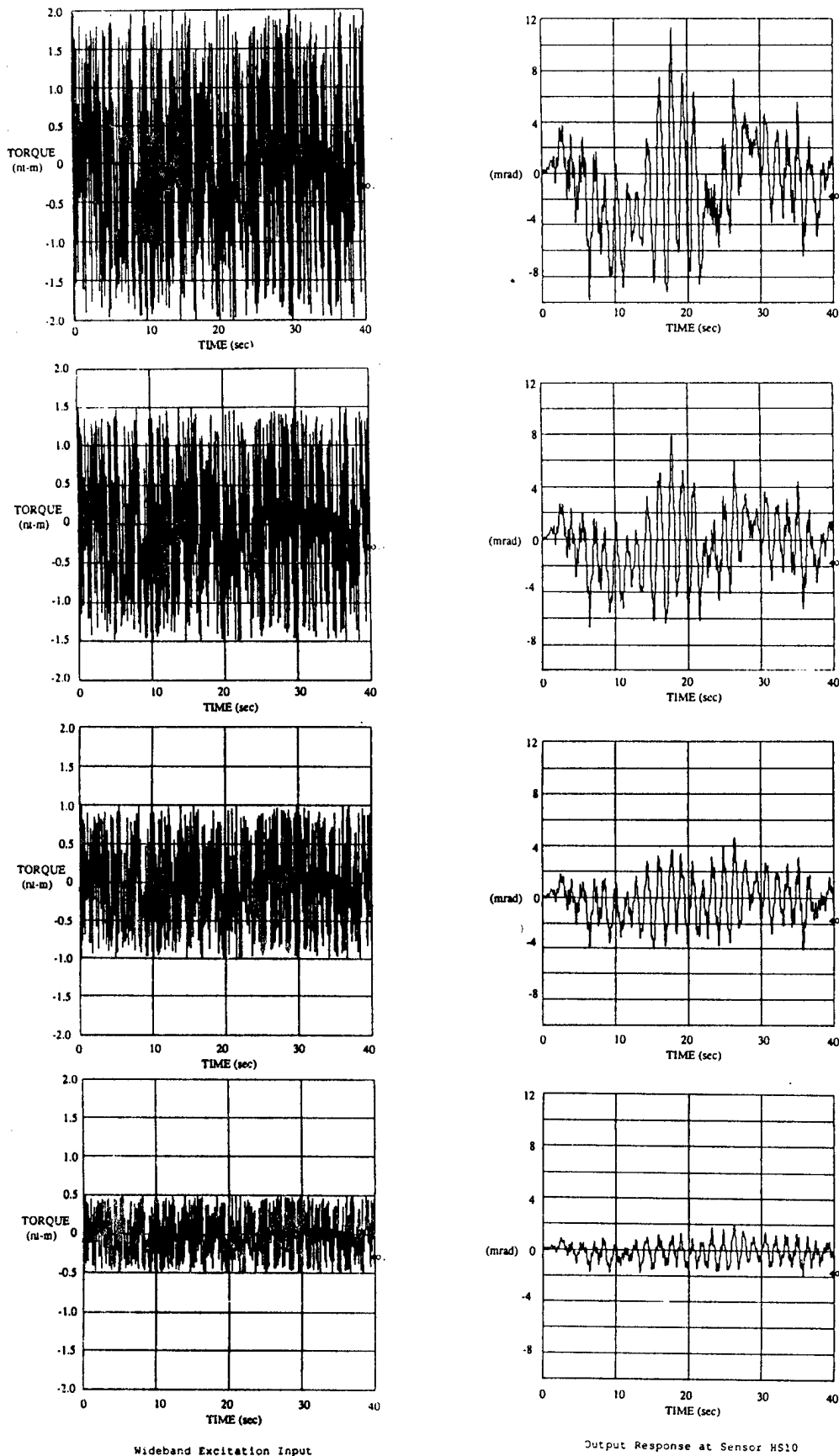
Fig. 3.4-1 Comparison of Output Responses at Sensor HS10, LI1, and LO1 Subjected to Wideband Excitations of Maximum Amplitudes 2 nt-m, 1.5 nt-m, 1.0 nt-m, and 0.5 nt-m at Actuator HA1.

176

case of 0.5 nt-m actuation amplitude.

The third column in figure 3.4-1 shows the excursions as observed at the inner levitator sensor on rib #1. As discussed before, the 4th mode at around 2.7 Hz was not as prominently observed here as with the hub sensor. Also, the component of the 1st mode drops off faster at decreasing input excitation than that of the hub angular sensor. As the input excitation amplitudes go from 2 nt-m to 1.5 nt-m, the 1st modal component seems to decrease by a factor of 3, and almost disappears in the following experiments with smaller excitation amplitudes. The dominant 2nd mode at around 0.64 Hz, however, seems linear for all experiments.

The fourth column compares the responses as measured by the outer levitator sensor. Again, the the 1st modal component drops off quickly at decreasing excitation. As discussed before, there is less of the 2nd modal component in the responses and the 4th mode around 2.7 Hz is clearly not noticeable. Due to its observability, the remaining 2nd mode now does not seem linear at weak excitations.

Several points are to be noted from the above discussion. First, observations by the three sensors seem to be consistent with the mode shapes of the structure as calculated from finite element method. Second, the lowest frequency 1st mode seems to drop off rapidly at low excitations. There seems to be a damping mechanism acting strongest on low frequency modes. Third, the drop off rate of the 1st mode is faster for the levitator sensor measurements, pointing to perhaps a localized damping mechanism. Fourth, more or less, the stronger modal component of the 2nd mode retains its linearity even at small excitation. Fifth, all told, linearity of the system depends on the sensor being utilized as well as the levels of actuation. When using the hub sensor, the system can be regarded as linear if the excitation amplitude ranges from 1.5 nt-m to 2 nt-m, resulting in hub angle rotations of ranging from 7 mrad to 15 mrad.

3.4.2 Sine-Dwell Excitation Approach

The previous section showed that the 2nd system mode at around 0.64 Hz mode is the strongest among all observable modes. It constitutes the most dominant component and adheres more or less to linearity even at low excitation inputs. In this section, sine-dwell investigation will be performed on this mode for a better understanding of its behavior in frequency domain.

The investigation utilizes 0.63 Hz sinusoidal inputs of various amplitudes to excite the system. Hub torquer HA1 and angular sensor HS10 corresponding to the 4-10 axis were used for instrumentations. The frequency of 0.63 Hz was chosen as it is close to the identified frequency of the 2nd system mode under investigation. The sampling frequency was 20 Hz. Each sine-dwell experiment lasted 300 sec.

Figure 3.4-2 shows, for 200 sec, the system responses of the 0.63 Hz sinusoidal experiments. The amplitudes of the inputs were 0.1 nt-m, 0.2 nt-m, 0.3 nt-m, 0.4 nt-m, and 0.5 nt-m. Note that responses for input amplitudes of 0.5 nt-m, 0.4 nt-m, and 0.3 nt-m have roughly the same peak time for their envelopes, 35 sec. Maximum excursions of the envelopes are, roughly, 37 mrad, 30 mrad, and 23 mrad. Steady state excursions of the

envelopes are 27 mrad, 22 mrad, and 17 mrad. These values of the envelopes are in proportion to their respective sine-dwell amplitudes of 5, 4, and 3. In contrast, the envelope of the response corresponding to a input amplitude of 0.2 nt-m has a peak time of 50 sec, while that of the 0.1 nt-m input amplitude seems not to peak at all. Their excursion values are also not consistent with the relative ratio of their input amplitudes. As such, figure 3.4-2 indicated that the system behaves as a linear system at sinusoidal input amplitude ranging from 0.3 nt-m to 0.5 nt-m.

The same observation can be obtained from table 3.4.1 which lists the phase values of the system as computed from the sine-dwell data of real and imaginary parts of the transfer function. The output responses in figure 3.4-2 had indicated that steady states have been reached at around 200 sec. Computed at around 300 sec, the phase values were indeed near stationary for individual experiments. Table 3.4.1 shows that the phase values are -199.1, -196.9, -190.3, -185.4, and -70.4 degrees in order of decreasing input amplitudes. The near constancy of the phases for the first three and maybe four experiments indicates linearity at those input amplitudes. Also shown in Table 3.4.1 are the modal frequencies and damping coefficients as calculated by the envelope of the responses. Again, the values for the first three or four experiments are approximately equal and an indication of a linear system. The frequency and damping values were calculated on the simplified analysis that the 2nd mode is the only mode existed in the system. This explains why they are somewhat different from that obtained through transfer function curve fitting.

In short, the present investigation concludes that at low actuation levels, the system tends to be nonlinear. The low bound of the linear range depends on sensor location and the modal component of interest. The present analysis conducts its model identification as though the system is linear. It can be argued that the model identified is thus good only for the level of actuation utilized and has a limit range of validity. Such considerations underscore the importance of careful system identification.

3.5 Parameter Selection and Variation

This section discusses the underlying reasonings for selecting the nominal values of spectral estimation parameters and smoothing factor for curve fitting. The effects of parameter variations from their nominal values on the identification results are also presented.

3.5.1 Spectral Estimation Input Parameters

Except for the 3-6 Hz narrowband experiment, spectral estimation parameters adopted for present analysis were: MSE=2048, NSE=32768, LSE=1024 AND NFFT=2048. Their selection were based on the following considerations:

1. The spectral estimation algorithm computes the power spectral density by taking the Fourier transform of the correlation, with LSE being the number of correlation values utilized for the computation. The resultant frequency resolution for the power spectral densities follows to be 1/(LSE*T) where T is the sampling period. For the present case where the lowest frequency mode is around 0.1 Hz and the sampling frequency is 20 Hz, LSE is selected to be 1024 to achieve the desired resolution of approximately 0.02 Hz.
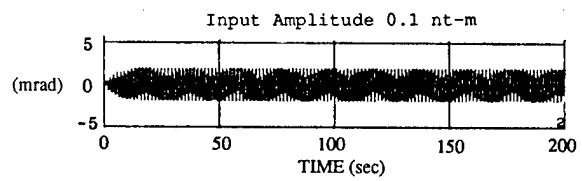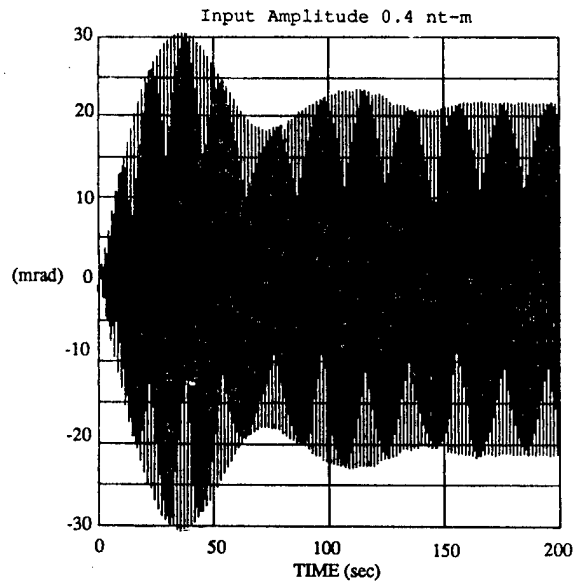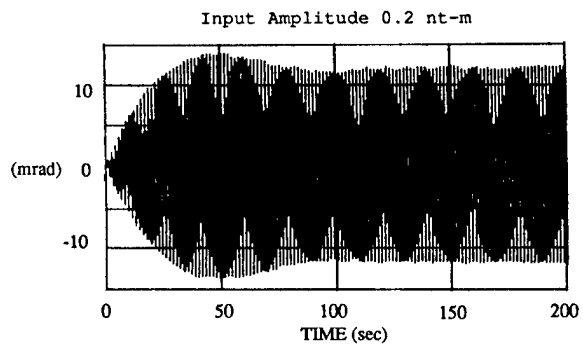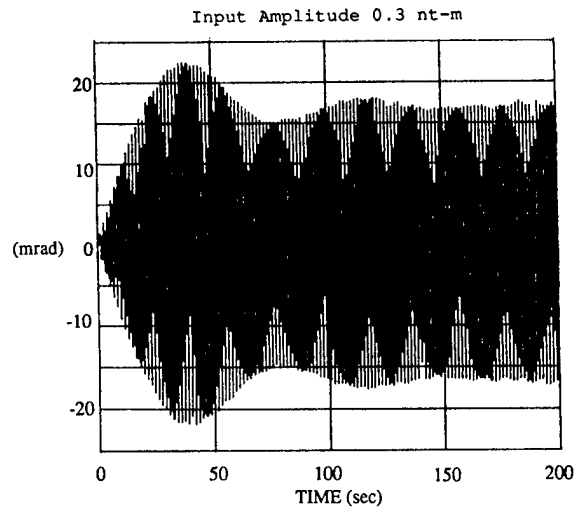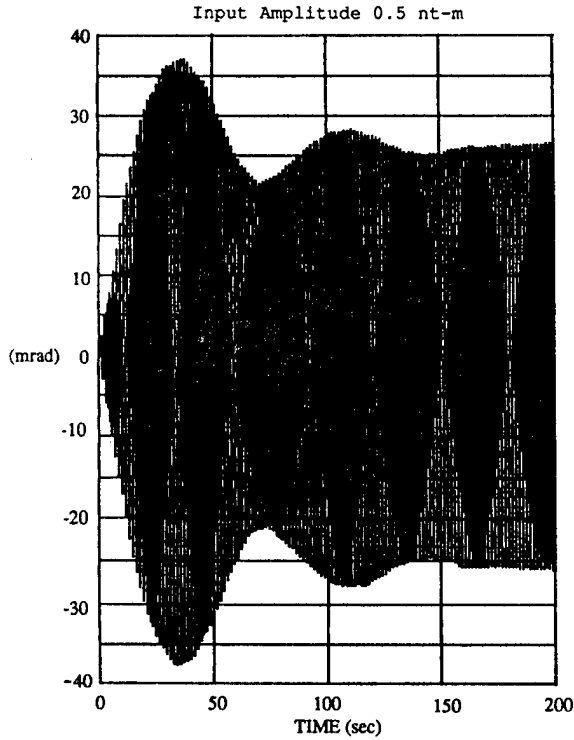
Fig. 3.4-2 Comparison of Output Responses at Sensor HS10 Subjected to
Sinusoidal Input Excitations of 0.64 Hz and Amplitudes
0.5 nt-m, 0.4 nt-m, 0.3 nt-m, 0.2 nt-m, and 0.1 nt-m at
Actuator HA1.

180

Table 3.4.1
Computed Phase Value, Frequency, and Damping Coefficient
at Different Sine-Dwell Input Amplitudes

Sine-Dwell Input Amplitude (nt-m)	Phase (degrees)	Frequency (Hz)	Damping Coefficient
0.5	−199.1	0.642	0.006
0.4	−196.9	0.642	0.006
0.3	−190.3	0.642	0.007
0.2	−185.4	0.64	0.01
0.1	−70.4	0.64	0.03

2. The number NFFT is the FFT size (power of 2) used to compute the power spectral densities from the correlations. Note that with the same LSE, increasing NFFT only represents a more detailed representation of the same power spectral density estimate, and not a more accurate estimate of the spectrum. The estimate of the spectrum is determined solely by the choice of LSE. The minimum value of NFFT is 2*LSE-1. For the present case, NFFT is selected to be 2*LSE.

3. The number MSE is the section size. Its relevancy lies in the fact that it governs the number of correlation values generated by the spectral estimation algorithm which is MSE/2+1. This, together with the fact that LSE=1024 correlation values are to be used for computing the power spectral densities, leads to the selected value of 2048 for MSE.

4. Finally, the total number of data points, NSE, is to be set. On given NSE, the algorithm divides the data array of NSE points into sections each consisting of MSE data points. The correlation values as generated from each section will be averaged out to yield the final results. The size N thus relates to the standard deviation of the correlation values and hence that of the power spectrum. To have an accurate estimate of correlation and power spectral density values, NSE>>MSE is recommended. It was determined by experiences that NSE=16*MSE=32768 yields quite satisfactory results. With NSE=32768 and t=0.05 sec for 20 Hz sampling, the experiment run time, which equals NSE*T, turns out to be 1638.4 sec.

The aforementioned nominal parameters are utilized for the analysis of wideband experiments and the 0-3 Hz narrowband experiments all of which involve the 0.1 Hz mode in their identification. A different set of spectral estimation parameters was set, however, for the 3-6 Hz narrowband experiment investigating the 5th system mode which is roughly 5 Hz frequency. As a resolution of roughly 0.1 Hz would suffice for this mode, LSE is set to be 256. By the same reasoning as above, this subsequently yielded NFFT=512, MSE=512, and NSE=8192. These were the parameters adopted for spectral analysis in section 3.3.1.

To have a better understanding of their effects on the identification results, input and output data from the same wideband experiment run as presented in section 3.2.3 was processed adopting different sets of spectral estimation input paramters. First, main results of section 3.2.3 are repeated here for comparison. Figure 3.5-1, figure 3.5-2, figure 3.5-3, and figure 3.5-4 show respectively the gain of the TFSE P_{uy}/P_{uu}, the gain of the 3 mode identified parametric model, the output error e, and the additive uncertainty Δ of the wideband experiment. They were generated using the nominal spectral estimation parameters of MSE=2048, NSE=32768, LSE=1024, and NFFT=2048, and are the same as figure 3.2-29, figure 3.2-33, figure 3.2-35, and figure 3.2-37 of section 3.2.3.

The identification process was repeated using the same input and output data but a different set of spectral estimation parameters of MSE=4096, NSE=32768, LSE=2048, and NFFT=4096. Figure 3.5-5 shows the TFSE P_{uy}/P_{uu}. Compared with figure 3.5-1, it has a finer frequency resolution but is more jittery. This is expected as a larger LSE yields a finer frequency resolution but also a larger section size MSE which would lead to a smaller number of averaging sections with NSE kept constant. The spectral data obtained averaging over this smaller number of sections thus has more peaks and spikes
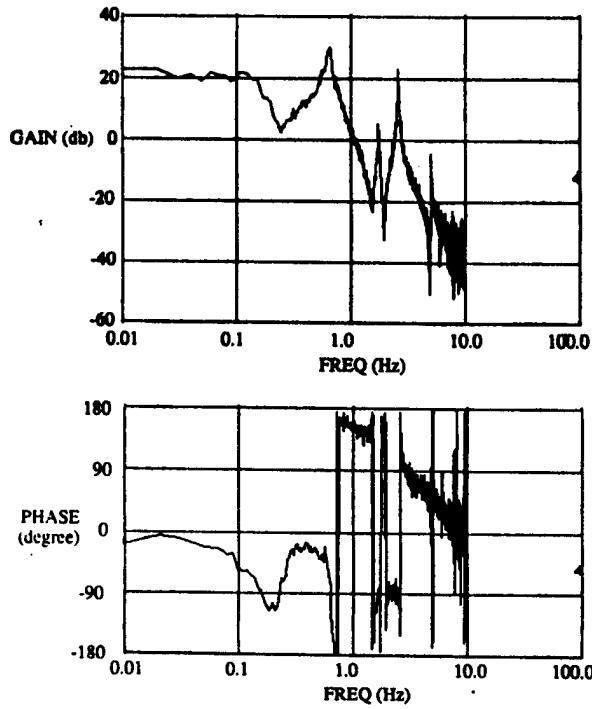
Fig. 3.5-1 Transfer Function Spectral Estimate Generated With Input Parameters MSE=2048, NSE=32768, LSE=1024, and NFFT=2048.

FREQUENCY (Hz)	DAMPING COEFFICIENT
2.57117709973122	6.042845974054128E-003
0.636639669353661	3.641059295623022E-002
0.113709508062294	0.400310467878806

NUMERATOR COEFFICIENT	DENOMINATOR COEFFICIENT
0.313828565339137	0.948448754545826
-1.34219134539618	-5.11306033867448
2.43393981621130	11.9651322910484
-2.36853003555418	-15.6773058644137
1.27677741665536	12.1685830156099
-0.356802485010616	-5.29176230790066
4.333607662209583E-002	1.00000000000000
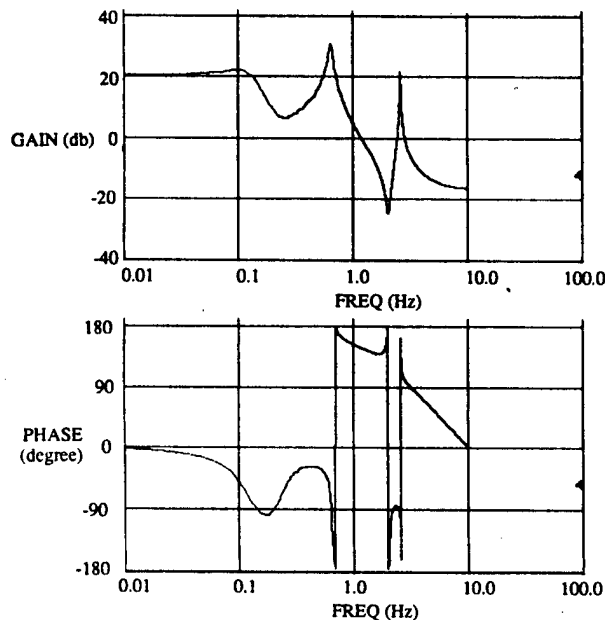
Fig. 3.5-2 The Identified Parametric Model For the Case of Input Parameters MSE=2048, NSE=32768, LSE=1024, and NFFT=2048.
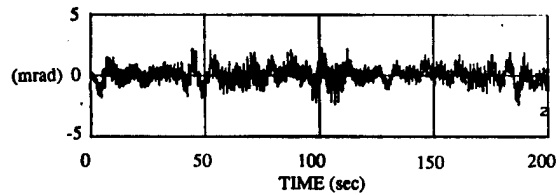
Fig. 3.5-3 Output Error $e = y - \hat{y}$ of the Identified Parametric Model for the Case of Input Parameters MSE=2048, NSE=32768, LSE=1024, and NFFT=2048.
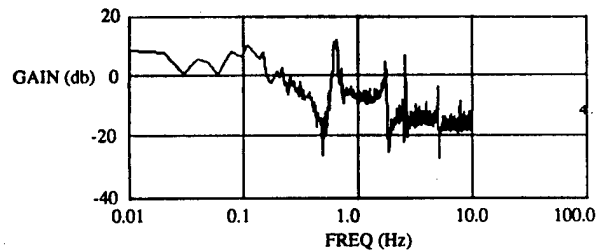
Fig. 3.5-4 Additive Uncertainty of the Identified Parametric Model for the Case of Input Parameters MSE=2048, NSE=32768, LSE=1024, and NFFT=2048.

183

in its profiles. Figure 3.5-6 presents the 3 mode identified parametric model through curve fitting the spectral data of figure 3.5-5. The modal data compare reasonably well with previous results except maybe for the damping coefficient of the 1st mode. The reliability of this identified parametric model is indicated in figure 3.5-7 and figure 3.5-8 which show respectively the output error e and additive uncertainty Δ. They do not show any improvement over that utilizing the nominal parameters. The additive uncertainty even shows a slightly higher maximum value of 15.12 db as compared to 11.37 db for the nominal parameter case. The output error is comparable.

The above comparison indicates that although there is a compromise between frequency resolution and smoothness of the spectral data, for a reasonable selection the curve fitting algorithm will in effect yield an identified model the reliability of which will be insensitive to any fine parameter adjustment.

In the above cases, the whole duration of 1638.4 sec of input and output data were used for analysis. In what follows results obtained by processing only the first 409.6 sec of these data are presented. They also represent the identification results of the shorter experiment. The adopted spectral estimation parameters were MSE=2048, NSE=8192, LSE=1024, and NFFT=2048. Note that the parameters were the same as for the nomimal case, except that here NSE=8912 which reflects the duration of 409.6 sec. The present case has the same frequency resolution as before, but with a reduced number of averaging sections. Hence, more jittery spectral data are expected for the present case, as demonstrated by figure 3.5-9 which shows the TFSE. In fact, it seems that the spikes may be too strong for the curve fitting algorithm to handle. This is indeed the case as indicated in figure 3.5-10 which shows in the 3 mode identified parametric model, the algorithm mistook one of the spikes as a mode. The identification results as obtained yield a large output error and are unacceptable as an estimate of the system model.

Another analysis which also utilizes the data length of 409.6 sec was performed. This time the section number is increased at the expense of frequency resolution. The parameters adopted for spectral estimation were MSE=1024, NSE=8192, LSE=512, and NFFT=1024. Figure 3.5-11 shows the TFSE P_{uy}/P_{uu}. The smoothness of the spectral data is improved greatly over that of figure 3.5-9. This is the result of a reduced spectral data standard deviation due to averaging over an increased number of sections, as well as plotting against frequency values with wider separation. Figure 3.5-12 shows the 3 mode identified parametric model. The modal data seem to agree in general with that of the nominal case. Figure 3.5-13 and 3.5-14 show, respectively, the output error and the additive uncertainty for the identified model. Compared to figure 3.5-3 and figure 3.5-4, they are inferior than that of the nominal case. Figure 3.5-14 has a maximum value of 22.85 db, more than 2 times the nominal values. The output error e is roughly 30% larger in amplitude than the nominal case. These results reflect the tradeoff in identification performance and the length of the identification experiment.

The results in this section underscore the importance of adequate experiment run time in achieving a certain performance. For short experiments, in order to get any performance at all one should give more preference to smoothing out the spectral data in the selection of spectral estimation parameters. For longer experiment, parameter selection which yields

184
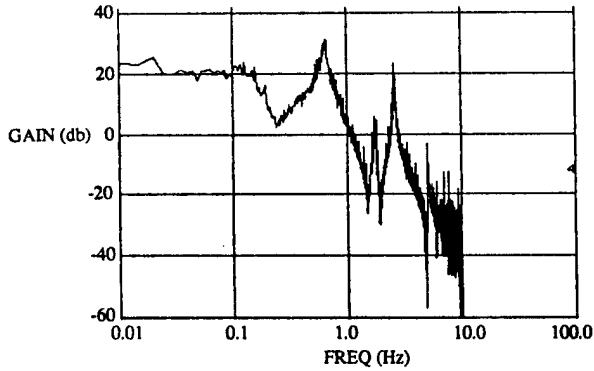
Fig. 3.5-5 Transfer Function Spectral Estimate Generated With Input Parameters MSE=4096, NSE=32768, LSE=2048, and NFFT=4096.

FREQUENCY (Hz)	DAMPING COEFFICIENT
2.57205828578359	6.114618075949580E-003
0.636389853813634	3.512604095163507E-002
0.111894037321595	0.340951142883381

NUMERATOR COEFFICIENT	DENOMINATOR COEFFICIENT
0.350152168960976	0.953231385084840
-1.55056036016632	-5.13365033558000
2.94220765110511	12.0028676849968
-3.05435515824610	-15.7146908061066
1.82409119843728	12.1887000691087
-0.603454249376976	-5.29642479361900
9.225080674588144E-002	1.00000000000000

Fig. 3.5-7 Output Error $e = y - \hat{y}$ of the Identified Parametric Model for the case of Input Parameters MSE=4096, NSE=32768, LSE=2048, and NFFT=4096.
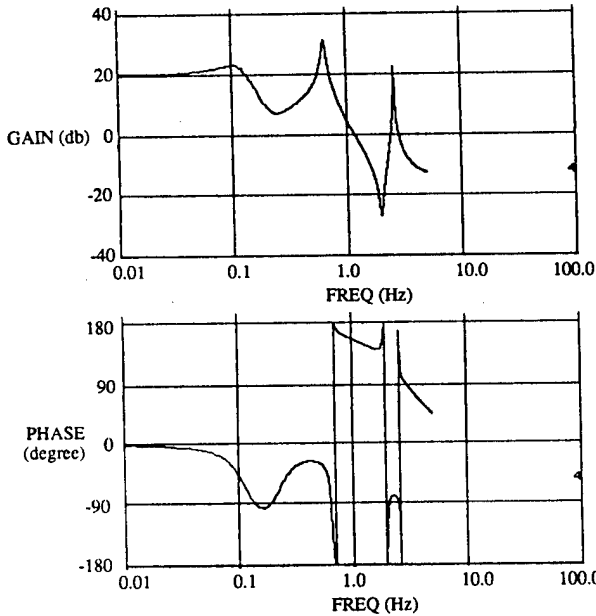
Fig. 3.5-6 The Identified Parametric Model For the Case of Input Parameters MSE=4096, NSE=32768, LSE=2048, and NFFT=4096.
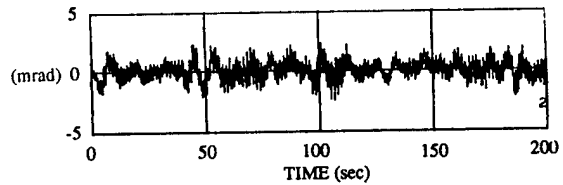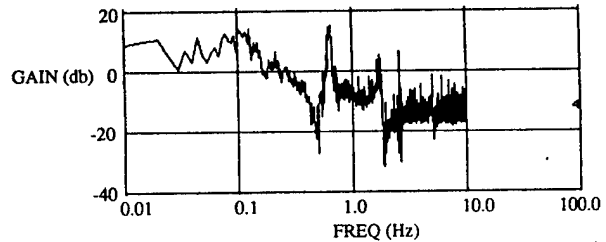
Fig. 3.5-8 Additive Uncertainty of the Identified Parametric Model for the Case of Input Parameters MSE=4096, NSE=32768, LSE=2048, and NFFT=4096.

185
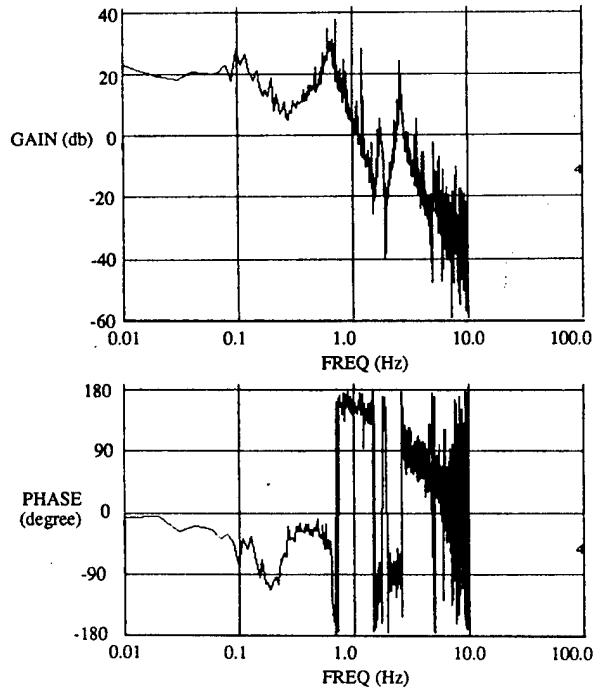
Fig. 3.5-9 Transfer Function Spectral Estimate Generated With Input Parameters MSE=2048, NSE=8192, LSE=1024, and NFFT=2048.

FREQUENCY (Hz)	DAMPING COEFFICIENT
0.903418670317764	1.432779154368610E-002
0.703807778400047	-1.771300318352196E-005
0.626472677230362	2.604034842062283E-002
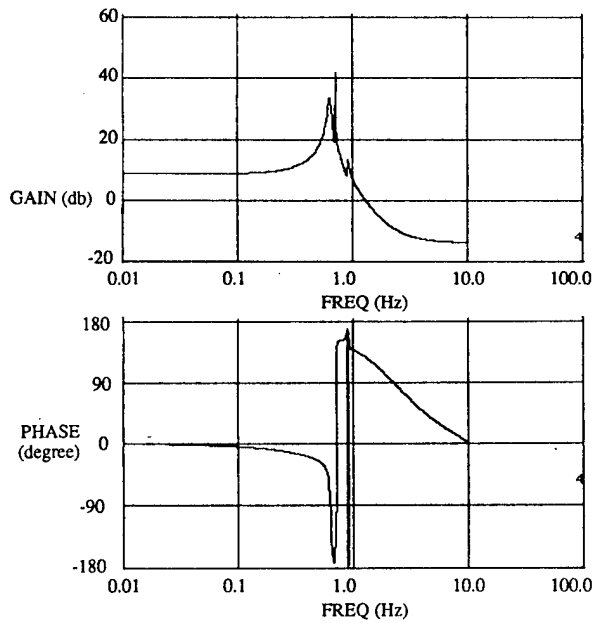
Fig. 3.5-10 The Identified Parametric Model For the Case of Input Parameters MSE=2048, NSE=8192, LSE=1024, and NFFT=2048.

186
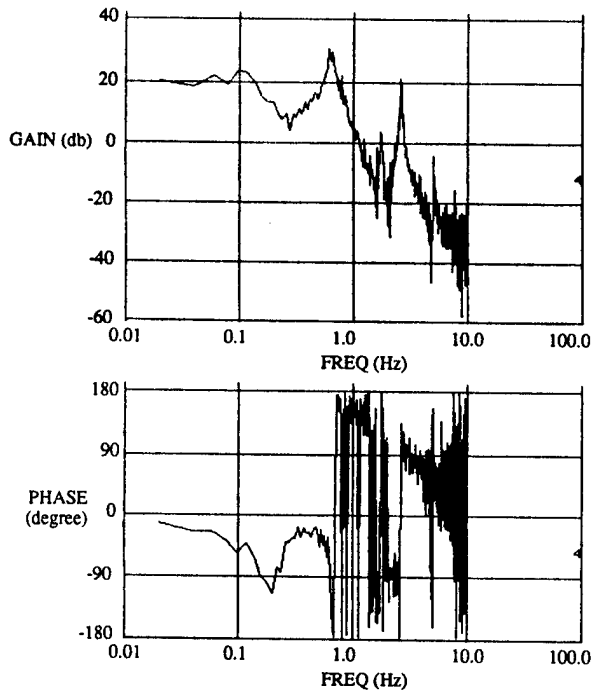
Fig. 3.5-11 Transfer Function Spectral Estimate Generated With Input Parameters MSE=1024, NSE=8192, LSE=512, and NFFT=1024.

FREQUENCY (Hz)	DAMPING COEFFICIENT
2.55706327738039	8.317125048557009E-003
0.637602836226816	3.032732498628372E-002
0.119940809835574	0.342526731048208

NUMERATOR COEFFICIENT	DENOMINATOR COEFFICIENT
0.352492432022151	0.949969364647798
-1.52057341536509	-5.12455258393469
2.79691069370128	11.9990689131527
-2.79780237697469	-15.7254267696356
1.59549920710508	12.2014579446566
-0.498645629605492	-5.30047903308622
7.247488117669851E-002	1.00000000000000
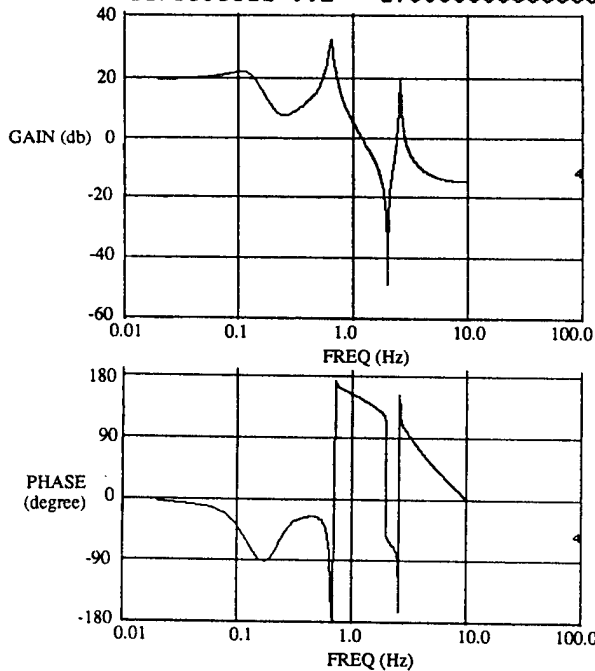
Fig. 3.5-12 The Identified Parametric Model For the Case of Input Parameters MSE=1024, NSE=8192, LSE=512, and NFFT=1024.
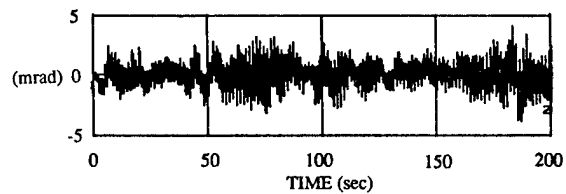
Fig. 3.5-13 Output Error $e = y - \hat{y}$ of the Identified Parametric Model for the case of Input Parameters MSE=1024, NSE=8192, LSE=512, and NFFT=1024.
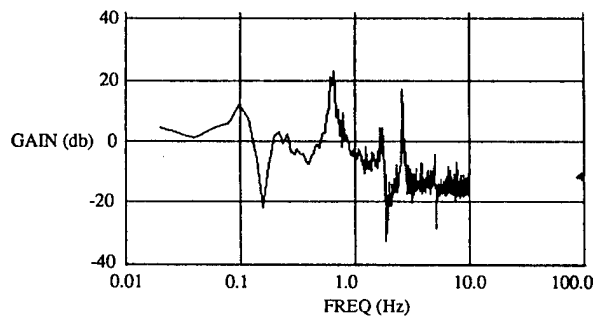
Fig. 3.5-14 Additive Uncertainty of the Identified Parametric Model for the Case of Input Parameters MSE=1024, NSE=8192, LSE=512, and NFFT=1024.

187

reasonable emphasis for both frequency resolution and spectral smoothness is possible. In this case the identification performance is less dependent on any fine adjustment of the parameters. As a final note, all analysis in this section adopted a smoothing factor SF of 0.9 in its curve fitting computation. The effect of varying SF is discussed in the next section.

3.5.2 Smoothing Factor SF

The automated identification procedures as depicted in figure 3.2-1 involve, for each assumed modal order, obtaining an initial transfer function estimate through uniform weighting of the spectral data (W=I in eqn. (2.9-21)), and then generating subsequent estimates via a non-uniform weighting (W$\neq$I) emphasizing the lower frequency portion of the spectrum (see Steps 0 through 4 in Section 2.9.4). The converged transfer function estimate is then adopted as the curve fitted model for the assumed modal order, and the curve fitted model with the lowest modal order that gives rise to the best possible output error performance is adopted as the identified model. The non-uniform weighting is computed based on the previous transfer function estimate as well as on the smoothing factor SF. With SF=1 corresponding to uniform weighting, the present investigation adopted the value of 0.9 for SF by experience. In this section, the effects of adopting different values for SF are discussed.

For comparison with the SF=0.9 case, the automated identification process was carried out using values at SF=0.7 and 0.5. This yielded identified models with modal order 3, in agreement with the SF=0.9 case. However, some differences were noted. In particular, when performing curve fitting computation assuming 4 modes, there were times where utilization of SF=0.7 and SF=0.5 led to transfer function estimates with unstable low frequency modes, while by experience, SF=0.9 always generated reasonable and well behaved estimates for all assumed modal orders. This is, however, consistent with theory: a smaller SF emphasizes poor quality resonance frequency estimates appearing early in the iterative process. For the lower SF cases, the algorithm attempted very fine modelling of these false resonances and led to unstable estimates.

The attention now turns to the 3 mode identified parametric models for the adopted SF values. In theory, lower SF values should result in enhanced identification accuracy in the vicinity of the resonance frequency peaks. Experiment results indicated that there although these phenomena occurred as expected, the actual resonance improvement was small. To demonstrate, in what follows the identified parametric model in section 3.3.1 obtained with the adopted value of SF=0.9 is compared to those obtained with SF=0.7 and SF=0.5. First, results in section 3.3.1 are repeated here for comparison. Figure 3.5-15, figure 3.5-16, and figure 3.3-17 show, respectively, the 3 mode identified parametric model, the output error e, and the additive uncertainty $\Delta = P_{ue}/P_{uu}$ for the 0-3 Hz narrowband experiment in section 3.3.1. They are the same as figure 3.2-56, figure 3.2-57, and figure 3.5-58. The identified parametric model in figure 3.5-15 was obtained via the automated identification procedures with SF=0.9.

To obtain the identified parametric model with SF=0.7, the curve fitting process was carried out for the assumed modal order of 3. However, this time the identified model in

figure 3.5-15 was utilized as a starting transfer function estimate instead of that obtained through uniform weighting. This is because lower SF values usually result in a strong weighting function, and it is therefore desirable to base the computation on a reliable transfer function estimate, as is the one in figure 3.5-15. Such practice also tends to speed up the process of a converging estimate. The identified parametric model was obtained for the present case after three curve fitting iterations with SF=0.7. Figure 3.5-18, figure 3.5-19, and figure 3.5-20 show respectively the identified model, the output error, and the corresponding additive uncertainty. A careful comparison of figures 3.5-17 and 3.5-20 shows that although the two cases are very similar, there is a slight improvement in the SF=0.7 case in the vicinity of the resonance frequency peaks.

Figures 3.5-21 to figure 3.5-23 present the the identification results for SF=0.5. They respectively show the identified parametric model, output error, and the additive uncertainty. For a similar reason, the identified model obtained by using SF=0.7 as given in figure 3.5-18 was taken to be the starting estimate here, rather than the one obtained with uniform weighting. Again, the modal data as presented in figure 3.5-21 is very comparable to those of SF=0.9 and 0.7. However, as expected, the output error and the additive uncertainty show a slight improvement in the vicinity of the resonance frequencies relative to the SF=0.9 and SF=0.7 cases.

This section compared the identification results as obtained adopting smoothing factors of SF=0.9, 0.7, and 0.5. The identified models for the three cases are very comparable with only small improvement in curve fit accuracy for the lower SF values. As expected from the theory, these improvements occur in the vicinity of the resonance frequency peaks. However, offsetting these advantages, using lower SF values often upsets the numerical robustness of the curve fit algorithm. In particular, low SF values seem to make a difference in the computations of curve fitted models when assuming an excessive modal order. Unstable transfer function estimates were obtained with SF=0.7 and 0.5 when the assumed modal order is 4. By experience, SF=0.9 always generated reasonable and well behaved curve fitted results for all cases under investigation. As such, it was adopted as the nominal value.

3.6 Noise Anomaly

The experiment data so far presented in this chapter are, in fact, from a second set of experiments conducted on the testbed structure. When the first set of identification experiments were performed it was observed that there existed high frequency noise in the amplifiers of both hub sensors, HS1 and HS10. Interaction of this noise with the data sampling rate resulted in aliased "resonance-like" data between 5 Hz and 6 Hz. As such, results from this set of experiment were not satisfactory, though valuable experience in anomaly detection was gained. To correct the situation, an analog filter was put at the amplifier output. With a cutoff frequency of 80 Hz, the filter dynamics were sufficiently separated from the structural dynamics, and eliminated the aliased noise.
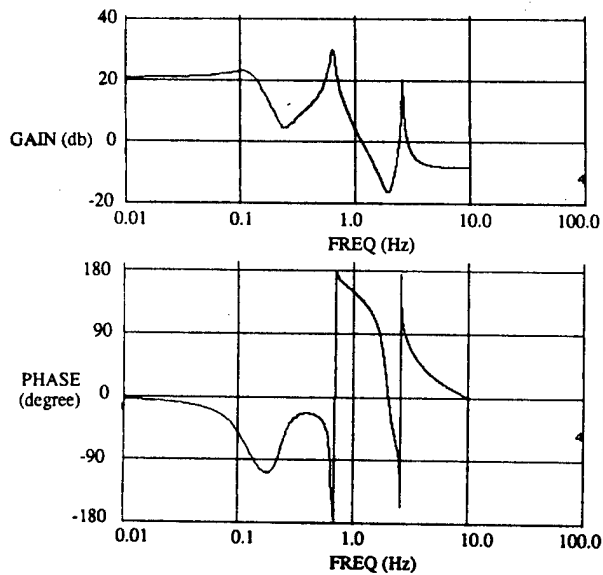
FREQUENCY (Hz)	DAMPING COEFFICIENT
2.56358370722263	7.608804875517834E-003
0.632041998399339	3.898615970482653E-002
0.117540339237004	0.368285236570123

NUMERATOR COEFFICIENT	DENOMINATOR COEFFICIENT
0.556150474832277	0.946544706814845
-2.60865169349456	-5.10769098624538
5.31082193679151	11.9626948396374
-6.02879199045097	-15.6835556824229
4.03453041630456	12.1764851971015
-1.51988896118575	-5.29444165114957
0.256223708213091	1.00000000000000

Fig. 3.5-15 The Identified Parametric Model Generated With Smoothing Factor SF=0.9 for the 4-10 Axis Narrowband (0-3 Hz) Excitation Case.
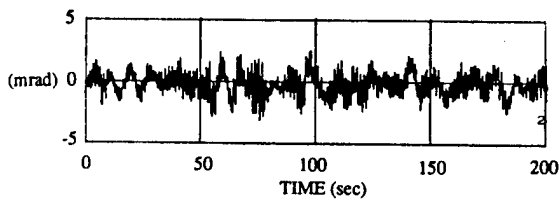

Fig. 3.5-16 Output Error $e = y - \hat{y}$ of the Identified Parametric Model Generated With SF=0.9 for the 4-10 Axis Narrowband (0-3 Hz) Excitation Case.
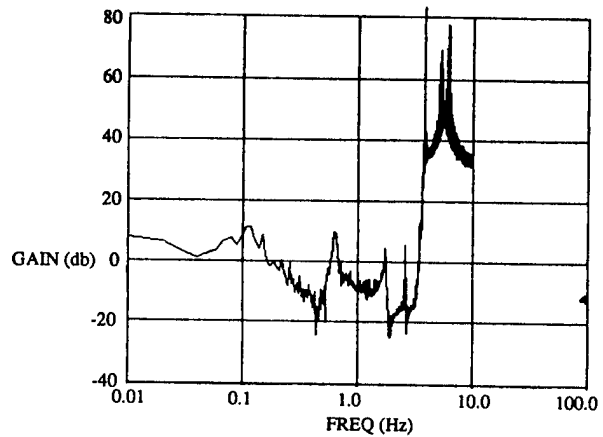

Fig. 3.5-17 Additive Uncertainty $\Delta = P_{ue}/P_{uu}$ of the Identified Parametric Model Generated With SF=0.9 for the 4-10 Axis Narrowband (0-3 Hz) Excitation Case.

190
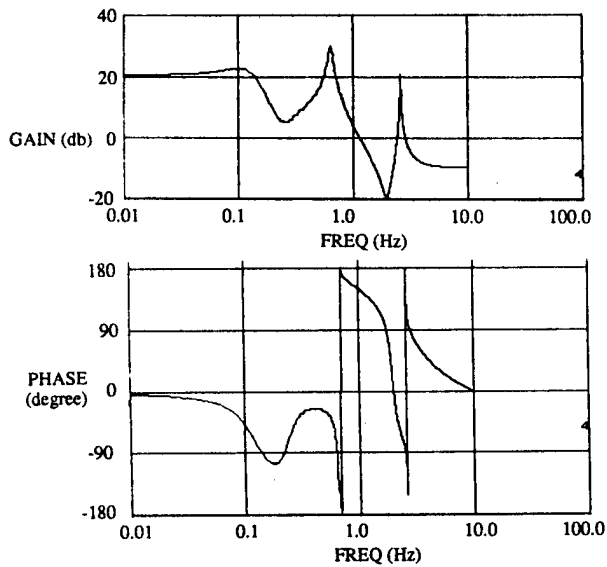
FREQUENCY (Hz)	DAMPING COEFFICIENT
2.56534203419177	7.195431691319261E-003
0.632409536227798	3.880313146857003E-002
0.117754553881829	0.375779421372669

NUMERATOR COEFFICIENT	DENOMINATOR COEFFICIENT
0.505844611324059	0.946655998504506
-2.35012209549786	-5.10767021193017
4.72849898748035	11.9608072144446
-5.28944476592453	-15.6796807405971
3.47651780340498	12.1733435471774
-1.28363430948101	-5.29351897976374.
0.212732416165314	1.00000000000000

Fig. 3.5-18 The Identified Parametric Model Generated With Smoothing Factor SF=0.7 for the 4-10 Axis Narrowband (0-3 Hz) Excitation Case.
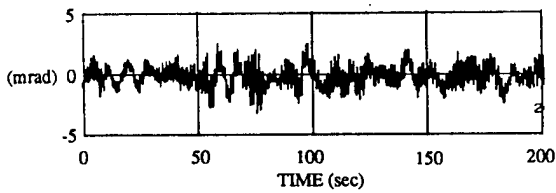

Fig. 3.5-19 Output Error $e = y - \hat{y}$ of the Identified Parametric Model Generated With SF=0.7 for the 4-10 Axis Narrowband (0-3 Hz) Excitation Case.
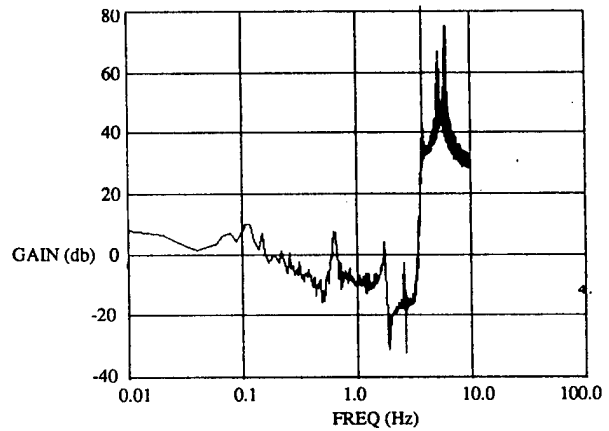

Fig. 3.5-20 Additive Uncertainty $\Delta = P_{ue}/P_{uu}$ of the Identified Parametric Model Generated With SF=0.7 for the 4-10 Axis Narrowband (0-3 Hz) Excitation Case.

191
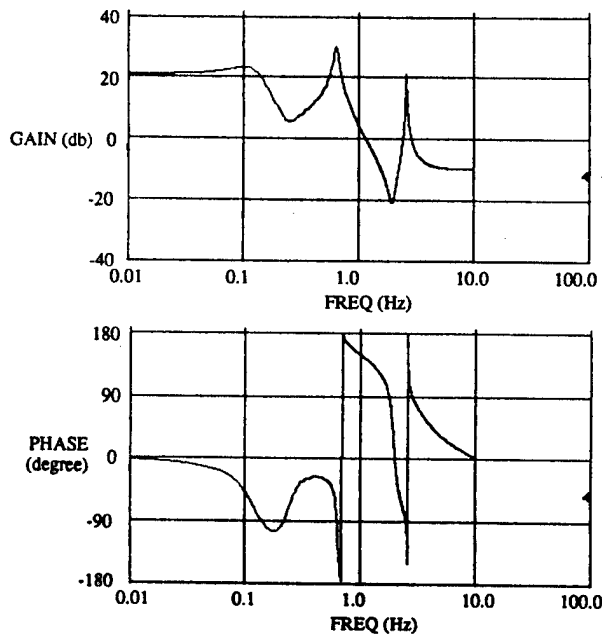
FREQUENCY (Hz)	DAMPING COEFFICIENT
2.56573383010066	7.0621017194786612E-003
0.632518027666067	3.869401099319726E-002
0.117782769843492	0.373174474083985

NUMERATOR COEFFICIENT	DENOMINATOR COEFFICIENT
0.489896452658187	0.947072627201221
-2.26806922238341	-5.10927813001621
4.54307914097654	11.9636288636767
-5.05306542245301	-15.6820420895290
3.29723752299239	12.1743537315201
-1.20719439661769	-5.29369817934793
0.198504070720536	1.00000000000000

Fig. 3.5-21 The Identified Parametric Model Generated With Smoothing Factor SF=0.5 for the 4-10 Axis Narrowband (0-3 Hz) Excitation Case.
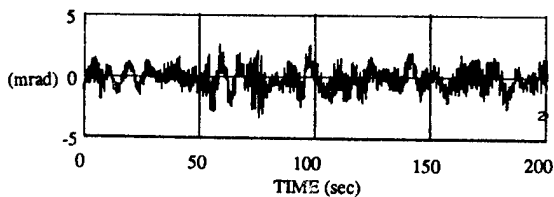
Fig. 3.5-22 Output Error $e = y - \hat{y}$ of the Identified Parametric Model Generated With SF=0.5 for the 4-10 Axis Narrowband (0-3 Hz) Excitation Case.
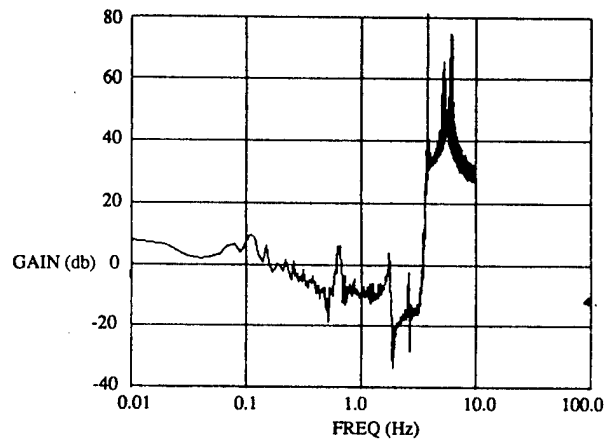
Fig. 3.5-23 Additive Uncertainty $\Delta = P_{uc}/P_{uu}$ of the Identified Parametric Model Generated With SF=0.5 for the 4-10 Axis Narrowband (0-3 Hz) Excitation Case.

192

For demonstration, figure 3.6-1 shows the response from the HS1 hub angular sensor without the analog filter. Figure 3.6-2 shows the same with the analog filter in place and subjected to the same input. The presence of the high frequency noise in figure 3.6-1 and the improvement in figure 3.6-2 are apparent. In addition, the figures show that except for the noise, the dynamics of the structure were not changed due to the addition of the filter. Figure 3.6-3 and figure 3.6-4 compare in more details the noise levels in the hub sensors. Figure 3.6-3 presents for the HS1 sensor the noise measurement and its corresponding power spectral density. On the left is shown the case without filter, and on the right, the case with filter. The power spectral densities were obtained by taking and processing noise measurements of 1638.4 sec duration adopting nominal spectral estimation parameters. Figure 3.6-4 presents the same quantities for the HS10 hub sensor. The figures reveal drastic improvement for the case with the analog filter in place. The noise amplitude of the HS1 hub sensor was 2 mrad without the filter. The power spectral density showed a base level of roughly -6 db and a strong modal peak of 38 db at around 6 Hz. This changed after the filter was put in. The noise amplitude was reduced to 0.05 mrad and the power spectral density showed a base value of -60 db with a modest modal peak of -38 db. Noise reduction of HS10 due to addition of the filter is just as drastic as demonstrated in figure 3.6-4.

In this section, identification results for the first set of experiments are presented. They serve to complement the experimental results of the improved hub sensors described in previous sections, as well as to demonstrate the performance of the identification algorithms and procedures under an extremely noisy environment. Only the wideband experimental results will be presented.

The 1-7 axis results are given first. Figure 3.6-5 shows the 200 sec time history of the system response as measured by hub sensor HS1 subjected to wideband excitation input at hub torquer HA10. The corresponding TFSE, generated adopting the nominal spectral estimation parameters, is shown in figure 3.6-6. Compared to figure 3.2-3 and 3.2.9 of the improved sensor case, the presence of noise in the present data, especially at high frequency, is obvious. In fact, the noise component is so strong that the 5th mode is being obscured in figure 3.6-6. Another thing noted is the enhanced damping of the 1st mode in the figure 3.2-9, which should not have been due to the noise improvement. The boom of the structure was taken down for servicing during the time when the analog filter was put in place. Increased damping of the 1st mode was then observed ever since the boom was replaced, in spite of the fact that great care has been taken to put the boom back in exactly the same position as before.

Figure 3.6-7 shows the identified parametric model generated with the same automated identification procedures as depicted before and with SF=0.9. On comparison with figure 3.2-17, while the frequency data are quite comparable, the damping of the 1st mode is almost doubled for the improved hub sensor case. Figure 3.6-8 and figure 3.6-9 show the output error and the additive uncertainty. As compared to the noise improved case of figure 3.2-19 and figure 3.2-21, the errors here seem to be larger with more of the high frequency components. This is due to the dominant colored noise from the hub sensor which is not modelled in the identified parametric model and, hence, showing up in e and Δ. The errors in the low frequency region, which reflect the modelling performance of the

193

low modes, however, are quite comparable for the two cases.

Similar results for the noisy 4-10 axis HS10 hub sensor are shown in figure 3.6-10 through 3.6-13. Figure 3.6-10 shows the system response as observed from HS10 subjected to a wideband excitation input at HA1. Figure 3.6-11 shows the corresponding TFSE. They are compared with figure 3.2-26 and figure 3.2-29 for the improved sensor case. Same as the 1-7 axis, the 1st mode here shows a lighter damping than before. Obviously, taking down and putting back the boom have the same effect on both axes. The identified parametric model is presented in figure 3.6-12. The modal data again comes quite close to the values as in the improved sensor case, except for the damping coefficient for the 1st mode. The frequency values are slightly different to that of the 1-7 axis for the noisy sensor case. This reflects the slight non-symmetry of the two axes of the structure which was also indicated by the results of the improved sensor case. Finally, figure 3.6-13 and figure 3.6-14 present the output error and the additive uncertainty. Compared to figure 3.2-35 and figure 3.2-37, they show comparable modelling performance in the low frequency portion of the spectrum. For the high frequency region, the performance is reduced due to the presence of colored noise.

In summary, this section shows that except for the increased damping, the modal data for the system before and after sensor improvement are quite agreeable, even to the extent of reflecting the slight non-symmetry in the structure. The performance of the present algorithm in curve fitting low frequency modes was not affected by the presence of strong higher frequency noise. The strong high frequency noise was passed on to become a high frequency component of Δ and result in a larger output error. The increased damping of the 1st mode due to the boom removal and restoration is interesting. A possible physical explanation is that the hub flexure bearing shifted its position. No matter the cause, however, such observation does underscore the importance of on-orbit system identification.
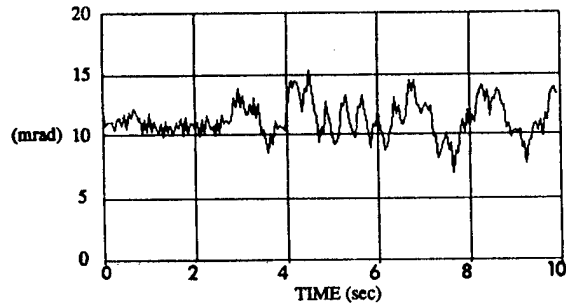
Fig. 3.6-1 Output Response at Hub Sensor HS1 Without Analog Filter Showing the Presence of Noise.
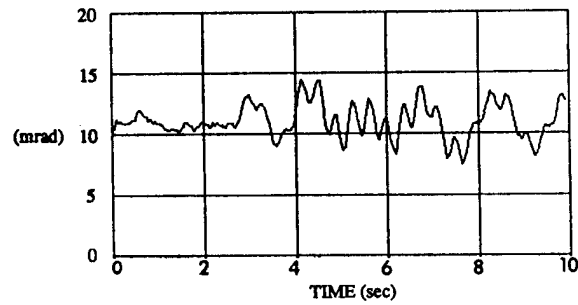

Fig. 3.6-2 Output Response at Hub Sensor HS1 With Analog Filter Showing the Reduction of Noise.
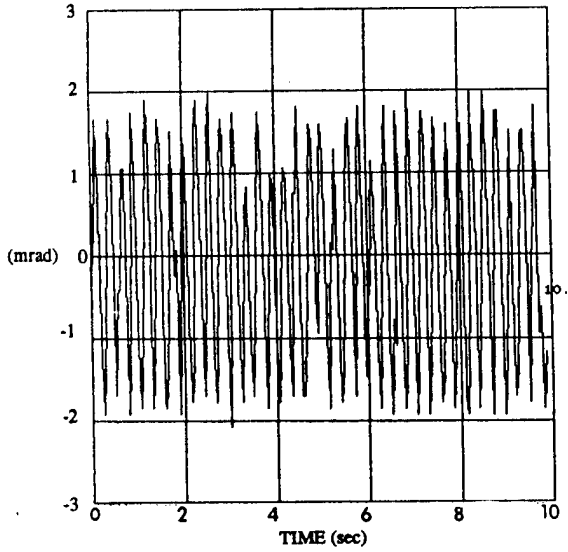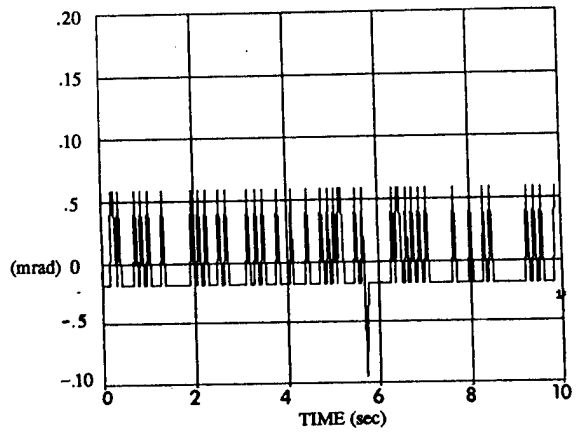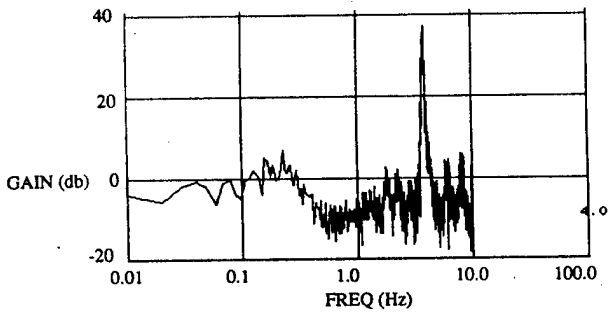
195
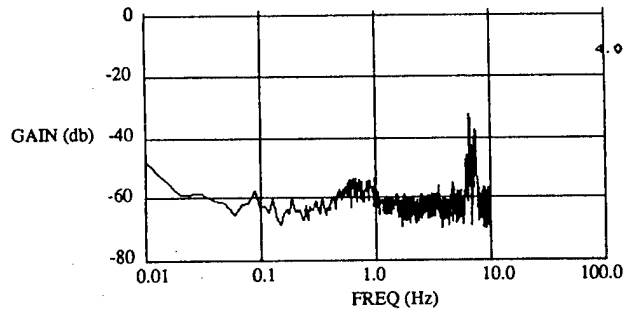
Fig. 3.6-3 Comparison of Noise Measurements and Power Spectral Densities For Hub Sensor
HS1 With and Without the Analog Filter.
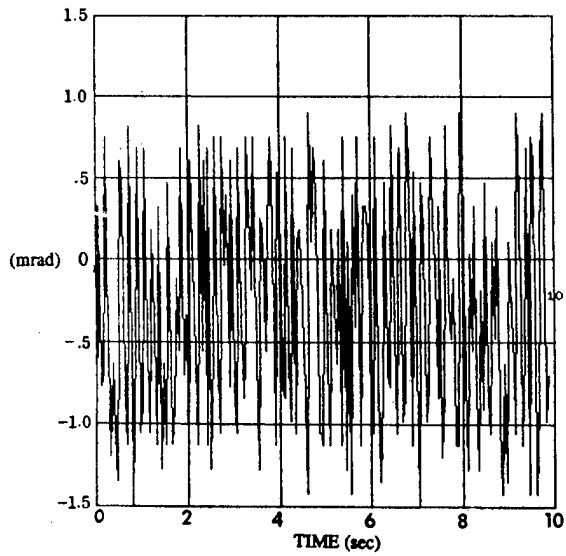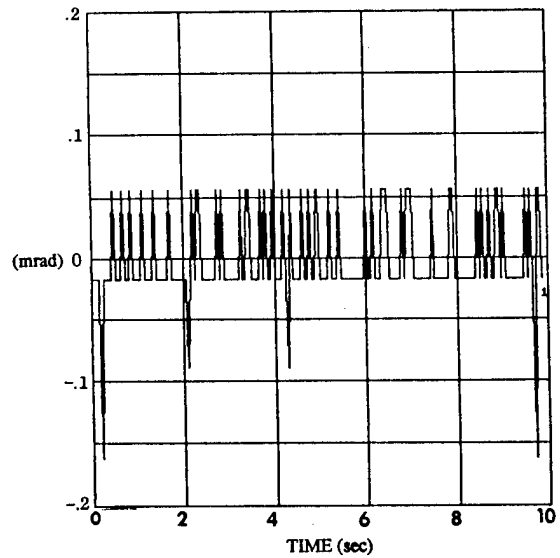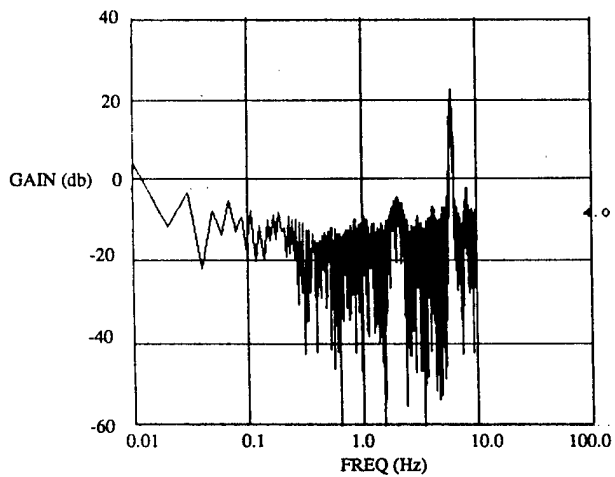
196
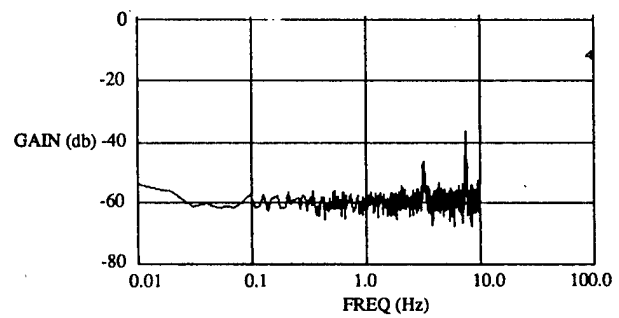
Fig. 3.6-4 Comparison of Noise Measurements and Power Spectral Densities For Hub Sensor
HS10 With and Without the Analog Filter.

197
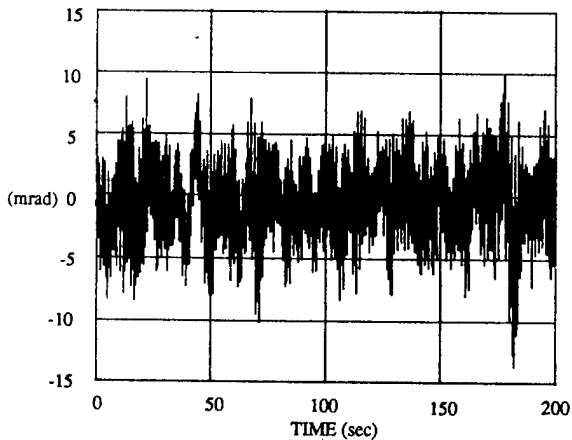
Fig. 3.6-5 Output Response for the 1-7 Axis Hub Actuator/Sensor Wideband Excitation Case measured at Sensor HS1 Without Analog Filter

FREQUENCY (Hz)	DAMPING COEFFICIENT
2.67547021112415	7.269643177317466E-003
0.653294464078347	3.917800284883050E-002
0.120437875403679	0.215618536974848

| NUMERATOR COEFFICIENT	DENOMINATOR COEFFICIENT
0.355168409423887	0.956361918122367
-1.52666269056204	-5.09845625812123
2.80215246570510	11.8362515016420
-2.79214778767787	-15.4536960580016
1.57069349623486	12.0102719384561
-0.471447358232452	-5.25069203225073
6.264311954156344E-002	1.00000000000000
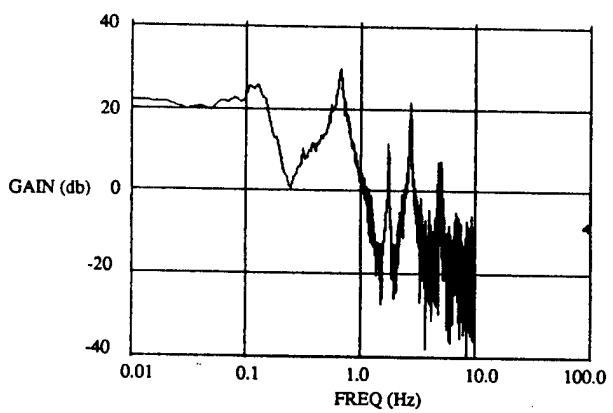
Fig. 3.6-6 Transfer Function Spectral Estimate for the 1-7 Axis Hub Actuator/Sensor Wideband Excitation Case Based on Noisy Sensor HS1 Measurements.
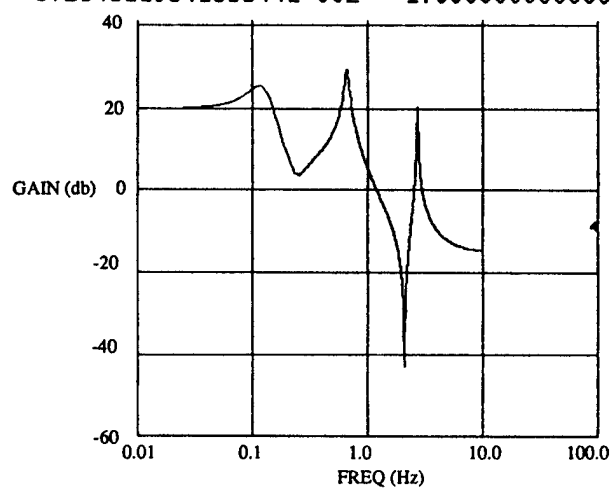

Fig. 3.6-7 The Identified Parametric Model for the 1-7 Axis Hub Actuator/Sensor Wideband Excitation Case based on Noisy Sensor HS1 Measurements.
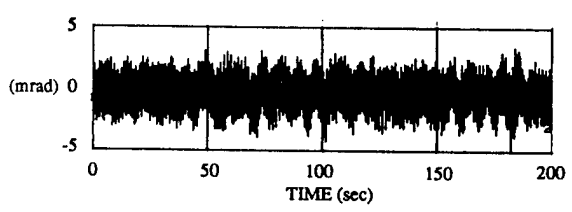

Fig. 3.6-8 Output Error of the Identified Parametric Model for the 1-7 Axis Hub Actuator/Sensor Wideband Excitation Case based on Noisy Sensor HS1 Measurements.
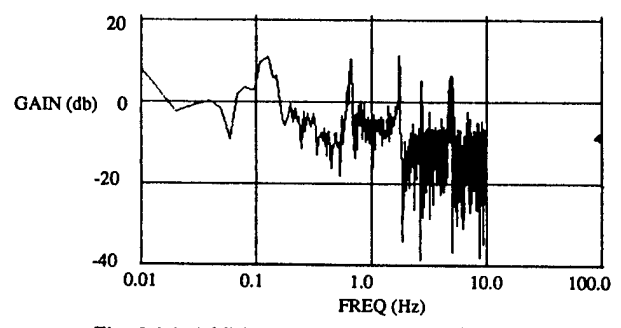

Fig. 3.6-9 Additive Uncertainty of the Identified Parametric Model for the 1-7 Axis Hub Actuator/Sensor Wideband Excitation Case based on Noisy Sensor HS1 Measurements.

198
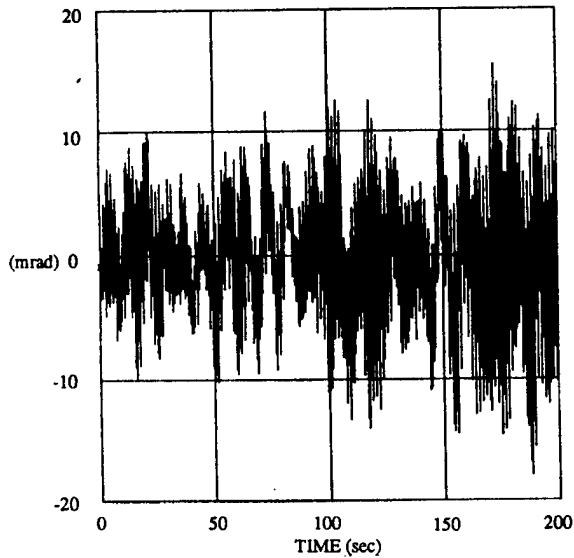
Fig. 3.6-10 Output Response for the 4-10 Axis Hub Actuator/Sensor Wideband Excitation Case measured at Sensor HS10 Without Analog Filter

FREQUENCY (Hz)	DAMPING COEFFICIENT
2.56884943455412	5.455356722170957E-003
0.621382047511895	1.368979649122936E-002
0.109041657208267	0.136614927020176

NUMERATOR COEFFICIENT	DENOMINATOR COEFFICIENT
0.394696450073707	0.976764222147167
-1.71155070162749	-5.24020890991247
3.16775158975491	12.2073862829902
-3.18478098471892	-15.9248859916982
1.81060678404179	12.3044619770214
-0.547862502604961	-5.32348989977886
7.150012603923322E-002	1.00000000000000
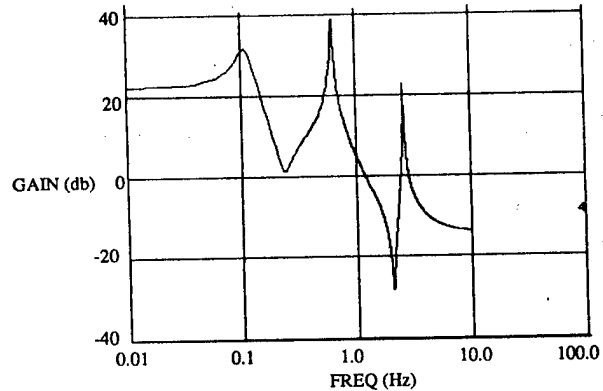
Fig. 3.6-11 Transfer Function Spectral Estimate for the 4-10 Axis Hub Actuator/Sensor Wideband Excitation Case based on Noisy Sensor HS10 Measurements.

Fig. 3.6-12 The Identified Parametric Model for the 4-10 Axis Hub Actuator/Sensor Wideband Excitation Case based on Noisy Sensor HS10 Measurements.

Fig. 3.6-13 Output Error of the Identified Parametric Model for the 4-10 Axis Hub Actuator/Sensor Wideband Excitation Case based on Noisy Sensor HS10 Measurements.
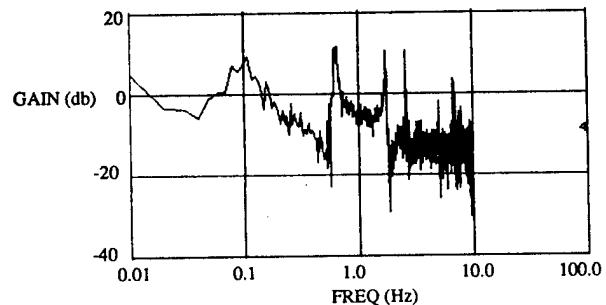
Fig. 3.6-14 Additive Uncertainty of the Identified Parametric Model for the 4-10 Axis Hub Actuator/Sensor Wideband Excitation Case based on Noisy Sensor HS10 Measurements.

199

CHAPTER 4. CONCLUSIONS

4.1 A General Perspective

In this study, we have been specifically interested in using the system identification results to enable the on-line design of robust high performance control systems. The use of real-time on-orbit information for control design has the potential to allow performance robustness and control accuracy far beyond that attainable by using nominal system descriptions obtained from ground testing and analysis alone.

The goal of supporting on-line robust control design has been particularly useful in focusing the identification task for realistic on-orbit testing applications. Rather than trying to estimate the entire structure, as is typically done in ground structural testing, only key transfer function parameters and uncertainty bounds are identified as are necessary for on-line design and tuning of robust controllers. This motivated the approach taken here of estimating transfer function coefficients as well as using the output error to characterize the additive uncertainty. This approach avoids recreating in an on-orbit environment the extensive instrumentation required for ground testing, and makes efficient use of the actuators and sensors already available on the system. Extensive and time-consuming testing is also avoided since identification bandwidths only need to be chosen compatible with control bandwidths.

Considerable experience was gained in developing and experimentally validating the on orbit frequency domain identification methodology. Overall, the basic results of the present investigation have been very encouraging and provide many practical insights into the problem of performing system identification in an on-orbit environment. These practical issues and other results obtained from both the theoretical and practical developments in the course of this work on the facility testbed are discussed in the following section.

4.2 Summary

The results of this investigation indicate that with the identification objectives suitably restricted towards supporting control design efforts, on-orbit identification is a realistic goal. This effort has successfully identified key transfer function coefficients and additive uncertainty bounds needed for robust control design efforts. Some of the practical issues associated with this approach for on-orbit identification are discussed below.

1) The length of the experiment time is driven by the frequency of the lowest mode. This has strong relevance to the on-orbit time allocated to performing on-orbit identification. In this study a 27.3 minute experiment was used in order to curve fit the 0.09 Hz mode with a good resolution.

2) The system identification was designed to operate with some degree of autonomy and to restrict the "human in the loop" requirements. Decisions are still to be made concerning the choice of bandwidths, initial model order estimate, and smoothing factors.

3) The present investigation considered identification of single-input single-output transfer functions. Multiple-input multiple-output system identification would also be accommodated with the present scheme by processing each input/output pair separately. More efficient processing is desired for the multiple-input multiple-output case.

4) Input signals considered here were wideband, narrowband, and sine-dwell processes. On-line capability of conducting digital filter design is available to support other input designs. The issue of "optimal" input design subject to on-orbit constraints is a topic for continuing investigation.

5) Numerical problems arose in finding roots of high-order polynomials. This was revealed to be due to the over-sampling of the low frequency modes whose roots coalesced to $1+j0$. A special routine was developed for rootfinding in such circumstances.

6) Model order is determined by successively increasing the number of modes in the curve fit until an adequate output error profile is observed. The search is initialized by the model order estimate obtained from a PMM test. Since searching by sequential curve fitting is a time consuming process, an accurate initial estimate of the model order from the PMM test is desired. In the PMM algorithm, this essentially amounts to proper choice of threshold value (on the determinant or determinant ratios), and proper treatment of noise disturbance effects. The present implementation of the PMM test appears to underestimate the model order, as compared to results of the sequential curve fit search. Modifications of the PMM along the lines outlined above remain to be investigated.

7) Two implementations were developed for the PMM test. The deterministic algorithm PMMD (i.e., exact assuming no measurement noise), gave consistently better performance than the stochastic algorithm PMMS (which approximates sums by correlations). Evidently, experiments on the order of half-an-hour may not be long enough to satisfy the infinite time requirement for the stochastic algorithm.

8) Special techniques for Sine-Dwell gain and phase estimation were required to avoid errors associated with using sampled data sinusoidal inputs. Standard correlation techniques produced very poor results, particularly with respect to the low frequency structural modes. A recursive least squares algorithm with exponential forgetting was developed to ensure robust and accurate estimation for this class of problems.

9) The additive uncertainty δ_m is estimated by the output error cross-correlation Δ. This approach is shown to provide a superior estimation to the additive uncertainty than the traditional approach of utilization of the curve fitted error τ.

10) It is well known that frequency domain curve fitting techniques based on equation error representations have implicit high frequency emphasis [10]. This problem was overcome in the present study by using an iterative reweighting scheme. A novel smoothing technique was also introduced to alleviate the problem of resonances estimated early in the sequence reinforcing themselves in the reweighting scheme and becoming fixed points of the iteration.

11) Experiments were performed on the two hub axes of the JPL/AFAL Flexible Testbed utilizing the collocated hub torquers and angular sensors. The identified frequencies

and damping coefficients of the three dominant modes of the 1-7 axis are 0.126 Hz, 0.666 Hz, and 2.68 Hz, and 0.32, 0.0564, and 0.00746. Those of the 4-10 axis are 0.114 Hz, 0.637 Hz, and 2.57 Hz, and 0.4, 0.0364, and 0.0604. The frequency values agree well with those of the finite element model of the structure, and confirm the slight nonsymmetry of the two axes. The dynamics of these modes are identified to within 10% to 30% as indicated by the additive uncertainty estimate Δ.

12) There were modes, apparent in the nonparametric estimate h, that were not fitted in the parametric plant estimate $\hat{p}$. The error resulting from omitting these modes, however, was no larger than the fitting error of the identified modes. This indicated that the curve fitting algorithm properly determined their omission and converged to a reduced-order model which tended to weight all frequencies equally in the final fit.

13) The damping of the first mode of the system increased after the boom was taken apart and replaced back. A possible explanation of this change is that the hub bearing had settled into a different position. Regardless of the cause, however, such observation serves to underscore the importance of a system identification capability.

CHAPTER 5. REFERENCES

[1]   H.C. Vivian, et al., *Flexible Structure Control Laboratory Development and Technology Demonstration*, Final Report prepared for USAF-AFAL/NASA-OAST, under Task Order 69006, through NASA Task Re-182, Amendment 431, Jet Propulsion Laboratory, October 1987.

[2]   W.H. Press, et al., *Numerical Recipes: The Art of Scientific Computing*, Cambridge University Press, New York, 1986.

[3]   C.J. Weinstein, et al., Eds., *Programs for Digital Signal Processing*, IEEE Press, New York, 1979.

[4]   C.L. Lawson and R.J. Hanson, *Solving Least Squares Problems*, Prentice-Hall, Englewood Cliffs, New Jersey, 1974.

[5]   G.E. Fleischer, "User's Command Interface to the RPL Demonstration -- System Software Design #2," JPL IOM 347-86-511, Internal Document, June 26, 1986.

[6]   D. Eldred, et al., "Large Flexible Structure Control Technology Experiment and Facility Design," Fourth IFAC Symposium on Control of Distributed Parameter Systems, July 1986.

[7]   D.S. Bayard, et al., "Nonparametric Identification Task Description for the JPL/AFAL Experiment" JPL EM 347-87-221, Internal Document, October 1987.

[8]   D.S. Bayard, et al., "Software Description for Nonparametric System ID on the JPL/AFAL Experiment: Revision 3," JPL EM 347-88-242, Internal Document, May 1988.

[9]   Y. Yam, "Nonparametric Identification Experiment," presented at USAF-AFAL/NASA-OAST Workshop on Model Determination for Large Space Systems, California Institute of Technology, March 1988.

[10] L. Ljung, *System Identification: Theory for the User*, Prentice-Hall, Englewood Cliffs, New Jersey, 1987.

[11] E. Mettler, M. Milman, and D.S. Bayard, "EOS Integrated Payload Articulation and Identification System," 11th Annual AAS Guidance and Control Conference, Keystone, Colorado, February 1988.

[12] R. L. Kosut, "On-Line Identification and Control Tuning of Large Space Structures," *Proc. Fifth Yale Conference on Adaptive Systems Theory*, Yale University, May 1987.

[13] M.H. Milman, E. Mettler, and D.S. Bayard, "Identification and Control Integration Strategies," presented at USAF-AFAL/NASA-OAST Workshop on Model Determination for Large Space Systems, California Institute of Technology, March 1988.

[14] Y. Yam and D.S. Bayard, "Integrated Cooling and Finalized Software Description for Nonparametric System ID on the JPL/AFAL Experiment," JPL EM 343-1127, Internal Document, April 1989.

[15] D.R. Meldrum, "A Step-by-Step Procedure for Running the Digital Filter Routine EQIIR," JPL IOM 347-87-522, Internal Document, June 1987.

[16] A.V. Oppenheim and R.W. Schafer, *Digital Signal Processing*, Chapter 10, pp. 292-293, Prentice-Hall, Englewood Cliffs, New Jersey, 1975.

[17] C.L. Thornton and G.J. Bierman, "UDU Covariance Factorization for Kalman Filtering," in *Control and Dynamic Systems*, C.T. Leondes, Ed., Academic Press, New York, 1980.

[18] F.B. Hildebrand, *Introduction to Numerical Analysis*, Dover Publications, New York, 1987.

[19] F.Y. Hadaegh, "Dynamic Model Structure Determination from Experimental Data," JPL EM 347-87-213, Internal Document, 1987.

[20] C.M. Woodside, "Estimation of the Order of Linear Systems," *Automatica*, vol. 7, pp. 727-733, 1971.

[21] R.C.K. Lee, *Optimal Estimation, Identification, and Control*, MIT Press, Cambridge, Massachusetts, 1964.

[22] A. Papoulis, *Probability, Random Variables, and Stochastic Processes*, McGraw-Hill, New York, 1965.

[23] F.Y. Hadaegh and R.E. Scheid, "A Product Moment Matrix Approach for Model Order Determination for the JPL/AFAL Ground Experiment Facility," JPL EM 347-88-240, Internal Document, May 1988.

[24] M. Vidyasagar, *Control System Synthesis: A Factorization Approach*, MIT Press, Cambridge, Massachusetts, 1985.

[25] The USAF-AFAL/NASA-OAST Workshop on Model Determination for Large Space Systems, California Institute of Technology, March 1988.

[26] G.C. Goodwin and K.S. Sin, *Adaptive Filtering Prediction and Control*, Prentice-Hall, Englewood Cliffs, New Jersey, 1984.

[27] L. Ljung and T. Soderstrom, *Theory and Practice of Recursive Identification*, MIT Press, Cambridge, Massachusetts, 1983.

[28] D.R. Meldrum, "A Description of the Changes to the IEEE Spectral Estimation Software Routines, CCSE and CMPSE," JPL IOM 347-87-567, Internal Document, June 1987.

[29] J.M. Mendel, *Discrete Techniques of Parameter Estimation: The Equation Error Formulation*, Marcel Dekker, Inc., New York, 1973.